A Contribution to Vibroacoustics of Highly Heterogeneous Metastructures through Wave Finite Element Scheme

Dongze Cui

Numéro d'ordre NNT: 024ECDL0031 Année: 2024

THÈSE DE DOCTORAT DE L'UNIVERSITÉ DE LYON
OPÉRÉE AU SEIN DE L'ÉCOLE CENTRALE DE LYON

ÉCOLE DOCTORALE MEGA
Mécanique, Enegétique, Génie civil et Acoustique

Spécialité: Génie Mécanique, productique acoustique

Soutenue le 26/09/2024 par

Dongze CUI

A Contribution to Vibroacoustics of Highly Heterogeneous Metastructures through Wave Finite Element Scheme
Une contribution à la vibroacoustique des métastructures hautement hétérogènes par le schéma d'éléments finis d'ondes

---

Devant le jury composé de:

Elisabetta Manconi	Professeur, Université de Parma	Rapportrice
Stéphane Moreau	Professeur, CRASH-UdeS, UdeS	Rapporteur
Mohamed-Ali Hamdi	Professeur, UTC Compiègne	Président
Raef Cherif	Professeur, Université du Québec à Rimouski	Examinateur
Mohamed Ichchou	Professeur, LTDS, ECL	Directeur
Noureddine Atalla	Professeur, CRASH-UdeS, UdeS	Co-Directeur
Abdelmalek Zine	Maître de Conférence, ICJ, ECL	Co-Directeur

Acknowledgements

Foremost, my appreciation goes to all the professors in the defense committee for their valuable contribution to this thesis. I would like to express the most sincere gratitude to all my supervisors, Prof. Abdel-Malek ZINE, Prof. Mohammed ICHCHOU, and Prof. Noureddine ATALLA, for their unwavering support, infinite knowledge, and inspiration throughout my Ph.D. journey. Their academic guidance helped me in all the time of research and writing of this thesis, they offered me the best scientific research training. Thanks also for their warm support and encouragement in the last four years, they are the nicest person to me.

Prof. Fabrice THOUVEREZ and Prof. Nacer HAMZAOUI assisted with my Comité de Suivi de Thèse at Université de Lyon, Prof. Olivier BAREILLE and Prof. Stéphane MOREAU attended my Définition de Projet de Recherche at Université de Sherbrooke. Their understanding and support enabled me to overcome challenges and continue my Ph.D. study.

I am grateful to all those with whom I have had the pleasure to work during my project. I am thankful for the stimulating discussions and camaraderie shared with my colleagues at LTDS over the three years, as well as my friends: CHEN Xi, CAO Xuan, CHENG Zhongyi, WANG Huaity, YUAN Hao, and so on, for our stimulating discussions, for all the fun we have had in the last three years in Lyon, and for the clearest support and clarification when I was being slandered, they have been the constant source of encouragement. My gratitude also goes to "Station des étudiants chinois en France" for organizing the hiking activities and scientific forums, which inspired my research work.

I am grateful to my supervisors for providing me the opportunity to pursue another Ph.D. degree in Québec. This experience allowed me to reflect deeply on my past, future, and dreams. I extend my sincere gratitude to Muhammad Najib Bin FAZAIL, FENG Xukun, and YIN Taishun for their care and companionship in Sherbrooke. The Ramadan I have joined every evening with my Muslim brothers relieved my endless loneliness. The Bombardier dXBel scholarship from Prof. Noureddine ATALLA was a significant relief to my awkward financial situation. I will not take all of the kindness for granted.

I am profoundly grateful to my family for their enduring love and guidance to me in whatever I pursue. They are the ultimate role models. Also, I wish to thank all my siblings, especially my little brother, CUI Donghan, twelve years younger than me, who provides never-ending unconditional love without hesitation.

Lastly, I cheer for myself, after my Ph.D. studies, I gradually overcame the weakness of my personality as kindly mentioned by my supervisors, I shall never escape from difficulties nor conflicts.

The correct physical interpretation of mathematical solutions is the key to science,
which finds its truest and fairest embrace/expression in engineering.
Dongze CUI

Abstract

The research aims to extend existing studies for heterogeneous metastructures with high contrast and high dissipation features. The multi-scale dynamics, vibroacoustic indicators, wave coupling effect, and high-order waves of heterogeneous metastructures are investigated within the wave-based frameworks.

The wave-based models for Highly Contrasted Structures (HCS) and Highly Dissipative Structures (HDS) are explored. Various methods for computing the vibroacoustic indicators, such as the wavenumber space, Damping Loss Factor (DLF), and Sound Transmission Loss (STL), are reviewed. Special attention is placed on the Asymptotic Homogenization Method (AHM) exploiting the Zig-Zag model and homogenization technique to predict the multi-scale dynamics of HCS by the bending wavenumbers. Meanwhile, the analytical Transfer Matrix Method (TMM) and its generalization for complex structures by the Finite Element (FE) model (General Transfer Matrix Method, GTMM), the semi-analytical General Laminate Model (GLM) employing Mindlin's displacement theory, the numerical Wave Finite Element (WFE) scheme are presented.

Evaluation on the robustness and accuracy of AHM and GLM is made by comparing the wavenumber space and DLF with the reference WFE method. The Nonlinear Eigenvalue Problem (NEP) in the WFE scheme for waves propagating in varying directions is solved by a Contour Integral (CI) solver, the complex wavenumbers are tracked based on the energy continuity criteria in the frequency domain. The validity limits of AHM and GLM are verified. The feasibility of applying the WFE method to sandwich structures with non-homogeneous components is shown using the classical FE-based Power Input Method (PIM-FEM).

The WFE framework is extended for accurately predicting the global DLF of HDS. It starts by deriving the forced responses of a Unit Cell (UC) representative of the periodic structure when excited by an impinging wave. Then it computes the DLF of the wave via the power balance equation. By employing the Bloch expansion, the response to a point force applied to the periodic structure is decomposed in the Brillouin zone, allowing the prediction of total response via integration over the wavenumber space. The global DLF is derived based on the principle of PIM. For HDS, results of GLM are exploited for validating the wave DLF, the PIM-FEM approach is provided as reference approach for the global DLF. The shrinking influence of bending waves on the DLF estimation for HDS is discussed, as well as the importance of Bloch mode orders.

Sound transmission coefficients can be exploited to depict the contribution from the wavenumber space to the STL of the heterogeneous metastructures. The WFE method is applied to study the wave coupling mechanisms influencing the sound insulation performance of HCS and HDS, as well as the importance of symmetric motion to the sandwich structures with a very thick soft core. The same approach is applied to waveguides with complex cross-sections to investigate the wave coupling effect and high-order waves on the accurate STL estimation by analytical TMM, WFE, and GTMM approaches. Special attention is paid to curved periodic structures, the bending-membrane coupling mechanisms influencing the STL are also investigated.

Keywords: Wave-based Methodology, Periodic Structures, Multi-scale Dynamics, Damping Loss Factor, Sound Transmission Loss, Wave Coupling

Résumé

La recherche vise à étendre les études existantes sur les métastructures hétérogènes présentant des caractéristiques de fort contraste et de forte dissipation. Les dynamiques multi-échelles, les indicateurs vibroacoustiques, l'effet de couplage des ondes et les ondes d'ordre élevé sont étudiés dans le cadre des méthodologies basées sur les ondes.

Les modèles pour les structures à forts contrastes (Highly Contrasted Structures, HCS) et haute dissipation (Highly Dissipative Structures, HDS) sont explorés. Diverses méthodes de calcul des indicateurs vibroacoustiques tels que l'espace des nombres d'onde, le facteur de perte par amortissement (Damping Loss Factor, DLF) et la perte de transmission sonore (Sound Transmission Loss, STL) sont passées en revue. L'attention particulière est accordée à la méthode d'homogénéisation asymptotique (Asymptotic Homogenization Method, AHM) exploitant le modèle Zig-Zag et la technique d'homogénéisation pour prédire les dynamiques multi-échelles des HCS par les nombres d'onde de flexion. Parallèlement, la méthode analytique de la matrice de transfert (Transfer Matrix Method, TMM) et sa généralisation pour les structures complexes par le modèle des éléments finis (General Transfer Matrix Method, GTMM), le modèle stratifié général (General Laminate Model, GLM) utilisant la théorie de déplacement de Mindlin, et le schéma d'éléments finis d'ondes (Wave Finite Element, WFE) sont présentés.

L'évaluation de la robustesse et de la précision de AHM et GLM est réalisée en comparant l'espace des nombres d'onde et le DLF avec la méthode de référence WFE. Le problème des valeurs propres nonlinéaires (Nonlinear Eigenvalue Problem, NEP) dans le schéma WFE pour les ondes se propageant dans diverses directions est résolu par un solveur d'intégrale de contour (Contour Integral, CI), les nombres d'ondes complexes sont suivis en fonction des critères de continuité de l'énergie dans le domaine fréquentiel. Les limites de validité d'AHM et GLM sont vérifiées. La faisabilité d'appliquer la méthode WFE aux structures sandwich avec des composants non-homogènes est démontrée en utilisant la méthode d'entrée de puissance basée sur les éléments finis (FE-based Power Input Method, PIM-FEM).

Le cadre WFE est étendu pour prédire avec précision le DLF global des HDS. Il commence par dériver les réponses forcées d'une cellule unitaire (Unit Cell, UC) représentative de la structure périodique lorsqu'elle est excitée par une onde incidente. Ensuite, il calcule le DLF de l'onde via l'équation de bilan de puissance. En utilisant l'expansion de Bloch, la réponse à une force ponctuelle appliquée à la structure périodique est décomposée dans la zone de Brillouin, permettant la prédiction de la réponse totale par intégration sur l'espace des nombres d'onde. Le DLF global est dérivé sur la base du principe de PIM. Pour les HDS, les résultats du GLM sont exploités pour valider le DLF des ondes, tandis que l'approche PIM-FEM est utilisée comme référence pour le DLF global. L'influence réduite des ondes de flexion sur l'estimation du DLF pour les HDS est discutée, ainsi que l'importance des ordres des modes de Bloch.

Les coefficients de transmission du son peuvent être exploités pour représenter la contribution des nombres d'onde à la STL des métastructures hétérogènes. La méthode WFE est appliquée pour étudier les mécanismes de couplage des ondes influençant la performance d'isolation acoustique des HCS et HDS, ainsi que l'importance du mouvement symétrique pour les structures sandwich avec un couche centrale souple très épais. La même approche est utilisée pour les guides d'ondes avec des sections transversales complexes afin d'analyser l'effet de couplage des ondes et des ondes d'ordre élevé sur l'estimation précise de la STL par les approches TMM, WFE et GTMM. Une attention particulière est accordée aux structures courbées Les mécanismes de couplage entre les ondes de flexion et de membrane influençant la STL sont également étudiés.

Mots-clés: Méthodologie basée sur les ondes, structures périodiques, dynamique multi-échelle, facteur de perte d'amortissement, perte de transmission sonore, effet de couplage d'ondes

List of Publications

The following manuscript is based on these manuscripts and/or part of them.

International Journals (Peer-Review)

- **D. Cui**, N. Atalla, M. Ichchou, A-M. Zine. (2024). Damping Prediction of Highly Dissipative Meta-structures through a Wave Finite Element Methodology. *Mechanical Systems and Signal Processing*, 215, 111408, 2024. doi: 10.1016/j.ymssp.2024.111408.
- **D. Cui**, M. Ichchou, N. Atalla, A-M. Zine. (2024). On the Wave-based Approaches for Wavespace of Highly Contrasted Structures with Viscoelastic Damping. *Chinese Journal of Aeronautics*, Accepted.

International Conferences

- **D. Cui**, M. Ichchou, A-M. Zine, N. Atalla. (2023, May, Marrakech, Maroc). Multi-scale Dynamics and Nonlinear Eigenvalue Problem of Heterogeneous Metastructures using a Wave Finite Element Scheme and Modal Strain Energy Method. In *Advances in Nonlinear Dynamics and Control of Mechanical and Physical Systems. CSNDD INCREASE 2023 2022.* (pp. 2272-2279). Springer Proceedings in Physics, vol 301. Springer, Singapore.
- **D. Cui**, M. Ichchou, A-M. Zine, N. Atalla, (2024, May, Université Cadi Ayyad - Marrakech, Maroc). Computation of the Sound Transmission Loss of Curved Periodic Structure using the Wave-based Methodologies. In *16e édition du Congrès de Mécanique (CMM2024).* Springer Nature Publishing Inc.
- **D. Cui**, N. Atalla, M. Ichchou, A-M. Zine, (2024, June, Southampton, United Kingdom). Damping Estimation of Highly Dissipative Structures using Bloch Expansion and Wave Finite Element Scheme. In *International Conference on Recent Advances in Structural Dynamics (RASD 2024).* Springer Nature Publishing Inc.
- **D. Cui**, M. Ichchou, N. Atalla, A-M. Zine, (2024, August, Nantes, FRANCE). Computation of the Sound Transmission Loss of Heterogeneous Periodic Structure using the Wave Finite Element-based Methodology. In *53rd International Congress and Exposition on Noise Control Engineering (Inter-Noise 2024).* Springer Nature Publishing Inc.

Contents

Chapter 1

Introduction

Contents

1.1 Motivations

In numerous engineering sectors, the constraints of conventional solutions for vibration and noise control are being addressed by exploring innovative structural concepts. These concepts are designed with the dual aims of fulfilling economic (lightweight structures for reduced fuel consumption) and ecological (lower carbon emission and better soundproofing capacity) requirements. This is in accordance with the concurrent industrial application, as depicted in Fig. 1.1 by taking the C919 airliner as an example, as well as the increasingly stringent airworthiness demands. Innovative structures are also widely used in automotive as shown in Fig. 1.2. Moreover, innovative structures are envisaged for potential integration into manufacturing processes. A frequently employed strategy involves the use of heterogeneous metastructures, which assemble a variety of materials to meet both economic and ecological demands and are feasible in the manufacturing process.

The metastructures have found extensive application in numerous transportation sectors due to their superior vibroacoustic insulation properties compared to conventional structures. Among all types of heterogeneous metastructures, Highly Contrasted Structures (HCS) are prevalently utilized in transportation engineering. HCS typically comprises flexible materials sandwiched between rigid skins as depicted in Fig. 1.3, such configurations find practical applications across diverse engineering domains, for instance, in the sector of architectures, Laminated Glass (LG) which consists of thick glass layers bonded by thin viscoelastic polymers, has become a popular choice for modern skyscrapers, vehicles and so on, due to its mechanical properties and aesthetic advantages. Attributes such as lightweight, superior vibration mitigation performance, and sound absorption capacities are characteristics of HCS. This is because the energy introduced by external acoustic excitation dissipates when traversing the heterogeneous metastructures with contrasted properties. Furthermore, HCS is also found in other engineering fields where stiff layers are bonded with a thick material, such as the sandwich plate composed of two aluminum skins stuck up by a Shape Memory Polymer (SMP) core, which is extensively used in transportation engineering.

On the other hand, the mechanism of energy dissipation in metastructures is gaining increasing importance in industrial design to reduce vibrations and enhance sound-proofing capacity. Consequently, the increasing application of viscoelastic materials in damping technology has become commonplace

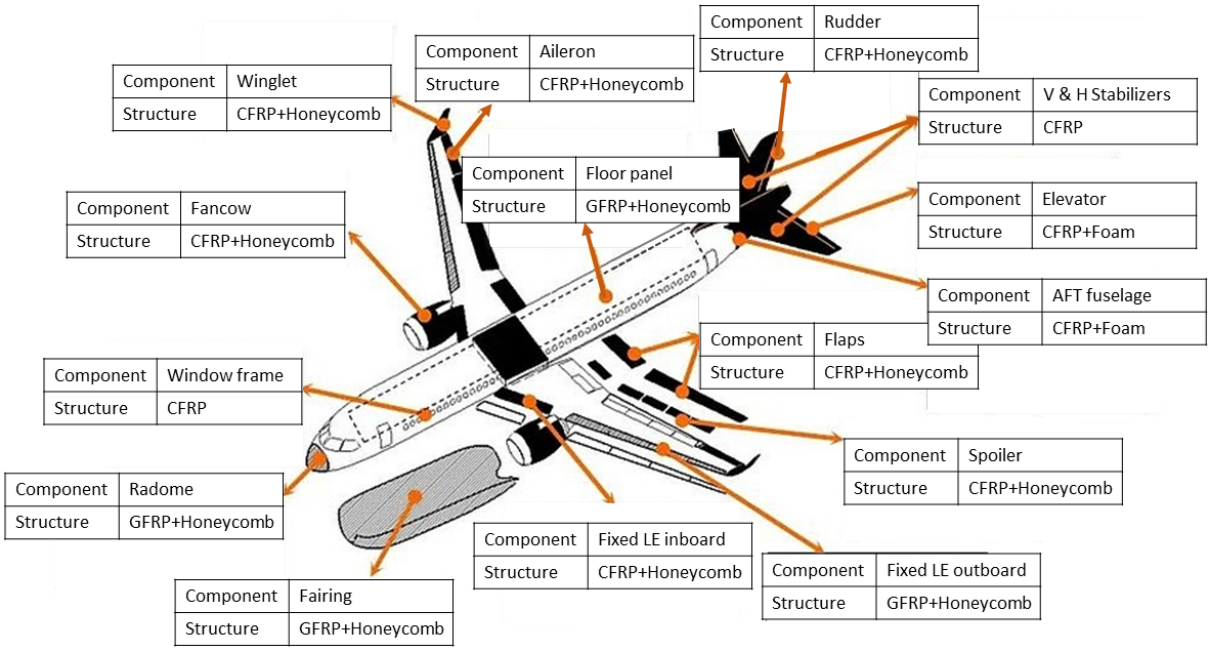

Fig. 1.1. The components using metastructures in COMAC C919. CFRP refers to the carbon fiber-reinforced plastic, GFRP the Glass Fiber Reinforced Polymer/Plastic.

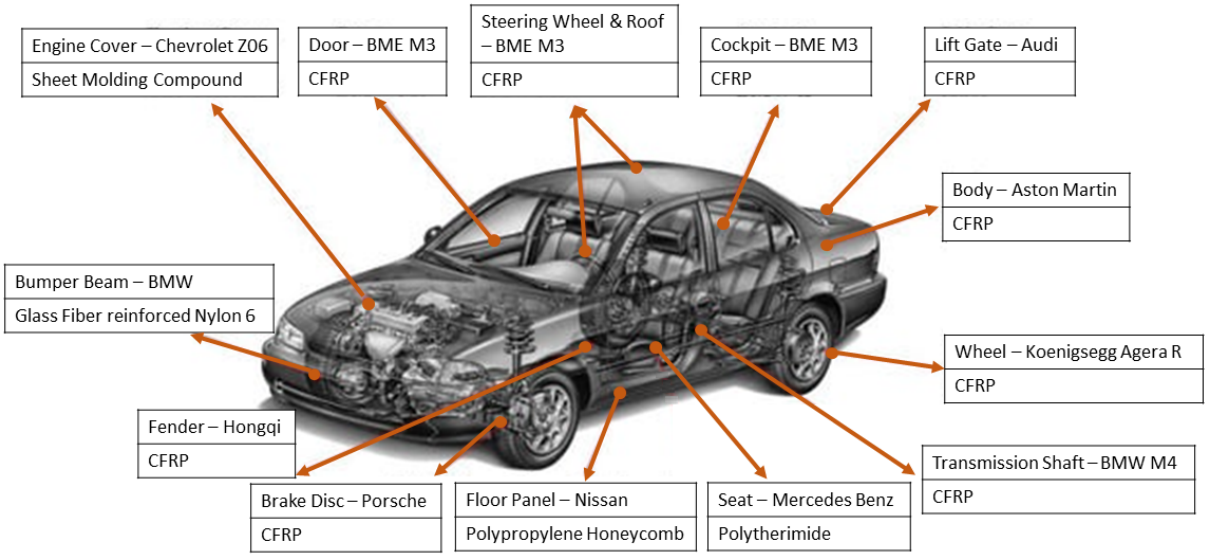

Fig. 1.2. The components using metastructures in automotives.

across nearly all industrial sectors. The SMP material used for the sandwich structures shown in Fig. 1.3 demonstrates the versatile utility of the viscoelastic material across numerous fields, including but not limited to actuators, electromechanical systems, textile production, adaptive and expandable space structures, self-healing, biomedical devices and so on [1–5]. For these reasons, heterogeneous metastructures incorporating viscoelastic constituents are emerging as competitive media for the design and manufacture of primary structures in various engineering fields, particularly in the aeronautics industry and automotive sectors. This introduces another significant concept, the Highly Dissipative Structures (HDS). HDS is designed to efficiently dissipate mechanical energy, thereby mitigating the effects of vibrations and sound transmission.

Fig. 1.3. Left: Laminated glass with PolyVinyl Butyral core [6]. Right: Sandwich plate with Shape Memory Polymer core [7].

Given their potential for transformative innovations, both HCS and HDS are currently attracting considerable attention in their respective fields. Moreover, the inherent softness of viscoelastic materials establishes a connection between the two concepts. Therefore, heterogeneous metastructures such as HCS and HDS are currently attracting increasing attention and are becoming a critical challenge to be addressed in the present work.

1.2 Research Questions

The emerging demand for efficient and accurate modeling methodologies tailored to heterogeneous metastructures is particularly pronounced for structural designs that exhibit high contrast and high dissipation characteristics. This dissertation aims to establish an accurate and robust computational framework to address the complexities inherent in such metastructures, facilitating efficient prediction and analysis of their dynamic behavior under various operational conditions.

In order to meet the current requirements in the modeling techniqeus of heterogeneous metastructures, the primary objective of the present research can be encapsulated by the following question: How to numerically predict the vibroacoustic indicators of heterogeneous metastructures by a computing-efficient and accurate method, especially for the HCS and HDS? The main research question can be divided into four specific questions:

1. In view of the challenges resulting from the heterogeneous metastructures with the characteristics of high stiffness contrast between constituents, how to verify the multi-scale dynamics of HCS, which was predicted by the bending wavenumbers computed by the analytical Asymptotic Homogenization Method (AHM)?

2. Considering the obstacles such as the Nonlinear Eigenvalue Problem (NEP) induced by varying wave propagating directions in the numerical wave-based approach, how to establish a robust NEP solver and track the eigensolutions corresponding to a specific wave, and then evaluate the vibroacoustic indicators of heterogeneous metastructures such as the complex wavenumber space and the Damping Loss Factor (DLF)?

3. Since high dissipation is the essence of this thesis, the presence of viscoelastic constituents in the heterogeneous metastructures can considerably affect the global vibro-acoustic performance, therefore, how to calculate the global/composite DLF of HDS where bending wave no longer dominates the dynamic motion of the heterogeneous metastructure?

4. As the influence of wave coupling effects within heterogeneous metastructures is pivotal for the accurate determination of acoustic indicators, notably the Sound Transmission Loss (STL), how to precisely estimate the STL while elucidating the wave coupling phenomena in HCS and HDS, and particularly in curved configurations where the bending motion is influenced by the membrane stress before the ring frequency?

1.3 Research Objectives

The main objective of this thesis is to develop and validate a wave-based methodology for predicting vibroacoustic indicators of heterogeneous metastructures, with a particular focus on HCS and HDS. To achieve this, four specific objectives are proposed:

1. Conduct a comprehensive literature review. This review will examine the multi-scale dynamics in HCS and damping mechanisms in HDS. It will critically assess the limitations in current research on heterogeneous metastructures with high contrast and high dissipation features. Additionally, it will synthesize existing wave-based computational models used for predicting vibroacoustic indicators, emphasizing metrics such as wavenumber space, DLF, and STL.

2. Perform a multi-scale dynamics analysis of HCS using wave-based approaches. This analysis will compute vibroacoustic indicators using wave-based methods and characterize the multi-scale dynamics of HCS by analyzing the variations of bending wavenumbers and their corresponding wavemodes. The analysis will compare the bending wavenumbers of HCS obtained from the developed WFE scheme with the analytical AHM and semi-analytical General Laminate Model (GLM) based on Mindlin's plate theory of discrete layers. Through this comparison, the robustness, accuracy, and validity domains of AHM and GLM will be evaluated against the WFE scheme.

3. Develop a methodology to estimate the damping performance of HDS. This will address scenarios where wave coupling is significant and estimating the DLF from a single-wave is insufficient. It will be based on the implementation of the Power Input Method (PIM) using a wave synthesis of the forced response of periodic structures. The wave synthesis will account for Bloch modes to handle cases where large representative Unit Cells (UC) are necessary. The proposed computational approach will be validated by comparing results from the PIM-FEM approach.

4. Demonstrate the robustness of the wave-based approach through transmission loss computations. This will focus on HCS and HDS and in particular sandwich structures with very thick soft cores and laminated structures with complex layups that generate high-order waves. The effects of curvature will also be examined. To validate the wave-based approach, WFE results will be compared against two established methods, the analytical Transfer Matrix Method (TMM) and its generalization for complex structures, known as Generalized Transfer Matrix Method (GTMM).

The aforementioned research questions will be addressed in the subsequent chapters to achieve the established research objectives.

1.4 Thesis Outline

This dissertation is organized as follows:

- Chapter 2 introduces the physics of heterogeneous periodic structures, including the HCS and the HDS. Present methodologies for computing the wavenumber space are summarized. The damping estimation techniques and the methods for calculating the acoustic indicators such as the Sound Transmission Loss are reviewed. Finally, the proposed wave-based methodologies for the current thesis are listed in detail.
- Chapter 3 presents the WFE scheme extended for HCS, validated through various examples by comparison with AHM and GLM models. The limit behaviors of HCS are studied by depicting the wavemode calculated by the WFE scheme. A sandwich plate with a thick core, lying outside the validity domain of AHM, is presented to study the limit of analytical AHM. The versatility of WFE is verified by a sandwich plate with an inhomogeneous core, where structural DLF is given by the Power Input Method based on the data from FE analysis.
- Chapter 4 develops the current WFE framework for the computation of global DLF by integrating forced response spanning the whole Brillouin zone. For the typical HDS configuration, the wave DLF is computed by the WFE and GLM approaches introduced in Chapter 2, the shrinking dominance of bending wave on the global flexural motion is proved by the difference between global and wave DLF of HDS. The requirement for Bloch modes in the computational methodology is demonstrated by a periodic structure with a large UC.
- Chapter 5 addresses issues neglected in Chapter 3 and Chapter 4, to show that WFE can accurately handle complex metastructures depicting wave coupling and curved configurations. Numerical cases include the typical HCS and HDS cases, an aluminum plate with a thick soft melamine core showing the symmetric (dilatation) motion, the Cross-Laminated Timber plates with the wave coupling effect and high-order waves, and curved periodic structures for the bending-membrane coupling around the ring frequency. For all examples, the STL is predicted and compared with other wave-based approaches such as the analytical TMM, semi-analytical GLM, and the hybrid FE-TMM model known as the GTMM.
- Chapter 6 and Chapter 7 draw the concluding remarks and future perspectives related to the current research work, written in English and French as required by both École Centrale de Lyon and Université de Sherbrooke.

A conceptual scheme is proposed in Fig. 1.4.

Fig. 1.4. Conceptual map of the present work.

Chapter 2

Literature Review and State-of-the-Art

Abstract: In this chapter, we focus on heterogeneous metastructures with high contrast and dissipation features. First, the multi-scale dynamics of Highly Contrasted Structure (HCS) and the dissipation mechanism of Highly Dissipative Structure (HDS) are investigated to showcase the importance and complexity of the current study. The vibroacoustic indicators, such as wavenumber space, Damping Loss Factor (DLF), and Sound Transmission Loss (STL) are investigated, the different methods for computing the metrics are elaborated, especially the wave-based approaches, namely, the Asymptotic Homogenization Method (AHM), General Laminated Model (GLM), Transfer Matrix Method (TMM), General Transfer Matrix Method (GTMM), and the Wave Finite Element Method (WFEM). The limitations of current research towards heterogeneous metastructures, specifically the HCS and HDS are summarized.

Contents

2.1 Introduction

Heterogeneous metastructures, by definition, are engineered structures that exhibit mechanical properties not observed in naturally occurring structures. Examples of such structures include laminated glass, which comprises multiple layers of glass held together by one or more intermediate viscoelastic polymer layers, and sandwich structures, which often feature stiff thin skins and a soft thick core, sometimes with specially designed inclusions within the core. These structures find extensive application in various fields of modern engineering [8], particularly in contexts where a high contrast in stiffness is emphasized. Heterogeneous metastructures, characterized by their lightweight, aesthetic appeal, and resilience, have attracted considerable attention in recent years.

This chapter introduces the physical behaviors of heterogeneous metastructures, such as multi-scale dynamics resulting from high contrast and high dissipation attributable to the viscoelastic constituents, in section 2.2. Section 2.3 presents the modeling approaches available for computing the wavenumber space of heterogeneous metastructures and comprehensively compares these methods. Subsequently, section 2.4 reports on different methods for computing the indicators used for evaluating the dissipative performances of planar structures. The extension of current methods for computing the acoustic indicators is developed in section 2.5. The chapter concludes in section 2.6.

2.2 Physics of Heterogeneous Metastructures

In this study, we investigate heterogeneous metastructures that exhibit variations in mechanical properties along the thickness direction. Such metastructures are referred to as Highly Contrast Structures (HCS) where the stiffness moduli of the skins and core significantly differ, The core layers of HCS transfer shear stresses between stiff skins through its sliding motion [9], making the interlayer dynamics difficult to characterize due to complex interlayer interactions from varying scales of bending and shear motion within the skins and the core [10]. This leaves the overall bending-shear coupling behavior in the sandwich structure an open question.

HCS can be found in many engineering applications, such as civil engineering where soundproofing and thermal insulation are achieved by gluing stiff thin layers with a soft matter (usually a soft viscoelastic polymer layer). The reverse configuration, i.e., a thin viscoelastic or other damped layer sandwiched between two thick stiff layers with low damping, has also been explored, mainly for Constrained Layer Damping (CLD) to reduce vibration. The multi-scale behavior of heterogeneous metastructures is governed by the interactions between the local shear of the viscoelastic interlayers, the local bending of the skins, and the global bending of the overall structures along the thickness direction. The contrast in thickness and material properties among the adjacent layers also affects the multi-scale behavior of HCS.

Additionally, the use of soft viscoelastic materials in Highly Dissipative Structures (HDS) is gaining attention due to their advantages in reducing structural vibrations, including simplicity in design, construction, maintenance, and installation. The study of HDS requires special attention to the modeling and numerical aspects of the problem. The high damping ratio leads to nonlinearities in the eigenvalue problem, such as the wavenumber space and the wave tracking for computing the modal strain energy and kinetic energy. Moreover, the damping phenomena are often dependent on the working conditions, such as the frequency range and the temperature, which are of engineering interest. Hence, two key aspects of heterogeneous metastructures, namely high contrast, and high dissipation, need to be considered for optimal design and accurate determination of the relevant fields, which are still open challenges for effective solutions of the vibroacoustic indicators of heterogeneous metastructures.

In general, while sandwich structures offer numerous advantages, their complex behavior necessitates ongoing research to fully exploit their potential in various engineering applications. The continued development of advanced models and computational tools will undoubtedly play a crucial role in this

endeavor.

2.2.1 Highly Contrasted Structures

The origin of heterogeneity lies in the variations of physical properties in the seismic layers due to the effects of gravity, pressure, temperature, etc. Incorporating heterogeneity in the physical model is essential for realistic seismic analysis and other engineering sectors.

Norville et al. [11] made pioneering contributions to the structural mechanics of HCS by highlighting the two limit behaviors of HCS structures, namely, the monolithic and bi-layer limit kinematics depending on stiffness contrast, as depicted in Fig. 2.1. In the monolithic limit, observed with low stiffness contrast between skins and core, the structure behaves as a homogeneous material with uniform deformation and even stress distribution. Conversely, in the bi-layer limit, seen with high stiffness contrast in Fig. 2.1, the whole structure acts as two separate layers, with the skins bearing most of the load and the soft core primarily maintaining separation between them. The transition between these behaviors is influenced by the variation of stiffness contrast between the skins and the core, and involves complex changes in stress distribution, deformation patterns, and overall mechanical response.

Since the stiffness contrast affects the structural behavior, the difference between the limit behaviors of laminated structures with different levels of contrast is so sharp that a comprehensive assessment of the actual behavior of the heterogeneous laminate structures is needed for encapsulating at least the phenomena of global bending (for weak contrast), local bending and shear (for high contrast).

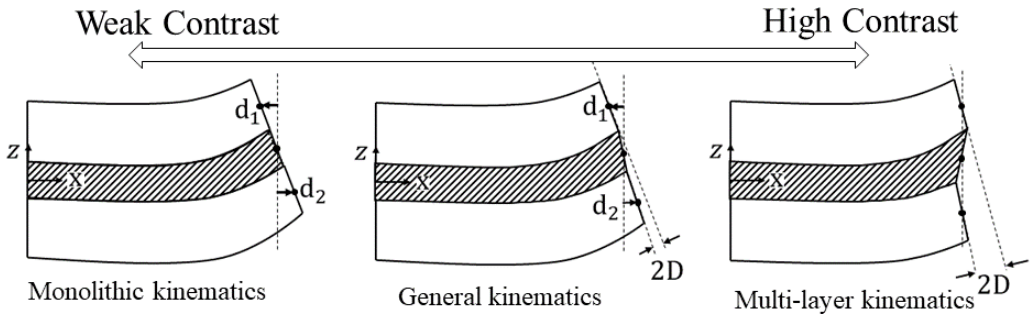

Fig. 2.1. Different kinematic regimes for laminate plate with different levels of contrast. Left: monolithic kinematics with D=0 for extremely low contrast. Center: general kinematics for moderate contrast. Right: multi-layer kinematics with d=0 for extremely high contrast.

Boutin et al. [12] have studied the kinematic regimes of the laminate plate with varying contrast levels using a general three-layer plate as an example. Two variables that respect the plate kinematics to evaluate the kinematics of the target structure are defined, namely, the differential in-plane motion between the two stiff layers D and the differential in-plane motion between the middle planes of the stiff layers d, the three different kinematics regimes are summarized illustrated in Fig. 2.1:

- When the interlayer has the same stiffness as the stiff layers, the whole structure acts as a monolithic plate and $D = 0$.
- When the interlayer is very soft, resulting in high contrast, the whole structure behaves as a multi-layer plate and $d_1 = d_2 = 0$.
- When the interlayer has a moderate stiffness relative to the stiff layers, the whole structure exhibits the general kinematics and $D \neq 0$ and $d \neq 0$.

Thus for the dynamic motion of HCS, the kinematics involve the bending effect of the stiff layers and the shear effect of the soft layer, such a full shear-bending coupling emerges when transverse forces in both constituents contribute to the overall structure at the same level [13].

When it comes to the HCS plates with more stiff layers, such as three stiff layers and two soft cores, the differential in-plane motion can be further decomposed as the combination of asymmetric and symmetric ones [13], the kinematic decomposition in Fig. 2.3 can be updated for further analysis.

2.2.2 Highly Dissipative Structures

The previous literature review showed that the bending motion of laminated plates is strongly influenced by the high contrast of stiffness between adjacent layers. High dissipation is also often encountered in the laminated structures since different layers are always bonded by a viscoelastic layer such as epoxy resin and Polyvinyl Butyral (PVB) appearing with a high damping ratio. Furthermore, high dissipation is also desired in engineering structures to control the structural vibrations, and to reduce noise, because the viscoelastic layer does not transmit the energy transported by the incoming wave but dissipates most of it. This feature is exploited in industrial applications ranging from aircraft constructions to submarines and land vehicles. Since the response of heterogeneous metastructures depends to a high degree on the damping performance, it is desirable to develop solutions enabling its quantification, such as the Damping Loss Factor (DLF).

An attractive and easy-manufacture method to enhance the dissipation mechanism in laminated structure is to design the optimal dimensioning of the viscoelastic interlayers to control the vibration through the mitigation of wave propagation at the desired frequency range, therefore, viscoelastic constituents can be applied to control the structural vibrations and noise of the whole structure. The application of viscoelastic materials in HDS has received considerable attention, the earliest benchmark study for the tri-layer structure with a constrained viscoelastic core, the Ross-Kerwin-Ungar (RKU) model [14–16] dates back to 1950s, a benchmark study from the 1950s for the tri-layer structure with a constrained viscoelastic core, acknowledged that energy dissipation in the core results from its shear deformation. The RKU model recognized that the energy dissipation in the core is a result of its shear deformation.

Viscoelastic damping has been identified as the dominant damping mechanism [17] occurring in composite materials, heterogeneous laminated plates with viscoelastic interlayers will be the focus of HDS in the current study. The viscoelastic damping has laid the groundwork for further research, resulting in advanced models that incorporate temperature effects, frequency-dependent material properties, and non-linear dynamics. Such progress has substantially improved insights into the behavior of sandwich structures.

Moreover, material damping is a fundamental characteristic of various materials and structural configurations, including metallic panels with CLD [18] and sandwich panels [19]. Omitting these dissipation mechanisms during modeling leads to inaccurate forecasts [20]. Although the study of the impact of material damping on wave behavior is relatively recent [21], Chan and Cawley's analytical investigation into how material attenuation affects elastic wave dispersion has been influential[22].

In the wave-based methodologies, Bernard et al. [23] conducted a study on the energy velocity of wave attenuation in plates, corroborated by experimental data. Simonetti et al. [24, 25] explored shear wave in elastic plates with viscoelastic coatings, finding that high material attenuation can cause the intersection of real parts of wavenumbers and eliminate the original wave veering effect. Bartoli et al. [26] employed the Semi-Analytical Finite Element (SAFE) method to model wave propagation in viscoelastic plates, assessing energy velocity and wave attenuation. They compared results from hysteretic and Kelvin–Voigt viscoelastic models in orthotropic plates, revealing minimal impact on phase and energy velocity. Taupin et al. [27] also utilized the SAFE method to examine elastic guided waves in composite viscoelastic plates with varying stack sequences. Collet et al. [28] proved that for undamped systems exhibiting either propagative or evanescent waves corresponding to eigen solutions that are either purely

real or imaginary, introducing additional damping effects transforms these eigen solutions into complex values, necessitating a novel analytical approach. For this purpose, Ghinet and Atalla [29] proposed a semi-analytical method grounded in Mindlin's displacement theory for laminated structures, where damping is represented through the complex modulus model. Similarly, Manconi [21] enhanced the numerical WFEM for viscoelastic systems using a complex modulus model, enabling DLF predictions via the power balance method. Further, Manconi et al. [20] refined WFEM by incorporating pre-stress effects on the damping characteristics of curved panels.

The investigation of HDS is essential, especially in the context of HCS due to the viscoelastic properties of the materials. Ichchou et al. [30] proved that bending waves are not the exclusive influence on the flexural displacement of HDS. As a result, the DLF associated with bending waves falls short for evaluating the damping performance of HDS. The development of a new method for calculating the global DLF is critically needed to enhance the study of vibroacoustic in metastructures. Wave-based methodologies are preferred because they allow for the analysis of individual wave contributions to the global DLF, also aiding in the thorough examination of HCS dynamics and the calculation of the global DLF for HDS.

2.3 Wavenumber Space

For computing the wavenumber space of heterogeneous metastructures, no easily-implemented technique exists according to the author's knowledge, moreover, the successful application of heterogeneous metastructures largely depends on the prediction of the mechanical properties and dynamic behaviors through the development of the appropriate mechanical models. Therefore, we are looking for mechanical models that are neither too complicated to be developed and implemented nor too simple that cannot reveal the actual mechanical properties and behavior, the efficiency and accuracy are also considered when selecting the computational models.

Recent studies mainly focus on analytical methods such as classical analytical methods, Asymptotic Homogenization Method (AHM) [13], General Laminate Model (GLM) [29], and Wave-based Finite Element Method (WFEM).

2.3.1 Classical Analytical Methods

In real-world scenarios, the stiffness of the core affects the bending-shear coupling behavior of the laminate, which is present in high-contrast cases but absent in low-contrast scenarios. A stiff core makes the two skins behave as a monolithic plate with global bending motion, while a deformable core allows the two skins to slide independently with their bending motions. A medium core stiffness results in a complex transition between the two limits, influenced by the shear behavior within the core. These multi-scale dynamics of metastructures are challenging to capture due to the complex interactions caused by the contrasted rigidities of adjacent layers [31].

The physics of periodic structures made of different materials with a moderate contrast is now well understood since the homogenization of periodic elastic materials has already been extensively studied, and some formulas give the homogenized stiffness matrix through the Unit Cell (UC, or PnC, short of Phononic Crystal of metastructures) [32–34].

If all elastic moduli of the constituents in a stratified plate are of the same order, i.e., for a quasi-homogeneous structure with weak contrast [35], regardless of the number of the layers in the plate, the normal to the mid-surface of the plane remains normal after deformation, thus the behaviors of the plate can be predicted accurately by the classical monolithic plate theory, such as Kirchhoff–Love Thin Plate Theory (2D extension of Euler-Bernoulli Beam Theory) accounting mainly for bending motion and

Reissnere-Mindlin Theory (2D extension of Timoshenko Beam Theory) that incorporates a correction to account for transverse shear deformation in thick plates [36].

However, monolithic plate theories are limited in modeling the continuity of fields at interfaces in laminated structures, especially when the core and skins have contrasted rigidities. Higher-order Shear Deformation plate Theory (HSDT) is then introduced to correct the limitation of the Reissnere-Mindlin model in nonlinear displacement fields. HSDT is based on the assumption that the displacement field takes the form of cubic variation and obtains a parabolic characteristic of the corresponding shear deformation field (Vlasov-Reddy theory of the third order in 1984 [37]). It has the advantage of calculating the displacement field without additional variables compared to the Reissner-Mindlin Theory while obeying the nullity of the constraint conditions of the shear stresses in the interfaces. Nevertheless, it remains an approximate solution and is difficult to generalize in the case of laminated plates which implies continuity conditions of displacements and shear stresses at the interfaces between the layers.

Theories based on displacements or hybrid approaches have been proposed to model laminated composite structures [38]. Displacement-based theories use the displacement field as the primary unknown. First-order theories, such as the Shear Deformation Theory (SDT, also known as Mindlin's plate theories) [39], use a linear displacement field that leads to a constant transverse shear stress and a zero transverse normal stress. Based on first-order SDT [36], analytical models of higher-order SDT are being pursued to encapsulate the multi-layer dynamics due to the transverse shear motion of the core. From the Second-order SDT [40], Third-order SDT [37, 41] to Fourth-order SDT [42] considering the transverse shear rigidity of the core. These theories are limited in modeling the continuity of fields at interfaces in laminated structures [43], they cannot describe the Zig-Zag distribution of in-plane displacements for HCS in Fig. 2.1.

Higher-order theories, such as the Zig-Zag theory [44, 45], use a nonlinear displacement field that allows for a variable transverse shear stress and a nonzero transverse normal stress, which can more accurately capture the transverse stresses than first-order theories. Discrete Layer Theory treats each layer separately and uses a discontinuous displacement field within each layer [46]. Hybrid theories use both displacement and stress (or strain) fields as the primary unknowns and apply a variational principle [47] or Hybrid Stress Element Method [48] to obtain the governing equations. Hybrid theories can capture the layerwise variation of the stress and strain fields more accurately than single-layer theories, but they also require more computational effort and complexity. For Layer-wise theory, Naumenko et al. [49] derived a plate theory for the structural analysis of HCS, concluding the generalized deflection and the relative in-plane displacement vector of skin layers. Altenbach et al. [50] derived the shear corrections factors for Mindlin's plate theory, three-layered plates of HCS are studied, the principle can be extended for thin viscoelastic layer [51, 52]. Analytical models dealing with layered structures have been thoroughly investigated, e.g., see [36, 45, 53] to name a few. However, considerations for HCS are more restricted [54], Boutin et al. [12, 13] provides an up-to-date review of the most relevant literature.

The definition of highly contrasted periodic medium was proposed by Figotin et al. [55]. Smyshlyaev [56] investigated the homogenization of periodic beams with moderate contrast and proposed the scaling technique of the contrast level in HCS. Berdichevsky [35] derived the governing equations for sandwich plates, and proved that the high contract of stiffness changes the character of the asymptotics, the classical plate theory works for HCS only within a certain range of contrast level. Cherdantsev et al. [57] have proposed a two-scale homogenization approach for periodic composites exhibiting high contrast. Chapman [58] developed a 4th-order equation to approximate the dispersion relation for a three-layered plate, HCS is included in the theory. Kaplunov et al. [59] proposed a homogenization procedure for 1D waveguides with high heterogeneity. Tovstik et al. [60] used the Timoshenko-Reissner model for orthotropic linearly elastic material heterogeneous in the thickness direction, they reduced the multilayer plate to a homogenized plate with equivalent properties. Kudaibergenov et al. [61] studied the free vibration of a string with two materials of high contrasts. Boutin et al. [12] introduced an asymptotic method that incorporates stiffness

scaling to establish a theoretical framework for analyzing the behavior of HCS having symmetric skin thickness.

For metastructures with a high level of contrast among the constituents, current analytical methods fail to predict accurate results. Another drawback of classical analytical methods for HCS is that its solutions are limited in the low-frequency range and their frequency range of operation because this method requires impractical sizes and masses.

2.3.2 Asymptotic Homogenization Method

Given the drawbacks of classical analytical methods, researchers came up with an intuitive way to overcome the difficulty by replacing the laminated structures with equivalent material models, which are usually named as Asymptotic Homogenization Method (AHM). According to Willis [62], the numerous methods for contrasted laminate structures can be casually classified into three broad categories: asymptotic method [35], homogenization method [63] and variational method [64], there are no rigorous boundaries between these categories. Therefore, these methods will be summarized as AHM to present their common features and mathematical developments.

The classical models for homogeneous plates have been theoretically justified by Ciarlet and Destuynder [32]. They introduced a multi-scale asymptotic method based on the scale ratio ε, which compares the plate thickness (h) to the characteristic size of the phenomena's evolution in the plane of the plate (l), such that

$$\varepsilon = \frac{h}{l} \ll 1 \tag{2.1}$$

The mathematical theory of homogenization developed in the 1970s is used as an equivalent approach to find the effective properties of the equivalent homogenized material [65]. This theory can be applied in many areas of physics and engineering having finely heterogeneous continuous media, like heat transfer or fluid flow in porous media or electromagnetism in composites [66]. The multi-scale AHM has found widespread application in deriving effective descriptions for periodic plates [67], corrugated plates, stratified plates [68], and even plates with crack damage. In this approach, the elastic properties of the constituents are assumed to be of the same order of magnitude. The resulting inner stress distribution, which governs effective behavior, emerges from these foundational assumptions.

So long as there is a scale separation between the plate thickness and the characteristic size of kinematics field variations, the asymptotic expansion method can be applied to the study of laminated structures. The method provides a synthetic and consistent formulation, integrating the dual efforts of the macroscopic descriptors, in-plane and out-of-plane balance equations, and the constitutive laws of the laminate. The asymptotic procedure consists of introducing the scaled formulation and the expansions in the initial 3D description. Separating the terms of identical power in ε leads to a series of problems to be solved order by order. The resolution yields a 2D model that fulfills asymptotically, i.e., when $\varepsilon \to 0$, the requirements of stress and displacement continuity at the interfaces, and the balance of momentum within the layers. AHM is based on the description in the leading order.

Although the asymptotic approach makes it possible to predict the global and local properties of HCS. From a mathematical point of view, asymptotic approaches are limited since they apply asymptotic expansions and the assumption of periodicity to substitute the differential equations with rapidly oscillating coefficients in differential forms whose coefficients are constant or slowly varying so that the solutions are close to the original equations [69]. Besides, these models are more suitable for recovering the properties of heterogeneous structures and obtaining a better correspondence compared to isotropic models.

On the other hand, the results obtained by conventional homogenization methods for heterogeneous plates implicitly assume that the elastic properties of the constituents are of the same order of magnitude. However, if one or more constituents are viscoelastic, their mechanical properties vary and the case

with significant stiffness contrasts are the focus of this study. As Boutin has dealt with the soft matrix reinforced by long rigid inclusions [70], the effects of bending-shear coupling were taken into account to establish a complete model that reflects the mechanical contrast. Nevertheless, the high contrast in the heterogeneous laminate plates has rarely been studied up to now.

Recently, Boutin et al. [13] developed AHM that concludes the two limit kinematic regimes of HCS using a 6th-order equation to provide closed-form solutions for HCS. AHM applies the Zig-Zag model to describe the stress and displacement continuity at the interlayers and the force/moment equilibrium of each layer [45, 53], the homogenization approach is employed to deal with the different scales induced by ε, the high contrast of stiffness in HCS by stiffness scaling is also accounted for [13, 71, 72]. With the computation of complex wavenumbers, AHM accurately predicts the variation of the dynamic behavior in HCS [13], the DLF is obtained by deriving the group and phase velocities from the complex wavenumbers in the frequency domain.

The AHM is recalled through the application of asymptotic techniques tailored to the formulation of plate theories. The derivation begins with considerations of the 3D isotropic elasticity of the constituents, the imposition of perfect contact conditions among different layers, the assumption of incompressibility of the layer thickness, and adherence to the geometric condition of small thickness.

To address the multi-scale dynamics inherent in HCS, AHM employs the dynamic description of Zig-Zag models to accurately depict the variation of the in-plane displacement field between successive layers, as depicted in Fig. 2.3, grounded on the principles of continuity and equilibrium about each layer.

Nonetheless, the asymptotic Zig-Zag model falls short in incorporating viscoelastic effects. So, AHM employs the conventional homogenization approach [71, 72], effectively addressing the contrast of material deformability through proper stiffness scaling [12]. The application of the complex shear moduli comprising both elastic and loss counterparts facilitates the further development of DLF.

AHM proves its validity in describing HCS's dynamic behavior [13], it considers the bending-shear coupling effect of the HCS, thereby providing a clear definition of the effective plate behavior through the balance equations and constitutive laws. AHM also retains accurate solutions for HCS with viscoelastic interlayers and overcomes the ambiguity that previous homogenization methods encountered in identifying the different dynamics involved in each layer.

2.3.2.1 In-plane Kinematic Decomposition of Highly Contrasted Structures

To provide the fundamental procedures of AHM, a comprehensive explanation of the asymptotic derivation and the force/momentum balances of HCS are outlined.

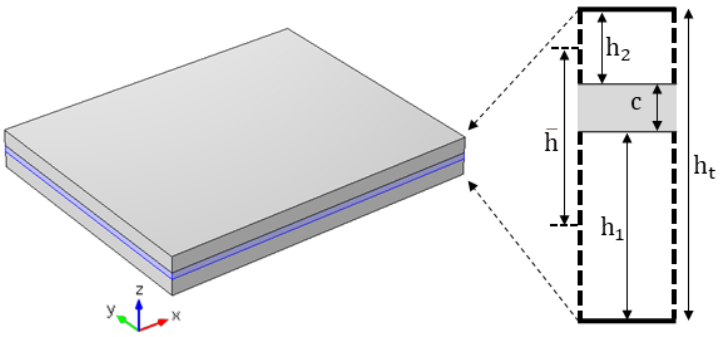

Fig. 2.2. Notations for HCS plate along thickness axis.

The Kirchhoff plate model's kinematic descriptors include out-of-plane deflection $w(x, y)$, normal fiber rotation $\boldsymbol{\nabla} w(x, y)$, and in-plane displacement $\boldsymbol{U}(x, y)$. The significant softness of the core necessitates an additional kinematic descriptor, the sliding vector $\boldsymbol{\delta}(x, y)$. Boutin et al. [12] have theoretically and

experimentally shown that the in-plane kinematics of the HCS model can be represented as a superposition of three distinct kinematics shown in Fig. 2.3:

$$\boldsymbol{u}(x,y,z) = -\varphi_w(z)\boldsymbol{\nabla} w(x,y) + \varphi_\delta(z)\boldsymbol{\delta}(x,y) + \boldsymbol{U}(x,y) \tag{2.2}$$

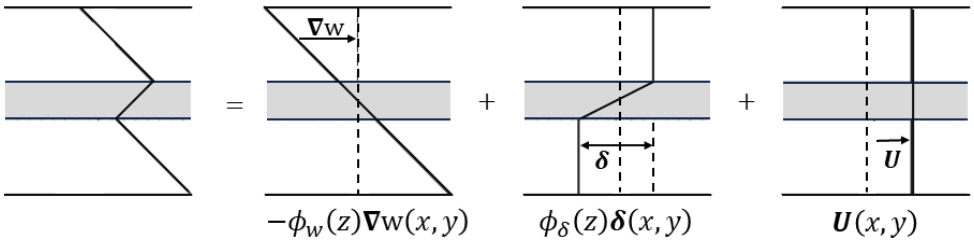

Fig. 2.3. In-plane kinematic decomposition of HCS. $\varphi_w(z)$ and $\varphi_\delta(z)$ are the basic shape functions of Zig-Zag model.

The general Zig-Zag in-plane kinematic is decomposed into [13]:

- the in-plane displacement of the whole plate $\boldsymbol{U}\,(x,y)$.
- the Kirchhoff plate kinematics for two skins with identical deflections $-\varphi_w(z)\boldsymbol{\nabla} w(x,y)$.
- the shear motion in the soft core resulting in opposing tangential stresses on the interfaces with the skins $\varphi_\delta(z)\boldsymbol{\delta}(x,y)$

Shape functions, $\varphi_w(z)$ and $\varphi_\delta(z)$, are proposed to establish the basis for Zig-Zag in-plane kinematics in Eq. 2.2. Here, $\boldsymbol{\nabla} w(x,y)$ and $\boldsymbol{\delta}(x,y)$ are independent variables. The two shape functions are expressed as follows:

- $\varphi_x(z)$ is linear and non-symmetric for $h_2 \neq h_1$ with a zero mean value across both skins, is given by:

$$\begin{aligned} &\varphi_w(z) = z - \frac{c}{2}\frac{h_2 - h_1}{h_2 + h_1} \\ &\langle \varphi_w(z) \rangle = 0 \end{aligned} \tag{2.3}$$

  where $\langle\ \rangle$ stands for the average along the thickness of the skins, c, h_1, h_2 and h_t are presented in Figure A.1.

- $\varphi_\delta(z)$, which is continuous and constant across both skins, linear in the core, and also has a zero mean value over the two skins (i.e., $\langle \varphi_\delta(z) \rangle = 0$), is defined as follows:

$$\begin{cases} \varphi_\delta\,(z) = -\dfrac{h_2}{h_2 + h_1}, & \text{for } -\dfrac{h_t}{2} < z < -\dfrac{h_t}{2} + h_1 \\ \varphi_\delta\,(z) = \dfrac{h_1}{h_2 + h_1}, & \text{for } \dfrac{h_t}{2} - h_2 < z < \dfrac{h_t}{2} \\ \varphi_\delta\,(z) = \dfrac{z}{c} - \dfrac{h_2 - h_1}{h_2 + h_1}\dfrac{h_1 + h_2 - c}{2c}, & \text{for } -\dfrac{h_t}{2} + h_1 < z < \dfrac{h_t}{2} - h_2 \end{cases} \tag{2.4}$$

The overall in-plane displacement, $\boldsymbol{U}(x,y) = \boldsymbol{u}(x,y,z)$, uniform across the plate thickness, is exclusively associated with the in-plane deformations of the plate.

The in-plane displacement between the lower ($z = -\frac{h_t}{2} + h_1$) and upper ($z = \frac{h_t}{2} - h_2$) interfaces of the soft core is governed by $-c\boldsymbol{\nabla} w + \boldsymbol{\delta}$. The shear strain of the core in the X and Y directions, caused by

both in-plane displacement and the deflection gradient of the bottom and top skins, is represented by the vector $(-c\boldsymbol{\nabla} w + \boldsymbol{\delta})/c + \boldsymbol{\nabla} w$/x=$\boldsymbol{\delta}$/(2c).

The relative in-plane displacement between the middle planes of the bottom skin ($z = \frac{h_t - h_1}{2}$) and the top skin ($z = \frac{h_t - h_2}{2}$) is $-\bar{h}\boldsymbol{\nabla} w + \boldsymbol{\delta}$. This displacement defines the overall rotation vector $\boldsymbol{\alpha}(x, y)$:

$$\begin{aligned} \boldsymbol{\alpha} &= \boldsymbol{\nabla} w - \boldsymbol{\delta}/\bar{h} \\ \boldsymbol{\delta}/c &= (\boldsymbol{\nabla} w - \boldsymbol{\alpha})\bar{h}/c \end{aligned} \tag{2.5}$$

2.3.2.2 Force/Momentum Balances of Highly Contrasted Structures

The strain and stress fields in each layer can be derived by the kinematic decomposition in Eq. 2.2. The 3D local balance equations, weighted by the shape functions φ_w and φ_δ, are then integrated over the plane thickness, leading to the 2D governing equations of the laminated plate at the leading order. This set reveals the two torsors governing the mechanics of the plate. The detailed theoretical procedure is available in Ref. [12]. Here, we only explain the physical meaning of the torsors shown in Fig. 2.4.

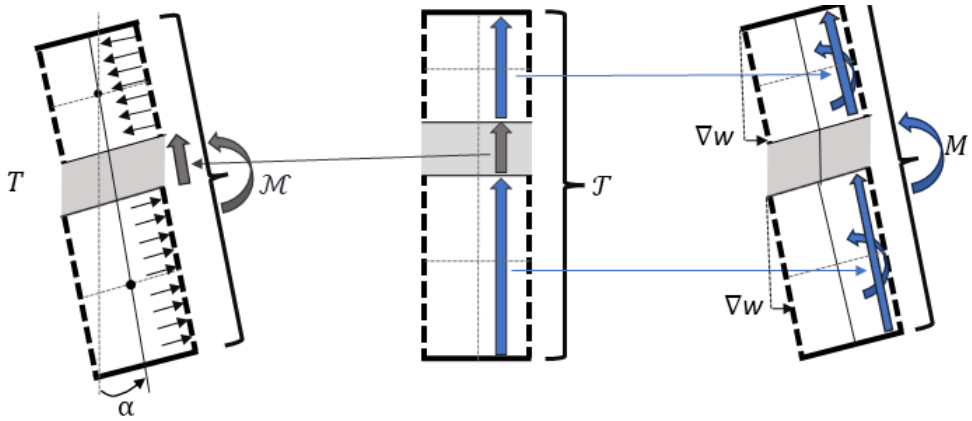

Fig. 2.4. The Forces and Momentum involved in the bi-torsor description and their physical meaning.

Eq. 2.2 illustrated in Fig. 2.3 is divided into two components for the bending motion:

- $\varphi_w(z)\boldsymbol{\nabla} w(x, y)$ aligns with the traditional Kirchhoff plate kinematics for the two rigid layers, each having identical deflection. This results in each layer maintaining an internal momentum counterbalanced by an internal shear force. Collectively, the sum of these internal momenta defines the inner momentum tensor $\boldsymbol{M}$, explicitly expressed as (the differential operator $\boldsymbol{\mathscr{E}}$ is defined in Appendix A).

$$\boldsymbol{M} = E_0 I \boldsymbol{\mathscr{E}}(\boldsymbol{\nabla} w) \tag{2.6}$$

  $\boldsymbol{M}$ is balanced by the sum of internal shear forces, corresponding to $-\boldsymbol{div}(\boldsymbol{M})$. Note that due to the significantly lower stiffness of the core, the momentum in the core is negligible at the leading order.

- $\varphi_\delta(z)\boldsymbol{\delta}(x, y)$ induces shear motion in the soft layer, imposing opposing tangential stresses on the interfaces with the rigid layers. To achieve balance, these stresses result in two opposing normal (axial) forces in the top and bottom skins. Consequently, an overall momentum tensor $\boldsymbol{\mathscr{M}}$ is generated, the balance of which is achieved by the shear force $\boldsymbol{T}$ acting within the soft layer. This momentum is directly related to the variation of $\boldsymbol{\alpha}$, as the axial forces lead to a variation of the relative in-plane displacement between the middle planes of the lower and upper ply, i.e., $-\bar{h}\boldsymbol{\alpha}$.

The constitutive laws of $\boldsymbol{\mathscr{M}}$ and $\boldsymbol{T}$ are explicitly derived from the mechanical properties and the geometry of each layer. They are expressed as follows:

$$\begin{aligned} \boldsymbol{\mathscr{M}} &= E_0(\mathscr{I} - I)\boldsymbol{\mathscr{E}}(\boldsymbol{\alpha}) \\ \boldsymbol{T} &= \mu\bar{h}(\boldsymbol{\delta}/c) = K(\boldsymbol{\nabla} w - \boldsymbol{\alpha}) \end{aligned} \tag{2.7}$$

The overall transverse force $\boldsymbol{\mathscr{T}}$ in the plate is the cumulative sum of the internal shear forces of the two rigid layers and the shear force in the soft layer. In summary, the forces and momentum duals corresponding to the kinematic descriptors of the HCS plate are as follows:

- the inner momentum tensor $\boldsymbol{M}$, which is dual to the gradient of deflection $\boldsymbol{\nabla} w$,
- the inner shear force $\boldsymbol{T}$, which is dual to the sliding vector $\boldsymbol{\delta}$,
- the overall momentum tensor $\boldsymbol{\mathscr{M}}$, which is dual to the overall rotation vector $\boldsymbol{\alpha}$,
- the overall transverse force $\boldsymbol{\mathscr{T}}$, which is dual to the deflection w.

With these variables, the comprehensive description of the out-of-plane behavior of the elastic HCS, subjected to a normal surface force f, is provided by the following balance equations [12]:

$$\begin{aligned} &\mathrm{div}(\boldsymbol{\mathscr{T}}) + f = 0 \\ &\boldsymbol{\mathscr{T}} = -\mathrm{div}(\boldsymbol{M}) + \boldsymbol{T} \\ &\boldsymbol{T} = -\mathrm{div}(\boldsymbol{\mathscr{M}}) \end{aligned} \tag{2.8}$$

Eq. 2.8 offers a consistent bi-torsor representation $\{(\boldsymbol{\mathscr{T}}, \boldsymbol{\mathscr{M}});\ (\boldsymbol{T}, \boldsymbol{M})\}$, directly reflecting the physical mechanisms within the HCS. The proposed model comprises the synthetic analytic Eqs. 2.6-2.7-2.8, corresponding to a generalized plate model with enhanced kinematics.

The asymptotic approach covers the assumptions implicitly and explicitly used in the above approaches. However, the proposed 2D HSC model differs from the aforementioned studies in two key aspects:

- The sliding motion is here treated as an additional kinematic descriptor instead of an internal system variable.
- The shear stress in the core is encapsulated here as an additional torsor acting on the plate to take into its effect as a system of internal stresses.

Besides, the 2D HCS model includes symmetrical and non-symmetric plates, viscoelastic constituents, and dynamic behavior within the same framework, greatly simplifying the updates of classical plate theories for HCS.

2.3.2.3 Energy Balance and Boundary Conditions

The standard boundary conditions have to be re-evaluated since an additional variable $\boldsymbol{\delta}$ is introduced. The appropriate conditions can be determined by expressing the energy balance of a plate with surface S and border ∂S, and $\boldsymbol{n}$ is the normal of the plate. The total energy produced by the deflection w under the normal load f is given by $\int_S fwds$. By transforming this expression using the balance Eq. 2.8, we obtain:

$$\begin{aligned} 0 = K\int_S |\boldsymbol{\nabla} 2 - \boldsymbol{\alpha}|^2 ds + E_0 I \int_S \mathbb{E}_\nu(\boldsymbol{\nabla} w) ds + E_0(\mathscr{I} - I)\int_S \mathbb{E}_\nu(\boldsymbol{\alpha}) ds \\ + \int_S fwds + \int_{\partial S} \{\boldsymbol{\mathscr{T}}\boldsymbol{n} w + (\boldsymbol{\mathscr{M}}\boldsymbol{n})\boldsymbol{\alpha} + (\boldsymbol{M}\boldsymbol{n})\boldsymbol{\nabla} w\} dl \end{aligned} \tag{2.9}$$

in which $\mathbb{E}_\nu(\boldsymbol{v}) = (1-\nu)|\boldsymbol{e}(\boldsymbol{v})|^2 + \nu \mathrm{div}^2(\boldsymbol{v})$. The first three integrals in Eq. 2.9 correspond to the deformation energy generated by i) the shear motion of the core, ii) the inner bending of each layer, and

iii) the overall bending of the plate. The integral over ∂S represents the energy provided at the border, revealing that the boundary conditions of the 2D HCS model can be expressed via static variables $\boldsymbol{\mathcal{T}}$, $\boldsymbol{\mathcal{M}}$, and $\boldsymbol{M}$, and/or by the kinematic variables w, $\boldsymbol{\alpha}$, and $\boldsymbol{\nabla} w$. So, the conditions can be derived:

- Free boundary: $\boldsymbol{\mathcal{T}}\boldsymbol{n} = 0$ and $\boldsymbol{\mathcal{M}}\boldsymbol{n} = \boldsymbol{M}\boldsymbol{n} = 0$,
- Clamped boundary: $w = 0$, $\boldsymbol{\nabla} w = \boldsymbol{\alpha} = 0$, and consequently $\boldsymbol{\delta} = 0$,
- Simply supported boundary: $w = 0$ and $\boldsymbol{\mathcal{M}}\boldsymbol{n} = \boldsymbol{M}\boldsymbol{n} = 0$,

Focusing on the wavenumber space, the free boundary condition is applied.

2.3.2.4 Bending Waves of HCS Model with Viscoelasticity

In the dynamic harmonic regime $exp(i\omega t)$, the plate is subject to an inertial force $f = \rho_t h_t \omega^2 w$, where ρ_t is the mean density defined in Appendix A. The analysis will be conducted in the frequency domain, thus, the time dependency is omitted in the following derivation.

The viscoelasticity is accounted for by taking the complex-valued modulus in the computation, with the real part representative of the elastic modulus while the imaginary part the loss modulus.

To derive the differential equation governing the deflection w, the constitutive laws 2.6–2.7 and the balance equation 2.8 are combined, retaining w as the sole variable. This involves i) rewriting the balance 2.8-b as $\boldsymbol{div}(\boldsymbol{\mathcal{M}}) = -\boldsymbol{div}(\boldsymbol{M}) - \boldsymbol{\mathcal{T}}$ and introducing the constitutive laws of $\boldsymbol{\mathcal{M}}$ and $\boldsymbol{M}$, and ii) formulating the balance 2.8-c with the constitutive laws of $\boldsymbol{\mathcal{M}}$ and $\boldsymbol{T}$. This results in the following set:

$$\begin{aligned} E_0(\mathcal{I} - I)\boldsymbol{div}(\boldsymbol{\mathcal{E}}(\boldsymbol{\alpha})) &= -E_0 I \boldsymbol{div}(\boldsymbol{\mathcal{E}}(\boldsymbol{\nabla} w)) - \boldsymbol{\mathcal{T}} \\ E_0(\mathcal{I} - I)\boldsymbol{div}(\boldsymbol{\mathcal{E}}(\boldsymbol{\alpha})) - K\boldsymbol{\alpha} &= -K\boldsymbol{\nabla} w \end{aligned} \tag{2.10}$$

Upon taking the divergence and observing that $\mathrm{div}(\boldsymbol{div}(\boldsymbol{\mathcal{E}}(\,))) = \mathrm{div}(\boldsymbol{\Delta}(\,))$, we arrive at the following:

$$\begin{aligned} \mathrm{div}(E_0(\mathcal{I} - I)\boldsymbol{\Delta\alpha}) &= -E_0 I \Delta^2 w - div(\boldsymbol{\mathcal{T}}) \\ \mathrm{div}(E_0(\mathcal{I} - I)\boldsymbol{\Delta\alpha} - K\boldsymbol{\alpha}) &= -K\nabla w \end{aligned} \tag{2.11}$$

By applying the differential operator $E_0(\mathcal{I} - I)\Delta - K$ to the first equation and $E_0(\mathcal{I} - I)\Delta$ to the second equation, and then subtracting the two, we eliminate $\boldsymbol{\alpha}$. The resulting equation is as follows:

$$(E_0(\mathcal{I} - I)\Delta - K)(E_0 I \Delta^2 w + \mathrm{div}(\boldsymbol{\mathcal{T}})) - E_0(\mathcal{I} - I)K\Delta^2 w = 0 \tag{2.12}$$

By substituting $\mathrm{div}(\boldsymbol{\mathcal{T}})$ with $-\rho_t h_t \omega^2 w$, the Tri-Laplacian equation is derived:

$$E_0 I E_0(\mathcal{I} - I)\Delta^3 - E_0 \mathcal{I} K \Delta^2 w - E_0(\mathcal{I} - I)\rho_t h_t \omega^2 \Delta w + K\rho_t h_t \omega^2 w = 0 \tag{2.13}$$

The equation can be reformulated to disclose the underlying monolithic and bi-layer plate equations:

$$E_0(\mathcal{I} - I)\Delta(E_0 I \Delta^2 w - \rho_t h_t \omega^2 w) - K(E_0 \mathcal{I} \Delta^2 w - \rho_t h_t \omega^2 w) = 0 \tag{2.14}$$

Incidentally, Δw and $\mathrm{div}(\boldsymbol{\alpha})$ are related by the differential equation:

$$K(\Delta w - \mathrm{div}(\boldsymbol{\alpha})) = -E_0(\mathcal{I} - I)\mathrm{div}(\boldsymbol{\Delta}(\boldsymbol{\alpha})) \tag{2.15}$$

To discern the bending modes, one can consider plane bending waves propagating along a specific direction of an isotropic plate, for instance, the x-axis. In this case:

$$w(x, y, t) = w\exp(\kappa x)\exp(i\omega t) \tag{2.16}$$

where κ is the frequency-dependent real or complex wave number. This expression introduced in the Tri-Laplacian equation 2.13 provides the dispersion equation:

$$E_0\mathcal{I}E_0(\mathcal{I}-I)\kappa^6 - E_0\mathcal{I}K\kappa^4 - E_0(\mathcal{I}-I)\rho_t h_t\omega^2\kappa^2 + K\rho_t h_t\omega^2 = 0 \tag{2.17}$$

where:

$$\begin{aligned} a &= \frac{\mathcal{I}}{\mathcal{I}-I} \\ A &= \frac{K}{E_0 I} \\ \Omega &= \frac{\rho_t h_t \omega^2}{K} \end{aligned} \tag{2.18}$$

2.3.2.5 Advantages of the Highly Contrasted Structure Model

The HCS plate model is comprehensive and includes the classical analytical plate models, which are concluded in the 2D HCS model as limit cases

- For a very soft core where ($\mu \to 0$), it results in ($\boldsymbol{T} \to 0$). This corresponds to the bi-layer Kirchhoff plate with total inertia I, and is represented by $\mathcal{T} = -\boldsymbol{div}(M) = \boldsymbol{div}(E_0 I\mathscr{E}(\boldsymbol{\nabla} w))$,
- For a very stiff core where ($\mu \to \infty$), it imposes $\boldsymbol{\nabla} w - \boldsymbol{\alpha} \to 0$. This results in a monolithic Kirchhoff plate with global inertia $\mathcal{T}$ and shear force $\boldsymbol{T} = \boldsymbol{div}(\mathscr{M} + \boldsymbol{M}) = \mathrm{div}(E_0\mathcal{I}\mathscr{E}(\boldsymbol{\nabla} w))$,
- For a very large overall inertia where ($\mathcal{I} \to \infty$), it imposes $\boldsymbol{\alpha} \to 0$, indicating that the inner bending motion dominates. This case leads to the Shear-Bending Sandwich model:

$$\begin{aligned} &\mathrm{div}(\boldsymbol{\mathcal{T}}) + f = 0 \\ &\boldsymbol{\mathcal{T}} = -\boldsymbol{div}(\boldsymbol{M}) + \boldsymbol{T} \\ &\boldsymbol{T} = K\boldsymbol{\nabla} w \\ &\boldsymbol{M} = E_0 I\mathscr{E}(\boldsymbol{\nabla} w) \end{aligned} \tag{2.19}$$

  The Shear-Bending Sandwich model degenerates into a bi-layer Kirchhoff plate when ($\mu \to 0$).

- For a very small inner bending inertia, i.e., ($I \to 0$), it implies that $\boldsymbol{M} \to 0$ and the inner bending effect vanishes. Consequently, a Reissner-Mindlin model is obtained. The specifics of this model are as follows:

$$\begin{aligned} &\mathrm{div}(\boldsymbol{\mathcal{T}}) + f = 0 \\ &\boldsymbol{\mathcal{T}} = \boldsymbol{T} \\ &\boldsymbol{T} = -\boldsymbol{div}(\mathscr{M}) \\ &\boldsymbol{T} = K(\boldsymbol{\nabla} w - \boldsymbol{\alpha}) \\ &\mathscr{M} = E_0\mathcal{I}\mathscr{E}(\boldsymbol{\alpha}) \end{aligned} \tag{2.20}$$

  The latter degenerates into a monolithic Kirchhoff plate when ($\mu \to \infty$).

As outlined in Ref. [12], the specific conditions that lead to different limit behaviors can be quantitatively defined using dimensionless parameters, which are scaled with the plate's flatness parameter.

It's important to note that both the Reissner-Mindlin model and the Shear-Bending Sandwich model converge towards the same pure shear plate model, $\mathrm{div}(\boldsymbol{\mathcal{T}}) + f = 0$; $\boldsymbol{\mathcal{T}} = \boldsymbol{T} = K\boldsymbol{\nabla} w$, when ($\mu \to 0$).

However, this shear plate model does not align with the actual HCS limit behavior as a bi-layer or monolithic plate.

The HCS model addresses some limitations of finite element models, which struggle with contrasting mechanical and geometrical parameters in elasto-static and, more so, in visco-elasto-dynamic situations. It also surpasses the inherent limitations of empirical and semi-empirical approaches based on effective stiffness or resistance factor [73, 74]. These approaches fail to accurately describe dynamic phenomena as the internal kinematics (Zig-Zag shape) identified in elasto-static mode are not applicable in a dynamic regime. Furthermore, the HCS model allows for the direct retrieval of the local state of formation and stress of the components from the HCS variables.

2.3.2.6 Limitations of the Highly Contrasted Structure Model

The 2D HCS model, like any 2D plate model, necessitates a significant scale separation between the small thickness and the large in-plane variation of the physical variables. As a result, in dynamics, the applicability of the HCS model is confined to a specific frequency range. The exact conditions for the frequency range in which the HCS model is applicable are:

- the bending wavelength should be larger than the thickness of the skins, i.e. $\omega < \Omega_b = h_j^{-1}\sqrt{E_0/\rho}$.
- the soft core should experience a quasi-static regime, i.e. $\omega < \Omega_c = c^{-1}\sqrt{\mu/\rho_c}$.

At frequencies beyond $h_j^{-1}\sqrt{E_0/\rho}$, the j-th layer behaves as a guide of waves instead as a plate and when $\omega \gtrsim c^{-1}\sqrt{\mu/\rho_c}$ the response of the core becomes elastodynamic. Such a case is not accounted for in the model. These two limitations in the low-frequency range are implicitly satisfied in the 2D HCS model.

It should also be noted that high stiffness contrast can lead to a specific through-thickness resonance mode in the structure, akin to a mass-spring system with mass m essentially equivalent to the stiff skins $m = \rho(h_1 + h_2)$, the spring k_c being formed by the soft layer $k_c = \mu/c$. An estimate of the resonance frequency of this mode is therefore $\Omega_r = \sqrt{k_c/m} = \sqrt{\mu/\rho}\sqrt{c(h_1 + h_2)}^{-1}$. Considering the stiffness contrast, the resonance frequency Ω_r is notably lower than both Ω_b and Ω_c. The through-thickness resonant mode is primarily linked to anti-plane shear kinematics, contrasting with out-of-plane bending kinematics. This difference leads to an additional dispersion branch, as studied in Ref. [75], which lies beyond the validity domain of the 2D HCS model.

For a sandwich plate with a highly compressible core, the stiff skins could become almost uncoupled and exhibit different flexural motion, this scenario is also out of the validity domain of the 2D HCS model.

2.3.3 General Laminate Model

An alternative approach for determining the vibroacoustic indicators of HCS is the GLM, it models the displacement-constraint relationships based on Mindlin's displacement field [29], the rotational inertia, in-plane stress, bending and transverse shear stress of each layer are taken into account. GLM numerically accounts for the orthotropic plies orientations of each layer, it handles thin/thick laminates and sandwich panels accurately. The dynamic equilibrium equations of the sandwich panel are derived in a wave-based approach and expressed by a polynomial complex Eigenvalue Problem (EVP), the DLF is derived using the eigenvectors of the wave solutions.

GLM is grounded in a discrete layer description using a wave approach [29], each layer is described by Mindlin's displacement field, leading to a dynamic equilibrium system that accounts for rotational inertia, in-plane stress, bending, and transverse shear stress. Numerically, each layer is treated as a laminate, with orthotropic ply orientations taken into account. The dynamic equilibrium equations are expressed in the

form of a polynomial complex Eigenvalue Problem (EVP), in terms of the displacement-force vector. The discrete layer description enables accurate modeling of thin and thick laminates and sandwich plates across the audible frequency band. Notably, GLM delivers precise and rapid solutions for multi-layered damped configurations, it does not make assumptions about material stiffness, thus it applies to a wide range of materials, from hard to soft, including viscoelastic materials. The main equations are recalled below.

In the initial stage, each layer employs orthotropic ply directions. Bending displacements and rotations are presumed within each layer, leading to a displacement field of Mindlin's type for the i-th discrete layer.

$$\begin{gathered} u^i(x,y,z) = u_0^i(x,y) + z\varphi_x^i(x,y) \\ v^i(x,y,z) = v_0^i(x,y) + z\varphi_y^i(x,y) \\ w^i(x,y,z) = w_0^i(x,y) \end{gathered} \tag{2.21}$$

Between any two layers, three are transverse shear stress forces, in-plane stress forces, and stress moments. This results in $3\,(N-1)$ interlayer force variables, where N is the number of layers. Consequently, five equilibrium equations are established for the i-th layer.

$$\begin{gathered} N_{x,x}^i + N_{xy,y}^i + F_x^i - F_x^{i-1} = m_s^i u_{x,tt}^i + I_{z2}^i \varphi_{x,tt}^i \\ N_{xy,x}^i + N_{y,y}^i + F_y^i - F_y^{i-1} = m_s^i v_{y,tt}^i + I_{z2}^i \varphi_{y,tt}^i \\ Q_{x,x}^i + Q_{y,y}^i - Q_x^i + z^i F_x^i - z^{i-1} F_x^{i-1} = m_s^i w_{z,tt}^i \\ M_{x,x}^i + M_{xy,y}^i - Q_x^i + z^i F_x^i - z^{i-1} F_x^{i-1} = I_z^i \varphi_{x,tt}^i + I_{z2}^i u_{x,tt}^i \\ M_{xy,x}^i + M_{y,y}^i - Q_x^i + z^i F_y^i - z^{i-1} F_y^{i-1} = I_z^i \varphi_{y,tt}^i + I_{z2}^i v_{y,tt}^i \end{gathered} \tag{2.22}$$

Each layer accounts for rotational inertia, in-plane motion, bending, and transverse shearing effects. The external surfaces of the structure are assumed to be stress-free. Therefore, in the system of five equilibrium equations (referenced as 2.22), the top face of the first layer has $F_x^0 = F_y^0 = F_z^0 = 0$, while the bottom face of the N-th layer has $F_x^N = F_y^N = F_z^N = 0$. The transverse shear stress forces Q_i, the in-plane stress forces N_i, the inertia term I_i, and the stress moments M_{ij} of each layer are presented in Appendix B by the relations B.5 to B.8.

Assuming N layers in the considered structure, to include the 5 equations of dynamic equilibrium for each of the N layers and 3 equations of the $(N-1)$ interlayer continuity of displacement, the dynamic equilibrium system has a total of $5N+3\,(N-1)$ variables grouped in two vectors: a displacement–rotation vector $\{\mathbf{U}\}$, and an interlayer forces vector $\{\mathbf{F}\}$:

$$\begin{gathered} \{\mathbf{U}\} = \left\{u^1; v^1; w^1; \varphi_x^1; \varphi_y^1; u^2; v^2; w^2; \varphi_x^2; \varphi_y^2; \ldots; u^N; v^N; w^N; \varphi_x^N; \varphi_y^N\right\} \\ \{\mathbf{F}\} = \left\{F_x^1; F_y^1; F_z^1; F_x^2; F_y^2; F_z^2; \ldots; F_x^{N-1}; F_y^{N-1}; F_z^{N-1}\right\} \end{gathered} \tag{2.23}$$

where u, v, w denote the displacement in x, y, z directions, respectively, the subscripts x, y, z signify the corresponding axis for the rotation φ and the force F, the superscripts $1, ..., N$ are the numbers of the layer and interlayer.

To solve the dispersion relations, the dynamic equilibrium system is expressed in terms of a hybrid displacement-force vector:

$$\langle \mathbf{e} \rangle = \{\mathbf{U}; \mathbf{F}\} \tag{2.24}$$

Assuming a harmonic solution $\langle \mathbf{e} \rangle = \{e\}\, exp(i\kappa_x x + i\kappa_y y - i\omega t)$, the system is re-formulated as a generalized complex EVP as follows:

$$\left(\kappa_c^2\,[\mathbf{A}_2] - i\kappa_c\,[\mathbf{A}_1] - [\mathbf{A}_0]\right)\langle \mathbf{e} \rangle = 0 \tag{2.25}$$

where $\kappa_c = \sqrt{\kappa_x^2 + \kappa_y^2}$, κ_x and κ_y denote the wavenumbers in X and Y directions, respectively. The square matrices $[\mathbf{A}_0]$, $[\mathbf{A}_1]$, $[\mathbf{A}_2]$ are of dimension $5N + 3\,(N-1)$, see Appendix B for detailed derivation.

The quadratic matrix EVP 2.25 can be solved by *polyeig* function in MATLAB and produces $2\,(5N + 3\,(N-1))$ complex conjugate eigenvalues, signifying the dispersion relations of the laminated composite structure.

2.3.4 Wave-based Finite Element Method and Dynamic Condensation

Since WFEM is a useful tool to predict the dispersion relations of periodic structures which is usually the case of heterogeneous metastructures. It is of great prospect to study the effect of the heterogeneities, such as stiffness, thickness, and so on, on the elastic waves propagating in an infinite periodic structure/media.

Literature on the WFE scheme is extensive and covers a vast scope of applications, ranging from damage detection [76], metamaterials [10, 30], vibro-acoustics [77], inverse identification [78]. The study of wave propagation in periodic systems was initially explored by Brillouin [79] within the field of electrical engineering. Subsequently, Mead [80] and Abrahamson [81] utilized the Rayleigh-Ritz technique to address non-uniform periodic structures. Later, Orris and Petyt [82, 83] employed the Finite Element (FE) technique for wave propagation analysis. WFE approach utilizes Periodic Structures Theory (PST), simplifying the analysis of the overall structure to a single representative Unit Cell (UC) using the Bloch-Floquet theorem established by Brillouin [84]. WFE is based on the wave propagation principles with Bloch-Floquet Periodic Structures Theory [84, 85].

Ichchou et al. [86] developed the WFE scheme by formulating a propagative approach based on the FE model to efficiently calculate the dispersion curves of complex guided structures and tackled the problem of wave diffusion at substructures coupling locations. Then they modified the WFE method that improves the numerical analysis of wave propagation in multi-layered elastic systems by using dynamic substructuring to overcome the limitations of the traditional WFE approach [87]. The WFE approach then has been widely used for elastic media, Droz et al [88] presented the diffusion formulation for the WFEM and applied it to design the locally resonant structures. Zhou et al. [84, 89–92] combined the advantages of Component Mode Synthesis (CMS) and WFEM to analyze the local behavior of the UC using a reduced modal basis, this approach was applied to study wave propagation characteristics in perforated plates and stiffened plate. Thierry [93] then combined the strengths of CMS and WFE to enhance computational efficiency in analyzing wave propagation in anisotropic textile composites by using the homogenized properties. Christen et al. [94] extended the WFEM for the computation of transmission loss and conducted a sensitivity analysis of the impact of mechanical parameters on features of interest. Zergoune [95] applied the WFEM to predict the flexural vibroacoustic behavior of honeycomb sandwich structures in the low-mid frequency. Mencik [96] developed a numerical approach using the WFE approach to calculate 2D wave modes in cyclically symmetric periodic structures, demonstrating the superiority of the WFE approach over the full Finite Element (FE) analysis. Boukadia [97] introduced a second-order optimization technique within the WFEM framework for the optimization of infinite 2D structures, particularly for improving the vibroacoustic performance of metabeams with clamped-free boundaries. Additionally, Guenfoud [98] investigated systems with multi-layer and rectangular core topologies created through layer stacking. Yang et al. applied the Second Strain Gradient theory into the WFE framework to analyze dynamic behaviors of micro-sized beams and torsion bars [99], and they also explored the wave propagation characteristics [100] and effects of higher-order parameters on the dispersion relation [101]. Errico et al. have dealt with random excitations on the periodic structures [102] and combined with a wavenumber-space load synthesis to simulate the sound transmission of infinite periodic structures [103–107]. Manconi et al. developed the modeling technique within the WFE framework for planar and curved structures to analyze the wave propagation characteristics [108],

advanced the damping estimation techniques for WFEM [20, 21], and studied the wave characteristics of laminated cylinders filled with an acoustic fluid [109]. Mace et al. have promoted the computation of acoustic indicators within the WFE framework [110–113], taking into account acoustic-vibration interactions [114] and examining the impact of individual waves on sound transmission [115].

WFEM has been proven to be advantageous over FEM [84, 89–92, 116, 117], such as reduced model sizes, increased computational efficiency, and enhanced high-frequency capabilities. WFEM is also accurate and efficient in damping estimation [10, 20, 21]. However, its application to HCS and HDS has been underexplored due to the NEP caused by varying wave propagation direction and the lack of a robust wave track technique.

The WFE framework is based on the post-processing of FE analysis of the UC representative of the periodic structure. The response of a 2-dimensional periodic structure in the time and space harmonic excitation takes the form $e^{i(\omega t-\kappa_x x-\kappa_y y)}$ is assumed to act on the structure where κ_x and κ_y are the wavenumber components in the x- and y-directions. Let $\widetilde{\mathbf{D}}$ represent the Dynamic Stiffness Matrix of the UC. This matrix is computed utilizing the stiffness matrix $\widetilde{\mathbf{K}}$ and mass matrix $\widetilde{\mathbf{M}}$ exported from an in-house FE package. The harmonic equation of motion governing the UC is expressed as follows:

$$\widetilde{\mathbf{K}}\mathbf{q}+\widetilde{\mathbf{M}}\ddot{\mathbf{q}}=\left[\widetilde{\mathbf{K}}-\omega^2\widetilde{\mathbf{M}}\right]\mathbf{q}=\widetilde{\mathbf{D}}\mathbf{q}=\mathbf{f} \tag{2.26}$$

where ω denotes the circular frequency, $\mathbf{q}$ signifies the nodal displacement vector of the UC, $\mathbf{f}$ corresponds to the imposed nodal forces, $\ddot{\mathbf{q}}$ denotes the second derivatives of the displacement vector in the time domain.

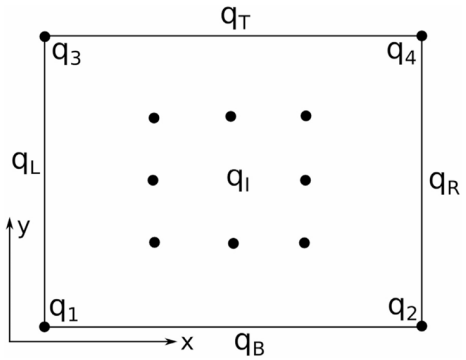

Fig. 2.5. Nodes definition of unit cell in two-dimensional periodic structure [84].

The displacement vector $\mathbf{q}$ containing all the Degrees of Freedom (DOFs) is divided based on the corresponding hypernodes, as illustrated in Fig. 2.5:

$$\mathbf{q}=\left[\mathbf{q}_1^T\ \mathbf{q}_2^T\ \mathbf{q}_3^T\ \mathbf{q}_4^T\ \mathbf{q}_L^T\ \mathbf{q}_B^T\ \mathbf{q}_R^T\ \mathbf{q}_T^T\ \mathbf{q}_I^T\right]^T \tag{2.27}$$

Similarly, the force vector is partitioned in the same manner.

The matrix equations may be partitioned as follows:

$$\begin{bmatrix}\widetilde{\mathbf{M}}_{bb} & \widetilde{\mathbf{M}}_{bi}\\ \widetilde{\mathbf{M}}_{ib} & \widetilde{\mathbf{M}}_{ii}\end{bmatrix}\begin{bmatrix}\ddot{\mathbf{q}}_b\\ \ddot{\mathbf{q}}_i\end{bmatrix}+\begin{bmatrix}\widetilde{\mathbf{K}}_{bb} & \widetilde{\mathbf{K}}_{bi}\\ \widetilde{\mathbf{K}}_{ib} & \widetilde{\mathbf{K}}_{ii}\end{bmatrix}\begin{bmatrix}\mathbf{q}_b\\ \mathbf{q}_i\end{bmatrix}=\begin{bmatrix}\mathbf{F}_b\\ \mathbf{F}_i\end{bmatrix} \tag{2.28}$$

The displacement and the force of the boundary nodes are denoted $\mathbf{q}_b$ and $\mathbf{F}_b$, while $\mathbf{q}_i$ and $\mathbf{F}_i$ represent the internal nodal displacement and force.

The equation of motion 2.28 can be rewritten with the dynamic stiffness matrix when given the frequency. For static modes, assuming zero inertia effects, i.e., the force term $\mathbf{F}_i = 0$, leading to:

$$\begin{bmatrix} \widetilde{\mathbf{D}}_{bb} & \widetilde{\mathbf{D}}_{bi} \\ \widetilde{\mathbf{D}}_{ib} & \widetilde{\mathbf{D}}_{ii} \end{bmatrix} \begin{bmatrix} \mathbf{q}_b \\ \mathbf{q}_i \end{bmatrix} = \begin{bmatrix} \mathbf{F}_b \\ 0 \end{bmatrix} \tag{2.29}$$

From the 2^{nd} equation of the matrix equation 2.29, we find for $\mathbf{q}_i$,

$$\begin{aligned} \widetilde{\mathbf{D}}_{ii}\mathbf{q}_i + \widetilde{\mathbf{D}}_{ib}\mathbf{q}_b &= 0 \\ \mathbf{q}_i &= -\widetilde{\mathbf{D}}_{ii}^{-1}\widetilde{\mathbf{D}}_{ib}\mathbf{q}_b \end{aligned} \tag{2.30}$$

and therefore, the 1^{st} line of the matrix equation 2.29 transformation matrix becomes:

$$\left(\widetilde{\mathbf{D}}_{bb} - \widetilde{\mathbf{D}}_{bi}\widetilde{\mathbf{D}}_{ii}^{-1}\widetilde{\mathbf{D}}_{ib}\right)\mathbf{q}_b = \mathbf{F}_b \tag{2.31}$$

In this case, the internal nodes of the UC are condensed into the reduced dynamic stiffness matrix by the dynamic condensation technique:

$$\widetilde{\mathbf{D}}_c = \widetilde{\mathbf{D}}_{bb} - \widetilde{\mathbf{D}}_{bi}\widetilde{\mathbf{D}}_{ii}^{-1}\widetilde{\mathbf{D}}_{ib} \tag{2.32}$$

where matrix $\widetilde{\mathbf{D}}_c$ is of the same size of the boundary DOFs, i.e., the size of $\mathbf{q}_b$.

In the context of free wave propagation, the external forces of all elements connected to boundary hypernodes obey the Periodic Structure Theory (PST) [118]:

$$\mathbf{q}_2 = \lambda_x\mathbf{q}_1;\ \mathbf{q}_3 = \lambda_x\mathbf{q}_1;\ \mathbf{q}_4 = \lambda_x\lambda_y\mathbf{q}_1;\ \mathbf{q}_R = \lambda_x\mathbf{q}_L;\ \mathbf{q}_T = \lambda_y\mathbf{q}_B; \tag{2.33}$$

where $\lambda_x = e^{-i\kappa_x L_x}$ and $\lambda_y = e^{-i\kappa_y L_y}$ represent the propagation constants in the 2D periodicity directions X and Y, respectively. The variables κ_x and κ_y are associated with the wavevector propagating in the X and Y directions, respectively.

Eq. 2.33 can be rewritten in the matrix format:

$$\mathbf{q}_b = \begin{bmatrix} \mathbf{q}_1 \\ \mathbf{q}_2 \\ \mathbf{q}_3 \\ \mathbf{q}_4 \\ \mathbf{q}_L \\ \mathbf{q}_B \\ \mathbf{q}_R \\ \mathbf{q}_T \end{bmatrix} = \begin{bmatrix} \mathbf{I}_s & 0 & 0 \\ \lambda_x\mathbf{I}_s & 0 & 0 \\ \lambda_y\mathbf{I}_s & 0 & 0 \\ \lambda_x\lambda_y\mathbf{I}_s & 0 & 0 \\ 0 & \mathbf{I}_{ms} & 0 \\ 0 & 0 & \mathbf{I}_{ns} \\ 0 & \lambda_x\mathbf{I}_{ms} & 0 \\ 0 & 0 & \lambda_y\mathbf{I}_{ns} \end{bmatrix} \begin{bmatrix} \mathbf{q}_1 \\ \mathbf{q}_L \\ \mathbf{q}_B \end{bmatrix} = \mathbf{\Lambda}_R \begin{bmatrix} \mathbf{q}_1 \\ \mathbf{q}_L \\ \mathbf{q}_B \end{bmatrix} \tag{2.34}$$

where $\mathbf{I}_s$, $\mathbf{I}_{sn}$, $\mathbf{I}_{sm}$ are the identity matrix of size s, sn, sm respectively. The reduced vector is of $(s + ns + ms)$ lines, and $\mathbf{\Lambda}_R$ is of $(4s + 2ns + 2ms)$ lines and $(s + ns + ms)$ columns.

Similarly, the nodal forces are also linked by PST:

$$\begin{bmatrix} \mathbf{I}_s & \lambda_x^{-1}\mathbf{I}_s & \lambda_y^{-1}\mathbf{I}_s & \lambda_x^{-1}\lambda_y^{-1}\mathbf{I}_s & 0 & 0 & 0 & 0 \\ 0 & 0 & 0 & 0 & \mathbf{I}_{ms} & 0 & \lambda_x^{-1}\mathbf{I}_{ms} & 0 \\ 0 & 0 & 0 & 0 & 0 & \mathbf{I}_{ns} & 0 & \lambda_y^{-1}\mathbf{I}_{ns} \end{bmatrix} \mathbf{f} = \mathbf{0} \tag{2.35}$$

So, the Time-Harmonic Equation of Motion 2.26 becomes:

$$\mathbf{\Lambda}_L \left[\widetilde{\mathbf{D}}_c(\omega, \kappa_x, \kappa_y)\right] \mathbf{\Lambda}_R \begin{bmatrix} \mathbf{q}_1 \\ \mathbf{q}_L \\ \mathbf{q}_B \end{bmatrix} = 0 \tag{2.36}$$

where $\widetilde{\mathbf{D}}$ is the dynamic matrix containing the reduced set of DOFs in Eq. 2.32. This matrix equation can be solved by formulating a quadratic Eigenvalue Problem (EVP) for the wavenumbers in predefined propagating directions, as outlined in [84]. Note that once the waves are obtained and sorted, the DLF associated with each wave can be computed from a power balance equation.

Suppose frequency ω one of (λ_x, λ_y) is given, for instance λ_y. Eq. 2.36 then becomes a quadratic eigenvalue problem in λ_x as follows:

$$\frac{1}{\lambda_x}\left(\lambda_x^2 \mathbf{A} + \lambda_x \mathbf{B} + \mathbf{C}\right) \begin{bmatrix} q_1 \\ q_L \\ q_B \end{bmatrix} = 0 \tag{2.37}$$

where

$$\mathbf{A} = \begin{bmatrix} A_{11} & A_{1L} & A_{1B} \\ A_{L1} & A_{LL} & A_{LB} \\ A_{B1} & A_{BL} & A_{BB} \end{bmatrix} \tag{2.38}$$

$$\mathbf{B} = \begin{bmatrix} B_{11} & B_{1L} & B_{1B} \\ B_{L1} & B_{LL} & B_{LB} \\ B_{B1} & B_{BL} & B_{BB} \end{bmatrix} \tag{2.39}$$

$$\mathbf{C} = \begin{bmatrix} C_{11} & C_{1L} & C_{1B} \\ C_{L1} & C_{LL} & C_{LB} \\ C_{B1} & C_{BL} & C_{BB} \end{bmatrix} \tag{2.40}$$

The coefficients in the matrices **A**, **B** and **C** are presented in detail in Appendix C, the quadratic Eigenvalue Problem (EVP) can be solved using the $polyeig$ function in MATLAB, of which there are $2(s + ns + ms)$ solutions.

The quadratic EVP of Eq. 2.37 can also be solved using the following linearization:

$$\begin{bmatrix} -\boldsymbol{C} & 0 \\ 0 & I \end{bmatrix} \begin{bmatrix} q \\ \lambda_x q \end{bmatrix} = \lambda_x \begin{bmatrix} \boldsymbol{B} & \boldsymbol{A} \\ I & 0 \end{bmatrix} \begin{bmatrix} q \\ \lambda_x q \end{bmatrix} \tag{2.41}$$

Both quadratic and linear forms, calculated respectively by $polyeig$ and eig functions in MATLAB, lead to the same eigenvalue κ and eigenvector ϕ.

The wavemode corresponds to the internal hypernode obtained by

$$\mathbf{q}_{ii} = -\frac{\mathbf{D}_{ib}}{\mathbf{D}_{ii}} \mathbf{q}_{bd}^T \tag{2.42}$$

The full set of eigenvectors can then be assembled in the order of Eq. 2.27, the eigenvector represents the dynamic response of all the nodes in the UC when the corresponding wave propagates in the structure.

Wave propagation has been widely studied in the WFE scheme for elastic media appearing including complex geometries using Periodic Structures Theory [84] and Bloch-Floquet periodicity Boundary Condition [85]. Based on the system matrices obtained via conventional FE software, a TM relating the two state vectors at the chosen UC is formulated [84], and an EVP can then be derived and solved for the wavenumbers and wavemodes. WFEM has been successfully applied in structures such as viscoelastic media [20], fluid-filled cylinders [119], rib-stiffened plates [86], laminated structures [87], sandwich

structures [107] and poroelastic media [120, 121], it has also been used for crack damage detection [122] and coupling effects between two coupled parallel waveguides [123], the effects of damping on wave propagation in flat panels is also studied [20].

Moreover, the WFE scheme has wide application prospects in the optimization of prediction frameworks to tackle the drawbacks of FEM using the theory of wave propagation in periodic structures. Despite the sophisticated mathematical derivation in numerical integrations of complex wave functions (real part for the wave propagation, while imaginary part for the wave evanescence), previous research proves that the WFE scheme is beneficial in comparison with the FEM [84, 89–92, 116, 117]:

- Model sizes in the WFE scheme are substantially smaller than those in element-based methods. Since the proposed field variable expansions satisfy the governing dynamic equations, approximation errors might be only involved in the equations representing the boundary conditions.
- WFE scheme is not constrained by Low-Frequency assumptions for Classical Analytical Methods (e.g., the cross-section remains plane after deformation), and the expansions for derived secondary field variables, such as fluid velocity and structural stress, have the same spatial variation as the primary field variables, such as acoustic pressure and structural displacement. This is advantageous for the convergence rate in vibroacoustic problems in the WFE scheme, for which the effect of the fluid on the structure is pressure-controlled, but the effect of the structure on the fluid is velocity-controlled.
- Due to the enhanced computational efficiency, the practical frequency limitation of the WFE scheme is substantially higher than the existing techniques, the wave-based prediction technique enables accurate predictions in the mid-frequency range, while the computational efforts of element-based models in the mid-frequency range are prohibitively large.

However, the main drawbacks of the WFE scheme are that,

- When varying the propagating direction of the wave, which is necessary for periodic structures with complex geometries or non-isotropic properties, it leads to a Nonlinear Eigenvalue Problem (NEP) of wavenumber (i.e., eigenvalue) and wavemode (i.e., eigenvector). Solving the NEP is the main challenge because an optimal strategy has not been devised until now [124].
- The wavenumber and wavemode are not sequenced in the correct order along frequency for a specific wave, the numerical issue of wave track is fatal to the following calculation such as the wavenumber space, DLF, etc.

As a result, the application of the WFEM to contrasted and damped media has not received much attention in the past, despite its unquestionable advantage of formulating the problem from standard FE libraries [118].

2.4 Damping Estimation Techniques

The growing significance of energy dissipation mechanisms in HDS for vibration reduction has brought enriched materials and structures into the spotlight. Highly dissipative materials have emerged as a leading damping mechanism in composite structures [17]. The damping technology is now emerging as a competitive medium for structural design across various domains, particularly in the transportation engineering sector where accurate and robust simulation tools are paramount to predict vibroacoustic indicators for vehicle design. The prediction of the DLF to quantify the structural damping efficacy by the ratio of dissipated energy to total energy as defined by Rao [125], has become a focal point of interest.

2.4.1 Classical Methods

Classical methods offer avenues for predicting DLF from the frequency response functions to random or harmonic excitations acquired analytically, experimentally, or numerically [126]. Methods encompass the modal technique (half-power bandwidth method) [127], Decay Rate Method (DRM or logarithmic decrement method) [128], and PIM [129], [126], etc.

2.4.1.1 Modal Technique (Half-Power Bandwidth Method)

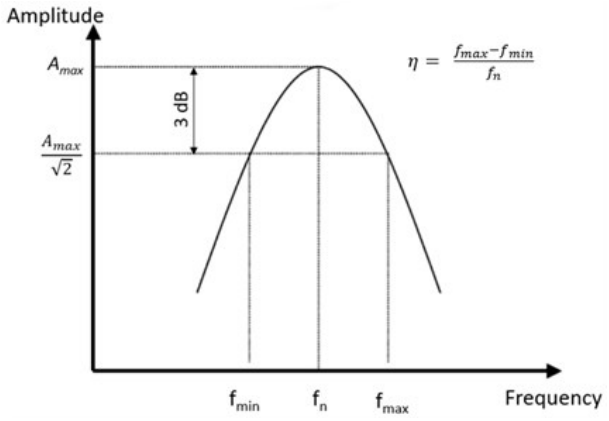

Fig. 2.6. Modal damping determination using the Half-Power Bandwidth Method [126].

The Half-Power Bandwidth Method (HPBM), a recognized modal technique for damping estimation, is employed in this study for validation purposes, given its restriction to the determination of damping for individual modes [130]. The method involves measuring the bandwidth corresponding to a 3 dB drop in power for each mode. Fig. 2.6 illustrates the displacement modulus versus frequency for a basic spring-mass-damper oscillator [131].

The DLF is consequently expressed about the HPBM as follows:

$$\eta = \frac{\Delta f}{f_n} \tag{2.43}$$

where f_n denotes the mode's natural frequency.

The procedure necessitates repetition at multiple excitation and response points due to mode dependency on these positions and the need to minimize experimental errors. The averaged modal DLF is then computed from all measurements. For Statistical Energy Analysis (SEA), the procedure is repeated for all modes within a specific 1/3 octave frequency band to obtain a band-averaged DLF value.

However, the limitation lies in its requirement to be repeated for each mode, which is impractical in the SEA context due to high modal density and overlap at higher frequencies [130]. Additionally, the HPBM is often challenging and unsuitable for estimating the DLF of complex structures [132].

2.4.1.2 Decay Rate Method

The DRM, recognized by acousticians for room reverberation time measurement, utilizes the transient response of a resonant mode with linear damping to measure damping. In a single Degree of Freedom (DOF) system, the envelopes of the displacement of the system exponentially decay as $e^{-\eta\omega t}$ upon cessation of excitation (see Fig. 2.7). This principle extends to multi DOF systems like plates or beams, where each structural mode's energy also decays exponentially over time [133]. A common acoustic

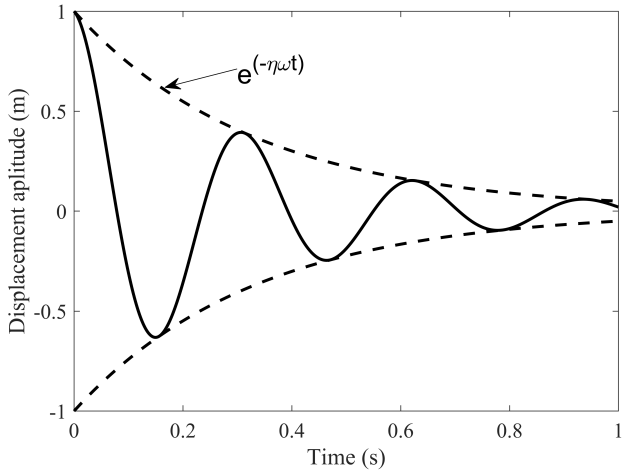

Fig. 2.7. Energy decay of a damped single DOF system. −: Displacement amplitude. −−: Envelopes.

damping measure is the reverberation time, which is the duration required for vibrational energy to reduce by a factor of 1 millionth [134]. Thus,

$$e^{-\omega_0 \eta T_R} = 10^{-6} \tag{2.44}$$

which results in the well-known expression:

$$\eta = \frac{2.2}{f T_R} \tag{2.45}$$

here T_R represents the reverberation time. The concept of reverberation time, as applied to DLF measurements via DRM, is defined solely by the 60 dB reduction in energy over a specific period.

Eq. 2.44 pertains to room acoustics physics and assumes a reverberant field. Reverberation time is influenced by both frequency and room absorption [135]. The DRM, which is based on the logarithmic decrease of the transient response post-excitation, presumes an exponential decay across all modes within the frequency band. The DLF is determined using the decay rate of the decay curves. However, DRM has limitations for HDS and does not apply to the high-frequency range.

2.4.1.3 Power Input Method

In the framework of Statistical Energy Analysis (SEA), the Power Input Method (PIM) offers cost-effective solutions across a wide frequency spectrum, especially at high frequencies with substantial modal density. The PIM, grounded in the SEA power balance formulation, is defined as the ratio of power injected into the structure to the system's global vibrational energy. For an isolated subsystem, the power balance equation simplifies to [132]:

$$\eta = \frac{\langle P_{in} \rangle_{x,t,f}}{\omega \langle E \rangle_{x,t,f}} \tag{2.46}$$

where η is the band-averaged DLF for that isolated subsystem and $\langle\ \rangle_{x,t,f}$ denotes spatial, temporal, and frequency averaging.

The measured DLF quantifies the total damping capacity of the structure, a summation of various energy dissipation sources within a system. The total DLF accounts for internal energy dissipation, radiation dissipation, edge dissipation at the system's boundaries, and energy lost to neighboring subsystems if any. Therefore, the total dissipated power becomes:

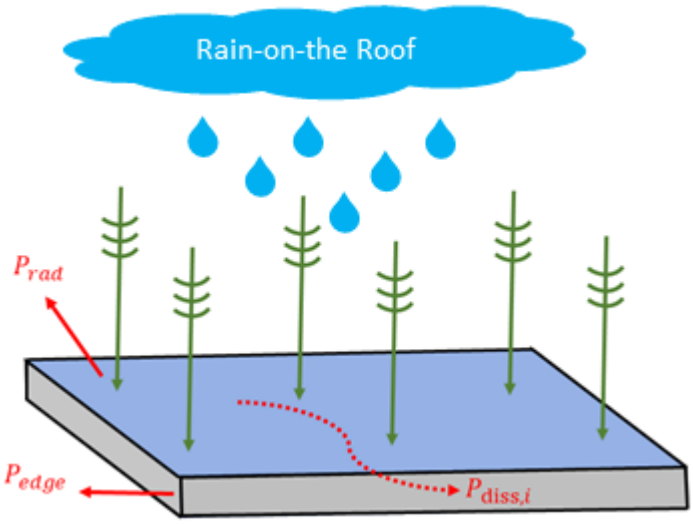

Fig. 2.8. Sketch showing the mechanism of the Power Input Method for a plate structure.

$$P_{total} = P_{diss,i} + P_{rad} + P_{edge} \tag{2.47}$$

Energy loss at the system boundaries can be disregarded with a careful selection of system limits. For rigid boundaries with a loss factor smaller than the structural internal loss factor, it can be assumed that ($\eta_{edge} \ll \eta_{diss}$). The radiation loss factor is associated with radiation efficiency, which is related to the radiated power and can be directly calculated [132]:

$$\begin{aligned} \eta_{rad} &= \frac{\sigma \rho_0 c_0}{\omega \rho_i h} \\ \sigma &= \frac{P_{rad}}{\rho_0 c_0 A v^2} \end{aligned} \tag{2.48}$$

where σ is the radiation efficiency, ρ_0 the density of the surrounding fluid, c_0 the speed of sound in the surrounding fluid, ρ_i the subsystem density, h the subsystem thickness, P_{rad} the radiated power, A the subsystem area, and v^2 the mean squared velocity over the entire test surface.

The DLF estimation using the PIM requires the measurement of the band-averaged power input to the structure, estimated from the time-averaged product of force and velocity at the driving point:

$$P_{in} = \bar{f}(t)\bar{v}(t) \tag{2.49}$$

The time averaging is performed over one period. When expressed in the frequency domain, it reads:

$$\langle P_{in} \rangle_t = \frac{1}{T} \int_0^T f(t)v(t)dt = \frac{1}{2} Re(\langle FV^* \rangle_t) \tag{2.50}$$

where FV^* is the cross-spectrum of force and velocity at the driving point.

The band-averaged power input into the a plate structure considering the space, time, and frequency averaging is therefore:

$$\langle P_{in} \rangle_{x,t,f} = \frac{1}{T} \int_0^T f(t)v(t)dt = \frac{1}{2} Re(\langle FV^* \rangle_{x,t,f}) \tag{2.51}$$

Due to the challenge of measuring internal stresses, and because SEA addresses modal behavior, the

mechanical energy is determined as twice the kinetic energy, estimated by integrating the product of mass, M, and time-averaged square velocity. So, for the power input, the time averaging is performed over one period. When expressed in frequency terms it becomes:

$$\left\langle v^2(t)\right\rangle_t = \frac{1}{T}\int_0^T v(t)v(t)dt = \frac{1}{2}Re(\langle VV^*\rangle_t) \tag{2.52}$$

where VV^* is the velocity auto-spectrum, the band-averaged modal energy is given by:

$$\langle E\rangle_{x,t,f} = M\frac{1}{2}Re(\langle VV^*\rangle_{x,t,f}) \tag{2.53}$$

The DLF, the ratio of power input to the global subsystem energy, both band-averaged, becomes:

$$\eta_i = \frac{\frac{1}{2}Re(\langle FV^*\rangle_{t,f})}{\omega M\frac{1}{2}\langle VV^*\rangle_{t,f}} \tag{2.54}$$

here η_i denotes the DLF for one excitation location.

To meet the SEA requirement of modal independence, the DLF should be evaluated by the *Rain-on-the-Roof* excitation locations using Eq. 2.54 [136]. The averaged DLF in the spatial domain is then computed as [137]:

$$\eta = \frac{1}{N}\sum_{n=1}^{N}\eta_i \tag{2.55}$$

The DLF from Eq. 2.55 is the averaged DLF obtained from each excitation point. The PIM has advantages over the other two classical methods, including independence from mode shapes and natural frequency assumptions, compatibility with multiple modes [138], and applicability to all damping levels and frequency ranges [139], thereby providing reference results for the global DLF of HDS.

2.4.2 Damping Loss Factor approximated by Complex Wavenumbers

The harmonic oscillations exhibited in a 2-dimensional structure can be illustrated by a plane wave with complex wavenumber κ propagating at the angular frequency ω [29]:

$$u\,(x,t) = \tilde{U}e^{-i\kappa x}e^{i\omega t} \tag{2.56}$$

where x represents the distance the wave has travelled, and t denotes the time.

For an infinite system, the presence of damping leads to an exponential decay in vibration amplitude concerning distance and time [31]. The spatial decay is defined by the imaginary part of κ:

$$\Delta x = 20log\left(e^{Im(\kappa)}\right) = \frac{20Im\,(\kappa)}{ln\,(10)} \tag{2.57}$$

The principle of temporal decay rate is predicated on the notion that the energy of a system decreases exponentially over time following the termination of excitation. This decay is represented by the equation $e^{-\omega\eta\Delta t}$ as depicted in Fig. 2.7. Here, the structural DLF, η, is employed to determine the temporal decay rate [140]:

$$\Delta t = 20log\left(e^{-\eta\omega/2}\right) = \frac{-10\eta\omega}{ln\,(10)} \tag{2.58}$$

The spatial and temporal decay rates are linked by the relationship $\Delta t = \Delta x C_g$, where group velocity $C_g = \frac{\partial\omega}{\partial\kappa}$ represents the energy transmission speed in the structure [141]. Consequently, the DLF can be

calculated:

$$\eta = -2\frac{Im\left(\kappa\right)}{\omega}C_g = -2\frac{Im\left(\kappa\right)}{Re\left(\kappa\right)}\frac{C_g}{C_\varphi} \tag{2.59}$$

where $C_\varphi = \frac{\omega}{\kappa}$ denotes the phase velocity.

2.4.3 Damping Loss Factor using the Power Balance

Following the solution of the EVP in the GLM (detailed in Section 2.3.3) and the WFE framework (detailed in Section 3.3), once the waves are tracked, DLF associated with any wave can be computed by the power balance equation [142]:

$$\eta = \frac{P_{diss}}{\omega\left(E_k + E_s\right)} \tag{2.60}$$

where P_{diss} denotes the total time-averaged dissipated power, while E_k and E_s represent the time-averaged kinetic and strain energies, respectively.

The expression for the time-averaged kinetic energy, E_k, reads:

$$E_k = \frac{\omega^2}{4}\boldsymbol{\phi}^H\boldsymbol{M}\boldsymbol{\phi} \tag{2.61}$$

The time-averaged strain energy is determined by analogously employing the stiffness matrix.

$$E_s = \frac{1}{4}Re\left\{\boldsymbol{\phi}^H\boldsymbol{K}\boldsymbol{\phi}\right\} \tag{2.62}$$

The correlation between the total power dissipation and strain energy is established based on the research conducted by Manconi et al. [21]:

$$P_{diss} = \frac{\omega}{2}Im\left\{\boldsymbol{\phi}^H\boldsymbol{K}\boldsymbol{\phi}\right\} \tag{2.63}$$

Substituting Eqs. 2.61, 2.62 and 2.63 into Eq. 2.60 gives:

$$\eta\left(\omega,\theta\right) = \frac{P_{diss}}{\omega\left(E_s + E_k\right)} = \frac{\frac{\omega}{2}Im\left\{\phi^H\mathbf{K}\phi\right\}}{\omega\left(\frac{1}{4}Re\left\{\phi^H\mathbf{K}\phi\right\} + \frac{\omega^2}{4}Re\left\{\phi^H\mathbf{M}\phi\right\}\right)} \tag{2.64}$$

Eq. 2.64 denotes the DLF for a wave propagating at angle θ.

2.4.4 Average Damping Loss Factor

For isotropic structures, the DLF is spatially uniform. However, for anisotropic structures, the average DLF is a function of θ because the modal density differs for each propagating angle. A general formulation for averaging the DLF is necessary to evaluate the damping effect.

It is useful to apply the angular modal density $N\left(\omega,\theta\right)$ which is obtained theoretically at each propagation angle of interest [130]:

$$N\left(\omega,T,\theta\right) = \frac{S}{\pi^2}\kappa\left(\theta,T,\omega\right)\frac{\partial\kappa\left(\theta,T,\omega\right)}{\partial\omega} \tag{2.65}$$

where S is the UC's surface, and $\kappa\left(\theta,\omega\right)$ denotes the wavenumbers at the propagation direction θ, temperature T, and frequency ω.

Using Eq. 2.65, the average DLF can be calculated using the following integration over all directions:

$$\bar{\eta}(\omega, T) = \frac{\int_0^{2\pi} \eta(\omega, T, \theta)\, dN}{\int_0^{2\pi} dN} \tag{2.66}$$

Eq. 2.66 allows a straightforward numerical evaluation of the average DLF of non-isotropic systems.

2.5 Calculation Methods of Sound Transmission Loss

Recent years have seen a rise in the use of multi-layered structures over single-wall structures due to their superior acoustic comfort and noise reduction capabilities. These structures provide designers more flexibility in adjusting vibroacoustic performance, leading to enhanced sound insulation. Such multi-layer systems are exemplified by advanced heterogeneous metastructures, which are increasingly used in industries such as aerospace and energy.

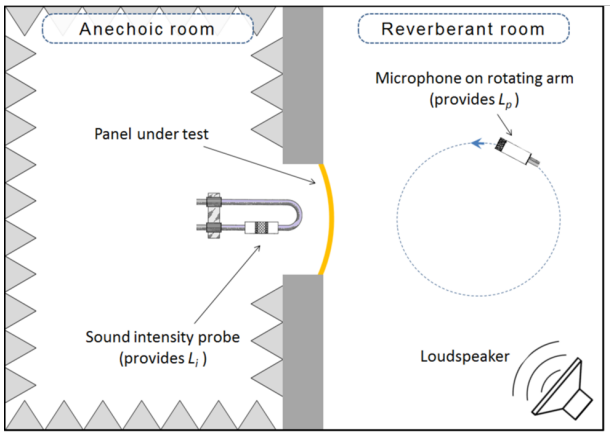

Fig. 2.9. Illustration of the test facility with coupled reverberant-anechoic rooms [143].

The efficiency of a noise-reducing treatment can be assessed by a variety of indicators, the Sound Transmission Loss (STL) will be discussed in this thesis, the STL is a characteristic of the structure, with no account of source and receiving media, expressed in decibels. The measurement facility is depicted in Fig. 2.9 to offer a clear comprehension: for a canonical transmission problem, a plate-like structure separates two rooms, one of which contains a noise source (anechoic room), the other being the reverberant room [107]. Provided the sound intensity of both rooms, the STL is defined as the ratio between the power of the incident (P_i) and transmitted (P_t) sound fields, expressed in decibels:

$$STL = 10 log_{10} \frac{P_i}{P_t} \quad \text{in dB} \tag{2.67}$$

For an infinite plate, STL is defined as the power transmitted per unit surface. STL of metastructures will be an important indicator for the current study since its value tells the noise insulation performance of the designed structure. STL in general describes the accumulated decrease (usually the logarithmic ratio) in the intensity of incident and transmitted energies as the wave propagates across the structure. STL solved by the analytical method is only available for planar geometry, complex geometry is currently computable through numerical methods such as FEM, TMM, GTMM, and WFE by careful setup. However, the resources consumed by the numerical computation through FEM exceed far beyond the most conservative expectation, therefore, TMM, GTMM, and WFE will be considered as the main numerical methods in this thesis.

2.5.1 Analytical Methods based on Classical Models

Various analytical vibroacoustic models of varying complexity have been developed to predict the sound insulation properties of plate structures, especially noise attenuation problems. An early model was developed by Cremer [31] which was applied to the computation of the TL across infinite, thin walls. Related work approaching the same problem of computing the acoustic insulation indicators of a thin wall is presented in [144–146]. In Cremer's model, it is assumed that the motion of the plate is described only by the bending wave equation, which is based on the classical plate theory [147].

Analytical approaches to calculate STL typically involve mathematical models and equations incorporating factors such as material properties, sound frequency, and incidence angle. Cremer [31] initially devised a model for computing STL across infinite, thin walls, utilizing the bending wave equation from classical plate theory. However, this model is constrained to frequencies below the critical frequency due to inherent limitations in its assumptions [148]. Heckl and Donner [149] subsequently refined Cremer's theory, introducing a model based on the first-order shear deformation theory (FSDT) [150–152], which considers both flexural and transverse shear motion in thicker walls. The corrected STL formulation accounting for the plates' shear deformation is provided in Ref. [153]. However, the FSDT model is valid only for frequencies well below the first symmetric frequency of the plate, as it does not account for through-thickness dilatation motion, potentially causing discrepancies in predictions, particularly for soft materials and at higher frequencies [149]. To encompass both antisymmetric and symmetric plate motions, Ljunggren [153, 154] presents a comprehensive expression for calculating the STL of an infinite wall with uniform thickness.

Various theoretical models address the behavior of multi-layer structures, as categorized by Carrera [155, 156] into three main types:

- Equivalent Single Layer (ESL) models
- Layer Wise (LW) models
- Hybrid or Zig-Zag models

ESL models characterize the whole laminated plate dynamics via the displacement field of an equivalent layer, providing flexibility in employing shear deformation theories of order one [150–152] and higher [37, 157–159]. LW models, conversely, describe the displacement field within each layer [29, 160–166], necessitating higher computational efforts due to increasing unknowns with layer count. Hybrid or Zig-Zag models combine aspects of ESL and LW models, leveraging interface continuity conditions to reduce the number of unknown functions, independent of layer count. Various studies [167–172] have applied these models to analyze the dynamic response of multi-layer systems

Given the diverse materials utilized in industrial multi-layer structures, the detailed finite element modeling required for their analysis incurs a considerable computational burden. Consequently, there is a need to simplify the representation of multi-layer systems into single-layer equivalents. A seminal development in this direction occurred with the introduction of a simplified equivalent thin plate model for sandwich structures featuring a viscoelastic core, as documented by Ross et al. [14], Kerwin et al. [15], and Ungar [16]. Subsequently, Guyader and Cacciolati [173] extended this approach, presenting an equivalent thin plate model applicable to multi-layer structures comprising isotropic layers. Following suit, Marchetti et al. [140] recently introduced an equivalent thin plate model tailored for laminated structures composed of orthotropic layers. These equivalent plate models aim to determine the frequency-dependent mechanical parameters of the equivalent thin plate, encompassing both bending and shear motions inherent in multi-layer structures. However, it is imperative to establish the frequency domain within which these equivalent plate models remain valid, as conventional plate theories neglect the through-thickness dilatation motion of the structure. Hence, delineating the frequency range of applicability is crucial for the prudent utilization of these equivalent plate models.

Arasan et al. [174] have scrutinized the underlying assumptions of thin and thick plate theories beyond a specified frequency threshold. These two simple analytical expressions for computing the limit of thin and thick plate theories can be useful in choosing the appropriate model in each case. Deviations of the STL predictions obtained from different models are observed above these two limiting frequencies and can be applied to layers of finite sidelengths. They also observed that plate theories quickly fail for materials that are too soft in terms of longitudinal compression [174].

2.5.2 General Laminate Model

As presented in Section 2.3.3, GLM uses a complete and mathematically coherent discrete layer theory for the wavenumber space of heterogeneous meta-structures. The theory is also developed for. Both symmetrical laminate composite and discrete thick laminate composite are modeled by Ghinet et al. [175], a symmetric singly curved sandwich made up of a bottom skin laminate, a shearing core, and a top skin laminate [176].

The incident plane wave on the structure is defined by incidence angle θ and azimuthal angle φ, as represented in Fig. 2.10.

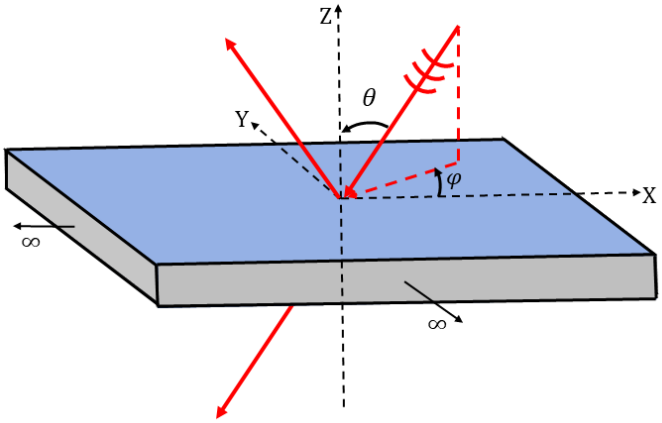

Fig. 2.10. Acoustic Waves Impinging on the Infinite Structure.

The acoustic wavenumber from the ambient media of the incident side, $\kappa_i = \omega/c_0$, is decomposed as $\kappa_x = \kappa_i sin\theta cos\varphi$, $\kappa_y = \kappa_i sin\theta sin\varphi$ and $\kappa_z = \kappa_i cos\theta$. The acoustic excitation of a plane wave with the trace wavenumber components writes:

$$p_i(\omega, \theta, \varphi) = P_i exp\left[-i(x\kappa_x + y\kappa_y)\right] exp\left[-iz\kappa_Z\right] \tag{2.68}$$

By adding the wave excitation term on the right-hand side of Eq. 2.25, the acoustic wave is imposed to propagate in the structure and the relation is rewritten in the form of a linear equations system as follows:

$$\left(\kappa^2(\omega, \theta, \varphi)\left[\mathbf{A}_2(\varphi)\right] - i\kappa(\omega, \theta, \varphi)\left[\mathbf{A}_1(\varphi)\right] - \left[\mathbf{A}_0(\varphi)\right]\right)\langle \mathbf{e}\rangle = \langle \mathbf{f}\rangle \tag{2.69}$$

where $\langle \mathbf{f}\rangle = \{0, 0, p, 0, 0\}^T$, p is the amplitude of the acoustical pressure of excitation.

The surface impedance is recovered using:

$$Z_s(\omega, \theta, \varphi) = \frac{\mathbf{f}(3)}{\mathbf{e}(3)} \tag{2.70}$$

where $\mathbf{e}(3)$ denotes the normal displacement of the excited face (the third element of the solution vector $\langle \mathbf{e}(\kappa, \theta, \varphi)\rangle$), the same for $\mathbf{f}(3)$.

The associated transmission coefficient (or transparency) of an incident acoustic wave is given by:

$$\tau(\omega, \theta, \varphi) = \frac{4Z_0^2}{|Z_s + 2Z_0|^2} \tag{2.71}$$

where $Z_0 = \rho_0 c_0$ with ρ_0 the density and c_0 the speed of sound in the ambient medium (incident side or transmitted side).

Considering the acoustic transmission in a Diffuse Acoustic Field (DAF) through the structure in flat or curved infinite configurations.

$$\tau(\omega) = \frac{\int_0^{2\pi}\int_0^{\theta_{max}} \tau(\omega,\theta,\varphi) sin\theta cos\theta d\theta d\varphi}{\int_0^{2\pi}\int_0^{\theta_{max}} sin\theta cos\theta d\theta d\varphi} = \frac{\int_0^{2\pi}\int_0^{\theta_{max}} \tau(\omega,\theta,\varphi) sin\theta cos\theta d\theta d\varphi}{\pi(1 - cos^2(\theta_{max}))} \tag{2.72}$$

Typically, set $\theta_{max} = 78^o$ for field incidence and $\theta_{max} = 90^o$ for an ideal DAF.

2.5.3 Transfer Matrix Method

The TMM is a widely used semi-analytical wave-based method applied to simulate the elastic wave propagation laminated structures at any frequency range with very high computational efficiency [177, 178]. The TMM initially examines a flat infinite panel that is excited by an incident pressure field. The TM, which connects the two adjacent layers of the structure, is derived based on the wavenumbers propagating within the medium. Matrix representation of wave propagation serves as an efficient and widely used tool for modeling plane acoustic fields in stratified media. In the classical TMM, all the waves propagating within each layer of the structure are assumed to have the same in-plane wavenumber components of the plane wave excitation coming from a bounding semi-infinite fluid.

Fig. 2.11. Plane wave impinging on a multi-layer domain [177].

The semi-analytical TMM assumes in-plane waves propagating in laterally infinite homogeneous media. In conventional TMM for calculating the STL, transfer condition within a layer, coupling condition between adjacent layers, excitation and termination conditions should be included in the process. The layers can be of various types (plates, composites, sandwich structures, solids (2D and 3D), fluids, porous, ...). Moreover, the finite size can be corrected for. Details of the TMM methodology are found in [177].

For simplicity, we limit the example to equivalent fluid models, for the transmission of one layer, the equations of pressure and velocity are:

$$\begin{aligned} p(x) &= Ae^{-i\kappa_1 x} + Be^{i\kappa_1 x} \\ v(x) &= \frac{A}{Z_1}e^{-i\kappa_1 x} - \frac{B}{Z_1}e^{i\kappa_1 x} \end{aligned} \tag{2.73}$$

where κ_1 and Z_1 denote the complex wave number and characteristic impedance of medium 1, respectively, A and B, are the unknown amplitude of negative- and positive-going waves.

Therefore, the following equation system of acoustic pressure and velocity is obtained:

$$\begin{array}{ll} p_1 = p(0) = A + B & p_2 = p(x_1) = Ae^{-i\kappa_1 x_1} + Be^{i\kappa_1 x_1} \\ v_1 = v(0) = \frac{A-B}{Z_1} & v_2 = v(x_1) = \frac{A}{Z_1}e^{-i\kappa_1 x_1} - \frac{B}{Z_1}e^{i\kappa_1 x_1} \end{array} \tag{2.74}$$

leading to the following relation of the transfer matrix:

$$\begin{pmatrix} p_1 \\ v_1 \end{pmatrix} = \begin{bmatrix} cos(\kappa_1 x_1) & iZ_1 sin(\kappa_1 x_1) \\ \frac{isin(\kappa_1 x_1)}{Z_1} & cos(\kappa_1 x_1) \end{bmatrix} \begin{pmatrix} p_2 \\ v_2 \end{pmatrix} = \mathbf{T}_1 \begin{pmatrix} p_2 \\ v_2 \end{pmatrix} \tag{2.75}$$

Then we consider the transmission through a multi-layer structure as depicted in Fig. 2.11, the transfer matrices of all the layers can then be assembled. Assuming three solid layers in the structure, the three transfer matrices should be combined in series as follows:

$$\begin{pmatrix} p_1 \\ v_1 \end{pmatrix} = \mathbf{T}_1\mathbf{T}_2\mathbf{T}_3 \begin{pmatrix} p_4 \\ v_4 \end{pmatrix} = \mathbf{T}_G \begin{pmatrix} p_4 \\ v_4 \end{pmatrix} \tag{2.76}$$

Since the STL of wave excitation is defined as a logarithm ratio of the sound energy transmitted through the structures versus the amount of sound energy on the incident side as presented in Eq. 2.67, the ratio of energy can also be calculated by the squared ratio of the acoustic pressure. Once Eq. 2.76 is solved, the acoustic transmission coefficient, $\tau = \left|\frac{p_4}{p_1}\right|^2$, can be obtained, STL for a plane wave is then derived:

$$STL(\omega, \theta, \varphi) = -10log_{10}\tau \tag{2.77}$$

A classical double-wall problem with the STL calculated by TMM is presented in Fig. 2.12:

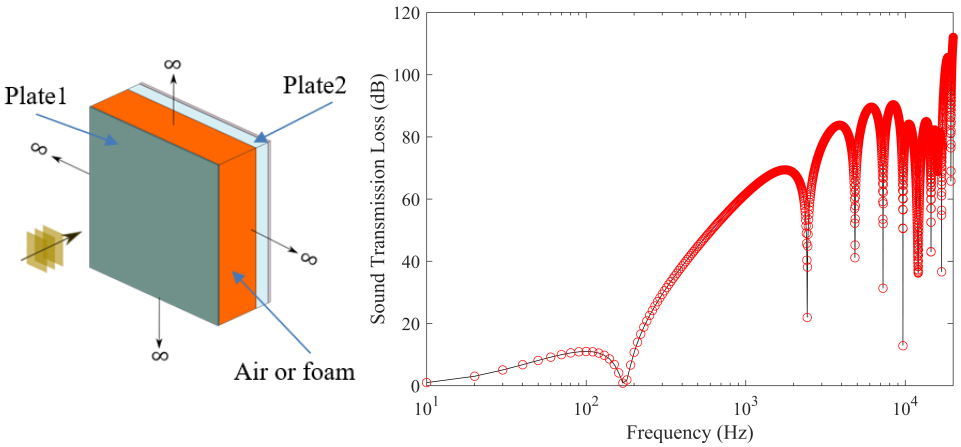

Fig. 2.12. Application of Analytical TMM. Left: A system of double aluminum walls with air foam in between. Right: STL of a 45^o impinging wave. – TMM results. ○ Analytical results.

However, due to the pre-assumption regarding the in-plane wavenumber components, the TMM fails to fully capture the physics of sound propagation in periodic structures when the in-plane dimensions of the UCs are similar to or greater than the excitation wavelength. In fact, within a heterogeneous layer, a plane wave excitation can generate different waves due to the periodicity. These additional waves are known as Bloch modes and can propagate within the structure, significantly contributing to sound

propagation. In the following section, a generalized version of the TMM (GTMM) accounting for these modes and heterogeneous layers is discussed.

2.5.4 General Transfer Matrix Method

Analytical expressions for the TMs are only available for homogeneous media. The General TMM (GTMM), developed by Parrinello and Atalla [179–181] for computing the acoustic indicators of periodic structures, uses the same Bloch theorem as in the WFE scheme, the TM of a layer is obtained by manipulating the Dynamic Stiffness Matrix (DSM) of the UC representative of the periodic structure [131].

By exploiting the Bloch wave approach, the transfer matrix of a periodic planar layer is obtained first for cases of small UCs in Parrinello and Ghiringhelli [182] and afterwards for cases of large UCs in Parrinello et al. [179] by accounting for Bloch modes. A TMM for the sound transmission through infinite heterogeneous cylinders is presented in Parrinello et al. [180] and extended to account for size effects (baffled multilayered curved shells) in Parrinello et al. [181].

The method is named as general since different physics are allowed for within a layer and different materials with the same physics are allowed for at the interlayer boundaries. The main procedures conclude the derivation of acoustic excitation and impedances, determination of TM of each layer, the interface conditions, and then the assembling of global TM and the computation of acoustic indicators.

2.5.4.1 Acoustic Excitation and Impedances

The structure is excited by a plane wave traveling in the lower fluid and impinging its bottom surface with an incident angle, θ, concerning the z-axis and a heading angle, φ, for the x-axis. The incident pressure field can be expressed as

$$P_I = p_0 e^{i(\omega t - \kappa_x x - \kappa_y y - \kappa_z z)} \tag{2.78}$$

where p_0 is the wave amplitude and the wavenumber components are

$$\begin{cases} \kappa_x = \dfrac{\omega}{c_B} sin\theta cos\varphi \\ \kappa_y = \dfrac{\omega}{c_B} sin\theta sin\varphi \\ \kappa_z = \dfrac{\omega}{c_B} cos\theta \end{cases} \tag{2.79}$$

where c denotes the sound speed in the ambient media and the subscript B represents the bottom surface of the structures.

The blocked-wall pressure (i.e. the real excitation seen by the structure) is obtained by assuming a Neumann boundary at the blocked bottom surface, thus obtaining the total pressure field produced by the incident plane wave at the bottom surface:

$$p_b = 2p_0 e^{i(\omega t - \kappa_x x - \kappa_y y)} = p_b e^{i(\omega t - \kappa_x x - \kappa_y y)} \tag{2.80}$$

2.5.4.2 Transfer Matrix of Each Layer

In GTMM, the periodic UC of a layer is modeled using FE analysis and the related dynamic problem can be written the same as in Eq. 2.26 and partitioned in the same way as presented in Fig. 2.5. The Bloch theorem is also applied to the generalized displacement vector equation. 2.27.

Provided the assumption of real wavenumbers, the forces arising from neighboring UCs vanish from the dynamic problem [182], and the Equation of Motion becomes:

$$\mathbf{\Lambda_L D}\left(\omega\right)\mathbf{\Lambda_R q} = \mathbf{D'}\left(\omega,\kappa_x,\kappa_y\right)\mathbf{q'} = \mathbf{\Lambda}_L(\mathbf{f}+\mathbf{e}) = \mathbf{e'} \tag{2.81}$$

To evaluate the TM of the heterogeneous layer, the problem must be partitioned in terms of the top (T), bottom (B), and internal (I) sets along the thickness direction:

$$\begin{bmatrix}\mathbf{D'}_{BB} & \mathbf{D'}_{BI} & \mathbf{D'}_{BT}\\ \mathbf{D'}_{IB} & \mathbf{D'}_{II} & \mathbf{D'}_{IT}\\ \mathbf{D'}_{TB} & \mathbf{D'}_{TI} & \mathbf{D'}_{TT}\end{bmatrix}\begin{bmatrix}\mathbf{q'}_B\\ \mathbf{q'}_I\\ \mathbf{q'}_T\end{bmatrix} = \begin{bmatrix}\mathbf{e'}_B\\ \mathbf{0}\\ \mathbf{e'}_T\end{bmatrix} \tag{2.82}$$

Since no internal forces are applied, the same condensation skill in Eq. 2.30 can be applied, the set of internal DOFs, $\mathbf{q'_I}$, is condensed and the problem becomes:

$$\begin{bmatrix}\mathbf{D'}_{BB}-\mathbf{D'}_{BI}\mathbf{D'}_{II}^{-1}\mathbf{D'}_{IB} & \mathbf{D'}_{BT}-\mathbf{D'}_{BI}\mathbf{D'}_{II}^{-1}\mathbf{D'}_{IT}\\ \mathbf{D'}_{TB}-\mathbf{D'}_{TI}\mathbf{D'}_{II}^{-1}\mathbf{D'}_{IB} & \mathbf{D'}_{TT}-\mathbf{D'}_{TI}\mathbf{D'}_{II}^{-1}\mathbf{D'}_{IT}\end{bmatrix}\begin{bmatrix}\mathbf{q'}_B\\ \mathbf{q'}_T\end{bmatrix} = \mathbf{C'}\begin{bmatrix}\mathbf{q'}_B\\ \mathbf{q'}_T\end{bmatrix} = \begin{bmatrix}\mathbf{e'}_B\\ \mathbf{e'}_T\end{bmatrix} \tag{2.83}$$

Homogeneous layers can be modeled using UCs with no internal nodes, thus avoiding the above-mentioned factorization and the related cost. Such a possibility ensures to the proposed procedure a computational efficiency akin to analytical formulations.

To build the corresponding TM model, we first define the matrices:

$$\begin{aligned}\mathbf{L}_B &= \mathbf{I}_m \otimes exp\left(i\kappa_x\mathbf{x}_B + i\kappa_y\mathbf{y}_B\right)\\ \mathbf{L}_T &= \mathbf{I}_m \otimes exp\left(i\kappa_x\mathbf{x}_T + i\kappa_y\mathbf{y}_T\right)\end{aligned} \tag{2.84}$$

where $\mathbf{x}|\mathbf{y}_{B|T}$ are row vectors collecting nodal coordinates, m is the number of DOFs for each node (1 for fluid layer [183]) and $\otimes$ denotes the Kronecker product, I_m is the identity matrix of size m. Thus, a through-thickness 1D dynamic problem can be derived:

$$\begin{bmatrix}\mathbf{L}_B\mathbf{C'}_{BB}\mathbf{L}_B^H & \mathbf{L}_B\mathbf{C'}_{BT}\mathbf{L}_T^H\\ \mathbf{L}_T\mathbf{C'}_{TB}\mathbf{L}_B^H & \mathbf{L}_T\mathbf{C'}_{TT}\mathbf{L}_T^H\end{bmatrix}\begin{bmatrix}\hat{\mathbf{q}}_B\\ \hat{\mathbf{q}}_T\end{bmatrix} = \mathbf{C}\begin{bmatrix}\hat{\mathbf{q}}_B\\ \hat{\mathbf{q}}_T\end{bmatrix} = \begin{bmatrix}\hat{\mathbf{e}}_B\\ \hat{\mathbf{e}}_T\end{bmatrix} \tag{2.85}$$

Finally, a TM can be rearranged from the problem:

$$\begin{bmatrix}-\mathbf{C}_{TB}^{-1}\mathbf{C}_{TT} & \mathbf{C}_{TB}^{-1}\\ \mathbf{C}_{BT}-\mathbf{C}_{BB}\mathbf{C}_{TB}^{-1}\mathbf{C}_{TT} & \mathbf{C}_{BB}\mathbf{C}_{TB}^{-1}\end{bmatrix}\begin{bmatrix}\hat{\mathbf{q}}_T\\ \hat{\mathbf{e}}_T\end{bmatrix} = \mathbf{T'}\left(\omega,\kappa_x,\kappa_y\right)\begin{bmatrix}\hat{\mathbf{q}}_T\\ \hat{\mathbf{e}}_T\end{bmatrix} = \begin{bmatrix}\hat{\mathbf{q}}_B\\ \hat{\mathbf{e}}_B\end{bmatrix} \tag{2.86}$$

where $\mathbf{T'}\left(\omega,k_x,k_y\right)$ is the TM of the layer related to the original variables for an incident plane wave with wavenumber components (κ_x,κ_y). The TM $\mathbf{T'}$ is now modified to simplify the interface boundary conditions.

2.5.4.3 Interface Condition

The next step for the procedure which leads to the final TM, $\mathbf{T}$, of a periodic medium is to choose the variables at its interfaces.

The GTMM uses the transformation matrices $\mathbf{\Lambda}_T$ and $\mathbf{\Lambda}_B$ (defined below), new state vectors, $\mathbf{V}_T$ and $\mathbf{V}_B$, are related to the original state vectors, $\mathbf{V'}_T = \begin{bmatrix}\hat{\mathbf{q}}_T & \hat{\mathbf{e}}_T\end{bmatrix}^T$ and $\mathbf{V'}_B = \begin{bmatrix}\hat{\mathbf{q}}_B & \hat{\mathbf{e}}_B\end{bmatrix}^T$ as

$$\mathbf{V'}_T = \mathbf{\Lambda}_T\mathbf{V}_T \quad \mathbf{V}_B = \mathbf{\Lambda}_T\mathbf{V'}_B \tag{2.87}$$

thus obtaining the final TM via $\mathbf{T} = \mathbf{\Lambda}_B\mathbf{T'}\mathbf{\Lambda}_T$.

Three kinds of interfaces are allowed by the GTMM: fluid, solid, and porous. For the original TM of a layer with both fluid interfaces, the original and the chosen state vectors to describe the acoustic field in these interfaces are:

$$\mathbf{V}'_{fluid} = \begin{bmatrix} p & -i\omega A v_n^f \end{bmatrix}^T \quad \mathbf{V}_{fluid} = \begin{bmatrix} p & v_z^f \end{bmatrix}^T \tag{2.88}$$

where v_n^f is the (outward-pointing) normal velocity and $A = L_x L_y$ is the area of the UC, $v_z^f = \pm\frac{e_f}{i\omega\rho_f A}$ is the fluid velocity at the boundaries, the term is positive for the left surface and negative at the right surface, since positive displacement at the left boundary increases pressure and consequently fluid energy.

The quantities represented in the vector $\mathbf{V}_{\text{fluid}}$ can be expressed in terms of generalized variables for both the left and right surfaces as follows:

$$\begin{bmatrix} \hat{p}_L \\ v_z^f \end{bmatrix} = \begin{bmatrix} 1 & 0 \\ 0 & 1/(i\omega\rho_f A) \end{bmatrix} \begin{bmatrix} \hat{p}_L \\ \hat{e}_{Lf} \end{bmatrix}, \qquad \begin{bmatrix} \hat{p}_R \\ \hat{e}_{Rf} \end{bmatrix} = \begin{bmatrix} 1 & 0 \\ 0 & -i\omega\rho_f A \end{bmatrix} \begin{bmatrix} \hat{p}_L \\ v_z^f \end{bmatrix} \tag{2.89}$$

Consequently, the respective transformation matrices are:

$$\begin{aligned} \mathbf{\Lambda}_B &= diag\begin{bmatrix} 1 & 1/(i\omega A) \end{bmatrix} \\ \mathbf{\Lambda}_T &= diag\begin{bmatrix} 1 & -i\omega A \end{bmatrix} \end{aligned} \tag{2.90}$$

The final TM therefore becomes:

$$\mathbf{T} = \mathbf{\Lambda}_B \mathbf{T}' \mathbf{\Lambda}_T = \begin{bmatrix} 1 & 0 \\ 0 & 1/(i\omega A) \end{bmatrix} \mathbf{T}' \begin{bmatrix} 1 & 0 \\ 0 & -i\omega A \end{bmatrix} \tag{2.91}$$

Eq. 2.91 relates the acoustic field vectors at the right-hand-side boundaries of adjacent layers in the stratified medium. For the fluid interfaces, the product of transfer and interface matrices is used to calculate the global TM of a periodic medium.

The state vectors for a solid layer are [179, 180]:

$$\begin{aligned} \mathbf{V}'_{solid} &= \begin{bmatrix} u_x & u_y & u_z & F_x & F_y & F_z \end{bmatrix}^T \\ \mathbf{V}_{solid} &= \begin{bmatrix} v_x^s & v_y^s & v_z^s & \sigma_x z & \sigma_x y & \sigma_z z \end{bmatrix}^T \end{aligned} \tag{2.92}$$

where superscript s represents the solid media and the related transformation matrices are

$$\begin{aligned} \mathbf{\Lambda}_B &= diag\begin{bmatrix} i\omega & i\omega & i\omega & -1/A & -1/A & -1/A \end{bmatrix} \\ \mathbf{\Lambda}_T &= diag\begin{bmatrix} 1/i\omega & 1/i\omega & 1/i\omega & A & A & A \end{bmatrix} \end{aligned} \tag{2.93}$$

The state vectors for a poroelastic layer are

$$\mathbf{V}'_{porous} = \begin{bmatrix} u_x^s & u_y^s & u_z^s & p & F_x^s & F_y^s & F_z^s & -i\omega A(v_n^f + v_n^s\tilde{\gamma}/\Phi^2) \end{bmatrix}^T \tag{2.94}$$

where Φ is the layer porosity and $\tilde{\gamma}$ is the coupling coefficient between the solid and fluid phase of the porous media. Thus, the related transformation matrices are [183]

$$\mathbf{V}_{porous} = \begin{bmatrix} v_x^s & v_y^s & v_z^s & p & \sigma_{xz}^s & \sigma_{xy}^s & \sigma_{zz}^t & w \end{bmatrix}^T \tag{2.95}$$

where $w = \Phi(v_z^f - v_z^s)$ is the flux per unit area at the interface, $\overset{z}{_{tt}} = \sigma_{zz}^s + \sigma_{zz}^f$ is the total normal stress and $\sigma_{zz}^f = -p\Phi$ is the equivalent normal stress due to the fluid. The related transformation matrices are

$$\mathbf{\Lambda}_B = \left[\begin{array}{cccc|cccc} i\omega & 0 & 0 & 0 & 0 & 0 & 0 & 0 \\ 0 & i\omega & 0 & 0 & 0 & 0 & 0 & 0 \\ 0 & 0 & i\omega & 0 & 0 & 0 & 0 & 0 \\ 0 & 0 & 0 & 1 & 0 & 0 & 0 & 0 \\ 0 & 0 & 0 & 0 & -1/A & 0 & 0 & 0 \\ 0 & 0 & 0 & 0 & 0 & -1/A & 0 & 0 \\ 0 & 0 & 0 & -\Phi & 0 & 0 & -1/A & 0 \\ 0 & 0 & -g\Phi & 0 & 0 & 0 & 0 & \Phi/i\omega A \end{array}\right] \tag{2.96}$$

and

$$\mathbf{\Lambda}_T = \left[\begin{array}{cccc|cccc} 1/i\omega & 0 & 0 & 0 & 0 & 0 & 0 & 0 \\ 0 & 1/i\omega & 0 & 0 & 0 & 0 & 0 & 0 \\ 0 & 0 & 1/i\omega & 0 & 0 & 0 & 0 & 0 \\ 0 & 0 & 0 & 1 & 0 & 0 & 0 & 0 \\ 0 & 0 & 0 & 0 & A & 0 & 0 & 0 \\ 0 & 0 & 0 & 0 & 0 & A & 0 & 0 \\ 0 & 0 & 0 & \Phi A & 0 & 0 & A & 0 \\ 0 & 0 & -gA & 0 & 0 & 0 & 0 & -i\omega A/\Phi \end{array}\right] \tag{2.97}$$

where $g = i\omega(1 + \tilde{\gamma}/\Phi^2)$.

2.5.4.4 Assembling and Solution

The continuity conditions between adjacent layers must be added to simulate the wave transmission through a multi-layer structure as depicted in Fig. 2.13.

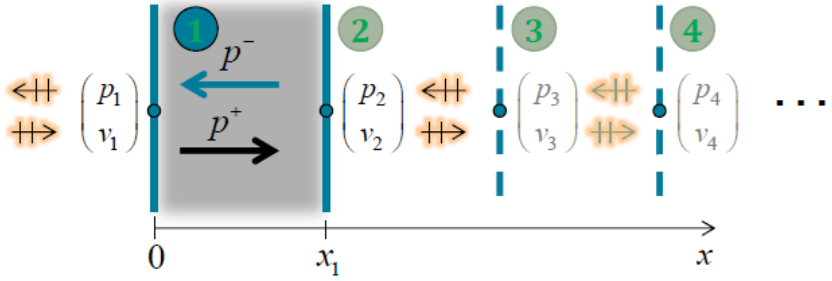

Fig. 2.13. Schematic of wave transmission in multi-layer structures.

In the case of a solid-fluid interface for instance, the following conditions must be imposed

$$\mathbf{I}_{sf}\mathbf{V}_s + \mathbf{J}_{sf}\mathbf{V}_f = \left[\begin{array}{cc|cccc} 0 & 0 & 1 & 0 & 0 & 0 \\ 0 & 0 & 0 & 1 & 0 & 0 \\ 0 & 0 & 0 & 0 & 1 & 0 \\ 0 & 0 & 0 & 0 & 1 & 0 \end{array}\right]\mathbf{V}_s + \begin{bmatrix} 0 & -1 \\ 0 & 0 \\ 0 & 0 \\ 1 & 0 \end{bmatrix}\mathbf{V}_f = \mathbf{0} \tag{2.98}$$

where $\mathbf{I}_{sf}$ and $\mathbf{J}_{sf}$ must be interchanged for a fluid-solid interface.

The state vector $\mathbf{V}_p$ defined by Eq. 2.95 considerably simplify the porous-porous and the porous-fluid interfaces, making interface conditions independent from the porosity, Φ. In fact, all the components of $\mathbf{V}_p$ are equal at each side of the boundary between two porous layers with frames bonded together. On the other hand, the following boundary conditions must be set for a porous-fluid interface

$$\mathbf{I}_{pf}\mathbf{V}_p + \mathbf{J}_{pf}\mathbf{V}_f = \left[\begin{array}{cc|ccccc|c} 0 & 0 & 1 & 0 & 0 & 0 & 0 & 1 \\ 0 & 0 & 0 & 1 & 0 & 0 & 0 & 0 \\ 0 & 0 & 0 & 0 & 1 & 0 & 0 & 0 \\ 0 & 0 & 0 & 0 & 0 & 1 & 0 & 0 \\ 0 & 0 & 0 & 0 & 0 & 0 & 1 & 0 \end{array}\right] \mathbf{V}_p + \begin{bmatrix} 0 & -1 \\ -1 & 0 \\ 0 & 0 \\ 1 & 0 \\ 1 & 0 \end{bmatrix} \mathbf{V}_f = \mathbf{0} \tag{2.99}$$

where matrices $\mathbf{I}_{pf}$ and $\mathbf{J}_{pf}$ must be interchanged for a fluid-porous interface.

In the case of a porous-solid interface the following boundary conditions must be set

$$\mathbf{I}_{ps}\mathbf{V}_p + \mathbf{J}_{ps}\mathbf{V}_s = \begin{bmatrix} [\mathbf{I}_3 & \mathbf{0}] \\ [\mathbf{0} & \mathbf{I}_4] \end{bmatrix} \mathbf{V}_p + \begin{bmatrix} -\mathbf{I}_6 \\ \mathbf{0} \end{bmatrix} \mathbf{V}_s = \mathbf{0} \tag{2.100}$$

where $\mathbf{I}_n$ is the identity matrix of size n. Matrices $\mathbf{I}_{ps}$ and $\mathbf{J}_{ps}$ must be interchanged for a solid-porous interface.

If two or more adjacent layers have the same nature (including porous layers) the global TM is simply equal to the product of the transfer matrices of the layers. Alternatively, if two adjacent layers, i and j, are defined by the same state vector $\mathbf{V}_{i|j}$ of size n, the interface matrices $\mathbf{I}_{ij} = \mathbf{I}_n$ and $\mathbf{J}_{ij} = -\mathbf{I}_n$ can be used to fulfill continuity conditions, thus retaining the state variables at the $i - j$ interface.

Stacking all the continuity conditions we obtain

$$\mathbf{BV} = \begin{bmatrix} \mathbf{I}_{f1} & \mathbf{J}_{f1}\mathbf{T}_1 & \mathbf{0} & \cdots & \mathbf{0} & \mathbf{0} \\ \mathbf{0} & \mathbf{I}_{12} & \mathbf{J}_{12}\mathbf{T}_2 & \cdots & \mathbf{0} & \mathbf{0} \\ \vdots & \vdots & \vdots & \ddots & \vdots & \vdots \\ \mathbf{0} & \mathbf{0} & \mathbf{0} & \cdots & \mathbf{I}_{lf} & \mathbf{J}_{lf} \\ \mathbf{0} & \mathbf{0} & \mathbf{0} & \cdots & \mathbf{0} & -1/Z_i \end{bmatrix} \left\{ \begin{array}{c} p_0 \\ v_0 \\ \vdots \\ p_i \\ p_i^f \end{array} \right\} = \mathbf{0} \tag{2.101}$$

where matrix $\mathbf{B}$ has dimensions $N \times (N+1)$, matrices $\mathbf{I}_{ij}$ and $\mathbf{J}_{ij}$ depend on the nature of the i-th and j-th layers, l is the number of layers, the suffix f denotes the fluid at the excitation and termination side and impedance condition is imposed at the termination side through the inner impedance, Z_i. The global state vector, $\mathbf{V}$, collects the variables at all interfaces only if interface matrices are employed even for adjacent layers of the same nature. Impedance condition and spectral blocked pressure must also be applied at the excitation (outer) side

$$\mathbf{B}_{2:N+1}\mathbf{V}_{2:N+1} = -\mathbf{B}_1 p_0 = -\mathbf{B}_1 (p_B - Z_0 v_0^f) \tag{2.102}$$

where $\mathbf{B}_i$ is the i-th column of matrix $\mathbf{B}$ and $\mathbf{B}_{i:j}$ is the matrix ranging from the i-th to the j-th column of $\mathbf{B}$. The problem can be rearranged by obtaining a square linear system with N unknowns:

$$\begin{bmatrix} \mathbf{B}_2 - Z_0\mathbf{B}_1 & \mathbf{B}_{3:N+1} \end{bmatrix} \mathbf{V}_{2:N+1} = -\mathbf{B}_1 p_B \tag{2.103}$$

where v_0^f and v_i^f are the first and the last element of vector $\mathbf{V}_{2:N+1}$ respectively.

All the acoustic indicators can be evaluated once the fluid velocities at the boundaries are determined. The blocked pressure can be evaluated by accounting for the M-th impedance condition as

$$p_b = 1 + Z_{B,M} v_{B,M}^f \tag{2.104}$$

where the amplitude of the incident plane wave is $p_0 = p_b/2$, the impedance $Z_{B,M} = \rho_B c_B cos\theta$ links the spectral pressure acting on the surface and the normal spectral velocity $v_{B,M}^f$. Consequently, the incident acoustic power per unit area on the bottom surface of the structure writes:

$$W_I(\theta) = \frac{p_0^2 cos\theta}{2\rho_B c_B} \tag{2.105}$$

The sound power per unit area exchanged between the structure and the semi-infinite fluid of the source domain becomes:

$$W_B(\omega, \theta, \varphi) = \frac{1}{2} Re(p_b v_{B,M}^f) - \frac{1}{2} \sum_{i=1}^{N} Re(Z_{B,i}) \left| v_{B,i}^f \right|^2 \tag{2.106}$$

When dealing with a semi-infinite fluid termination, the sound power per unit area radiated by the top surface into the receiving fluid can be expressed as follows:

$$W_T(\omega, \theta, \varphi) = \frac{1}{2} \sum_{i=1}^{N} Re(Z_{T,i}) \left| v_{T,i}^f \right|^2 \tag{2.107}$$

Thus, we obtain the power transmission coefficient $\tau = \frac{W_T}{W_I}$, the transmission loss STL = $10log_{10}(\tau)$, the power absorption coefficient $\alpha = \frac{W_B}{W_I}$, the power reflection coefficient $R = 1 - \alpha$ and the dissipation coefficient $C_{diss} = 1 - R - \tau$. The results of GTMM will be applied to validate the STL of the WFE scheme.

2.5.5 Wave-based Finite Element Method

For STL, we are concerned with an oblique incident plane wave impinging the plate on the incident side, with a known amplitude p_{inc}, as in Fig. 2.10. The interaction between this incident wave and the structure creates a reflected wave on the same side, and a transmitted wave on the other side, namely the transmitted side, whose respective amplitudes p_{ref} and p_{tra} are derived in this part. The STL in the DAF is then the integration of the structure-borne sound waves in the DAF.

As represented in Fig. 2.10, the acoustic pressure filed on the incident side is the superposition of the incident and reflected waves:

$$P_{inc} = p\ (x, y, z)|_{z>0} = p_{inc} exp\left(-ik_{z,inc} z\right) + p_{ref} exp\left(+ik_{z,inc} z\right) \tag{2.108}$$

The wavenumber components satisfy the relationship $\kappa_x^2 + \kappa_y^2 + \left(\kappa_{z,inc}\right)^2 = \kappa^2 = \left(\frac{\omega}{c_{inc}}\right)^2$ and c_{inc} is the speed of sound of the incident media. In the same way, the acoustic pressure filed on the transmitted side contains only the transmitted wave propagating in the same direction as the incident wave

$$P_{tra} = p\ (x, y, z)|_{z<0} = p_{tra} exp\left(-ik_{z,tra} z\right) \tag{2.109}$$

with the relationship $\kappa_x^2 + \kappa_y^2 + \left(\kappa_{z,tra}\right)^2 = \left(\frac{\omega}{c_{tra}}\right)^2$, where c_{tra} is the speed of sound of the transmitted media. Potential phase differences between the pressure fields are accounted for through the fact that the amplitudes p_{ref} and p_{tra} may be complex. The wavenumbers κ_x and κ_y are conserved across the plate, so only the κ_z component may vary with the nature of the fluid. We will consider in the following that the fluid is the same on both sides, thus $\rho_{inc} = \rho_{tra} = \rho_0$ and $c_{inc} = c_{tra} = c$.

In this case, the incidence angle θ is the angle between the wave vector and the normal of the plate, while the azimuthal angle φ gives its orientation in the plane. We therefore have $\kappa_x = \kappa sin\theta cos\varphi$, $\kappa_y = \kappa sin\theta sin\varphi$ and $\kappa_z = \kappa cos\theta$. The two transformation matrices in Equations 3.16 and 3.17 can then be assembled with κ_x and κ_y to diminish the dimensionality of the DOFs space.

The load imposed on the planar structure can be written from these two pressure fields lumped on the nodes of the FE model. Assuming that the pressure force is exerted along the normal to the structure, the

force with Z-direction component of the wavevector κ_z of forces imposed on hypernode **I** will be those relative to the DOFs in Z-direction on the incident side, $e_{I,inc}$, and on the transmitted side $e_{I,tra}$, for an elastic material, these quantities are scalar. Let $\mathbf{q}_{I,O}$ and $\mathbf{e}_{I,O}$ denote the displacement and force vectors on all other DOFs in the hypernode **I** and emerged into the $\mathbf{e}_O$. The force exerted on the hypernode **I** can be further partitioned in the following way:

$$\mathbf{e}_1 = \begin{bmatrix} e_{inc} \\ \mathbf{e}_O \\ e_{tra} \end{bmatrix} = \begin{bmatrix} S\left(p_{inc} + p_{ref}\right) \\ \mathbf{0} \\ S p_{tra} \end{bmatrix} \tag{2.110}$$

where S is the free surface of the UC, which is identical on both sides. All other vectors and matrices can be written following the same decomposition, allowing to rewrite the Dynamic Stiffness Matrix in Eq. 2.26 as follows:

$$\mathbf{D}_1\mathbf{q}_1 = \begin{bmatrix} d_{inc,inc} & \mathbf{D}_{inc,O} & d_{inc,tra} \\ \mathbf{D}_{O,inc} & \mathbf{D}_{O,O} & \mathbf{D}_{O,tra} \\ d_{tra,inc} & \mathbf{D}_{tra,O} & d_{tra,tra} \end{bmatrix} \begin{bmatrix} q_{inc} \\ \mathbf{q}_O \\ q_{tra} \end{bmatrix} = \begin{bmatrix} S\left(p_{inc} + p_{ref}\right) \\ \mathbf{0} \\ S p_{tra} \end{bmatrix} \tag{2.111}$$

The second line of Eq. 2.111 allows to condense Eq. 2.111 into

$$\begin{bmatrix} \widetilde{d}_{inc,inc} & \widetilde{d}_{inc,tra} \\ \widetilde{d}_{tra,inc} & \widetilde{d}_{tra,tra} \end{bmatrix} \begin{bmatrix} q_{inc} \\ q_{tra} \end{bmatrix} = \begin{bmatrix} S\left(p_{inc} + p_{ref}\right) \\ S p_{tra} \end{bmatrix} \tag{2.112}$$

with

$$\begin{aligned} \widetilde{d}_{inc,inc} &= d_{inc,inc} - \mathbf{D}_{inc,O}\mathbf{D}_{O,O}^{-1}\mathbf{D}_{O,inc} \\ \widetilde{d}_{inc,tra} &= d_{inc,tra} - \mathbf{D}_{inc,O}\mathbf{D}_{O,O}^{-1}\mathbf{D}_{O,tra} \\ \widetilde{d}_{tra,inc} &= d_{tra,inc} - \mathbf{D}_{tra,O}\mathbf{D}_{O,O}^{-1}\mathbf{D}_{O,inc} \\ \widetilde{d}_{tra,tra} &= d_{tra,tra} - \mathbf{D}_{tra,O}\mathbf{D}_{O,O}^{-1}\mathbf{D}_{O,tra} \end{aligned} \tag{2.113}$$

The continuity of normal particle velocity at the interface of ambient media and the structure is characterized by Fluid-Structure Interaction (FSI). This writes for both sides:

$$\begin{aligned} \rho_0\omega^2 q_{inc} &= \frac{\partial P_{inc}}{\partial z} = -i\kappa_z\left(p_{inc} - p_{ref}\right) \\ \rho_0\omega^2 q_{tra} &= \frac{\partial P_{tra}}{\partial z} = -i\kappa_z p_{tra} \end{aligned} \tag{2.114}$$

Introducing the acoustic admittance $Y_0 = cos\left(\theta\right)/(i\omega\rho_0 c_0)$, we obtain

$$\begin{aligned} q_{inc} &= Y_0\left(p_{inc} - p_{ref}\right) \\ q_{tra} &= Y_0 p_{tra} \end{aligned} \tag{2.115}$$

Substitute Eq. 2.114 and 2.115 for q_{inc} and q_{tra} into Eq. 2.112 leading to two scalar equations linking the unknowns p_{ref} and p_{tra} with the incident pressure p_{inc}:

$$\begin{bmatrix} \widetilde{d}_{inc,inc} + \frac{S}{Y_0} & -\widetilde{d}_{inc,tra} \\ \widetilde{d}_{tra,inc} & -\widetilde{d}_{tra,tra} - \frac{S}{Y_0} \end{bmatrix} \begin{bmatrix} p_{ref} \\ p_{tra} \end{bmatrix} = p_{inc} \begin{bmatrix} \widetilde{d}_{inc,inc} - \frac{S}{Y_0} \\ \widetilde{d}_{tra,inc} \end{bmatrix} \tag{2.116}$$

The acoustic transparency is defined as:

$$\tau = \left|\frac{p_{tra}}{p_{inc}}\right|^2 \tag{2.117}$$

and the absorption coefficient $\alpha = 1 - \left|\frac{p_{ref}}{p_{inc}}\right|^2$ can thus be obtained by solving this equation. STL for a

plane wave can be derived by Eq. 2.77.

STL in DAF is obtained by integrating over all possible incidence angles $\theta \in [0, \pi/2[$ and azimuthal directions $\varphi \in [0, 2\pi]$. The acoustic transparency in DAF is then:

$$\tau_d(\omega) = \frac{\int_0^{2\pi} \int_0^{\theta_{max}} \tau(\omega, \theta, \varphi) \, sin\theta cos\theta d\theta d\varphi}{\int_0^{2\pi} \int_0^{\theta_{max}} sin\theta cos\theta d\theta d\varphi} \tag{2.118}$$

The STL in DAF is finally computed by applying the same logarithmic operation as in Eq. 2.77. The integration over azimuthal angle can be neglected for planar structures made of isotropic materials. It is recommended to avoid the grazing incidences $\theta = \pi/2$ as numerical issues arise for evaluating the integral when θ_{max} approach 90^o.

The computation of STL to an incident wave in the ambient media and under DAF excitation is the main funding of this part.

2.6 Conclusions

The main objective of this thesis work is to develop methods able to simulate the vibroacoustic indicators of heterogeneous metastructures with the characteristics of high contrast and high dissipation, in a fast and accurate manner, independently of the structural complexity and curvature.

The proposed methodologies to achieve the research objectives listed in Chapter 1.3 are:

- Establish a numerical wave-based approach based on the FE model of a representative UC of the periodic structures, correctly track the eigensolution computed from the EVP by an energetic continuity criterion.
- Compare the bending wavenumbers of HCS calculated by the developed WFE scheme with an analytical AHM, as well as a semi-analytical GLM, depicting the corresponding wave modeshape to verify the multi-scale dynamics of the HCS.
- Check the accuracy of the conventional approach for the damping evaluation. For HDS where DLF of the bending wave no longer represent the damping level of the global structure, decompose the point force in the wave domain by Bloch expansion, then compute the global/composite DLF by integrating all the forced response to the waves spanning the whole Brillouin zone. The results will be validated using a PIM based on the FEM results.
- The sound transmission coefficients calculated by applying the plane wave excitation to the periodic structures, such as the STL and the acoustic transparency, can be exploited to study the vibroacoustic indicators such as the STL and the wave coupling effect of heterogeneous metastructures.

Then, the final target of the thesis work is to apply the numerical wave-based methodologies to investigate periodic metastructures such as HCS and HDS. In this context, the targets are:

- Extend the WFE framework to study the limit behaviors of HCS and study the limit of AHM.
- Study the damping mechanism of HDS and develop a valid approach to accurately predict the global DLF.
- Investigate the effects of wave coupling in heterogeneous metastructures and the influence on the vibroacoustic indicators.

Chapter 3

On the Wave-based Approaches for Wavespace of Highly Contrasted Structures with Viscoelastic Damping

---

Abstract: The present study explores wave-based models for Highly Contrasted Structures (HCS) and Highly Dissipative Structures (HDS). The Asymptotic Homogenization Method (AHM), exploits the asymptotic Zig-Zag model and homogenization technique to compute the bending wavenumbers via a 6th-order equation. The General Laminate Model (GLM) employs Mindlin's displacement field to establish displacement-constraint relationships and resolves a quadratic Eigenvalue Problem (EVP) of the dispersion relation. The Wave Finite Element (WFE) scheme formulates the Nonlinear Eigenvalue Problem (NEP) for waves in varying directions and tracks complex wavenumbers using Weighted Wave Assurance Criteria (WWAC). Two approaches are introduced to estimate the Damping Loss Factor (DLF) of HDS, with the average DLF calculated by the modal density at various angles where non-homogeneity is present. Evaluation of robustness and accuracy is made by comparing the wavenumbers and DLF obtained from AHM and GLM with WFE. WFE is finally extended to a sandwich plate with a non-homogeneous core, Power Input Method (PIM) with Finite Element Method (FEM) data is employed to assess the average DLF, demonstrating an enhanced DLF compared to layered configurations with the same material portion, indicating increased energy dissipation due to the bending-shear coupling effects. Note that the content of this chapter has been accepted for publication in the Chinese Journal of Aeronautics [184].

Contents

3.1 Introduction

The primary objectives are to assess AHM and GLM for the complex wavenumbers governing the multi-scale dynamics in HCS and to derive the DLF of HDS. In WFE, the NEP of waves propagating in omni-direction is solved by the Contour Integral (CI) method, and the wave solutions are tracked by the energetic continuity in the frequency domain. The robustness and accuracy of AHM and GLM are evaluated with two metrics, wavenumber and DLF, the wavemodes from WFE are plotted to affirm the two limit dynamics of HCS.

The chapter is structured as follows: Section 3.3 presents a novel methodology of the WFE scheme to compute the wavenumbers in all directions, the wave track technique is founded by Weighted Wave Assurance Criteria (WWAC). In Section 3.4, various examples are presented to study the multi-scale dynamics of HCS, the validity domain of AHM is assessed by a sandwich structure with a very thick, highly damped core. In Section 3.5, the application of multi-scale dynamics to HCS with non-homogeneous cores is investigated by WFE since it lies beyond the research scope of GLM. The discussion regarding the results is devoted in Section 3.6.

3.2 Asymptotic Homogenization Method

3.2.1 Basic Assumptions

AHM is recalled through the application of an asymptotic framework tailored to the formulation of plate theories, facilitating the reduction of the explicit 3D description of the layers and their interface conditions to an equivalent 2D plate model [32, 185]. The imposition of perfect contact conditions among different layers, the assumption of incompressibility of each layer, and adherence to the geometric condition of small thickness against the plate lengths.

To accurately describe the multi-scale dynamics inherent in HCS, AHM employs the Zig-Zag model as illustrated in Fig. 2.3:

Due to the potential deformation of the core, an additional kinematic descriptor defining its sliding, $\delta(x, y)$, is induced from the Zig-Zag model and the shape function is defined as $\phi_\delta(z)$, as outlined in A.

Beside the in-plane displacement $U(x, y)$, the in-plane kinematic in Fig. 2.3 is split into two terms to constitute the basis of the Zig-Zag model:

- The term $-\phi_w(z)\nabla w(x, y)$ encapsulates the Kirchhoff plate kinematics for the two skins exhibiting identical deflections [13].

- The term $\phi_\delta(z)\delta(x, y)$ introduces a shear motion of the soft core, leading to opposite tangential stresses applied on the interfaces with the skins.

AHM also employs the conventional homogenization approach [71, 72] to re-scale the out-of-plane variable and conduct the asymptotic expansions of any physical quantity, dimensional analysis is applied

to scale the stiffness to address the contrast of material deformability [12]. AHM retains accurate solutions for HCS and overcomes the ambiguity that previous homogenization methods encountered in identifying the different dynamics involved in each layer. The application of the complex shear moduli comprising both elastic and loss counterparts facilitates the computation of DLF for HDS.

3.2.2 Governing Equations for Wavenumbers

The governing equations are concisely outlined here. The details of asymptotic derivation and force/momentum balances in HCS can be referred to in Sec. 2.3.2.

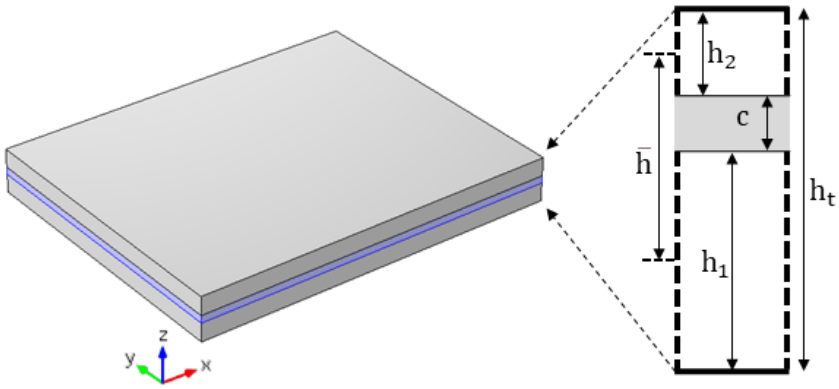

Fig. 3.1. Notations for HCS plate along thickness axis.

In AHM, the dispersion relation of HCS depicted in Fig. A.1 can be derived from Eq. 2.17, a 6th-order equation as a cubic equation in terms of the unknown k^2 reads:

$$\left(k^2\right)^3 - aA\left(k^2\right)^2 - A\Omega k^2 + (a-1)\,A^2\Omega = 0 \tag{3.1}$$

where $a = \frac{I}{I-I}$, $A = \frac{K}{E_0 I}$ and $\Omega = \frac{\rho_t h_t \omega^2}{K}$.

Eliminate the square term in the cubic equation by using Cardan's method with the substitution $k^2 = \frac{(1+X)aA}{3}$ [186]:

$$X^3 - 3PX - 2Q = 0;\ P = 1 + \frac{3\Omega}{a^2 A}, Q = 1 + 3\frac{3-2a}{2a}\frac{3\Omega}{a^2 A} \tag{3.2}$$

The discriminant of the equation, $\Delta = -\left(P^3 - Q^2\right)$, is real negative, leading to three distinct roots that are identified as follows:

$$\begin{gathered} k_{1,2}^2 = \frac{aA}{3}\left(1 + X_{1,2}\right) = \frac{aA}{3}\left(1 - \frac{1}{2}\left(s_1 + s_2\right) \pm \frac{i\sqrt{3}}{2}\left(s_1 - s_2\right)\right) \\ k_3^2 = \frac{aA}{3}\left(1 + X_3\right) = \frac{aA}{3}\left(1 + s_1 + s_2\right) \end{gathered} \tag{3.3}$$

where

$$\begin{aligned} s_1 &= \left[Q + \left(-P^3 + Q^2\right)^{\frac{1}{2}}\right]^{\frac{1}{3}} \\ s_2 &= \left[Q - \left(-P^3 + Q^2\right)^{\frac{1}{2}}\right]^{\frac{1}{3}} \end{aligned} \tag{3.4}$$

Consistently with the existence of three kinematic motions in HCS plates, there are three types of bending waves. As deduced in [13], one of the three waves is progressive of real wavenumber and takes the form of $exp(\pm ik_1 x)$, and the rest two waves are evanescent and take the form of $exp(\pm k_2 x)$ and $exp(\pm k_3 x)$. In AHM [13], wave k_1 is recognized as a progressive bending wave and is close to the

evanescent wave of the monolithic limit, k_2, at low-frequency range, k_1 approaches the evanescent wave of the bi-layer limit, k_3, at high frequencies.

In AHM, the wave propagation in the HCS, a non-symmetric plate made of two stiff skins (of thickness h_1 and h_2, identical material properties) and a soft core, depicted in Fig. A.1, is governed by the 6-order equation as a cubic equation in terms of the unknown k^2:

$$\left(k^2\right)^3 - aA\left(k^2\right)^2 - A\Omega k^2 + (a-1)\,A^2\Omega = 0 \tag{3.5}$$

Eliminate the square term in the cubic equation using Cardan's method with the substitution $k^2 = \frac{(1+X)aA}{3}$ [186]:

$$X^3 - 3PX - 2Q = 0;\ P = 1 + \frac{3\Omega}{a^2A}, Q = 1 + 3\frac{3-2a}{2a}\frac{3\Omega}{a^2A} \tag{3.6}$$

The discriminant of the cubic equation is expressed as outlined in Ref. [186]:

$$\Delta = -\left(P^3 - Q^2\right) \tag{3.7}$$

The discriminant is a real negative number since both P and Q are real and positive, three distinct roots are identified as follows:

$$\begin{gathered} k_{1,2}^2 = \frac{aA}{3}\left(1 + X_{1,2}\right) = \frac{aA}{3}\left(1 - \frac{1}{2}\left(s_1 + s_2\right) \pm \frac{i\sqrt{3}}{2}\left(s_1 - s_2\right)\right) \\ k_3^2 = \frac{aA}{3}\left(1 + X_3\right) = \frac{aA}{3}\left(1 + s_1 + s_2\right) \end{gathered} \tag{3.8}$$

where

$$\begin{aligned} s_1 &= \left[Q + \left(-P^3 + Q^2\right)^{\frac{1}{2}}\right]^{\frac{1}{3}} \\ s_2 &= \left[Q - \left(-P^3 + Q^2\right)^{\frac{1}{2}}\right]^{\frac{1}{3}} \end{aligned} \tag{3.9}$$

Consistently with the existence of three kinematic motions in HCS plates, there are three types of bending waves. As deduced in [13], one of the three waves is progressive of real wavenumber and takes the form of $exp(\pm ik_1x)$, and the rest two waves are evanescent and take the form of $exp(\pm k_2x)$ and $exp(\pm k_3x)$. In AHM [13], wave k_1 is recognized as a progressive bending wave and is close to the evanescent wave of the monolithic limit, k_2, at low-frequency range, k_1 approaches the evanescent wave of the bi-layer limit, k_3, at high frequencies.

3.3 Synthesis of Wave-based Finite Element Scheme

3.3.1 Nonlinear Eigenvalue Problem

The dynamic equilibrium of the UC in harmonic motion for a 2-dimensional periodic structure, as illustrated in Fig. 3.2, is defined as follows:

$$\left[\widetilde{\mathbf{K}} - \omega^2\widetilde{\mathbf{M}}\right]\mathbf{q} = \mathbf{f} + \mathbf{e} \tag{3.10}$$

where $\widetilde{\mathbf{K}}$ and $\widetilde{\mathbf{M}}$ represent the original stiffness and mass matrices, respectively, can be extracted from conventional FE packages or in-house FE framework. The generalized internal force due to the adjacent UCs is denoted by $\mathbf{f}$, $\mathbf{e}$ is the generalized external forces due to ambient media, both $\mathbf{f}$ and $\mathbf{e}$ are partitioned in the same way.

The nodal displacement $\mathbf{q}$ is partitioned according to Fig. 3.2, which is expressed as:

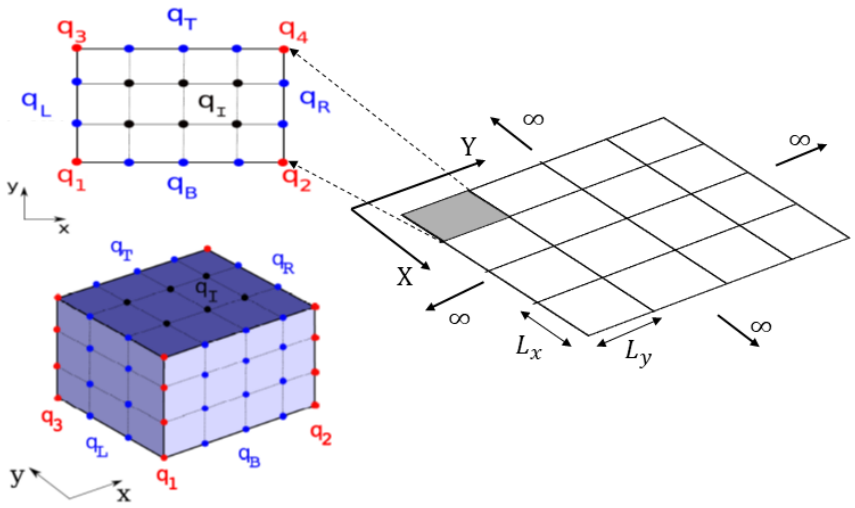

Fig. 3.2. Nodes definition of unit cell in two-dimensional periodic structure.

$$\mathbf{q} = \begin{bmatrix} \mathbf{q}_1 & \mathbf{q}_2 & \mathbf{q}_3 & \mathbf{q}_4 & \mathbf{q}_L & \mathbf{q}_B & \mathbf{q}_R & \mathbf{q}_T & \mathbf{q}_I \end{bmatrix}'. \tag{3.11}$$

where subvectors q_1, q_2, q_3 and q_4 represent the physical Degrees of Freedoms (DOFs) of the four corners of the UC, each has a size of s. Subvectors q_L and q_R denote the boundary DOFs at the left and right sides with sizes of ms, q_B and q_T correspond to the DOFs at the bottom and top sides with sizes of ns, while the internal DOFs q_I has the size of i.

When the UC incorporates materials that are dependent on temperature and frequency, the stiffness matrix tends to be complex and rheological.

$$\mathbf{K}(\omega, T) = \sum_{k=1}^{n} \left[\mathbf{K}_r^k(\omega, T) + i\mathbf{K}_i^k(\omega, T) \right] \tag{3.12}$$

where T represents the temperature, while $\mathbf{K}_r^k$ and $\mathbf{K}_i^k$ correspond to the real and imaginary parts, respectively, of the k^{th} element in the UC, which comprises n elements in total. It is essential in practice to assemble $\mathbf{K}(\omega, T)$ for each unique frequency and temperature under consideration.

The nodal displacements of a free wave propagating in a periodic structure are dictated by the principles of periodic boundary conditions, as outlined in [79]:

$$\begin{aligned} \mathbf{q}_T &= \lambda_y \mathbf{q}_B = e^{i\kappa_y L_y} \mathbf{I}_{ns} \mathbf{q}_B \\ \mathbf{q}_R &= \lambda_x \mathbf{q}_L = e^{i\kappa_x L_x} \mathbf{I}_{ns} \mathbf{q}_L \\ \mathbf{q}_2 &= \lambda_x \mathbf{q}_1 = e^{i\kappa_x L_x} \mathbf{I}_s \mathbf{q}_1 \\ \mathbf{q}_3 &= \lambda_y \mathbf{q}_1 = e^{i\kappa_y L_y} \mathbf{I}_s \mathbf{q}_1 \\ \mathbf{q}_4 &= \lambda_x \lambda_y \mathbf{q}_1 = e^{i(\kappa_x L_x + \kappa_y L_y)} \mathbf{I}_s \mathbf{q}_1 \end{aligned} \tag{3.13}$$

where the propagation constants corresponding to the in-plane directions X and Y are defined as:

$$\begin{aligned} \lambda_x &= \exp(-i\kappa_x L_x) \\ \lambda_y &= \exp(-i\kappa_y L_y) \end{aligned} \tag{3.14}$$

Additionally, $\kappa_x = \boldsymbol{\kappa} \cos\theta$ and $\kappa_y = \boldsymbol{\kappa} \sin\theta$ are recognized as the components of the wave vector $\boldsymbol{\kappa}$, which propagates in the direction θ.

The equilibrium of internal forces at the boundary nodes of the UC, under the influence of periodic conditions, necessitates the following conditions:

$$\begin{gathered} f_1 + \lambda_x^{-1} f_2 + \lambda_y^{-1} f_3 + \lambda_x^{-1}\lambda_y^{-1} f_4 = 0 \\ f_L + \lambda_x^{-1} f_R = 0 \\ f_B + \lambda_y^{-1} f_T = 0 \end{gathered} \tag{3.15}$$

The complete set of displacements can be projected onto the reduced set of displacements $\mathbf{q}_{red} = [q_1, q_L, q_B, q_I]^T$ using a transformation matrix $\mathbf{\Lambda}_R$, as facilitated by Eq. 3.13:

$$\mathbf{q} = \begin{bmatrix} \mathbf{I}_s & \mathbf{0} & \mathbf{0} & \mathbf{0} \\ \lambda_x \mathbf{I}_s & \mathbf{0} & \mathbf{0} & \mathbf{0} \\ \lambda_y \mathbf{I}_s & \mathbf{0} & \mathbf{0} & \mathbf{0} \\ \lambda_x \lambda_y \mathbf{I}_s & \mathbf{0} & \mathbf{0} & \mathbf{0} \\ \mathbf{0} & \mathbf{I}_{ms} & \mathbf{0} & \mathbf{0} \\ \mathbf{0} & \mathbf{0} & \mathbf{I}_{ns} & \mathbf{0} \\ \mathbf{0} & \lambda_x \mathbf{I}_{ms} & \mathbf{0} & \mathbf{0} \\ \mathbf{0} & \mathbf{0} & \lambda_y \mathbf{I}_{ns} & \mathbf{0} \\ \mathbf{0} & \mathbf{0} & \mathbf{0} & \mathbf{I}_i \end{bmatrix} \begin{bmatrix} \mathbf{q}_1 \\ \mathbf{q}_L \\ \mathbf{q}_B \\ \mathbf{q}_I \end{bmatrix} = \mathbf{\Lambda}_R \mathbf{q}_{red} \tag{3.16}$$

Similarly, Eq. 3.15 provides the transformation matrix $\mathbf{\Lambda}_L$, considering that no forces are acting on the internal nodes:

$$\begin{bmatrix} \mathbf{I}_s & \lambda_x^{-1}\mathbf{I}_s & \lambda_y^{-1}\mathbf{I}_s & \lambda_x^{-1}\lambda_y^{-1}\mathbf{I}_s & \mathbf{0} & \mathbf{0} & \mathbf{0} & \mathbf{0} & \mathbf{0} \\ \mathbf{0} & \mathbf{0} & \mathbf{0} & \mathbf{0} & \mathbf{I}_{ms} & \mathbf{0} & \lambda_x^{-1}\mathbf{I}_{ms} & \mathbf{0} & \mathbf{0} \\ \mathbf{0} & \mathbf{0} & \mathbf{0} & \mathbf{0} & \mathbf{0} & \mathbf{I}_{ns} & \mathbf{0} & \lambda_y^{-1}\mathbf{I}_{ns} & \mathbf{0} \\ \mathbf{0} & \mathbf{0} & \mathbf{0} & \mathbf{0} & \mathbf{0} & \mathbf{0} & \mathbf{0} & \mathbf{0} & \mathbf{I}_i \end{bmatrix} \mathbf{f} = \mathbf{0} \tag{3.17}$$

Utilizing Equations 3.13 and 3.15, a reduced eigenvalue problem is formulated, which correlates the wavevector $\boldsymbol{\kappa}$, wave propagation angle θ, and frequency ω:

$$\mathbf{\Lambda}_L(\kappa, \theta) \left[\widetilde{\mathbf{K}}(\omega) - \omega^2 \widetilde{\mathbf{M}} \right] \mathbf{\Lambda}_R(\kappa, \theta) \mathbf{q}_{red} = \left[\hat{\mathbf{K}}(\kappa, \theta, \omega) - \omega^2 \hat{\mathbf{M}} \right] \mathbf{q}_{red} = 0 \tag{3.18}$$

The eigenvalues of the determinant equation $\det(\hat{\mathbf{K}}(\kappa, \theta, \omega) - \omega^2 \hat{\mathbf{M}}) = 0$ are indicative of the complex wavenumbers associated with each wave propagating in the periodic structure, and the eigenvectors $\boldsymbol{\phi}$ of Eq. 3.18 are the wavemodes, i.e., the mode shapes for the corresponding waves.

However, Eq. 3.18 constitutes a NEP that correlates the wavevector $\boldsymbol{\kappa}$, propagation angle θ, and frequency ω. The NEP is resolved using the Contour Integration method (CI).

3.3.2 Contour Integral Solver

Addressing the NEP remains a complex task due to the absence of a definitive optimal strategy [124]. Consequently, the application of the WFE method to frequency-dependent parameters and damped media is underexplored, despite its integration with standard FE libraries being highly beneficial. The CI method is utilized for resolving the NEP within the WFE framework [187, 188]. This approach facilitates the extraction of eigenvalues enclosed by a contour in the complex plane, independent of the eigenvalue problem's non-linearity. The algorithm operates on multiple independent, typically sparse linear systems of varying sizes, which are amenable to efficient parallelization. Examples of this method's application in physics include the generalized EVP [189, 190] and NEP [191].

To simplify the practical calculations, introducing the non-dimensional wavenumber μ and the scaled propagation angle α proves helpful:

$$\begin{gathered}\mu = \kappa \left[(L_x cos\alpha)^2 + \left(L_y sin\alpha\right)^2 \right]^{-0.5} \\ tan\alpha = \frac{L_y}{L_x} tan\theta \end{gathered} \tag{3.19}$$

The propagation constants can be expressed:

$$\begin{gathered}\lambda_x = e^{-i\mu cos\alpha} \\ \lambda_y = e^{-i\mu sin\alpha} \end{gathered} \tag{3.20}$$

Hence, the NEP can be expressed in a more compact form as

$$\hat{\mathbf{D}}\left(\omega, \mu, \alpha\right) \mathbf{q}_{red} = 0 \tag{3.21}$$

where the dynamic stiffness matrix $\hat{\mathbf{D}}\left(\mu\right) \in \mathbb{C}^{n,n}$, n denotes the size of the reduced vector of displacement $\mathbf{q}_{red}$

CI solver hinges on the computation of moments linked to the dynamic stiffness matrix $\hat{\mathbf{D}}\left(\mu\right)$, which is defined as follows:

$$\mathbf{A}_p = \frac{1}{2\pi i} \int_{\Gamma} \mu^p \hat{\mathbf{D}}\left(\mu\right)^{-1} \hat{\mathbf{V}} d\mu \tag{3.22}$$

where p ranges from 0 to $\bar{p}$, and $\bar{p} \in \mathbb{N}$, $\hat{\mathbf{V}}\left(\mu\right) \in \mathbb{C}^{n,l}$ represents a random probe matrix, which is chosen for probing the matrix decomposition 3.22. Typically, the probe matrix is taken to be random to ensure a diverse range of directions in the complex plane [192], thus increasing the likelihood of capturing the desired eigenvalues.

The moments $\mathbf{A}_p$ encapsulate information about the spectrum of $\hat{\mathbf{D}}\left(\mu\right)$ within the contour Γ. To extract eigenvalues and eigenvectors, a total of $2\bar{p}$ moments are employed to construct $\bar{p}n \times \bar{p}l$ block Hankel matrices $\mathbf{B}_0$ and $\mathbf{B}_1 \in \mathbb{C}^{\bar{p}n,\bar{p}l}$, which are defined as follows:

$$\mathbf{B}_0 = \begin{bmatrix} \mathbf{A}_0 & \dots & \mathbf{A}_{\bar{p}-1} \\ \vdots & \ddots & \vdots \\ \mathbf{A}_{\bar{p}-1} & \dots & \mathbf{A}_{2\bar{p}-2} \end{bmatrix} \text{ and } \mathbf{B}_1 = \begin{bmatrix} \mathbf{A}_1 & \dots & \mathbf{A}_{\bar{p}} \\ \vdots & \ddots & \vdots \\ \mathbf{A}_{\bar{p}} & \dots & \mathbf{A}_{2\bar{p}-1} \end{bmatrix} \tag{3.23}$$

Thus, the computation of moments of order $p = 0, \ ..., \ 2\bar{p} - 1$ using Eq. 3.22 is necessary. Following this, performing the Singular Value Decomposition (SVD) of $\mathbf{B}_0 = \mathbf{V}\Sigma\mathbf{W}^H$ results in a Low Rank Approximation (LRA):

$$\mathbf{B}_0 \approx \mathbf{V}_0 \Sigma_0 {\mathbf{W}_0}^H \tag{3.24}$$

To achieve the approximation, a tolerance ε_{SVD} is introduced, which helps in selecting only the leading $\bar{m}$ singular values, along with their corresponding columns of $\mathbf{V}$ and $\mathbf{W}$, based on the sorting of the singular values $\sigma_1 \geq \ldots \geq \sigma_m \geq \varepsilon_{SVD} \geq \sigma_{\bar{m}+1} \approx \ldots \approx 0$.

Through the algebraic manipulation, matrix $\hat{\mathbf{B}} = \mathbf{V}_0^H \mathbf{B}_1 \mathbf{W}_0 \mathbf{\Sigma}^{-1} \in \mathbb{C}^{\bar{m},\bar{m}}$ is constructed, the same eigenvalues can be found within the contour Γ by both the original NEP and the linearized problem. The eigenvectors, denoted as $\mathbf{q}_{0_i}$, of the original NEP can be retrieved from the initial n rows of $\mathbf{V}_0 s_i$, where s_i are the eigenvectors of $\hat{\mathbf{B}}$. In this way, the NEP in Eq. 3.21 is restructured into a reduced-sized linear eigenvalue problem that retains the same eigenvalues within Γ.

It is important to mention that the choice of $\bar{p}$ and $\bar{m}$ should be made carefully. Typically, the value of $\bar{m}$ is expected to be equal to or exceed the count of eigenvalues present within the contour Γ. Additionally, $\bar{p}l$ should satisfy $\bar{p}l \geq n_{sol}$, and $\bar{p}$ may need to be greater than 1 if solutions with algebraic multiplicity greater than 1 are expected. It is recommended to keep the maximum order of moments as $\mathbf{2\bar{p} - 1}$ relatively

small for stability and accuracy reasons [193, 194].

In summary, the proposed algorithm involves several key steps to solve the NEP using the CI solver:

1. **Solution of Linear Systems:** For each desired eigenvalue μ_j within the contour Γ, solve N independent complex-valued linear systems $\hat{\mathbf{D}}\left(\mu_j\right)\mathbf{X}_j = \hat{\mathbf{V}}$, where $\hat{\mathbf{D}}$ is of size $n \times n$ and $\hat{\mathbf{V}}$ is of size $n \times l$. The parallelization of this step can be effective for UC with a large number of DOFs.

2. **Assembly of Hankel Matrices:** Assemble the Hankel matrices $\mathbf{B}_0$ and $\mathbf{B}_1$ based on the solutions from the previous step. These matrices are of the size $\bar{p}n \times \bar{p}l$.

3. **SVD Decomposition:** Perform the truncated SVD decomposition of the matrix $\mathbf{B}_0$ to obtain a LRA $\mathbf{B}_0 \approx \mathbf{V}_0\Sigma_0{\mathbf{W}_0}^H$. The LRA is achieved by selecting only the leading $\bar{m}$ singular values and their corresponding columns of $\mathbf{V}$ and $\mathbf{W}$, based on a tolerance parameter ε_{SVD}.

4. **Linear Eigenvalue Problem:** Solve the EVP using the matrix $\hat{\mathbf{B}} \in \mathbb{C}^{\bar{m},\bar{m}}$, where $\bar{m} \geq n_{sol}$, and n_{sol} is the number of eigenvalues expected within the contour Γ.

The outlined procedure can effectively extract wavenumbers from a WFE model within a closed contour on the complex plane. The latter can be chosen according to lateral dimensions of the UC, as the real part of the wavenumber can only assume values within the first Brillouin zone.

3.3.3 Solution Domain of the NEP

Considering the periodic structures illustrated in Fig. 3.3(a), the wave solutions to the EVP and thus the dispersion curves are 2π-periodic in the propagation constants $Re\left(\lambda_x\right)$ and $Re\left(\lambda_y\right)$ in the reciprocal wave space. The wave solutions can hence be divided into periodic zones in the wave domain, which are referred to as Brillouin Zones [79, 195]. Consequently, all the propagation constant information describing the wave propagation in the infinite periodic structure is contained within the first Brillouin Zone confined as the wavenumber space within $\left[-\frac{\pi}{L_x}, \frac{\pi}{L_x}\right] \times \left[-\frac{\pi}{L_y}, \frac{\pi}{L_y}\right]$ when considering a UC of size $L_x \times L_y$ in the reciprocal wave space (Fig. 3.3 (a)). The analyzed zone in the wave domain can be further confined by exploiting symmetries in the UC, leading to the Irreducible Brillouin Zone (IBZ, O-A-B-C-O), of which the shape depends on the type of symmetries [195, 196]. To characterize wave propagation in an infinite periodic structure, it suffices to calculate dispersion curves within the IBZ.

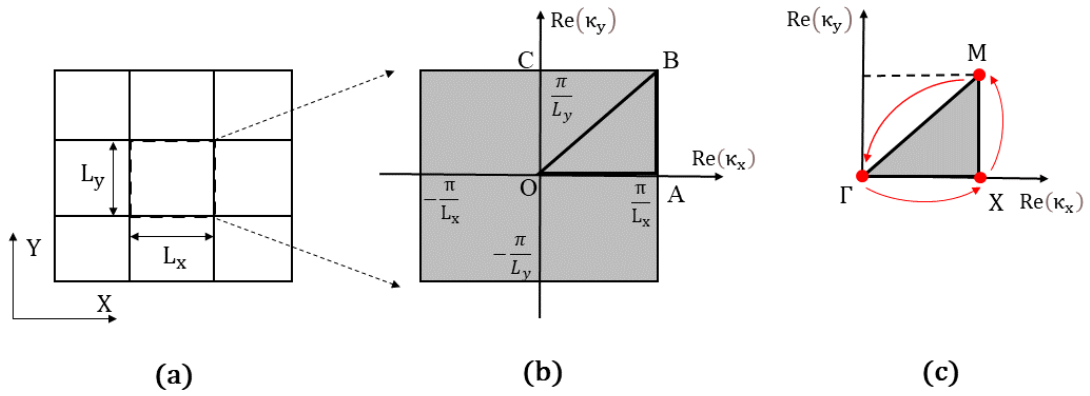

Fig. 3.3. Schematic of a Typical 2D periodic structure (figure a), First Brillouin Zone and the corresponding IBZ (O-A-B-C-O) and corresponding Reciprocal Lattice (O-A-B-O) for a square and symmetric UC (figure b), the IBC (figure c).

A numerical approximation of the integral in Eq. 3.22 is also necessary in practice. Let a parametrization of the contour be $\Gamma = \gamma + \rho\left(cost + i\beta sint\right)$, with $0 \leq t \leq 2\pi$. Under these circumstances, the integral

is approximated by an N-point trapezoidal rule, leading to the following discrete approximation of Eq. 3.22

$$A \simeq \frac{\rho}{N} \sum_{j=1}^{N} \mu_j^p w_j X_j \tag{3.25}$$

where μ_j are the integration points along Γ, $w_j = \left(\beta cost_j + isint_j\right)$ are the weights and $\hat{\mathbf{D}}\mathbf{X}_j = \hat{\mathbf{V}}$ are the N linear systems to be solved. Note that, to ensure numerical stability, a shift and scale transformation is applied to the spectrum, so that the monomial basis $((\mu - \gamma)\rho)^p$ is used in Eqs 3.21 and 3.26 in place of μ^p.

The procedure briefly outlined above can be successfully used to extract wavenumbers from a WFE model within a closed curve of the complex plane. The latter can be chosen according to the lateral dimensions of the cell, as the real part of the wavenumber can only assume values within the first Brillouin zone. Let a parametrization of the contour be $\Gamma = \gamma + \rho\,(cost + i\beta sint)$, with $0 \leq t \leq 2\pi$. The ρ should be chosen according to first Brillouin zone of the 2D PCs as illustrated in Fig. 3.3:

$$\rho = \frac{\pi}{2}\sqrt{\frac{1}{cos^2} + \frac{1}{sin^2}} \tag{3.26}$$

Note that ρ and γ should be chosen precisely so the boundary of the chosen contour encircles all the possible solutions.

It should be mentioned that, unless an efficient strategy is available to estimate n_{sol} (see Ref. [197] for instance), the parameters $\bar{p}$ and l should be adaptively selected to ensure that a clear separation occurs in the singular values and, consequently, a Low Rank Approximation of B_0 exists. However, such optimization is beyond the scope of this work, whose principal aim is to provide a first assessment of the CI method for the WFE application.

When the contour used for the extraction of the wavenumbers from the WFE model was chosen such that $\rho = \pi/8$, $\beta = 0.5$ and $\gamma = 0$ for instance. These values correspond to an ellipse with the major axis of 400 rad/m (i.e. maximum value of $\mathrm{Re}\{\kappa\}$) and minor axis of 200 rad/m (i.e. maximum value of $\mathrm{Im}\{\kappa\}$). Hence, whenever an eigenvalue enters the targeted region, for instance, because the imaginary part is decreasing with the frequency, a new curve appears in the dispersion relations [118].

After solving the NEP, the eigenvector corresponding to the j^{th} eigenvalue is represented as $\boldsymbol{\phi}_{j,\mathrm{red}}$. The complete set of wavemodes can be articulated as follows:

$$\boldsymbol{\phi}_j = \boldsymbol{\Lambda}_R \boldsymbol{\phi}_{j,red} \tag{3.27}$$

The eigenvectors represent the deformations associated with all degrees of freedom as a wave propagates through the structure, offering valuable insights into the behavior of the equivalent wave.

3.3.4 Wave Track Techniques

As discussed in the previous section, due to the veering effect caused by the highly contrasted components, the eigenvalues and eigenvectors after the numerical computation no longer take the correct order to reveal the characteristics of a specific wave. Various techniques have been investigated for the wave track purpose, such techniques aim at the optimization of mode pairing strategies that try to minimize the difference between the numerically obtained solutions.

3.3.4.1 Constant Frequency Gradient Method

To tackle the problem, Atalla and Ghinet used the Constant Frequency Gradient Method (CFGM) to track the eigenvalues and eigenvectors solved by the EVP [29]. The CFGM leverages the assumption that the slope of the progressive wave corresponding to the frequency remains constant and that the impact of damping on the amplitude of the wave is negligible. The method initially calculates the frequency slope of the progressive wave for both undamped and damped models within the frequency band of interest. These slopes are then employed to track the solutions. However, the implementation of CFGM is roundabout and encounters numerical issues when eigenvalues of different waves overlap or approach each other.

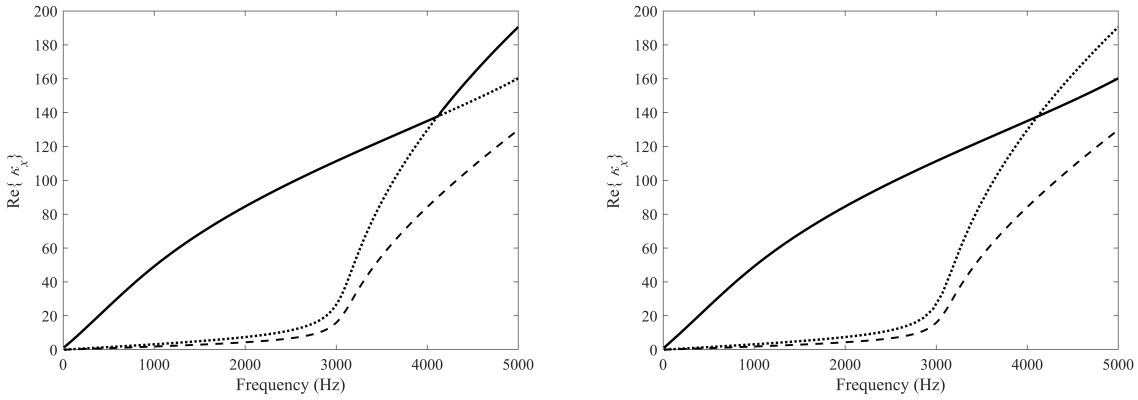

Fig. 3.4. Wave track by Constant Frequency Gradient Method (Left) and Weighted Wave Assurance Criteria (Right). − Bending wavenumbers, ··· Extensional wavenumbers, −− Shear wavenumbers.

Take the instance of a 5-layer symmetric sandwich plate as discussed in [198], the bending and extensional wavenumbers overlap, leading to incorrect tracking in the Constant Frequency Gradient Method (CFGM), as illustrated in Fig. 3.4.

3.3.4.2 Wave Assurance Criterion

An efficient technique to track the correlation between wavemodes of two consecutive frequency steps is the Wave Assurance Criterion (WAC) inspired by the pairing technique for experimentally obtained and numerically derived natural frequencies and mode shapes proposed by Allemang et al. [199], which is defined as:

$$\mathrm{WAC_{jk}} = \max\left(\frac{(\boldsymbol{\phi}_\mathrm{j}^\mathrm{H}\boldsymbol{\phi}_\mathrm{k})^2}{(\boldsymbol{\phi}_\mathrm{j}^\mathrm{H}\boldsymbol{\phi}_\mathrm{j})(\boldsymbol{\phi}_\mathrm{k}^\mathrm{H}\boldsymbol{\phi}_\mathrm{k})}\right) \tag{3.28}$$

where $\boldsymbol{\phi}_j$ and $\boldsymbol{\phi}_k$ denote the j^{th} and k^{th} numerical modes, respectively. The solution domain of WAC is $[0, 1]$, a value of 1 signifies perfect modal pairing in the subsequent frequency step.

The WAC is a purely mathematical criterion for checking the consistency between two eigenvectors. WAC_{jk} assigns the k^{th} numerical mode to the j^{th} mode. For perfectly correlated mode shapes that are in an appropriate order, the indices j and k should agree with each other.

Several other correlation measures are based on the WAC. For example, the Linear Wave Assurance Criterion (LWAC) was proposed to linearize the nonlinear behavior of the WAC [199], which reads:

$$\mathrm{LWAC_{jk}} = 1 - \frac{2}{\pi}\arccos\left(\sqrt{\mathrm{WAC_{jk}}}\right) \tag{3.29}$$

where solutions of $\left(\arccos\left(\sqrt{WAC_{jk}}\right)\right)$ lie in $[0, \frac{\pi}{2}]$, consequently a value of 1 means perfect modal pairing in the next frequency step.

3.3.4.3 Weighted Wave Assurance Criterion

Considering the principle of energetic continuity, an extension of WAC known as the WWAC becomes [200]:

$$\mathrm{WWAC_{jk}} = \max\left(\frac{\left(\boldsymbol{\phi}_{\mathrm{j}}^{\mathrm{H}}\mathbf{W}\boldsymbol{\phi}_{\mathrm{k}}\right)^{2}}{\left(\boldsymbol{\phi}_{\mathrm{j}}^{\mathrm{H}}\mathbf{W}\boldsymbol{\phi}_{\mathrm{j}}\right)\left(\boldsymbol{\phi}_{\mathrm{k}}^{\mathrm{H}}\mathbf{W}\boldsymbol{\phi}_{\mathrm{k}}\right)}\right) \tag{3.30}$$

WWAC enhances WAC by incorporating a weighting matrix $\mathbf{W}$. When the mass matrix is chosen, WWAC evaluates modal components associated with significant contributions to kinetic energy. On the other hand, if the stiffness matrix is selected, WWAC underscores the energetic continuity of strain energy. This weighting approach improves the precision of wave tracking, with correctly tracked wavenumbers illustrated in Fig. 3.4 for the case studied.

3.4 Numerical Validation

This section assesses the AHM for HCS and HDS by examining four laminated configurations with different skins, cores, and geometries.

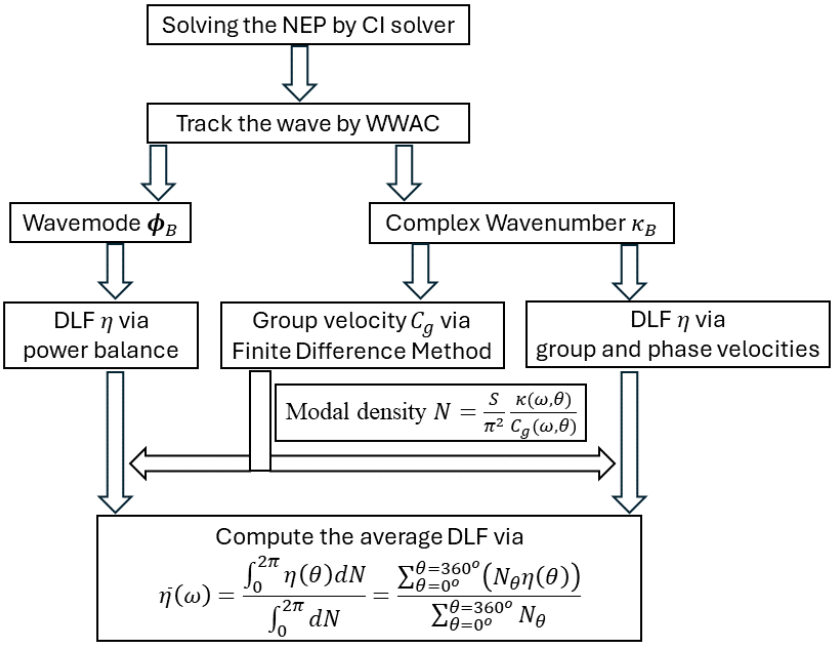

Fig. 3.5. Flowchart for numerical implementation procedures of the WFE framework.

The process of numerical implementation of the WFE scheme is depicted in Fig. 3.5. Note that for the group velocity C_g at the desired propagation direction in Eq. 2.65, the wavenumbers at the two adjacent frequencies $\omega + d\omega$ and $\omega - d\omega$ are calculated to fulfill the computation process via the Finite Difference Method.

Provided modal density $N = \frac{S}{\pi^2}\frac{\kappa(\omega,\theta)}{C_g(\omega,\theta)}$ in all directions, the numerical integration at angular frequency ω in Eq. 2.66 is computed by superposition:

$$\bar{\eta}(\omega) = \frac{\sum_{\theta=0^o}^{\theta=360^o}(N_\theta \eta(\theta))}{\sum_{\theta=0^o}^{\theta=360^o} N_\theta} \tag{3.31}$$

3.4.1 Asymmetric Sandwich Plate with Frequency-dependent Core

The first configuration comprises an asymmetric sandwich panel with aluminum skins of different thicknesses bounded by a frequency-dependent polymer core. The top skin, bottom skin, and polymer core have thicknesses of 0.1524 mm, 3.175 mm, and 0.254 mm, respectively.

Tab. 3.1. Material Properties of Aluminum.

Property	Aluminum	Polymer
Density	2700 kg/m^3	110 kg/m^3
Young's modulus	71GPa	Frequency-dependent
Poisson ratio	0.33	0.45
Damping ratio η	0.1%	Frequency-dependent

The aluminum skins and lightweight polymer core are characterized in Tab. 3.1, and the shear moduli and material damping ratio of the polymer are frequency-dependent.

3.4.1.1 Frequency-dependent Properties of Polymer

The frequency-dependent shear moduli and material damping ratio at 20°C are outlined in Tab. 3.2.

Tab. 3.2. Frequency Dependent Properties of the Polymer.

Frequency [Hz]	Shear Modulus [Pa]	Frequency [Hz]	Damping Ratio [1]
23.2883	174865	22.4675	0.523865
47.8247	214172	119.441	0.578205
95.5313	255139	221.197	0.602142
163.882	313068	476.257	0.629756
277.272	368391	835.017	0.649792
653.911	463362	2237.99	0.701886
1607.53	624842	3375.01	0.721125
3393.86	797921	4201.5	0.737815

The Young's modulus is derived from the equation $E = 2\mu(1+\nu)$. For frequency points not shown in Tab. 3.2, frequency-dependent properties are interpolated linearly.

3.4.1.2 Validation of Asymptotic Homogenization Method

In the WFE scheme, the UC is designed with a sidelength of 1 mm and is modeled using 2×2 ANSYS SOLID45 elements in the in-plane directions per layer, culminating in a total of 12 elements. Each element comprises 8 nodes, each possessing 3 DOFs that include in-plane and flexural displacements. A

total of 12 DOFs are allocated at each corner of the UC. Given the isotropic nature of this structure, the wavenumbers are independent of the direction of wave propagation, aligning with the research scope of the AHM.

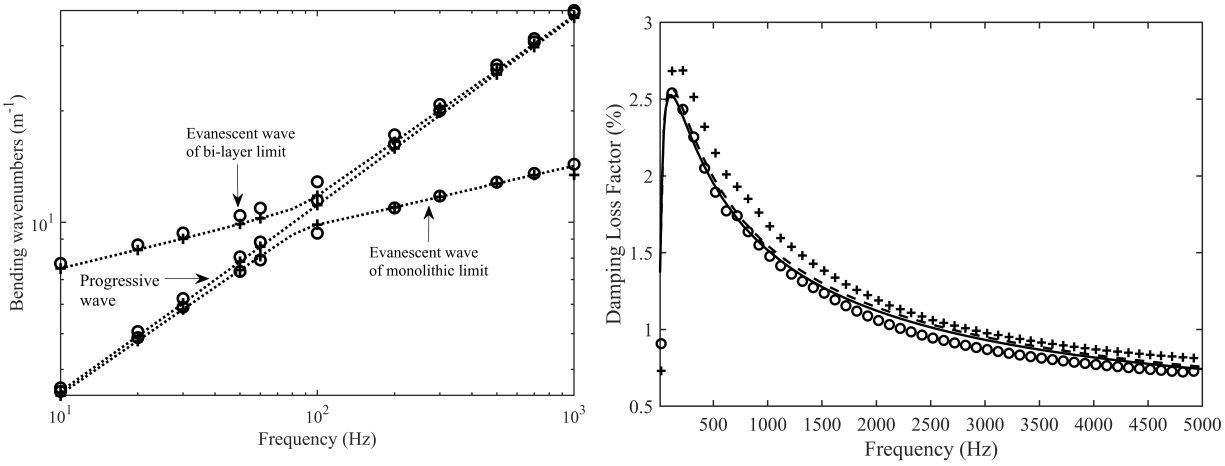

Fig. 3.6. Results for the sandwich panel. Left: Bending waves. ◯ Bending waves from AHM, + Bending waves from GLM, ⋯ Bending waves from WFE. Right: Dominant DLF. − Bending waves from WFE, ◯ Bending waves from GLM, + Bending waves from RKU, ▽ Bending waves from AHM.

Fig. 3.6 validates the multi-scale structural behavior. The three bending wavenumbers derived from AHM align with GLM and WFE within the relevant frequency range. This alignment affirms the multi-scale behavior, characterized by the monolithic limit motion at low frequency, the skin-dominated bi-layer limit motion at high frequency, and the core shear motion at mid-frequency.

Tab. 3.3. Material Properties of PVB type RB41.

Density	Young's modulus	Poisson ratio	Damping ratio
1070 kg/m^3	Rheological	0.499	Rheological

The DLF of the progressive wave, corresponding to the deflection motion coupled with in-plane shearing of the core, is maintained. This DLF, referred to as the dominant DLF, is utilized to assess the accuracy of AHM. The dominant wave's DLF from AHM aligns with those from WFE, GLM, and the RKU model [201], as depicted in Fig. 3.6.

3.4.2 Laminated Glass with a Rheological PVB Core

The second configuration involves LG with a rheological PVB core in two geometries to investigate the multi-scale dynamics of HCS.

A specific instance of HCS is demonstrated using a model where LG consists of two glass layers with properties listed in Tab. 3.3. The details of the two classic LG geometries are provided in Tab. 3.4.

3.4.2.1 Rheological Properties of PVB type RB41

The viscoelastic characteristics of PVB type RB41 are detailed in a harmonic regime at the reference temperature $T_0 = 20°C$ [13]. This characterization employs the rheological shear modulus, with the real

Tab. 3.4. Geometry of Laminated Glass.

	Glass layer thickness (mm)	PVB layer thickness (mm)
LG_a	10	0.76
LG_b	5	0.38

and imaginary components representing the elastic and loss moduli, respectively. The shear moduli of PVB are defined by spring constants G_k and dashpot viscosities $\eta_k = \tau_k G_k$ [202]:

$$\mu(\omega, T_0) = \sum_n \frac{i\omega\tau_k G_k}{1 + i\omega\tau_k} \tag{3.32}$$

Tab. 3.5. Parameters describing the shear modulus of PVB in Eq. 3.34.

$\tau_k(s)$	10^{-5}	10^{-4}	10^{-3}	10^{-2}	10^{-1}	1	10	10^2	10^3
	10^4	10^5	10^6	10^7	10^8				
$G_k(MPa)$	2.3	25.2	30.8	39.2	35.2	6.2	1.9	0.7	0.17
	0.07	0.08	0.11	0.10	0.14				

The experimentally determined characteristic times τ_k and G_k for PVB RB41 are provided in Tab. 3.5.

3.4.2.2 Multi-scale Dynamics and the Damping Loss Factor

To accurately depict the multi-scale dynamics, a finer mesh is utilized in the WFE scheme. In the out-of-plane direction, the skin is allocated 2 elements, while the interlayer is assigned 4 elements. The UC has a length of 1 mm, with 2 elements specified in each in-plane direction, culminating in a total of 32 elements and 27 DOFs at each corner.

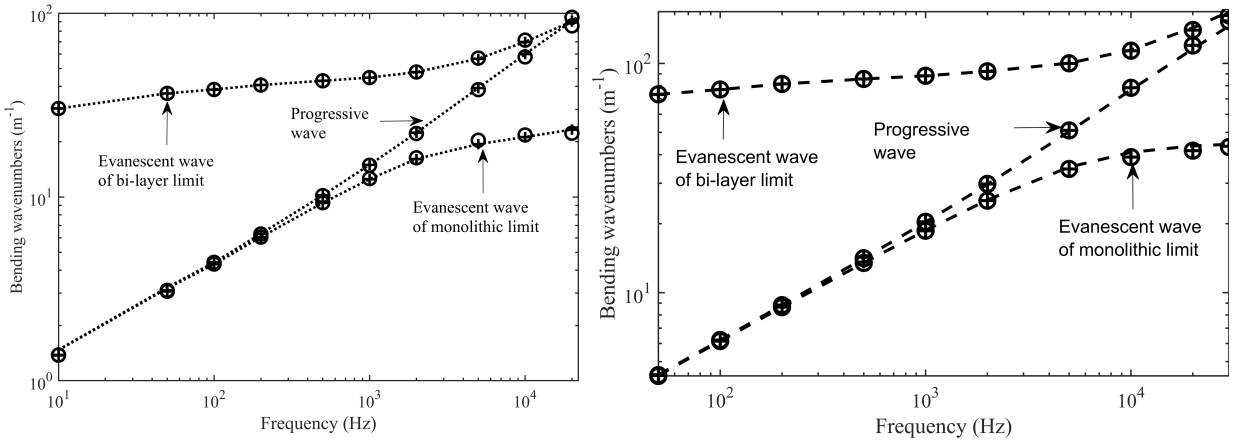

Fig. 3.7. Bending waves for LGa (left) and LGb (right). −− Bending waves from WFE, + Bending waves from GLM, ◯ Bending waves from AHM.

The bending wavenumbers effectively reflect the multi-scale dynamics of HCS, as depicted in Fig. 3.7. There is a notable agreement among all three models across the frequency range of 10 Hz to 30000 Hz.

The eigenvectors, derived from the CI solver, offer a perspective into the deformations. Fig. 3.8 presents the progressive wavemodes from WFE. This representation displays the deformations of the UC's cross-section, depicted at two distinct frequencies: 10 Hz and 4000 Hz. It should be noted that the wavemodes are not to scale: the in-plane displacements have been exaggerated relative to those along the Z-axis for clarity. These deformations confirm the manifestation of the two limit behaviors of the HCS at low and high frequencies, respectively.

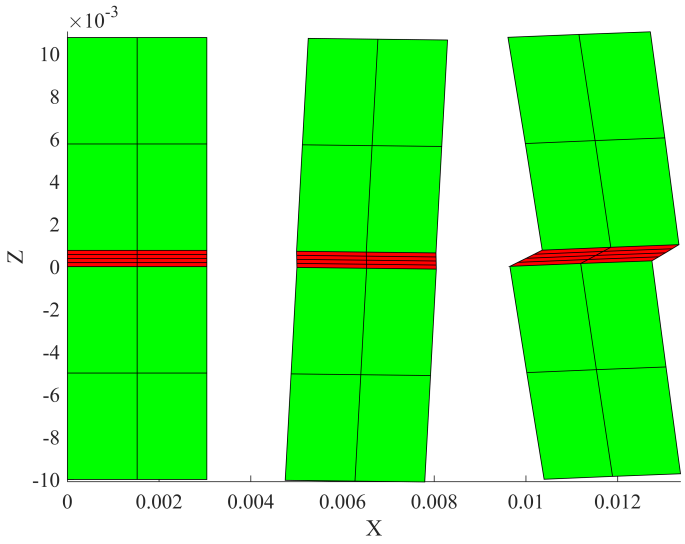

Fig. 3.8. Two limit dynamic of laminated glass with PVB core. Left: Original form. Middle: Monolithic limit dynamic at 20 °C *and* 10 Hz. Right: Bi-layer limit dynamic at 20 °C *and* 4000 Hz.

- At low-frequency range where weak contrast exists since PVB still has the stiffness modulus at the same order of magnitude as glass, the progressive bending waves are close to the evanescent waves of monolithic limit, which indicates that the whole LG structure behaves as a monolithic plate (Kirchhoff-Love plate theory, for example), the differential in-plane motion between the stiff layers, as depicted in Fig. 2.1, is still not appearing, which means $D = 0$.
- While at high frequency the high difference of stiffness between glass layers and PVB layer generates high contrast in LG structure, the evanescent waves of monolithic limit vanish to zero and the progressive bending waves are close to the evanescent waves of bi-layer limit, which indicates that the whole LG structure behaves as a bi-layer plate with shear (Sandwich shear-bending plate model), the differential in-plane motion between the middle planes of the stiff layers no longer appears, which means $d_1 = d_2 = 0$ in Fig. 2.1.

The dominant DLF determined by AHM, shows a significant correlation with both WFE and GLM, as illustrated in Fig. 3.9.

3.4.3 Sandwich Structure with Shape Memory Polymer Core at 50 °C

The third configuration involves a sandwich panel composed of aluminum skins and a tBA/PEGDMA (Shape Memory Polymer, SMP) core. SMP is employed as the core material in these laminated sandwich structures.

The external skins are made up of 0.5 mm thick aluminum panels, characterized by the properties in Tab. 3.1. The rheological properties of the SMP are detailed by Butaud [5].

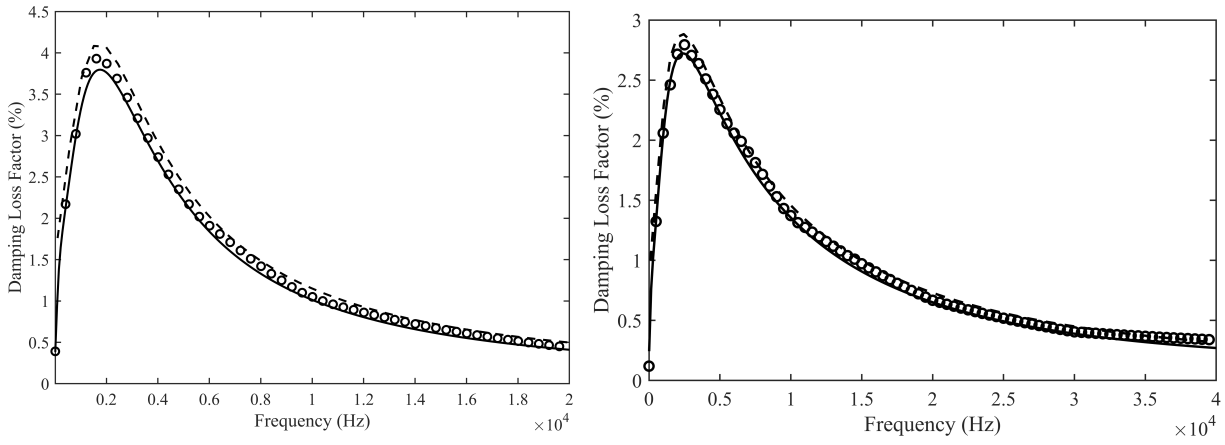

Fig. 3.9. Dominant DLF for LGa (left) and LGb (right). − DLF from WFE, ∘ DLF from GLM, −− DLF from AHM.

3.4.3.1 Frequency and Temperature-dependent Properties of Shape Memory Polymer (tBA/PEGDMA)

The complex Young's modulus of SMP conforms to the following relationship, as outlined in Butaud's study [5]:

$$E\left(\omega, T_0\right) = E_0 + \frac{\left(E_\infty - E_0\right)}{\left(1 + \gamma\left(i\omega\tau\right)^{-k} + \left(i\omega\tau\right)^{-h_i} + \left(i\omega\beta\tau\right)^{-1}\right)} \tag{3.33}$$

where $E_0 = 0.67$, $E_\infty = 2211$, $k = 0.16$, $h_i = 0.79$, $\gamma = 1.68$, $\beta = 3.8 \times 10^4$, and $\tau_0 = 0.61$.

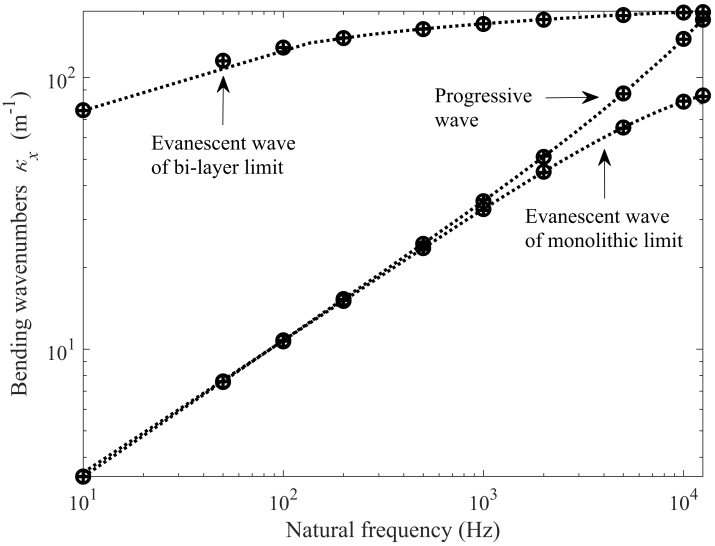

Fig. 3.10. Bending wavenumbers at 50 ^oC. −− Bending wavenumbers from WFE, ∘ Bending wavenumbers from AHM, + Bending wavenumbers from GLM.

Following the time-temperature superposition principle [13], SMP exhibits temperature-dependent behavior consistent with many polymers. The characteristic time, t_T, is related to t_{T_0} (the characteristic time at the reference temperature T_0) via a shift factor, a_T, as per the following relationship:

$$log\,(a_T) = -C_1 \frac{T - T_0}{C_2 + T - T_0} \tag{3.34}$$

where $C_1 = 10.87°C$, $C_2 = 32.57°C$, and $T_0 = 40°C$.

With Eq. 3.34, the rheological properties can be efficiently determined at any given angular frequency and temperature with $\mu(\omega, T) = \mu(\omega a_T, T_0)$.

3.4.3.2 Multi-scale Dynamics and the Damping Loss Factor

For sandwich structures with an SMP core at 50°C, a mesh identical to that of LG is applied. The bending wavenumbers, which depict the multi-scale dynamics of the HCS, are demonstrated in Fig. 3.10. The results show a high degree of consistency among all three models across the frequency range of 10 Hz to 12500 Hz.

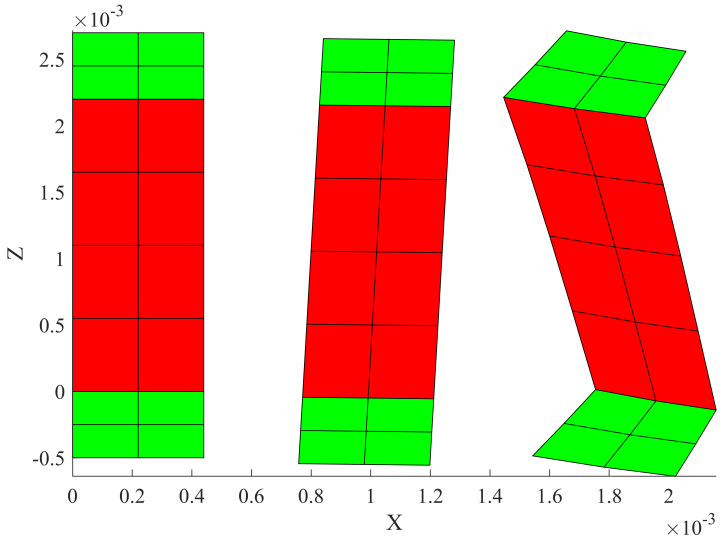

Fig. 3.11. Two limit dynamic of sandwich with SMP core. Left: Original form. Middle: Monolithic limit dynamic at 50°C *and* 100 Hz. Right: Bi-layer limit dynamic at 80°C *and* 5000 Hz.

The multi-scale behaviors are depicted in Fig. 3.11. The deformations within the UC, particularly where the core is relatively thick, provide a clear visualization of the frequency-dependent wave scattering across different media. This includes the progressive wave at low frequency, indicative of the bending dynamic of monolithic limit behavior, and the transition to the skins for the bending dynamic of bi-layer limit behavior at high frequency.

As depicted in Fig. 3.12, the concurrence of AHM to WFE and GLM in the DLF signifies the dominant role of the progressive wave in dictating the dynamic motion of the SMP50°C sandwich.

3.4.4 Orthotropic Epoxy Resin Sandwich

The sandwich panel made of 2.5mm PVB type RB41 core [203] (material properties are computed by parameters listed in Tab. 3.5) sandwiched between the 1 mm epoxy resin skins with material properties in Tab. 3.6.

The orthotropic sandwich panel is modelled by a 1mm square UC by an in-house MATLAB FE program using only C3D8 elements (8 nodes for each element), in the thickness direction, each layer in the skins is modelled by 1 element and 5 elements for the Rohacell foam core, 108 nodes are generated (3 DoFs each node), the wavenumbers at 100 Hz are calculated via CI solver implemented in the WFE

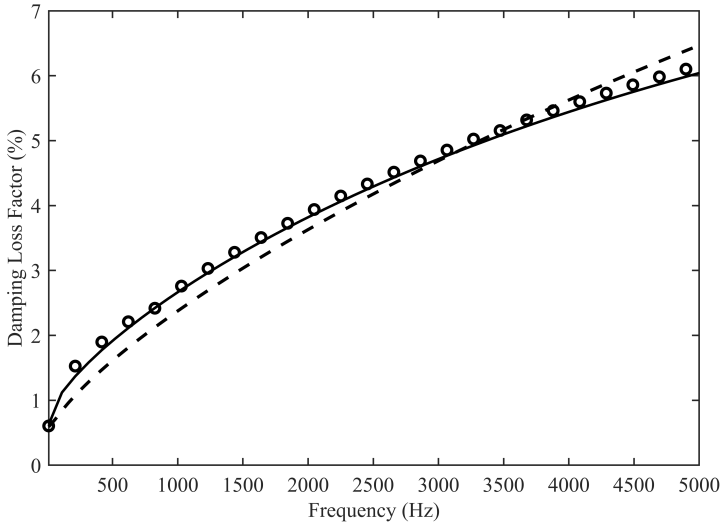

Fig. 3.12. DLF of Shape Memory Polymer Sandwich at 50 ^oC. − DLF of WFE. ∘ DLF of GLM. −− DLF of AHM.

Tab. 3.6. Material Properties of Epoxy Resin.

Property	Value
Density ρ	1550 kg/m^3
Young's moduli $\{E_x, E_y, E_z\}$	$\{1.336E10, 7.7E9, 7.7E9\}$Pa
Poisson ratios $\{\nu_{xy}, \nu_{yz}, \nu_{xz}\}$	$\{0.29, 0.0167, 0.0167\}$
Damping ratio η	1%

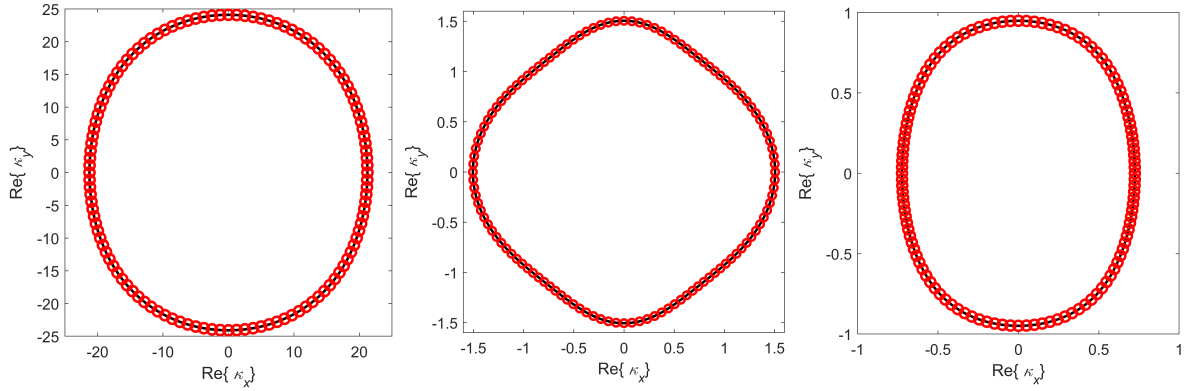

Fig. 3.13. Wavenumber Space of an Orthotropic Sandwich at 250 Hz. − GLM results. ∘ WFE results. Left: Bending Wavenumbers. Mid: Extensional Wavenumbers. Right: Shear Wavenumbers.

scheme. Bending, extensional and shear waves in omni-directions are sorted and compared with GLM [29] in Fig. 3.13, wavenumbers in all heading angles are in good agreement with the semi-analytical results, validating again the feasibility of the developed CI solver.

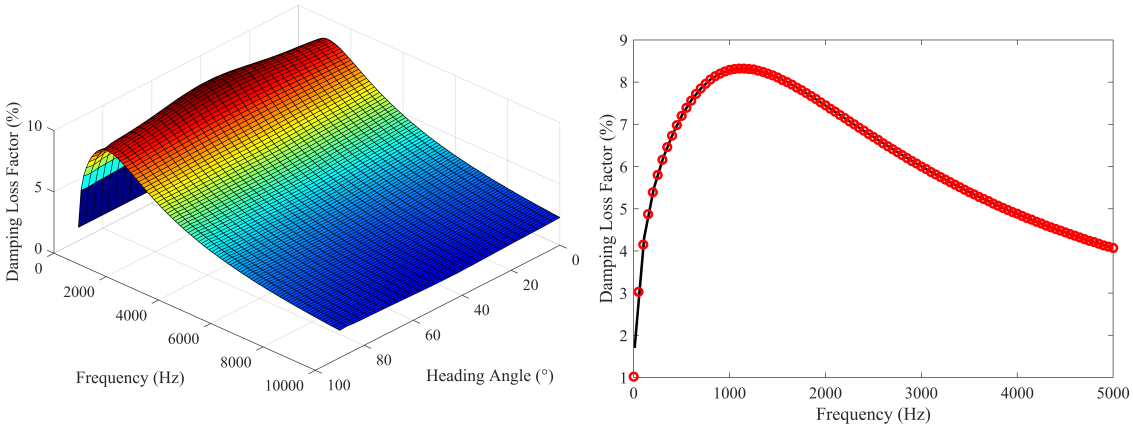

Fig. 3.14. Damping Loss Factor of Orthotropic Epoxy Resin Sandwich. – WFE results. ○ GLM results.

The DLF calculated using WFE in all directions is depicted in Fig. 3.14, and the average DLF is computed by Eq. 2.66 and compared with GLM [29]. The average DLF from WFE is calculated from the bending wave by Eq. 2.66, the results agree well with GLM, meaning the bending wave is donating the motion of the SMP50°C sandwich plate.

3.4.5 Sandwich Structure with a Thick Dissipative Core

Tab. 3.7. Material Properties of the Sandwich Plate with a Thick Dissipative Core.

Property	Highly damped core	Stiff skin
Density	1200 kg/m^3	2070 kg/m^3
Young's modulus	2.98 MPa	71 GPa
Poisson ratio	0.49	0.31
Damping ratio	65%	1%

The fourth configuration under consideration is designed to evaluate the validity of AHM to laminated structures with thick cores exhibiting high material damping. The core, with a thickness of 5.14 mm, is sandwiched between stiff skins of 0.8 mm thickness. The material properties used in the computation are listed in Tab. 3.7.

As depicted in Fig. 3.15, AHM concurs with WFE and GLM on the three bending wavenumbers solely at lower frequencies. At higher frequencies, AHM yields inaccurate wavenumbers, which subsequently results in incorrect predictions of phase and group velocities. Consequently, the DLF of AHM significantly deviates from that of WFE and GLM, as illustrated in Fig. 3.16.

The WFE scheme employs a refined mesh for the UC, it uses 1 element in each stiff skin and 10 elements in the core for the thickness direction, with 2×2 elements in the in-plane directions per layer. Fig. 3.17 illustrates the two limit dynamics of the sandwich panel to scrutinize the core motion. In the monolithic limit dynamic, the core mimics a rigid layer with uniform deformation, and $D = 0$. Conversely,

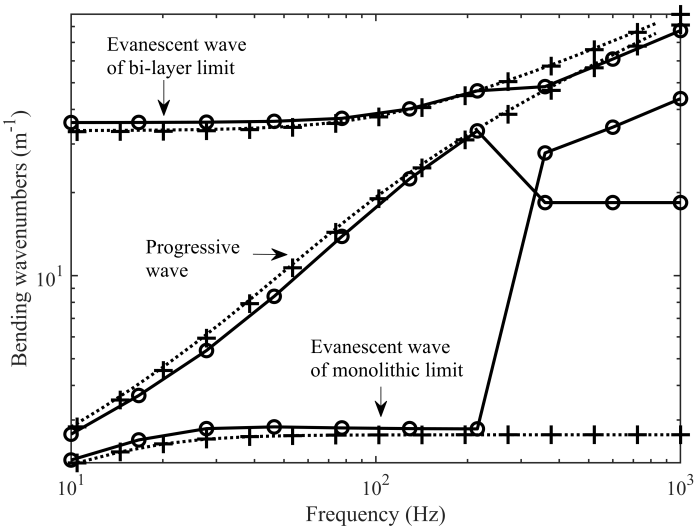

Fig. 3.15. Bending wavenumbers of sandwich panel with highly damped core. − ∘ − Bending wavenumbers from AHM, + Bending wavenumbers from GLM, − Bending wavenumbers from WFE

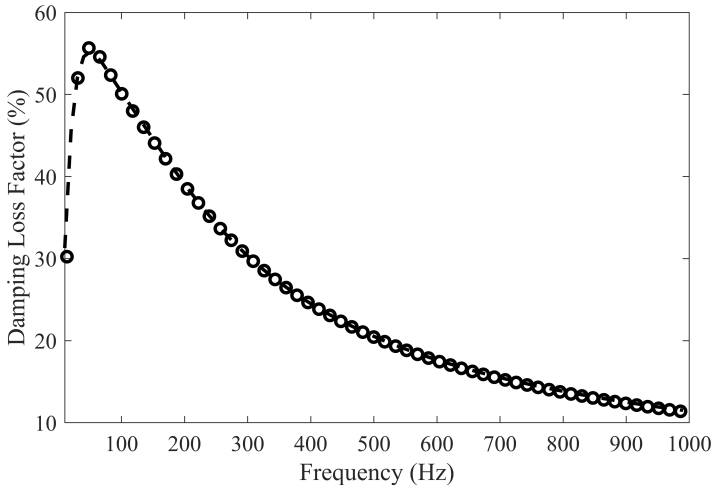

Fig. 3.16. Damping Loss Factor of Sandwich Panel with Highly Damped Core. ∘ DLF from WFE, −− GLM

in the bi-layer limit dynamic at high frequencies, the core exhibits non-uniform in-plane motion, thereby surpassing the validity domain of AHM for HCS.

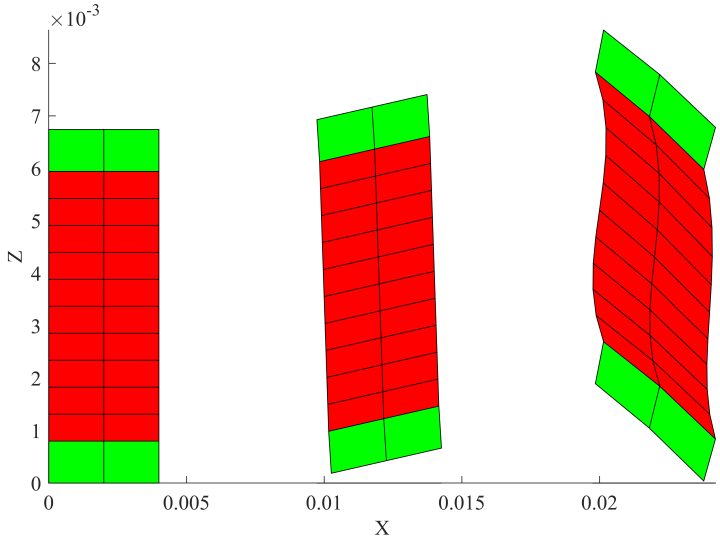

Fig. 3.17. Two limit dynamic of sandwich with thick dissipative core. Left: Original form. Middle: Monolithic limit dynamic at 100 Hz. Right: Bi-layer limit dynamic at 900 Hz.

Indeed, AHM assumes a small ratio of plate thickness to the characteristic length scale of the microstructure, and a series expansion of the field variables in a small parameter representing this ratio. This assumption is invalid for laminated structures with thick cores where the ratio falls beyond the validity domain of AHM, because the compressibility of the core causes non-uniform deformation and stress fields [12]. The high material damping ratio also affects the dynamic behavior and energy dissipation in the structure, which AHM cannot account for by the asymptotic expansion [12]. Therefore, AHM is unsuitable for sandwich structures with very thick cores.

3.5 Application to HCS with Non-homogeneous Cores

The WFE scheme can be applied for more complex structures in real-world scenarios, which is beyond the validity scope of GLM. A sandwich structure with non-homogeneous cores is analyzed by WFE, and the PIM based on FEM data is employed for assessment purposes [129].

3.5.1 Design of the Metastructures with Inclusions

The investigation focuses on a sandwich panel of dimensions $1.5m \times 1.2m$, featuring a 25.7 mm thick honeycomb core sandwiched between two 0.8 mm stiff skins, the material properties are listed in Tab. 3.8.

Fig. 3.18 illustrates the elastic strain energy density distribution across the panel for four pertinent natural modes. Traditional damping technology employs a layered approach, introducing an additional viscoelastic layer within the honeycomb core, exemplified by the SMP at 50 °C. However, this layered viscoelastic material configuration is suboptimal for vibration control due to the non-uniform elastic strain energy density distribution. This irregular distribution necessitates the incorporation of irregularly shaped viscoelastic components to effectively dissipate mechanical energy, thereby intelligently reducing the vibroacoustic response.

Inspired by the bending-shear coupling observed in the HCS, an equivalent mass of viscoelastic material is utilized in the form of Z-profile inclusions. These inclusions are designed as patches for easy

Tab. 3.8. Material Properties of Honeycomb.

Property	Honeycomb	Stiff skin
Density ρ	48 kg/m^3	1560 kg/m^3
Young's modulus	30MPa	210GPa
Poisson ratio	0.2	0.3
Damping ratio η	1%	1%

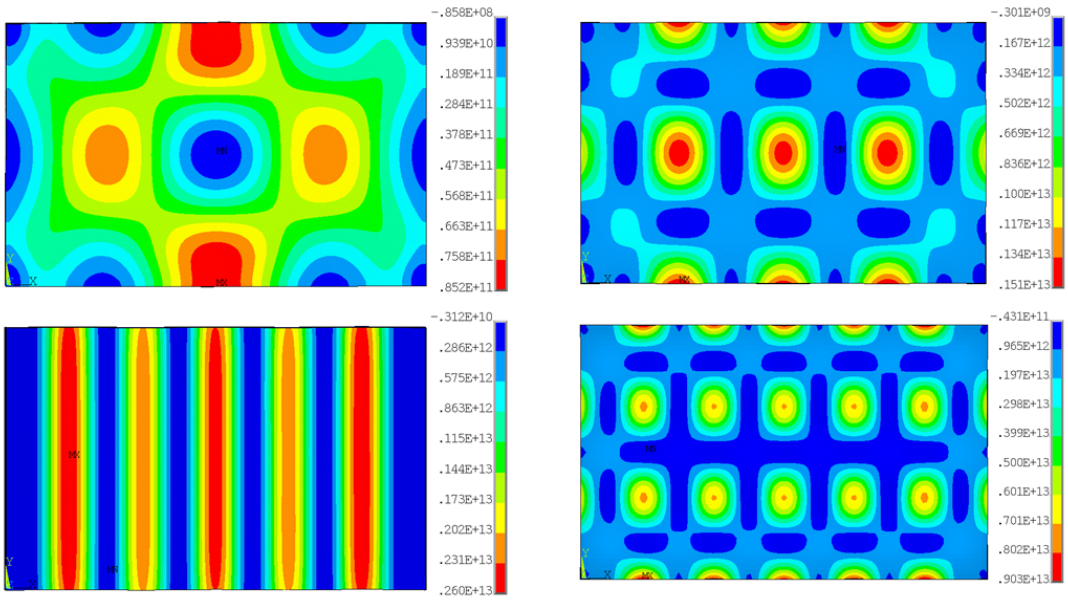

Fig. 3.18. Distribution of elastic strain energy density of the honeycomb sandwich plate. Top-left: 1244.2Hz. Top-right: 2778.3Hz. Bottom-left: 3652.8Hz. Bottom-right: 4839.7Hz.

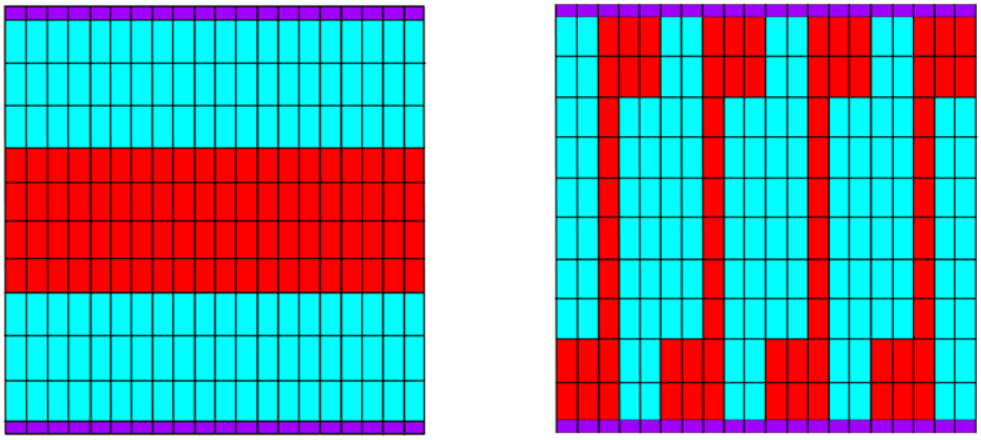

Fig. 3.19. Honeycomb sandwich structure with SMP50°C inclusions. Left: layered configuration. Right: Z patches

assembly into the metastructures, as depicted in Fig. 3.19. The patches are strategically placed in areas of highest strain energy. The implementation of Z-shaped patches enhances the bending-shear coupling effect inherent in HCS, leading to a significant increase in the structural DLF.

3.5.2 Enhanced Damping Loss Factor Estimation

A refined mesh is employed for the $2mm \times 5mm$ UC of the sandwich structure, as illustrated in Fig. 3.19. In the out-of-plane direction, each stiff layer is assigned one element with a thickness of 0.8mm, while the central layer comprises 10 elements. The in-plane directions are divided into 2 and 5 elements in the X and Y directions, respectively. Consequently, each skin contains 10 elements, and the core comprises a total of 100 elements. Of these, $9/25$ are allocated to SMP50°C. The rheological properties of the SMP50°C viscoelastic material are determined using Eq. 4.29.

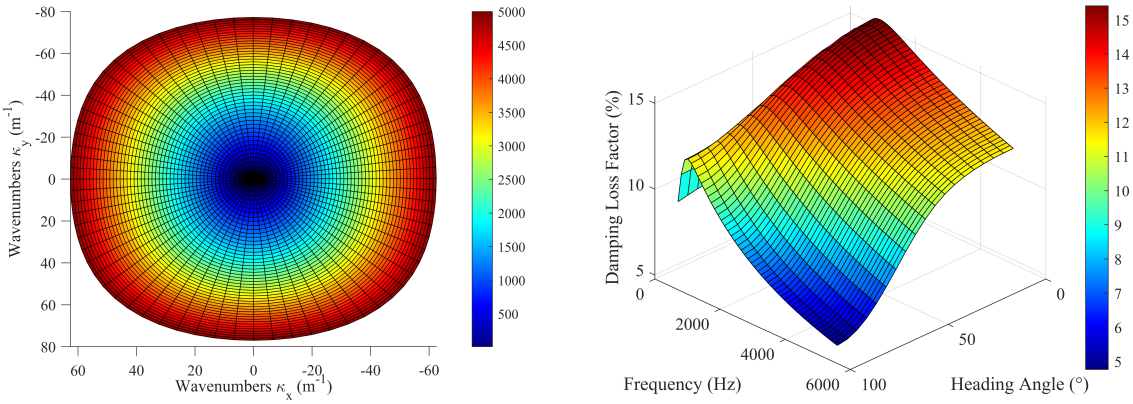

Fig. 3.20. Left: κ-space of the bending wave of the honeycomb sandwich with Z patches, the color bar represents the frequency range. Right: DLF in the heading angle from 0 to $\pi/2$, the color bar indicates the value.

Note that the sandwich structures with layer treatment and Z patches are compared at an equivalent mass, resulting in varying element thickness as shown in Fig. 3.19. These structures are designed by segmenting the viscoelastic layer into patches, which are then placed in areas of maximum deformation. For the layer treatment, $9/25$ of the core thickness is allocated to the SMP layer. Consequently, the surface density $\rho_s = 12.44498$ kg/m^2 is preserved in both the layer treatment and Z patches sandwich structures.

The average DLF is calculated using Eq. 2.66 with the bending wavenumbers depicted in Fig. 3.20. The concurrence of these results with those derived from the PIM-FEM approach validates the efficacy of the WFE approach in accurately computing energy transmission and motion dynamics.

In the low-frequency range, the high mode density necessitates an extremely dense mesh in traditional FEM to accurately capture these modes. However, such a fine mesh may exceed computational capabilities.

For the layered configuration, the DLF derived from WFE shows good agreement with GLM. It is observed that the average DLF of a honeycomb sandwich with Z patches exceeds that of the layer configuration, particularly in the frequency band of interest, suggesting an increased damping potential of the irregular inclusion design. The prevalence of bi-layer dynamics in the structure amplifies energy dissipation in the viscoelastic components.

3.6 Conclusions

This chapter has evaluated the robustness and accuracy of analytical AHM and GLM for sandwich structures in the scope of HCS and HDS. Some conclusions in the work are addressed as follow:

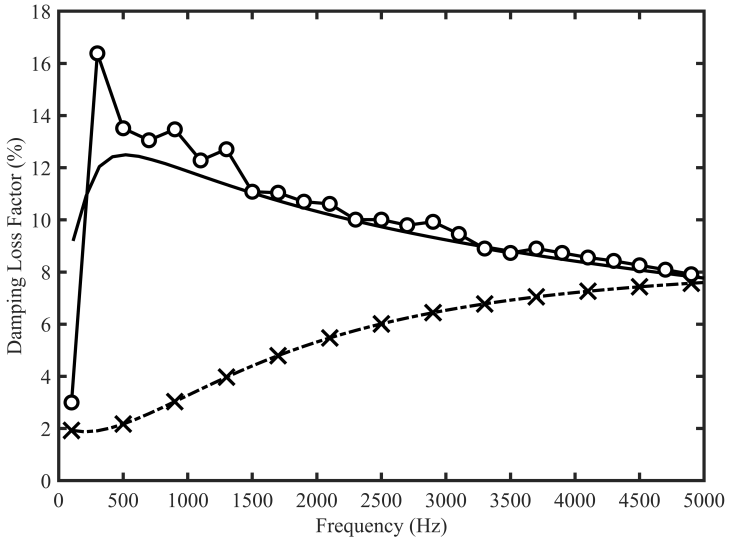

Fig. 3.21. Average DLF of honeycomb sandwich panel with Z patches. −− DLF of layered configuration from WFE. × DLF of layered configuration from GLM. − ∘ − DLF of Honeycomb Sandwich Panel with Z patches from PIM-FEM. − DLF of Honeycomb Sandwich Panel with Z patches from WFE.

- The two metrics used in the evaluation are κ-wave space and the DLF. The WFE scheme is exploited as the reference method for comparison. The results of AHM from diverse metastructures, including asymmetric sandwich plates, LG, and sandwich plates with SMP cores, are in line with GLM and WFE. The modeshapes derived from WFE validate the predictions of AHM, enhancing the visual understanding of HCS's multi-scale dynamics.

- The analytical AHM framework, with its capacity for rapid and precise wavenumber and DLF computation, is easily applicable in engineering due to its simplicity. However, sandwich structures with a thick, highly damped core fall outside the AHM's validity domain, AHM is limited by its assumption of uniform core layer deformation. The GLM, a potent tool based on the discrete laminate theoretical approach, also has limitations, particularly its inapplicability to sandwich structures with non-homogeneous components, a drawback inherent in this semi-analytical method.

- The WFE scheme addresses the NEP arising from varying propagation directions by the CI method. The WWAC technique accurately tracks wave solutions, providing stable results for the computation of wavenumbers and structural DLF in all directions. The angular modal density is utilized to compute the average DLF of non-isotropic structures.

- For sandwich structures with non-homogeneous cores, which fall outside the validity range of AHM and GLM, the average DLF from WFE is corroborated with the PIM-FEM approach. This confirms the accuracy of WFE for periodic metastructures across all propagation directions.

This chapter confirms the multi-scale dynamics of HCS, addressing the research questions. A robust CI method-based solver addresses the NEP from varying wave directions in the wave-based approach, with eigensolutions for specific waves identified through energy continuity criteria in frequency domain. The wavemode of bending wave illustrates the transition from monolithic to bi-layer dynamics as forecasted by the Asymptotic Homogenization Method (AHM). The DLF is determined through power balance, and its average is calculated using the modal density approach.

Chapter 4

Damping Prediction of Highly Dissipative Meta-structures through a Wave Finite Element Methodology

---

Abstract: Aiming at accurately predicting the global Damping Loss Factor (DLF) for Highly Dissipative Structures (HDS), the current study uses the Wave Finite Element (WFE) methodology. It starts by deriving the forced responses of a Unit Cell (UC) representative of the periodic meta-structure. Then it computes the DLF of the wave via the power balance. The Bloch expansion is employed. The response to a point force applied to the periodic structure is decomposed in the Brillouin zone, allowing the prediction via integration over the wavespace. The global DLF is derived based on the Power Input Method (PIM). The accuracy of the methodology is demonstrated through several cases from simple panels to complex meta-structures. For HDS, the results of the General Laminated Model (GLM) are exploited for wave DLF and PIM based on Finite Element Method (FEM) data is provided as a reference approach for global DLF. The study discusses the influence of bending waves on the damping loss factor estimation for HDS. A final case study with a meta-structure is also offered. The latter consists of a doubly periodic coated sphere in a host rubber, it demonstrates the importance of Bloch modes. Note that the content of this chapter has been published in the Mechanical Systems and Signal Processing [30].

Contents

4.1 Introduction

The main objective of the present work is to determine the global DLF by the balance between input power and dissipated energy using the WFE framework. Since wave DLF is no longer representative of HDS and periodic structures where wave coupling is important, the present paper provides a methodology for directly computing the global DLF through the forced response. Firstly, the forced response of a plane wave excitation is derived and the wave DLF is computed using the power balance. Secondly, using a Bloch wave expansion of a point force, the response, nodal displacements, input power and total mechanical energy to the force are achieved by integration over the Brillouin zone. The global DLF is subsequently derived using the PIM equation.

With regards to the aforementioned objectives and the state-of-the-art positioning, it appears the need for further investigation related to the DLF prediction. Specifically for highly dissipative and heterogeneous structures. The main claims of the paper can thus be summarised as follows:

- A computation methodology of DLF is implemented in the WFE scheme, including the wave DLF using the power balance principles, and the global DLF for HDS and heterogeneous structures are derived by Bloch wave expansion.

- The diminishing influence of bending wave contribution to the total response to a mechanical load of HDS is demonstrated by studying the difference between wave DLF and global DLF.

- The necessity of employing higher Bloch modes for the global DLF is studied by a periodic metastructure with large representative UC.

The structure of this paper is as follows: Section 4.2.1 outlines steps to calculate the response to a point load using Bloch wave expansion and the estimation of the global DLF via the power balance principle. Section 4.3 presents the validation of the proposed method against the analytical results, study cases involve simple isotropic aluminum plate and orthotropic timber plate vis-à-vis analytical results, highlighting the bending wave dominance in DLF. Section 4.4 presents various validation cases to corroborate the accuracy of the proposed methodology. First, the accuracy of the method for HDS, made up of a sandwich panel with a Shape Memory Polymer (SMP) at various temperatures, is highlighted using a full FE-based PIM calculation (PIM-FEM) as a reference for the global DLF and the analytical GLM model [29] as a reference for the wave DLF. Next, the necessity of integration with higher Bloch modes is demonstrated using a meta-structure with a large UC. Section 4.5 provides a discussion and conclusion of the results.

4.2 Extension of the Wave-based Finite Element Scheme

In this section, the Bloch expansion of a point force loaded onto the periodic structures in wave space is introduced, building upon the forced response to a plane wave excitation. Subsequently, the computation of the global response to a point force is undertaken through the integration of the forced response over all waves in the wave space. Ultimately, the determination of the global DLF for the periodic structure is achieved by employing the power balance principle within the UC.

4.2.1 Forced Response to a Plane Wave Excitation

Consider the special case of UC loaded by an imposed transverse plane wave with parameters (κ, θ). The nodal forces within $\mathbf{f}$ are all null except those that pertain to the transverse nodal displacement of the surface. By utilizing the transformation matrices $\hat{\mathbf{\Lambda}}_L$ in Eq. 3.16 and $\hat{\mathbf{\Lambda}}_R$ in Eq. 3.17, which are constructed based on a distinct wave vector κ propagating in the direction θ, Eq. 2.26 can be reformulated in the ensuing manner:

$$\left[\mathbf{\Lambda}_L(\kappa,\theta)\left(\mathbf{K}-\omega^2\mathbf{M}\right)\mathbf{\Lambda}_R(\kappa,\theta)\right]\mathbf{q}' = \mathbf{\Lambda}_L\mathbf{f} \tag{4.1}$$

The forced response of the wave under external forcing can be inverted:

$$q'(\kappa,\theta) = \left[\mathbf{\Lambda}_L(\kappa,\theta)\left(K-\omega^2 M\right)\mathbf{\Lambda}_R(\kappa,\theta)\right]^{-1}\mathbf{\Lambda}_L\mathbf{f} \tag{4.2}$$

Hence, the complete nodal response to the wave can be recovered from:

$$\mathbf{q} = \mathbf{\Lambda}_R\mathbf{q}' \tag{4.3}$$

The power input into the UC is determined by utilizing the velocities of all DOFs:

$$P_{input} = \frac{1}{2}Re\left\{\mathbf{f}^H\mathbf{q}\right\} = \frac{1}{2}Re\left\{i\omega\mathbf{f}^H\mathbf{q}\right\} \tag{4.4}$$

where superscript ^{H} signifies the Hermitian transpose (or complex conjugate), and $\mathbf{q}$ signifies the velocity of all the DOFs.

Assuming the steady-state equilibrium, the input power is completely dissipated within the UC, the power balance principle reads:

$$P_{input} = \omega\eta E_{mech} = \omega\eta\left(E_p + E_k\right) \tag{4.5}$$

where E_{mech} is the mechanical energy, while the kinetic and strain energy read:

$$\begin{aligned} E_p &= \tfrac{1}{4}Re\left((i\omega\mathbf{q})^H\mathbf{M}(i\omega\mathbf{q})\right) \\ E_k &= \tfrac{1}{4}Re\left(\mathbf{q}^H\mathbf{K}\mathbf{q}\right) \end{aligned} \tag{4.6}$$

Consequently, the DLF associated to wave (κ, θ) can be computed by employing the corresponding forced response to the wave:

$$\eta(\omega,\kappa,\theta) = \frac{P_{input}}{\omega E_{mech}} = \frac{\frac{1}{2}Re\left\{i\omega\mathbf{f}^H\mathbf{q}\right\}}{\omega\left(\frac{1}{4}\mathbf{q}^H\mathbf{K}_R(\omega)\,\mathbf{q} + \frac{\omega^2}{4}\mathbf{q}^H\mathbf{M}\mathbf{q}\right)} \tag{4.7}$$

where $\mathbf{K}_R(\omega)$ signifies the real part of the stiffness matrix at angular frequency ω.

The calculation of the forced response for a particular wave and the corresponding wave DLF constitutes the principal focus of this section.

4.2.2 Bloch Expansion of a Point Force

Consider a UC with dimensions L_x and L_y as illustrated in Fig. 3.2, and apply a force to a node (a DOF) on the structure as depicted in Fig. 4.1. The force function $f(x, y)$ can be expressed using the Fourier integral in the following manner:

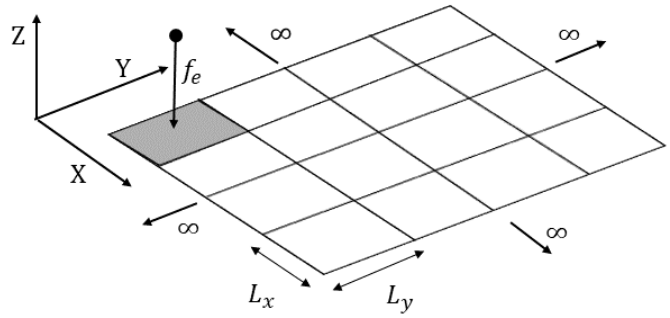

Fig. 4.1. Schematic showing a point force loaded on the periodic plate.

$$\begin{aligned} f(x,y) &= \tfrac{1}{4\pi^2}\int_{-\infty}^{\infty}\int_{-\infty}^{\infty}\widetilde{f}(\kappa_x,\kappa_y)\, e^{-i\left(\kappa_x x+\kappa_y y\right)}d\kappa_x d\kappa_y \\ \widetilde{f}(\kappa_x,\kappa_y) &= \int_{-\infty}^{\infty}\int_{-\infty}^{\infty} f(x,y)\, e^{i\left(\kappa_x x+\kappa_y y\right)}dxdy \end{aligned} \tag{4.8}$$

Due to the periodic nature of the function, the first integral in Eqs. 4.8 can be reformulated as a sum of double integrals:

$$f(x,y) = \frac{L_x L_y}{4\pi^2}\sum_{m=-\infty}^{m=+\infty}\sum_{n=-\infty}^{n=+\infty}\int_{\frac{(2m-1)\pi}{L_x}}^{\frac{(2m+1)\pi}{L_x}}\int_{\frac{(2n-1)\pi}{L_y}}^{\frac{(2n+1)\pi}{L_y}}\widetilde{f}(\kappa_x,\kappa_y)\, e^{-i\left(\kappa_x x+\kappa_y y\right)}d\kappa_x d\kappa_y \tag{4.9}$$

This equation can be simplified using a variable change of wavenumbers:

$$f(x,y) = \frac{L_x L_y}{4\pi^2}\sum_{m=-\infty}^{m=+\infty}\sum_{n=-\infty}^{n=+\infty}\int_{-\frac{\pi}{L_x}}^{\frac{\pi}{L_x}}\int_{-\frac{\pi}{L_y}}^{\frac{\pi}{L_y}}\widetilde{f}(\alpha_m,\alpha_n)\, e^{-i(\alpha_m x+\alpha_n y)}d\kappa_x d\kappa_y \tag{4.10}$$

with

$$\begin{aligned} \alpha_m &= \kappa_x + \frac{2\pi m}{L_x} \\ \alpha_n &= \kappa_y + \frac{2\pi n}{L_y} \end{aligned} \tag{4.11}$$

Eq. 4.10 represents the decomposition of the force function $f(x,y)$ into the excitation of plane waves with wave vectors $\vec{\kappa}+\vec{\kappa}_{mn} = \begin{Bmatrix}\alpha_m\\ \alpha_n\end{Bmatrix}$ and amplitude $\widetilde{f}(\alpha_m,\alpha_n)$. In this context, we use the notations $\vec{\kappa} = \begin{Bmatrix}\kappa_x\\ \kappa_y\end{Bmatrix}$ and $\vec{\kappa}_{mn} = \begin{Bmatrix}\kappa_m\\ \kappa_n\end{Bmatrix} = \begin{Bmatrix}2\pi m/L_x\\ 2\pi n/L_y\end{Bmatrix}$.

Let $\vec{\mathbf{x}}_e = \begin{Bmatrix}x_e\\ y_e\end{Bmatrix}$ denotes the locations (nodes where the force is applied) within the UC, and let $\vec{\mathbf{s}}_{pq} = \begin{Bmatrix}pL_x\\ qL_y\end{Bmatrix}$ represents the translation vector to the same locations within the $(p,q)^{th}$ adjacent cell. Equation4.10 leads to:

$$f\left(\vec{\mathbf{x}}_e+\vec{\mathbf{s}}_{pq}\right) = \frac{L_x L_y}{(2\pi)^2}\sum_{m=-\infty}^{m=+\infty}\sum_{n=-\infty}^{n=+\infty}\int_{\frac{-\pi}{L_x}}^{\frac{\pi}{L_x}}\int_{\frac{-\pi}{L_y}}^{\frac{\pi}{L_y}}\hat{f}\left(\vec{\mathbf{x}}_e,\vec{\mathbf{k}}+\vec{\mathbf{k}}_{mn}\right)e^{-i\left(\vec{\mathbf{k}}+\vec{\mathbf{k}}_{mn}\right)\cdot\vec{\mathbf{s}}_{pq}}d\kappa_x d\kappa_y \tag{4.12}$$

and

$$\hat{f}\left(\vec{\mathbf{x}}_e\,,\vec{\mathbf{k}}+\vec{\mathbf{k}}_{mn}\right) = \widetilde{f}\left(\vec{\mathbf{k}}+\vec{\mathbf{k}}_{mn}\right)e^{-i\left(\vec{\mathbf{k}}+\vec{\mathbf{k}}_{mn}\right)\cdot\vec{\mathbf{x}}_e} \tag{4.13}$$

4.2.3 Total Response to a Point Force

Denoting by $\hat{q}\left(\vec{\mathbf{x}}, \vec{\kappa} + \vec{\kappa}_{mn}\right)$ the response to the excitation of plane wave $\vec{\kappa} + \vec{\kappa}_{mn}$, the total response at position $\vec{\mathbf{x}}$ can be expressed as a double integration in the wave space:

$$q\left(\vec{\mathbf{x}}\right) = \frac{L_x L_y}{4\pi^2} \sum_{m=-\infty}^{m=+\infty} \sum_{n=-\infty}^{n=+\infty} \int_{-\pi/L_x}^{\pi/L_x} \int_{-\pi/L_y}^{\pi/L_y} \hat{q}\left(\vec{\mathbf{x}}, \vec{\kappa} + \vec{\kappa}_{mn}\right) d\kappa_x d\kappa_y \tag{4.14}$$

The forced response of the $(m,n)^{th}$ Bloch wave can be determined by applying the transformation matrices introduced in Eqs. 3.16 and 3.17:

$$\left[\mathbf{\Lambda}_L\left(\alpha_m, \alpha_n\right) \mathbf{D}\left(\omega\right) \mathbf{\Lambda}_R\left(\alpha_m, \alpha_n\right)\right] \hat{\mathbf{q}}'_{mn} = \mathbf{\Lambda}_L\left(\alpha_m, \alpha_n\right) \mathbf{e}_{mn} \tag{4.15}$$

The complete set of displacements in response to the excitation of the plane wave (α_m, α_n) can be expressed by Eq. 4.3. Therefore, representing the response $\hat{\mathbf{q}}$ to the plane wave excitation, the total response in the $(p,q)^{th}$ adjacent UC can be expressed using the translation vector:

$$\mathbf{q}\left(\vec{\mathbf{x}} + \vec{\mathbf{s}}_{pq}\right) = \frac{L_x L_y}{(2\pi)^2} \sum_{m=-\infty}^{m=+\infty} \sum_{n=-\infty}^{n=+\infty} \int_{\frac{-\pi}{L_x}}^{\frac{\pi}{L_x}} \int_{\frac{-\pi}{L_y}}^{\frac{\pi}{L_y}} \hat{\mathbf{q}} e^{-i\left(\vec{\mathbf{k}} + \vec{\mathbf{k}}_{mn}\right) \cdot \vec{\mathbf{s}}_{pq}} d\kappa_x d\kappa_y \tag{4.16}$$

If the response is evaluated within a small UC, the expansion can be truncated to the $m = n = 0$ term, resulting in a simplified nodal response vector:

$$\mathbf{q}\left(\vec{\mathbf{x}} + \vec{\mathbf{s}}_{pq}\right) = \frac{L_x L_y}{(2\pi)^2} \int_{\frac{-\pi}{L_x}}^{\frac{\pi}{L_x}} \int_{\frac{-\pi}{L_y}}^{\frac{\pi}{L_y}} \hat{\mathbf{q}}\left(\vec{\mathbf{k}}\right) e^{-i\vec{\mathbf{k}} \cdot \vec{\mathbf{s}}_{pq}} d\kappa_x d\kappa_y \tag{4.17}$$

It's worth noting that performing the double integral becomes more manageable in polar coordinates, considering the wavevectors in terms of their propagating directions.

4.2.4 Global DLF based on the Power Input Method

The PIM is a direct derivation from the Statistical Energy Analysis using the power balance equation. The DLF is obtained from the quantification of the power injected to the structure [204]:

$$P_{input} = \frac{1}{2} \left|F_0\right|^2 Re\left(\frac{v_0}{F_0}\right) \tag{4.18}$$

The global DLF is computed analogously to the power balance principle of Eq. 4.5. The input power of the UC is given by:

$$P_{input} = \frac{L_x L_y}{2\pi^2} \int_0^{\pi} \int_0^{\kappa(\theta)} \frac{\omega}{2} Im\left\{\mathbf{q}^H \mathbf{f}\right\} \kappa d\kappa d\theta \tag{4.19}$$

The mechanical energy of the UC is computed as the sum of both kinetic and potential energies:

$$E_{total} = \frac{L_x L_y}{2\pi^2} \int_0^{\pi} \int_0^{\kappa(\theta)} \varepsilon\left(\kappa, \theta\right) \kappa d\kappa d\theta \tag{4.20}$$

with

$$\varepsilon\left(\kappa, \theta\right) = \frac{1}{4} Re\left\{\mathbf{q}^H \mathbf{K} \mathbf{q} + \omega^2 \mathbf{q}^H \mathbf{M} \mathbf{q}\right\} \tag{4.21}$$

Eq. 4.19 presents the key expression for determining the global DLF of a periodic structure within the WFE scheme.

4.3 Validation with Analytical Results

This section demonstrates the accuracy of the proposed technique using several numerical examples of varying complexity: an isotropic aluminum plate and an orthotropic timber plate. The analytical derivation of input and transfer mobilities relies on the Kirchhoff-Love Thin Plate theory due to its simplicity.

4.3.1 Analytical Derivation of Mobilities

Input and transfer mobilities of a forced response are characterized as the ratio of velocity to the applied force. Input mobility pertains to the results at the driving point where the force is exerted, while transfer mobility refers to the results obtained elsewhere. As a widely utilized vibroacoustic indicator, it relies solely on directly measured data, facilitating comparison with computational results.

Given that the analytical GLM is unable to compute spatial transfer mobility, we now consider the bending response of an orthotropic plate based on classical theories. The input mobility of an infinite orthotropic plate is as follows:

$$H = \frac{\dot{q}(\vec{x}_e = \vec{0})}{F} = \frac{2K(\beta)}{8\pi} \frac{1}{\sqrt[4]{\rho_s^2 D_x D_y}} \tag{4.22}$$

where bending stiffness is defined as:

$$\begin{aligned} D_x &= \frac{E_{xy} L_z^3}{12(1-\nu_{xy}\nu_{yz})} \\ D_y &= \frac{E_{yz} L_z^3}{12(1-\nu_{xy}\nu_{yz})} \end{aligned} \tag{4.23}$$

with E_{xy} and E_{yz} are the Young's moduli, and $K(\beta)$ is the complete elliptic integral of the first kind, a value between $\pi/2$ to 1.85 should be assigned [31].

To derive the transfer mobility of an infinite orthotropic plate, we begin with the Equation of Motion for the forced response of an orthotropic plate:

$$D_{11}\frac{\partial^4 q}{\partial x^4} + 2(D_{12} + 2D_{66})\frac{\partial^4 q}{\partial x^2 \partial y^2} + D_{22}\frac{\partial^4 q}{\partial y^4} - \rho L z \omega^2 q = F(x,y)e^{-i\omega^2 t} \tag{4.24}$$

where the orthotropic material properties are: $D_{11} = \frac{E_1 L_z^3}{12(1-\nu_1\nu_2)}$, $D_{22} = \frac{E_2 L_z^3}{12(1-\nu_1\nu_2)}$, $D_{12} = \nu_2 D_{11} = \nu_1 D_{22}$ and $D_{66} = \frac{G L_z^3}{12}$.

The approximation of particular solution $q_F(x,y)$ for an infinite orthotropic plate in spherical coordinates is [205]:

$$q_F(x,y) \approx \frac{iF_0}{2\pi} \int_{\theta-\frac{\pi}{2}}^{\theta+\frac{\pi}{2}} \frac{exp(i\kappa_f(\alpha) r cos(\alpha-\theta))}{4\kappa_f^2 G(\alpha)} d\alpha \tag{4.25}$$

with a transformation of Cartesian coordinates into spherical coordinates:

$$\begin{aligned} x &= r cos\theta \\ y &= r sin\theta \end{aligned} \tag{4.26}$$

and the flexural wave number is defined as:

$$\kappa_f(\alpha) = (\frac{\omega^2 \rho L_z}{G(\alpha)})^{\frac{1}{4}} \tag{4.27}$$

where

$$G(\alpha) = D_{11}cos^4(\alpha) + 2(D_{11} + 2D_{66})cos^2(^2(\alpha) +_{D\ 22} sin^4(\alpha) \tag{4.28}$$

The formulations derived for the orthotropic plate can be readily simplified to the solution for the isotropic plate by employing identical directional material properties.

4.3.2 Forced Response of an Aluminum Plate

The investigation commences with the analysis of a 1mm thin aluminum plate characterized by the following material properties: with a density of $\rho = 2700\,\text{kg/m}^3$, Young's modulus of $E = 71 \times 10^9$ Pa, Poisson's ratio of $\nu = 0.33$, and a material damping ratio of $\eta = 1\%$. The objective is to validate the predictions of the WFE scheme for forced response and DLF, and to confirm the predominance of bending waves in flexural motion for simple structures.

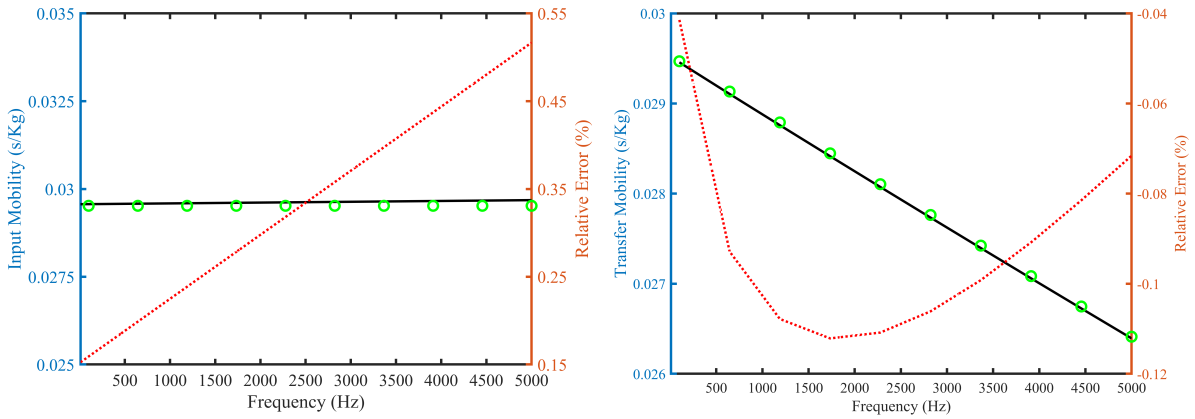

Fig. 4.2. Mobilities of Aluminum Plate. Left: Input Mobility, Right: Transfer Mobility. – WFE. *o* Analytical. ... Relative errors.

Since the system is homogeneous, a small UC is used and thus no Bloch modes are used for the simulation. The input mobility is obtained by WFE and compared with the analytical results, or simply using the Kirchhoff-Love Thin Plate Theory for isotropic cases, $H_0 = \frac{1}{8\sqrt{\rho_s D}}$ with the bending stiffness $D = \frac{EL_z^3}{12(1-\nu^2)}$. For the bending motion of an isotropic plate, the input mobility remains frequency-independent.

Subsequently, the transfer mobility is computed at the location (0.01,0.01) using Eq. 4.17. The results from WFE are compared with exhibit a close correspondence with the structural damping, as illustrated in Fig. 4.2. Overall, the relative error is negligible. For the transfer mobilities, errors at low frequencies are relatively high due to round-off errors of the inertia terms [206]. As the frequency increases, these errors decrease and then start increasing as FE discretization errors increase.

The DLF obtained by the forced response to the bending wave using Eq. 4.7 in Section 4.2.1 is presented in Fig. 4.3. Notably, it exhibits a remarkable alignment with the predefined structural damping of 1%, with the relative errors being negligibly small. The forced response resulting from a point force in the transverse direction is computed using Eq. 4.17. The out-of-plane response is plotted against the wave space in Fig. 4.4. Both GLM and WFE schemes are used to calculate the natural wavenumber associated with the propagating bending wave to identify the most significant contributor to the forced response.

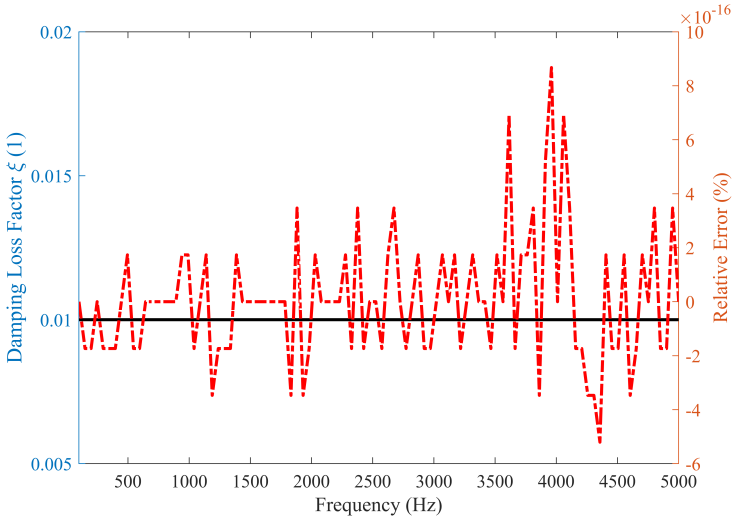

Fig. 4.3. Global DLF of 1 mm Aluminum Plate. Left axis: − DLF of WFE from bending wave. Right axis: −− Relative error.

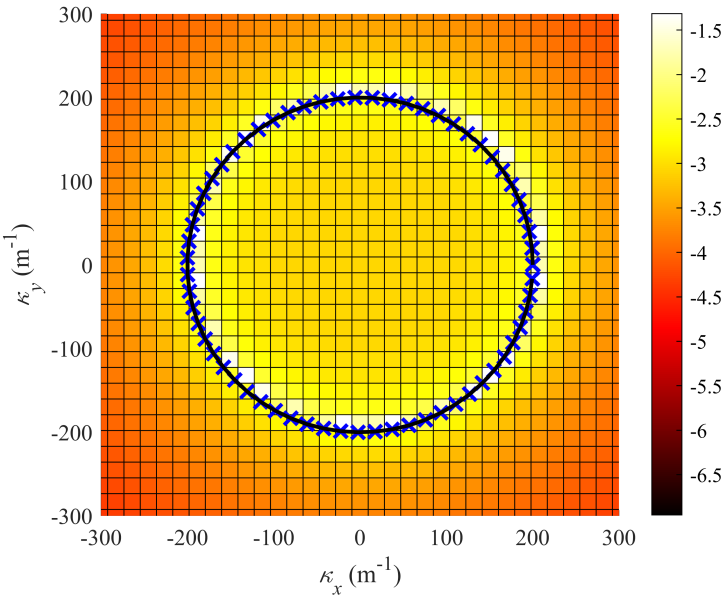

Fig. 4.4. Forced Response (flexural displacement in logarithm base 10) of Isotropic Aluminum Plate to a point force as a function of wavenumbers at 5000 Hz. − $Re\,(\kappa)$ for the bending wavenumbers predicted by GLM. × $Re\,(\kappa)$ for the bending wavenumbers predicted by WFE.

Tab. 4.1. Material Properties of Timber.

Property	Timber
Density	450 kg/m^3
$\{E_x, E_y, E_z\}$	$\{11000, 367, 367\} \times 10^6$ Pa
$\{\nu_{xy}, \nu_{xz}, \nu_{yz}\}$	$\{0.4196, 0.4196, 0.03\}$
$\{G_{xy}, G_{xz}, G_{yz}\}$	$\{690, 690, 69\}$ MPa

Analyzing Eq. 4.17, it becomes evident that the forced response remains relatively insignificant, except when the forcing wavenumber α_m closely approximates the medium's bending wavenumber κ_x. The circular pattern formed by the free wavenumber results from the inherent isotropic characteristics of the structure. By discretizing the integration contour selectively, the efficiency of calculating the forced response using Eq. 4.17 can be enhanced, as the contribution to the response becomes negligible in the higher wavenumber region.

4.3.3 Forced Response of a Timber Plate

The timber panel is employed as an example to verify the proposed WFE scheme for calculating the forced response of a non-isotropic structure since it stands for the most useful and important material for construction, especially in North America.

To verify the proposed methodology for calculating the forced response of a non-isotropic structure, a simple 1 mm thick timber panel is examined. The material properties of timber are shown in Tab. 4.1.

Fig. 4.5. Timber panel as the most useful and important construction material.

Despite the non-homogeneity of the structure, a small UC is utilized, thereby eliminating the need for Bloch modes in the computation. As depicted in Fig. 4.6, the input mobility is derived using the WFE method and compared with analytical results, demonstrating that the input mobility of the orthotropic structure is frequency-independent. The WFE results align well with the analytical findings. The transfer mobility is also calculated at the same location using Eq. 4.17. The WFE results closely match the analytical ones, with negligible errors across the entire frequency range.

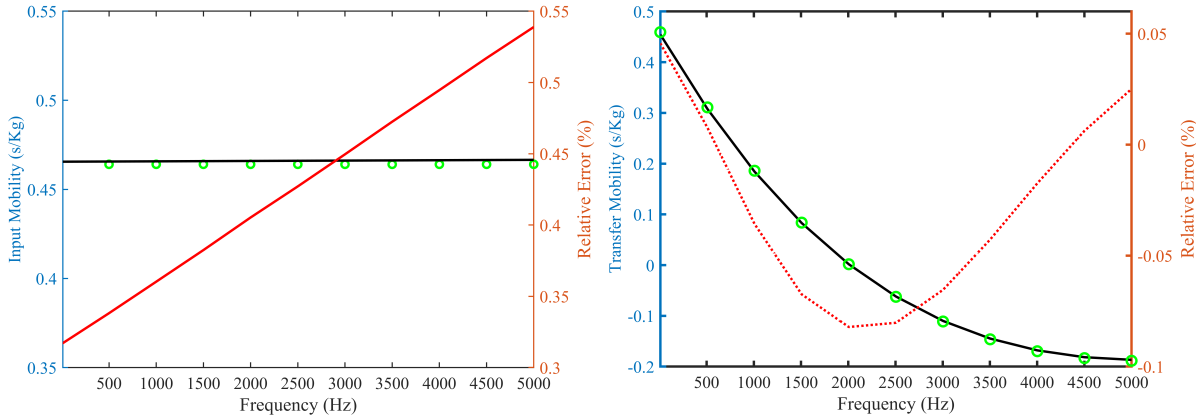

Fig. 4.6. Mobilities of Timber Plate. Left: Input Mobility, Right: Transfer Mobility. – WFE. *o* Analytical. ... Relative errors.

The DLF derived from the forced response is depicted in Fig. 4.7. It is noteworthy that it aligns remarkably well with the predefined material damping ratio of 2%, with the relative errors being insignificantly

small.

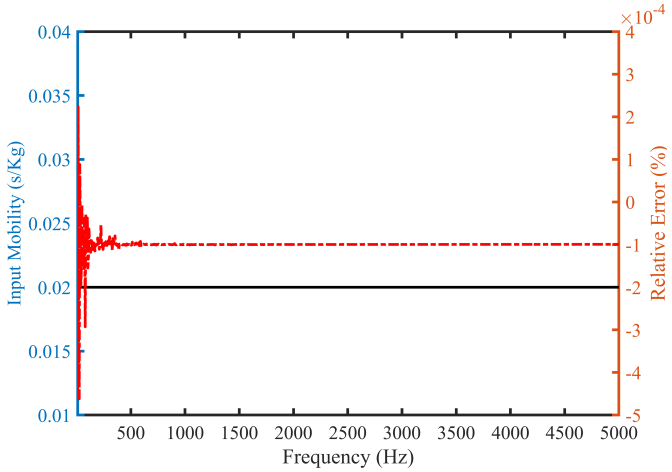

Fig. 4.7. Global DLF of 1 mm Aluminum Plate. Left axis: − DLF of WFE from bending wave. Right axis: −. Relative error.

The forced response, resulting from a point force applied in the transverse direction, is calculated using Eq. 4.17. The out-of-plane response is graphed against the wave space in Fig. 4.8. Both the GLM and WFE schemes are employed to compute the natural wavenumber linked to the propagating bending wave, thereby identifying the primary contributor to the forced response. Upon analyzing Eq. 4.17, it is clear that the forced response is relatively minor, except when the forcing wavenumber α_m closely matches the bending wavenumber κ_x of the medium. The circular pattern formed by the free wavenumber results from the inherent isotropic characteristics of the structure.

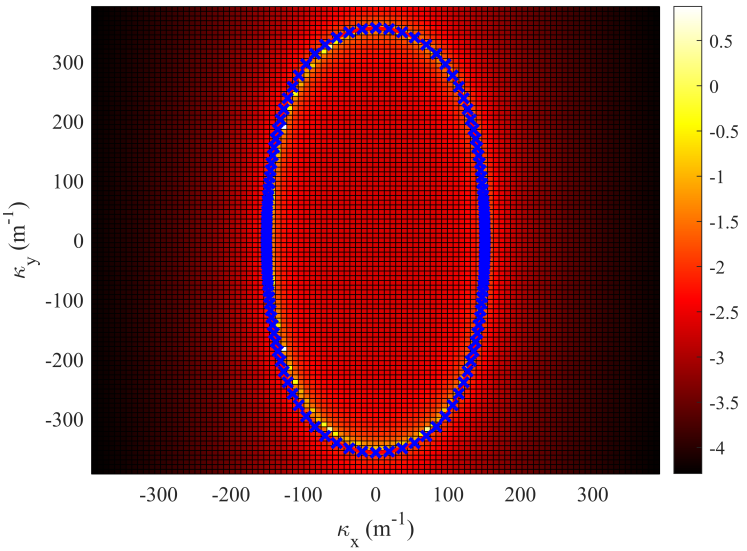

Fig. 4.8. Forced Response (flexural displacement in logarithm base 10) of Orthotropic Timber Plate to a point force as a function of wavenumbers at 5000 Hz. − $Re\,(\kappa)$ for the bending wavenumbers predicted by GLM. × $Re\,(\kappa)$ for the bending wavenumbers predicted by WFE.

4.4 Validation with Numerical Results

This section demonstrates the accuracy of the proposed technique using several numerical examples of varying complexity: a sandwich laminate with a Shape Memory Polymer core at different temperatures, and a doubly periodic coated sphere in a host rubber. For cases where analytical GLM results are not available, validation is conducted using the PIM-FEM approach [129].

Tab. 4.2. Material Properties.

	Density $[kg/m^3]$	Elastic modulus [Pa]	Poisson ratio	Damping ratio
tBA/PEGDMA	990	9.071E5	0.37	0.5
Silicon Rubber	1300	2E6	0.462	30%
Host rubber	1100	29.7E6	0.498	30%

The material properties used for the numerical validation are listed in Tab. 4.2.

4.4.1 Sandwich Structure with Shape Memory Polymer Core with Constant Damping

The first numerical example considers a HDS. It consists of a typical sandwich structure with a tBA/PEGDMA material (more commonly referred to as Shape Memory Polymer, SMP) core. The configuration consists of 0.5 mm aluminum skins, while the SMP core has a thickness of 2.2 mm with rheological Young's modulus and material damping ratio. The complex elastic modulus of SMP is governed by a relationship proposed and substantiated by Butaud [5], which writes as follows:

$$E\left(\omega, T_0\right) = E_0 + \frac{\left(E_\infty - E_0\right)}{\left(1 + \gamma\left(i\omega\tau\right)^{-k} + \left(i\omega\tau\right)^{-h_i} + \left(i\omega\beta\tau\right)^{-1}\right)} \tag{4.29}$$

where $E_0 = 0.67$ MPa, $E_\infty = 2211$ MPa, $k = 0.16$, $h_i = 0.79$, $\gamma = 1.68$, $\beta = 3.8 \times 10^4$, τ denotes the characteristic time estimated by the time-temperature superposition principle, $\tau(T) = a_T(T)\tau_0$ and $\tau_0 = 0.61$, $a_T(T)$ is the shift function given by [5]:

$$log\left(a_T\right) = -C_1 \frac{T - T_0}{C_2 + T - T_0} \tag{4.30}$$

where $C_1 = 10.87°C$, $C_2 = 32.57°C$, and the reference temperature $T_0 = 40°C$.

With Eq. 4.30, the rheological properties can be efficiently determined at any given angular frequency and temperature with

$$\mu(\omega, T) = \mu(\omega a_T, T_0) \tag{4.31}$$

The frequency-dependent complex elastic moduli are calculated using Eqs. 4.29 and 4.30, and is illustrated in Fig. 4.9. To accurately capture the attenuation characteristics of plane waves, it becomes imperative to subdivide the mesh to an extremely refined level due to the extremely high material damping ratio. The stiffness proportional materiawritesping ratio is applied in the FE analysis for the modeling of structural damping.

In order to evaluate the global DLF of HDS, the PIM based on the FEM results is employed to assess the accuracy of the proposed methodology based on the WFE scheme. According to the general derivation of PIM in Sec. 2.4.1.3, a more comprehensive derivation based on the FEM data is needed.

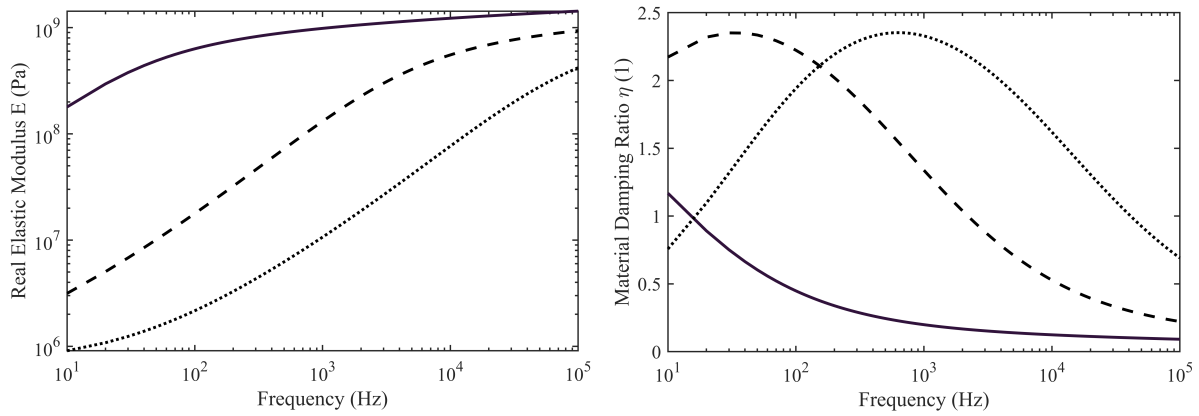

Fig. 4.9. Viscoelastic properties of tBA/PEGDMA. Left: Elastic modulus. − 50 °C. −− 65 °C. · · · 80 °C. Right: Material Damping Ratio. − 50 °C. −− 65 °C. · · · 80 °C.

The power input into a structure loaded with a point force at an arbitrary position write:

$$P_{input} = \frac{1}{2}|F_0|^2 \left(\frac{v_0}{F_0}\right) \tag{4.32}$$

where F_0 and v_0 denote the amplitudes of the exerted force and the velocity of the driving point, respectively, $\frac{v_0}{F_0}$ denotes the input mobility of the structure.

The mechanical energy of the structure can be calculated by assuming that the potential energy of the whole structure equals twice the kinetic energy in a steady state, the mechanical energy is thus:

$$E = M_{total}\langle v^2 \rangle = M_{total} \sum_{i=1}^{n} \frac{|v^2|}{2n} \tag{4.33}$$

where n is the total number of nodal velocity data from the FEM, $\langle . \rangle$ denotes the average velocity of all the nodes considered.

Given the relationship between input power and mechanical energy, an equation concluding the structural damping is derived:

$$P_{input} = \omega \eta E = \omega \eta M_{total} \langle v^2 \rangle \tag{4.34}$$

The DLF should be evaluated for multiple excitation locations using Eq. 4.32 to meet the SEA requirement of modal independence, the above procedures are repeated 5 times to get the equivalent DLF.

$$P_{input} = \frac{1}{2}|F_0|^2 \left(\frac{v_0}{F_0}\right) \tag{4.35}$$

In the WFE scheme, a representative UC with dimensions of 1 mm sidelengths is employed. This UC is composed of C3D8 elements created using an in-house FE package. The in-plane directions are discretized into a 2 by 2 grid of elements, while the out-of-plane direction is divided into 1 element for the skins and 4 elements for the core, resulting in a total of 24 elements within the UC.

On the other hand, the PIM, implemented through conventional FEM data, employs a rectangular panel with dimensions of $0.7m \times 0.5m$, the discretization involves 25688 TET10 solid elements. Notably, this high level of mesh density is essential to meet the precision demands of computational analysis for SMP with extremely high damping ratios.

The sandwich plate with a SMP core is first set with a constant material damping listed in Tab. 4.2, and

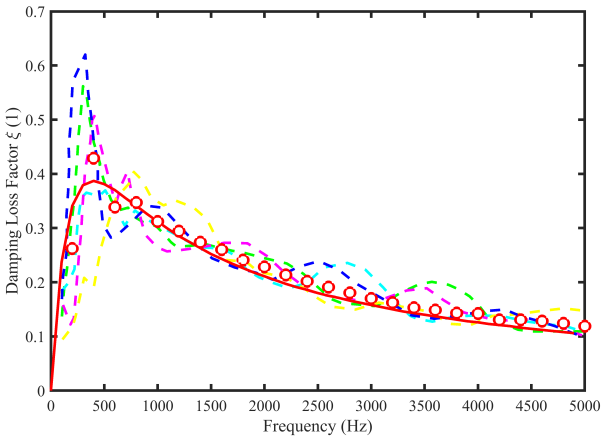

Fig. 4.10. Damping Loss Factor of sandwich structure with a Shape Memory Polymer Core with Constant Damping. ∘ Average DLF from PIM-FEM. – DLF from WFE: Power balance via forced response. −− DLF from PIM-FEM: Position 1. −− DLF from PIM-FEM: Position 2. −− DLF from PIM-FEM: Position 3. −− DLF from PIM-FEM: Position 4. −− DLF from PIM-FEM: Position 5.

the DLF results are depicted in Fig. 4.10. The average DLF from the PIM-FEM approach aligns well with the global DLF computed by the WFE scheme, despite a noticeable discrepancy at low frequency, this results from the low modal density in FE analysis at this frequency range, which violates the requirement of SEA's accuracy in the high modal density.

The FE settings in WFE and PIM-FEM approaches will be kept the same for the sandwich structure with the SMP core.

4.4.2 Sandwich Structure with Shape Memory Polymer Core at 50 °C

To show the results, consider first a temperature leading to a moderate damping (see Fig. 4.9). Fig. 4.11 illustrates a comparison encompassing the real part of wavenumbers and DLF of the bending wave, and the global DLF at 50°C. Remarkably, the real part of the bending wavenumbers obtained through the WFE scheme agrees well with the results from GLM [29]. The DLF of the bending wave from the WFE approach using an eigenvalue analysis aligns well with analytical solutions derived from GLM. This agreement underscores the reliability and accuracy of the proposed WFE scheme in capturing the intricate dynamics of the SMP50°C sandwich plate.

The global DLF computed by the wave synthesis using a forced analysis aligns with numerical results from the PIM-FEM method, validating the WFE's effectiveness in computing energy transport. This agreement, particularly across most frequency ranges, underscores the bending wave's pivotal role in governing energy transport in the SMP50°C sandwich plate. As demonstrated in Fig. 4.12, the bending wave primarily influences flexural displacement, while other waves have negligible contributions. It's important to mention that the actual Brillouin zone encompasses a significantly larger area than what is depicted in Fig. 4.12, the scale of the depicted region has been adjusted to enhance clarity.

4.4.3 Sandwich Structure with Shape Memory Polymer Core at 65 °C

Next, we consider a more damped configuration. Fig. 4.13 displays the bending wavenumbers and DLF for the SMP core sandwich at 65 °C. The bending wavenumbers exhibit excellent agreement with analytical GLM, further substantiating the accuracy and reliability of the analyses. The wave DLF and global DLF from the WFE approach are depicted alongside those from the GLM and PIM-FEM

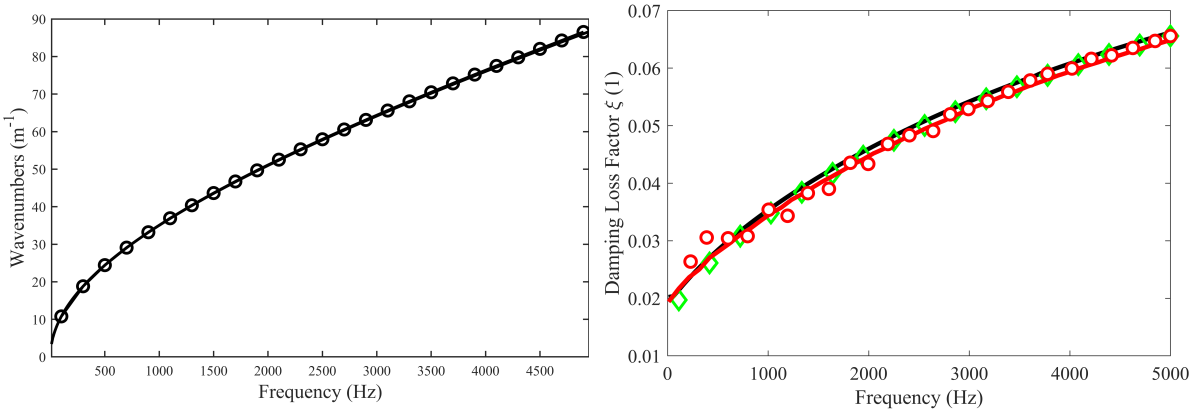

Fig. 4.11. Results for the SMP core Sandwich at 50 °C. Left: Bending wavenumbers. − WFE. ∘ GLM. Right: Damping Loss Factor. − DLF from WFE: Bending wave. ◇ DLF from GLM: Bending wave. ∘ DLF from PIM-FEM. − DLF from WFE: Power balance via forced response.

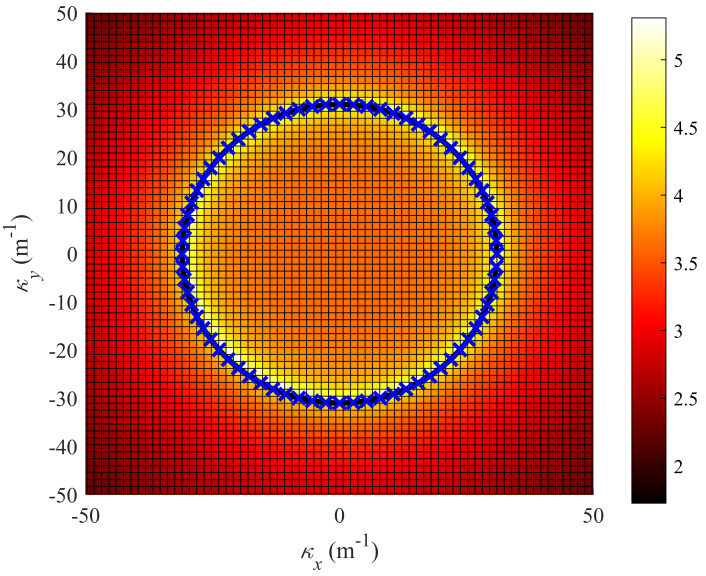

Fig. 4.12. Response (flexural displacement in logarithm base 10) of the SMP Sandwich at 50°C to a point force as a function of wavenumbers at 800 Hz. −: $Re\,(\kappa)$ of the bending wavenumbers predicted by GLM. ×: $Re\,(\kappa)$ of the bending wavenumbers predicted by WFE.

approaches.

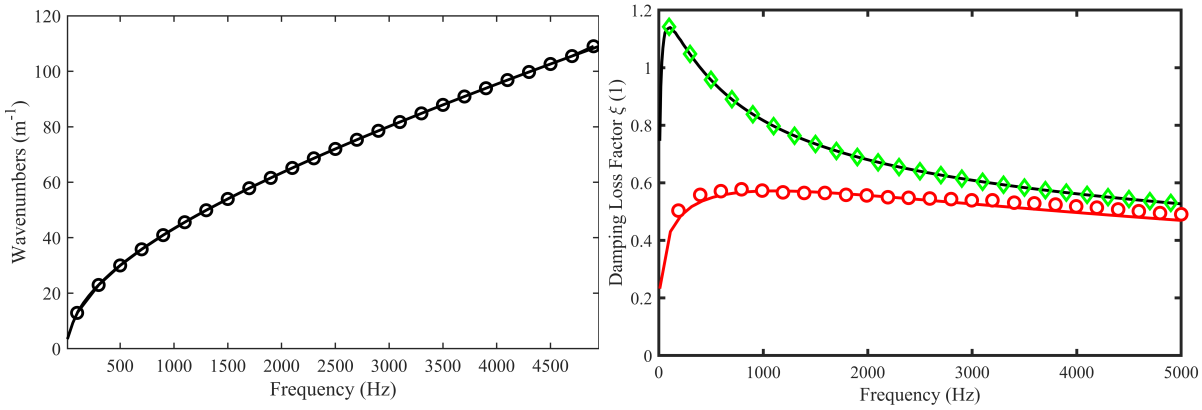

Fig. 4.13. Results for the SMP core Sandwich at 65 ^{o}C. Left: Bending wavenumbers. − WFE. ∘ GLM. Right: Damping Loss Factor. − DLF from WFE: Bending wave. ◇ DLF from GLM: Bending wave. ∘ DLF from PIM-FEM. − DLF from WFE: Power balance via forced response.

There are two sets of DLF, the wave DLF exceeds 1 within the frequency range of [20, 500] Hz, meaning that the power dissipated by the structural vibration is greater than the input energy, such a discrepancy violates the principle of energy conservation for the global structure. The other set is the global DLF calculated from the response to a point force, displaying excellent agreement with the reference PIM-FEM solution. Fig. 4.14 shows the contribution of waves to the forced response. Contrary to the low-damped configuration (SMP at 50°C), here the importance of adding waves beyond the bending wave is demonstrated.

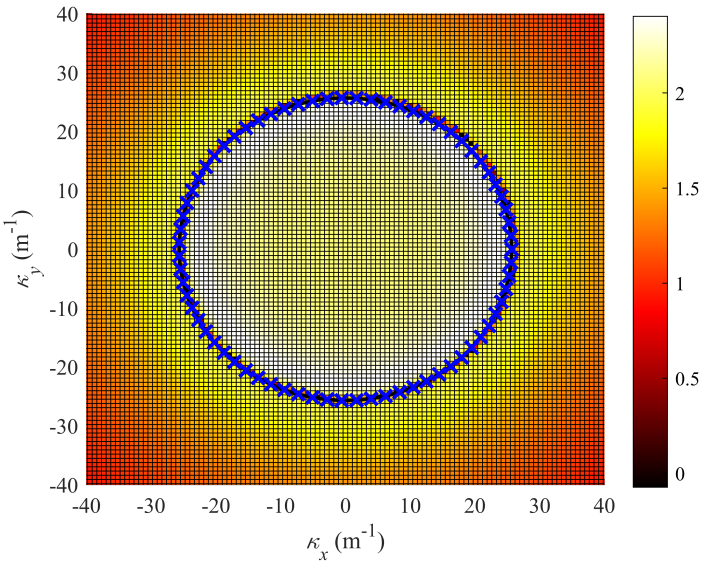

Fig. 4.14. Response (flexural displacement in logarithm base 10) of the SMP Sandwich at 65 °C to a point force as a function of wavenumbers at 400 Hz. −: $Re\,(\kappa)$ of the bending wavenumbers predicted by GLM. ×: $Re\,(\kappa)$ of the bending wavenumbers predicted by WFE.

4.4.4 Sandwich Structure with Shape Memory Polymer Core at 80 °C

To corroborate further this remark, Fig. 4.15 presents the real part of the bending wavenumbers and DLF for the SMP80 sandwich plate at 80°C. This is an extremely damped configuration (see Fig. 4.9). Again, the real part of the bending waves, as shown in the graph, exhibits a substantial concurrence between the WFE results and GLM solutions. However, a forced response is necessary to correctly capture the global DLF of the structure (compared to the reference PIM-FEM solution). As demonstrated in Fig. 4.16, apart from the bending wave contributions of the other waves make an indelible contribution, refined integration over this wavenumber domain allows the global DLF to converge.

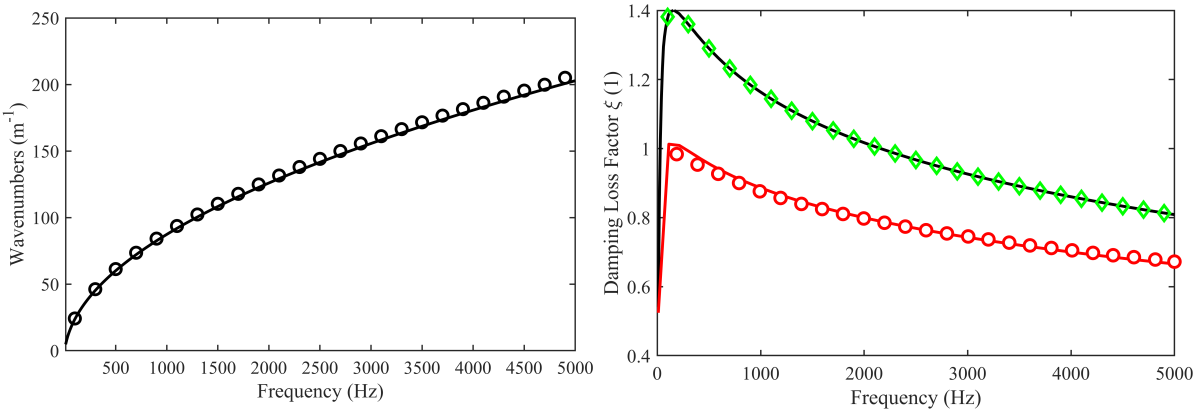

Fig. 4.15. Results for the SMP core Sandwich at 80 ^{o}C. Left: Bending wavenumbers. – WFE. ∘ GLM. Right: Damping Loss Factor at 80 ^{o}C. – DLF from WFE: Bending wave. ◇ DLF from GLM: Bending wave. ○ DLF from PIM-FEM. – DLF from WFE: Power balance via forced response.

In the WFE scheme, a noticeable transition in the dominance from bending waves to the full wavenumber space is observed as damping is increased (and stiffness of the core decreases). This transition suggests the increased involvement of various wave modes in influencing the dynamic response. Consequently, a comprehensive integration spanning the entire wavenumber field becomes essential to assess the global DLF for HDS. This phenomenon also reflects the advantage of the proposed method of neglecting the complex wave coupling behavior of HDS and directly providing the overall damping information.

4.4.5 Large Doubly Periodic Coated Sphere in a Host Rubber

The final example demonstrates the importance of Bloch modes for large unit cells. The scenario involves a doubly periodic coated sphere within a host rubber. The sphere's core is composed of aluminum alloy, while its coating consists of soft silicon rubber. The coating has an internal diameter of 10 mm and an external diameter of 15 mm, the host rubber is 19 mm thick. The material properties are listed in Tab. 4.2.

Half of the UC for the heterogeneous layer is depicted in Fig. 4.17, the UC is modeled with SOLID185 hexahedral elements, and a total of 3,968 elements are generated for effectively modeling the shear stress in the UC, thus guaranteeing an accurate computation of the global DLF. The global DLF is computed using the forced response to a point force loaded on the center of a surface.

Again, the reference PIM-FEM approach is used as the reference results to study the accuracy and convergence of the proposed methodology. The PIM-FEM employs a rectangular panel with 96×64 UC in the X and Y directions, respectively, the discretization involves a total of 24,379,392 SOLID185 elements in ANSYS 2023R2, such a large model guarantees the accuracy of the reference solution.

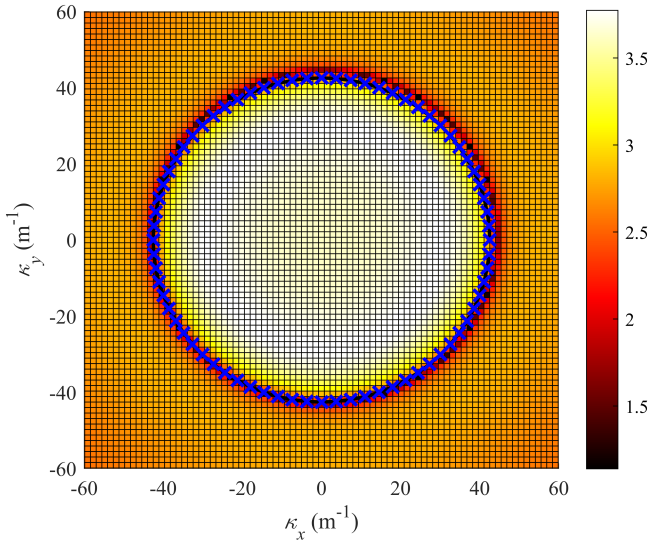

Fig. 4.16. Response (flexural displacement in logarithm base 10) of the SMP Sandwich at 80 $^{\circ}C$ to a point force as a function of wavenumbers at 800 Hz. $-$: $Re\,(\kappa)$ of the bending wavenumbers predicted by GLM. $\times$: $Re\,(\kappa)$ of the bending wavenumbers predicted by WFE.

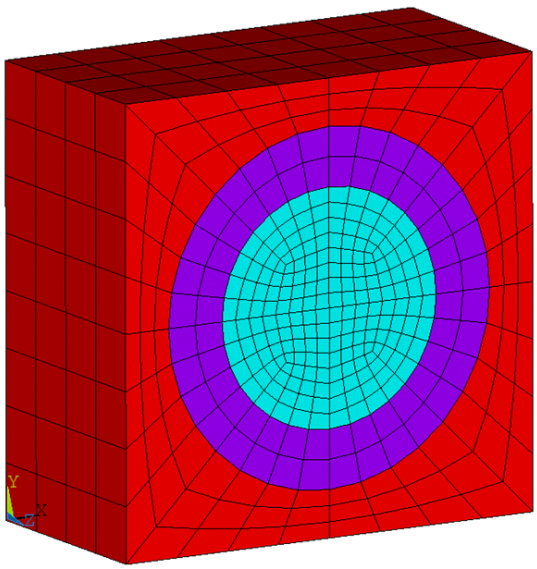

Fig. 4.17. Half UC of the doubly periodic coated sphere in a host rubber made of aluminum alloy (bleu), silicon rubber (purple), and host rubber (red).

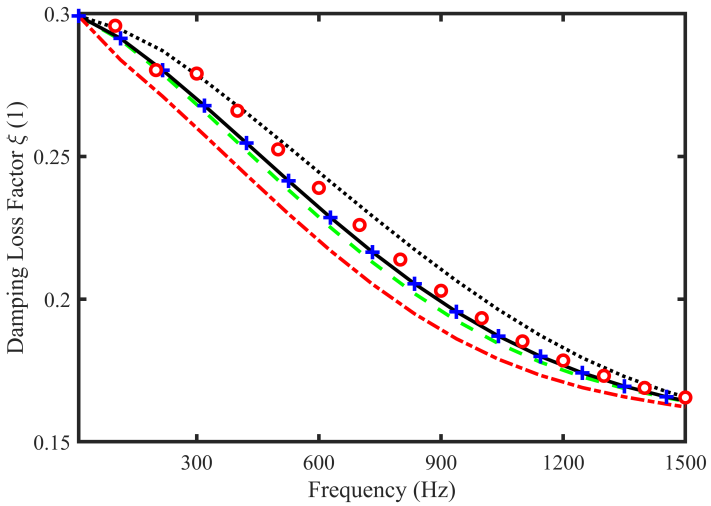

Fig. 4.18. The Damping Loss Factor of a rubber plate with spherical inclusions. · · ·: Bloch mode orders (0, 0). − · −: Bloch mode orders (1, 1). −−: Bloch mode orders (2, 2). −: Bloch mode orders (3, 3). +: Bloch mode orders (4, 4). ∘: DLF from PIM-FEM.

For complex non-homogeneous periodic structures, a large representative UC must be used to capture the geometry and its physics. In this case, the Brillouin zone is small and there are so many waves that are important for the structural dynamics, with wavenumbers beyond the Brillouin zone. One needs in consequence to add Bloch modes to capture these waves. Fig. 4.18 depicts the global DLF of the UC from Bloch mode orders ($m = 0$, $n = 0$) to Bloch mode orders ($m = 4$, $n = 4$). A satisfactory level of agreement between the global DLF computed by the WFE scheme and the PIM-FEM approach is observed between the two methods over the whole frequency range when the correct number of Bloch modes is added. Because of structural symmetry, the same order is needed for the two planar directions. The convergence of global DLF is attained when Bloch modes up to order (3,3) are used. Note that this result (importance of adding Bloch modes for convergence) is classical and was demonstrated in [180] for the same example using a transmission loss analysis.

4.5 Conclusions

In this chapter, a computational methodology based on the wave synthesis using a forced analysis was proposed for metastructures with highly dissipative characteristics. The most important points can be summarized as follows:

- The initial step in the WFE scheme is to calculate the forced response corresponding to a specific wave, the DLF of the wave is determined using a power balance approach. The WFE scheme is developed by Bloch expansion to compute the response to a point force by integrating the responses to the wavenumbers in the entire Brillouin zone and the global DLF is also derived using the power balance approach. The accuracy of the proposed method in predicting the global DLF is confirmed by its agreement with the PIM-FEM approach.

- For simple cases such as thin aluminum and timber plates, a careful comparison of the input and transfer mobilities with analytical results reveals negligible errors in the full frequency range, validating the proposed WFE scheme for the global forced response and the dominance of bending wave to the dynamic motion.

- It is shown that for a lightly damped structure, a classical methodology based on the power balance equation for the dominant wave is sufficient to capture the global damping loss factor of the structure. In this case, an eigenvalue analysis is sufficient. In contrast for highly dissipative media, the power balance equation should account for the excitation type and the contributions of all waves are necessary to capture the global DLF. In this case, a forced analysis is required. In addition, for metastructures where large unit cells are needed to model complex configurations, the importance of adding Bloch waves in the forced analysis is shown.

This chapter addresses the research questions by advancing the WFE scheme to calculate the global/composite DLF of HDS. The power balance is derived from the response of the UC to a point force, confirming the reduced impact of the bending wave on the flexural displacement through the forced response in the wave domain. The proposed methodology could be an efficient tool for planar periodic structures due to its adaptability and accuracy, aiding the ongoing extensive work in the vibroacoustic community on the development of metastructures.

Chapter 5

Sound Transmission Characteristics of Heterogeneous Metastructures using the Wave-based Methodologies

---

Abstract: Classical models employed for computing acoustic indicators of heterogeneous metastructures having limitations in terms of precision, especially for metastructures showing complex phenomena that involve the interaction between different wave branches (extensional, flexural, torsional, and high-order waves) within the structure, which significantly influences the sound transmission characteristics of the structure. The present study focuses on exploring the capability of wave-based methodologies to study the wave coupling effect on the accurate estimation of Sound Transmission Loss (STL) of these metastructures. It presents the transmission loss computation from WFE for the Unit Cell (UC) representative of the periodic structures, by applying a plane wave excitation from the ambient medium, such methodology is also exploited to reveal the effect of complex wave coupling on the acoustic behavior. STL under Diffuse Acoustic Field (DAF) is computed by integrating the wave STL over all possible incidence angles. Various configurations, HCS and HDS such as the laminated glass and sandwich plates with a Shape Memory Polymer (SMP) core, sandwich plates with a thick soft core, Cross-Laminated Timber (CLT) plate, and curved structures ranging from simple isotropic and orthotropic configurations to complex sandwich configurations, are presented to highlight the advantages of the proposed wave-based methodology.

Contents

5.1 Introduction

Since the WFE scheme offers an accurate and comprehensive numerical tool for examining the coupled wave motions and their impact on vibroacoustic indicators, this chapter aims to complement the previous chapters by validating the WFE model developed in Section 2.5.5 through the metrics of acoustic transparency and STL, especially when it comes to heterogeneous metastructures. Other classical models, such as the analytical TMM, the hybrid FE-TMM model (also known as General Transfer Matrix Method, GTMM) [179, 180], and GLM [29] are also exploited.

Because the bending wave no longer dominates the STL prediction for heterogeneous metastructures where the wave coupling effect becomes important, the present chapter provides a wave-based methodology for directly presenting the acoustic transparency of all the wavenumbers impinging on the structure from the ambient media. Then, the acoustic transparencies to all the waves inside the acoustic contour are integrated for the DAF excitation. The same methodology can also be applied to waveguides with complex cross-sections where the Poisson ratio differs, such as the CLT plate where the wave coupling effect alters the dispersion behavior and the wavemodes from those of the uncoupled model [203]. Besides, the onset of high-order wave branches and the coupling between through-thickness modes and in-plane waves in a structure lead to intricate dynamic behavior. Accurately capturing such effect is crucial for the computation of sound transmission capacity of the structures. In addition, the effect of curvature on the vibroacoustic indicators of periodic structures before the ring frequency is also a noteworthy subject [203].

The structure of this chapter is as follows: Section 5.2 validates the accuracy of the proposed wave-based methodologies on the computation of acoustic indicators, laminated glass with rheological PVB core is taken as an example of HCS. Section 5.3 studies the bending-shear coupling effect on the HDS, and the diminishing influence of bending wave contribution to the STL of HDS under DAF excitation is demonstrated. Section 5.4 outlines the importance of accounting for the symmetric motion of a sandwich plate with a thick soft core, the contribution of symmetric motion to the STL beyond the frequency corresponding to the first symmetric motion is confirmed by the acoustic transparency in the wave domain. Section 5.5 studies the effect of in-plane waves on the STL of the CLT plates. Section 5.6 depicts the STL of curved periodic structures to study the effect of curvature on the STL, the bending-membrane coupling effect is studied by the acoustic transparency in the wave domain, and the results of the WFE scheme are compared to those from GTMM. The discussion regarding the results is devoted in Section 5.7.

5.2 Validation of the Proposed Wave-based Methodologies

The first configuration consists of a laminated glass, it comprises two 5mm thick glass layers bonded together by a 0.38mm thick cohesive PVB type RB41 core. The properties of the glass and BVP layers are presented in Section 3.4.2.

In Fig. 5.1, a comparison between the proposed WFE method and GLM available is shown [29]. The wavenumbers of bending, extensional, and shear waves of the laminated glass are in good agreement with the GLM results, the intersection between the acoustic wavenumber and the bending wavenumber at 1315.88 Hz corresponds to the critical frequency.

The computation of STL includes two distinct excitations: an oblique plane wave with an incidence angle of $\theta = 45°$ and a DAF. For the WFE scheme, a UC with sidelengths of 1 mm is employed. The UC is constructed using twelve C3D8 elements through an in-house FE program, consisting of 2 elements in each in-plane direction and 1 element in the out-of-plane direction for both the skins and the core. In all presented results, the mesh used for the calculations is verified to converge in the frequency band

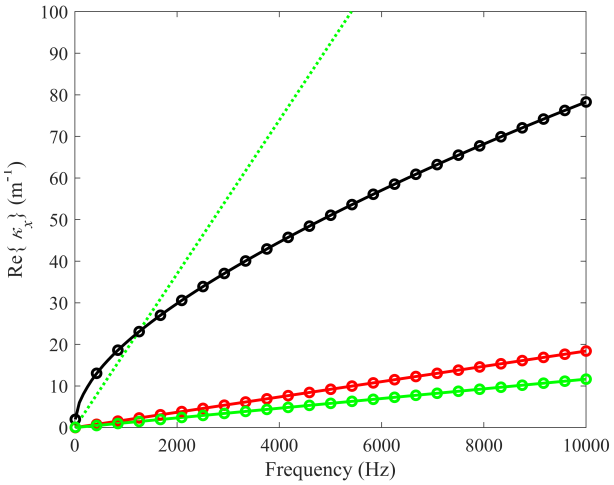

Fig. 5.1. Dispersion curves of the laminated glass.-: WFE result. ∘: GLM result. − and ∘: Bending wave. − and ∘: Extensional wave. - and ∘: Shear wave. · · ·: Wavenumber in air.

investigated. The STL is computed through the method presented by Christen et al. [94] and presented in Section 2.5.5.

The STL resulting from the oblique 45° wave incidence is graphed on a base-10 logarithmic scale in Fig. 5.2 (a). Analytical results from the TMM are also depicted for validation purposes [177]. Notably, the predictions from the WFE scheme align well with the analytical outcomes across all frequency ranges, correctly capturing the precise coincidence frequency at 3072.26 Hz. Specifically, for the STL to the incident wave excitation at angle 45^o, the maximum relative error is about 0.42% at the coincidence frequency.

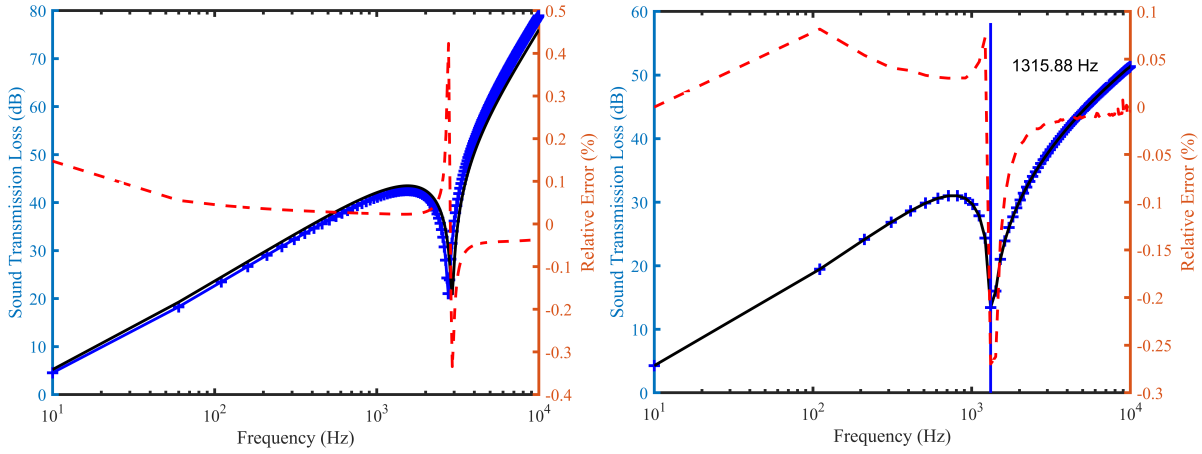

Fig. 5.2. Sound transmission loss of laminated glass. Left: Acoustic transparency at incidence angle 45^o. Right: Sound transmission loss at the diffuse acoustic field. +: TMM results. −: WFE results. −: Coincidence frequency. −−: Relative error.

The integration for the DAF is carried out using the same script as detailed in Section 2.5.5, and the WFE results are depicted in Fig. 5.2 (b). In this context, the WFE scheme shows perfect agreement with TMM, the relative error exhibits a difference of less than 0.3% across the entire frequency spectrum. The critical frequency at 1315.88 Hz in Fig. 5.1 is accurately computed by the WFE scheme by showing a sharp decrease in the value of STL to DAF excitation. Before the critical frequency, the STL to DAF of a flat plate is mainly controlled by the mass law [31], beyond the critical frequency, the STL is controlled

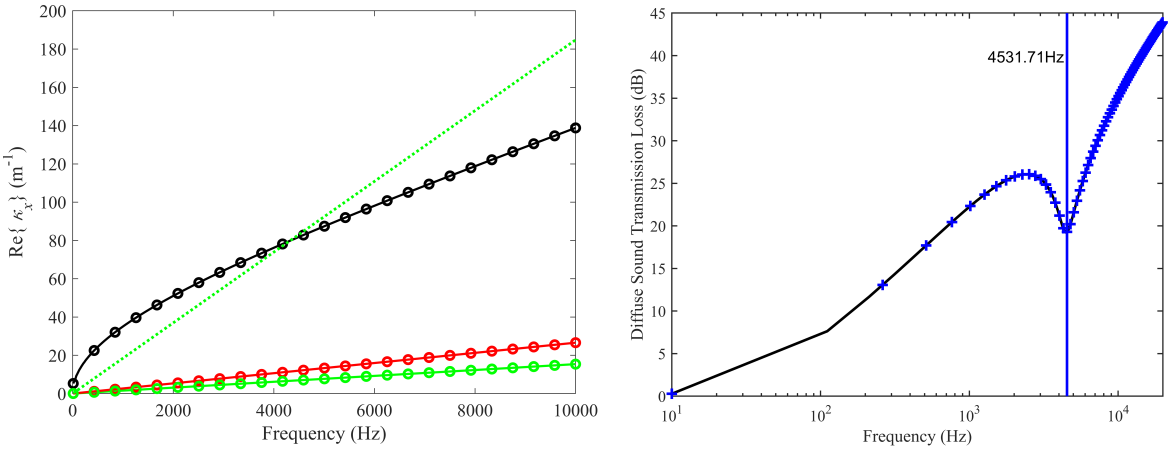

Fig. 5.3. Dispersion curves and Sound Transmission Loss of the sandwich plate with an SMP core under a Diffuse Acoustic Field at 50 °C. Left: -: WFE result. ∘: GLM result. − and ∘: Bending wave. − and ∘: Extensional wave. - and ∘: Shear wave. · · ·: Acoustic wavenumber in air. Right: -: WFE results. +: GLM results. −: Coincidence frequency.

by the damping and stiffness. Due to the meticulous discretization of incidence angles, the discrepancy in the coincidence frequency becomes imperceptible.

5.3 Effect of the Multi-scale Dynamics on the Sound Transmission Loss

Another classical HCS instance, the sandwich plate with an SMP core first presented in Chapter 3.4.3, is exploited to study the effect of multi-scale dynamics on the STL. The accuracy of the WFE scheme for STL of HCS and HDS is exemplified through this configuration for the study of multi-scale dynamics of HCS. The settings in FE analysis remain the same as introduced in Chapter 3.4.3.

5.3.1 Sandwich Structure with Shape Memory Polymer Core at 50 °C

Consider first a temperature leading to a moderate damping level at 50°C (see Fig. 4.9). Fig. 5.3 (a) illustrates a comparison encompassing the real part of wavenumbers, including main waves controlling the bending, extensional, and shear motions, and STL to DAF excitation. Remarkably, the real part of the wavenumbers obtained through the WFE scheme agrees well with the results from GLM [29]. The STL to DAF excitation from the WFE approach aligns well with GLM solutions [29]. The acoustic coincidence at 4531.71 Hz is shown by the intersection between the acoustic wavenumber and the bending wave, the critical frequency is also shown by the sharp decrease of STL curve in Fig. 5.3 (b). This agreement underscores the reliability and accuracy of the WFE scheme in capturing the acoustic dynamics of the SMP50°C sandwich plate.

Fig. 5.4 (a) illustrates the acoustic transparency (computed by Eq. 2.117), as a function of wavenumber, of the sandwich plate with a SMP core at 50 °C due to impinging plane waves from the air at 10000 Hz, a frequency above critical frequency. A limited wavenumber range is selected, considering only those smaller than the acoustic wavenumbers of the ambient air, as depicted by the green contours within the figures. The acoustic transparency to the impinging wavenumbers is also illustrated using $\tau = \left|\frac{p_{tra}}{p_{inc}}\right|^2$ derived in Chapter 2.5.5 using Eq. 2.116, the same slope is found in omni-direction due to the isotropy of the structure. In the audible frequency range up to 10000 Hz, the bending wave solely influences the STL due to its strong coupling with the ambient air. Wave branches such as the extensional or shear waves,

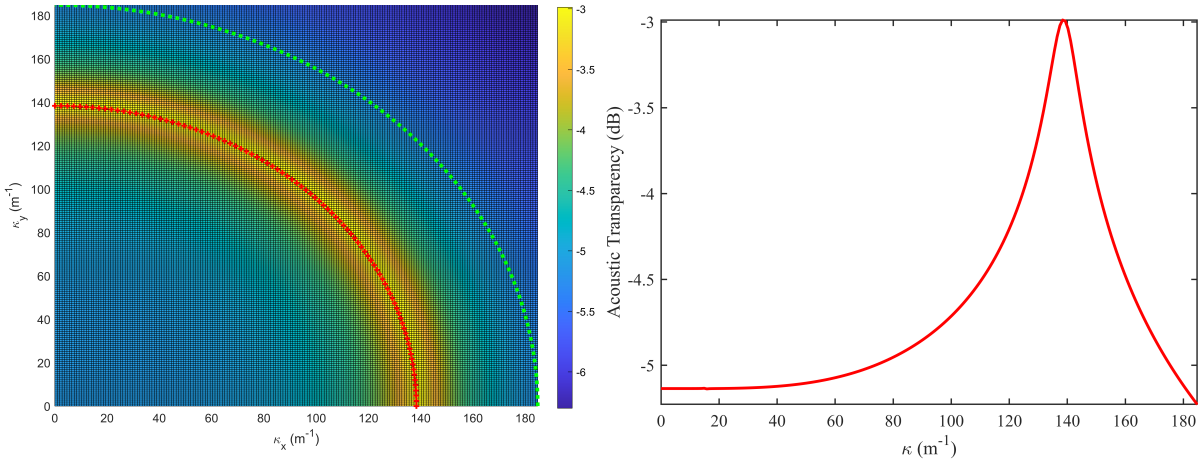

Fig. 5.4. Left: Acoustic Transparency of plane waves from the ambient media at 10000 Hz and 50 °C. +: Bending wavenumber. · · · : Acoustic wavenumber in air. Right: Acoustic Transparency against the wavenumber at 10000 Hz and 50 °C.

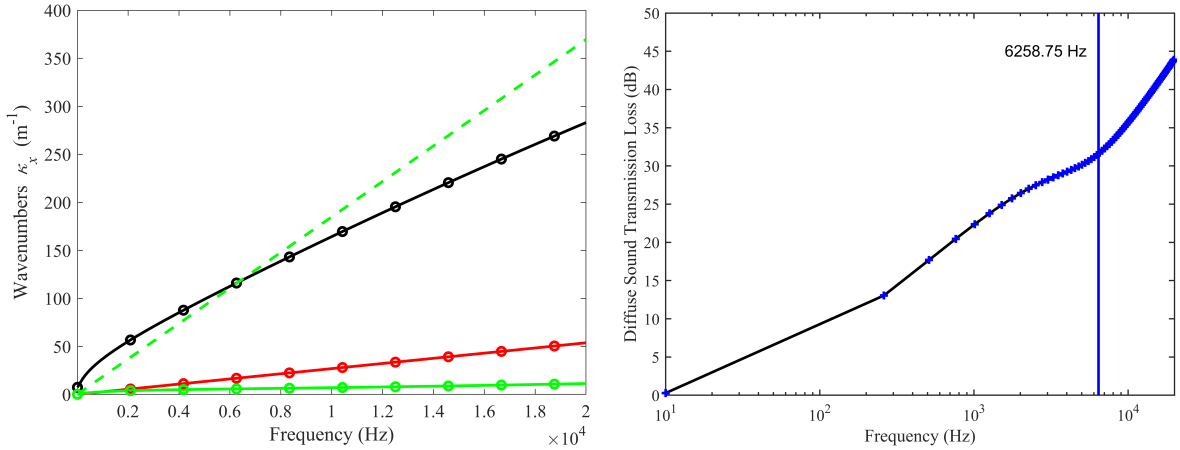

Fig. 5.5. Dispersion curves and Sound Transmission Loss of the sandwich plate with a SMP core under a Diffuse Acoustic Field at 65 °C. Left: −: WFE result. ∘: GLM result. − and ∘: Bending wave. − and ∘: Extensional wave. − and ∘: Shear wave. · · · : Acoustic wavenumber in air. Right: −: WFE results. +: GLM results. −: Coincidence frequency.

with primary in-plane displacements, do not couple with ambient media and thus minimally affect the STL behavior.

5.3.2 Sandwich Structure with Shape Memory Polymer Core at 65 °C

Next, we consider a highly damped configuration for the SMP core sandwich at 65 °C. Fig. 5.5 displays the real part of the wavenumbers for the main waves and STL to DAF excitation. The wavenumbers exhibit excellent agreement with GLM, further substantiating the accuracy and reliability of the analyses. The acoustic wavenumber of the air intersects with the bending wavenumbers at 6258.75 Hz. The STL to DAF excitation from the WFE approach is depicted alongside those from the GLM approach [29]. The STL curve shows a classical phenomenon for HDS: the critical frequency becomes wider and the STL curve exhibits a gradual increase rather than a sharp decline at the critical frequency.

Fig. 5.6 shows the contribution of waves to the STL to DAF excitation at the critical frequency, 6258.75 Hz. Contrary to the acoustic transparency of SMP50°C depicted in Fig. 5.4 (a), the acoustic transparency of SMP65°C depicted in Fig. 5.6 (a) shows a wider zone near the bending wave provides significant contribution to the STL under DAF excitation, the same phenomenon for the computation of

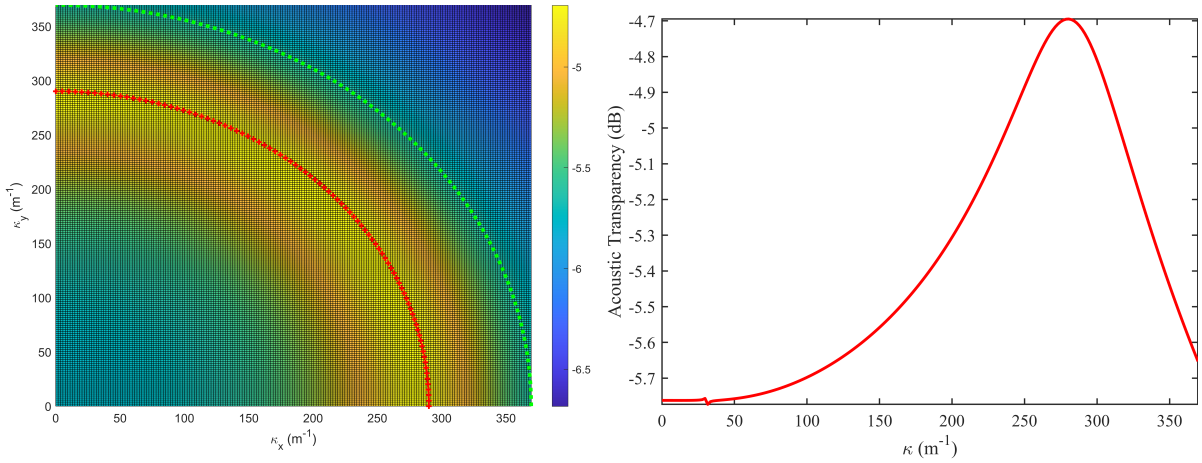

Fig. 5.6. Left: Acoustic Transparency of plane waves from the ambient media at 6258.75 Hz and 65 °C. +: Bending wavenumber. · · ·: Acoustic wavenumber in air. Right: Acoustic Transparency against the wavenumber at 6258.75 Hz and 65 °C.

the forced response was demonstrated in Fig. 4.14 in Chapter 4.4.3.

5.4 Symmetric Motion of Sandwich Plate with a Thick Soft Core

A special HCS instance is presented by the configuration of 2 mm skins and a 20 mm core [118]. The performance of the WFE scheme for soft thick cores is exemplified through this configuration for the examination of symmetric and asymmetric motions of HCS. The material properties are detailed in Tab. 5.1.

Tab. 5.1. Material properties used for the numerical validation.

Layer	Aluminum	Melamine
Density [kg/m^3]	2700	8.8
Elastic Modulus [Pa]	71×10^9	8×10^4
Poisson's ratio [−]	0.33	0.4
Damping ratio [−]	0.7%	17%

The angular frequency corresponding to the symmetric motion can be estimated analytically [207]:

$$\omega_{sym} = \sqrt{\frac{E_s * (1-\nu_c)}{(1+\nu_c)(1-2\nu_c)} \frac{\frac{1}{m_{s,1}} + \frac{1}{m_{s,2}}}{h_c}} \tag{5.1}$$

where subscripts s and c correspond to the skin and core, m denotes the surface density, h denotes the thickness.

The UC with 1 mm sidelengths is divided into two elements in the in-plane directions. In the thickness direction, the skins are modelled by 1 element, the core is modelled by 10 elements, generating a total of 48 elements and 117 nodes for the WFE scheme. In this scenario, the EVP exhibits ill-conditioning in the practice, rendering MATLAB's built-in function incapable of solving the results. Consequently, the CI solver developed in Section 3.3.2 is utilized. The contour parameters are set as $\rho = \pi/10$, $\beta = 0.5$ and $\gamma = 0$, these parameters define an ellipse with a major axis of 300 rad/m (representing the maximum

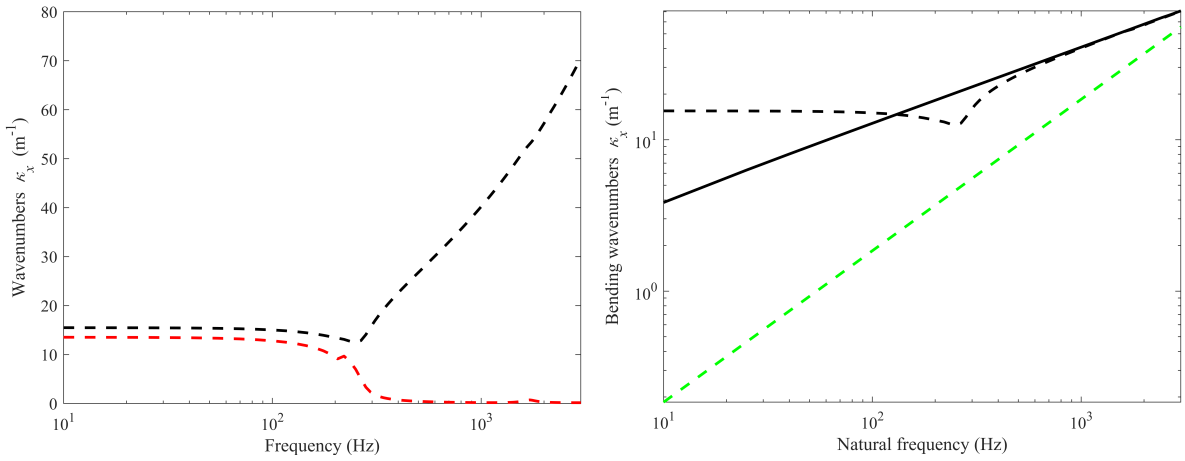

Fig. 5.7. Complex wavenumbers associated with symmetric and asymmetric motions in a sandwich plate with a thick core. Left: −− Real part of the symmetric wave. −− Imaginary part of symmetric wave. Right: −− Real part of the symmetric wave. − Real part of asymmetric wave. −− Acoustic wavenumber in air.

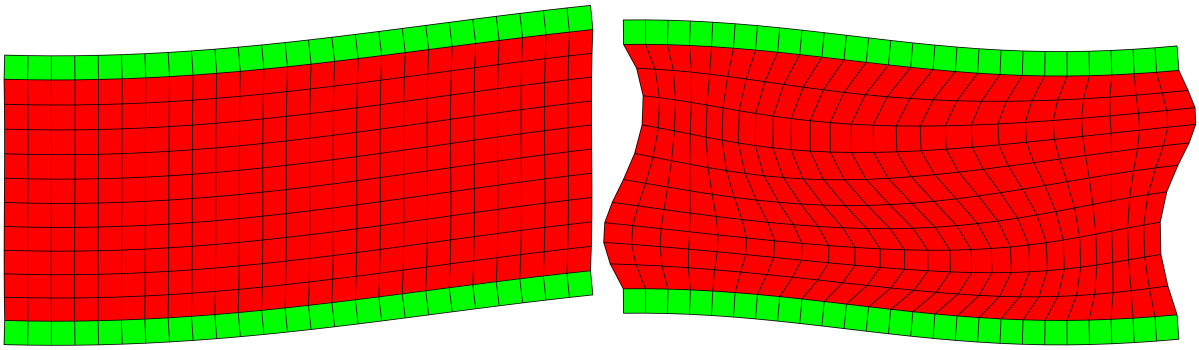

Fig. 5.8. Wavemotions of the asymmetric wave of the aluminum sandwich plate with a thick melamine core. Left: 1041 Hz. Right: 3000 Hz.

$Re(\kappa)$ value) and a minor axis of 150 rad/m (indicating the maximum $Im(\kappa)$ value), which is sufficient for capturing all the possible wavenumbers.

The real and imaginary parts of the wavenumber linked to symmetric motion are depicted in Fig. 5.7(a). Below the first out-of-phase symmetric mode at frequency f_{sym} = 281.4955 Hz calculated using Eq. 5.1, the wavenumber corresponding to the symmetric motion is evanescent with real and imaginary parts of similar magnitude, above this frequency, the wavenumber of the symmetric wave becomes propagative as its imaginary part reduces to zero. Fig. 5.7(b) illustrates the wavenumbers for symmetric and asymmetric motions. Note that the acoustic wavenumber is smaller than that of the asymmetric and symmetric wave, the corresponding wavenumber space in the following computation is enlarged for encapsulating all the waves to compute the acoustic transparency to investigate their contribution to the out-of-plane motion.

The wavemotions of asymmetric wave are depicted in Fig. 5.8, the length of the FE model equivalent to the wavelength of the target wave. The wavemode associated with the bending wave is asymmetric: at low frequency, the mode is purely bending, at a higher frequency, the mode is dominated by an out-of-plane bending with transverse shear. Therefore, for sandwich plate structures with thick cores, consideration of the shear effect in the asymmetric motion would be appropriate to compute the vibroacoustic indicators.

The wavemotions of symmetric waves are depicted in Fig. 5.9 for a visible comprehension of the dilatational modeshape. The symmetric wavemotion at low frequencies (but beyond f_{sym} = 281.4955 Hz)

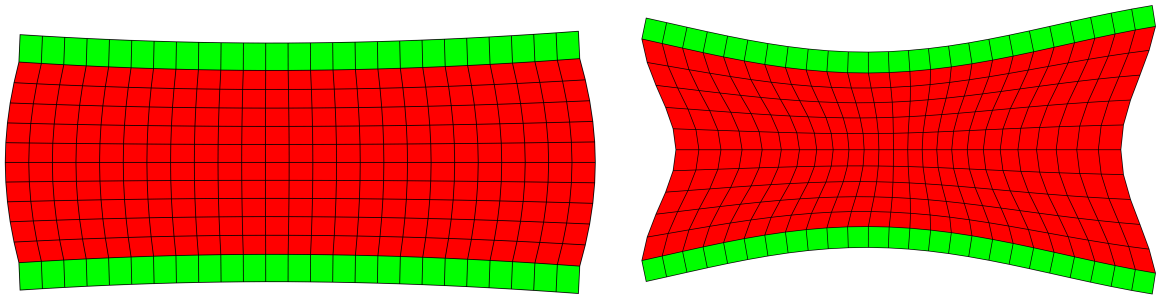

Fig. 5.9. Wavemotions of the symmetric wave of the aluminum sandwich plate with a thick melamine core. Left: 422 Hz. Right: 3000 Hz.

shows symmetric out-of-plane motion with in-plane extensional displacement, while at higher frequencies, it exhibits significant out-of-plane motion with dilatation behavior through the thickness direction.

Fig. 5.10 illustrates the STL under DAF excitation, both asymmetric and symmetric motions are accounted for in the methods presented, and the results are in good agreement among the WFE, TMM, and GTMM approaches. The frequency of symmetric motion, 281.4955 Hz, is accurately computed by all the three methods.

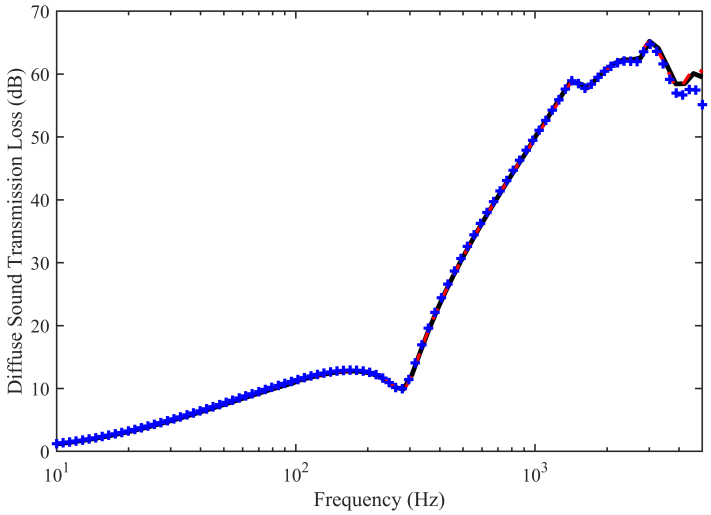

Fig. 5.10. Sound Transmission Loss at Diffuse Acoustic Field of Aluminum Sandwich Plate with a Thick Melamine Core. −: WFE results. +: GTMM results. −−: Analytical TMM results.

To investigate the wave dominance on the STL in DAF excitation, we start from the acoustic transparency at 200 Hz which is smaller than the frequency of the first dilatational mode, and the difference between the amplitudes of symmetric and asymmetric wavenumbers is large to visually recognize them in the wavenumber domain. As demonstrated in Fig. 5.11, the asymmetric bending wave is the sole dictator of the STL to DAF excitation.

Next, as demonstrated in Fig. 5.12, the acoustic transparency at frequency corresponds to the first dilatational mode shows a similar variation as the HDS case in Section 5.3.2, the contribution of wavenumbers smaller than the bending wave is visibly strong, meaning that all these waves, if excited, significantly contribute to the out-of-plane dynamic motion.

Lastly, Fig. 5.13 (a) depicts the acoustic transparency at 478 Hz where the symmetric wave becomes purely progressive. At higher frequency range, the asymmetric and symmetric waves approach each other, and becomes visually impossible to distinguish them in the wavenumber domain. As depicted in Fig. 5.13

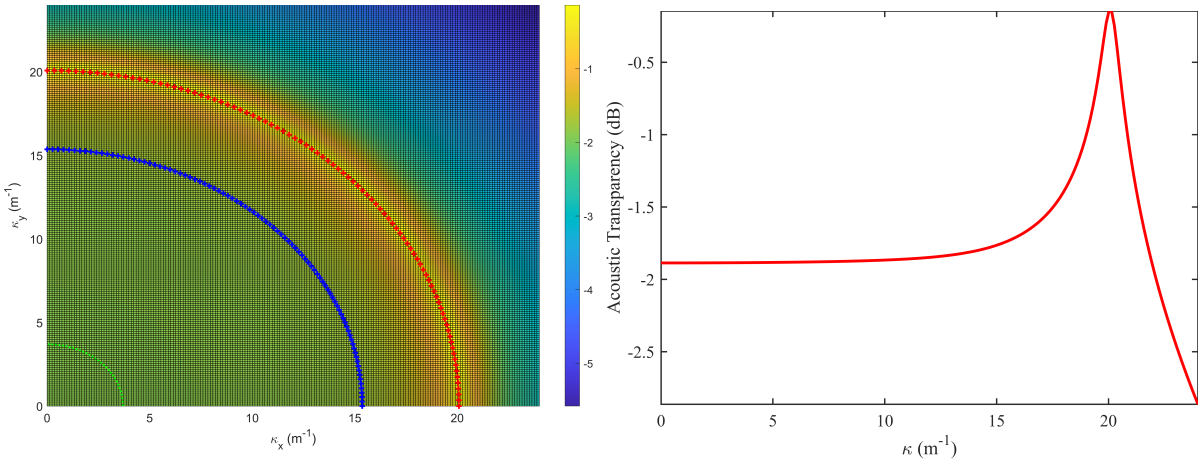

Fig. 5.11. Left: Acoustic Transparency of plane waves from the ambient media at 200 Hz. +: Asymmetric wavenumber. +: Symmetric wavenumber. · · ·: Acoustic wavenumber in air. Right: Acoustic Transparency against the wavenumber at 200 Hz.

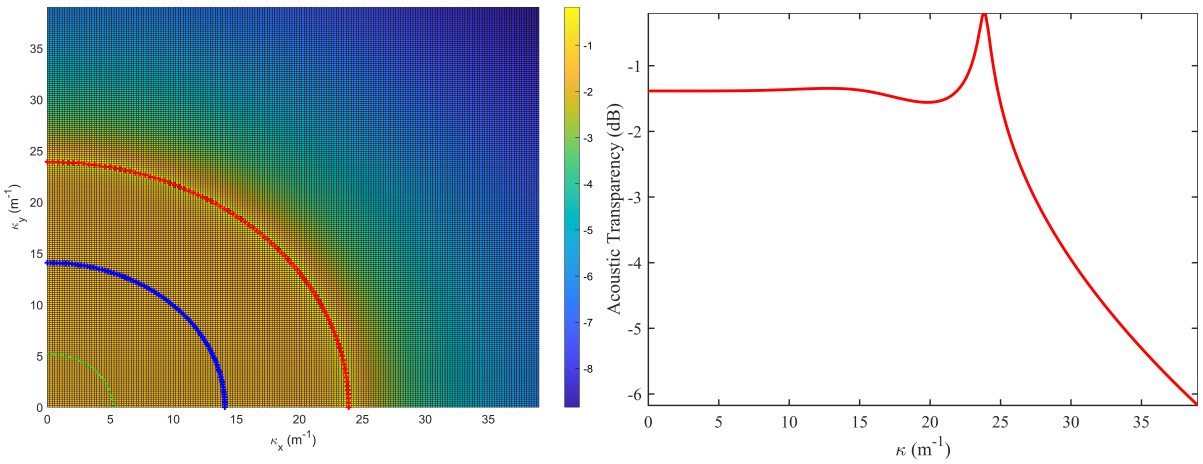

Fig. 5.12. Left: Acoustic Transparency of plane waves from the ambient media at 281.4955 Hz. +: Asymmetric wavenumber. +: Symmetric wavenumber. · · ·: Acoustic wavenumber in air. Right: Acoustic Transparency against the wavenumber at 281.4955 Hz.

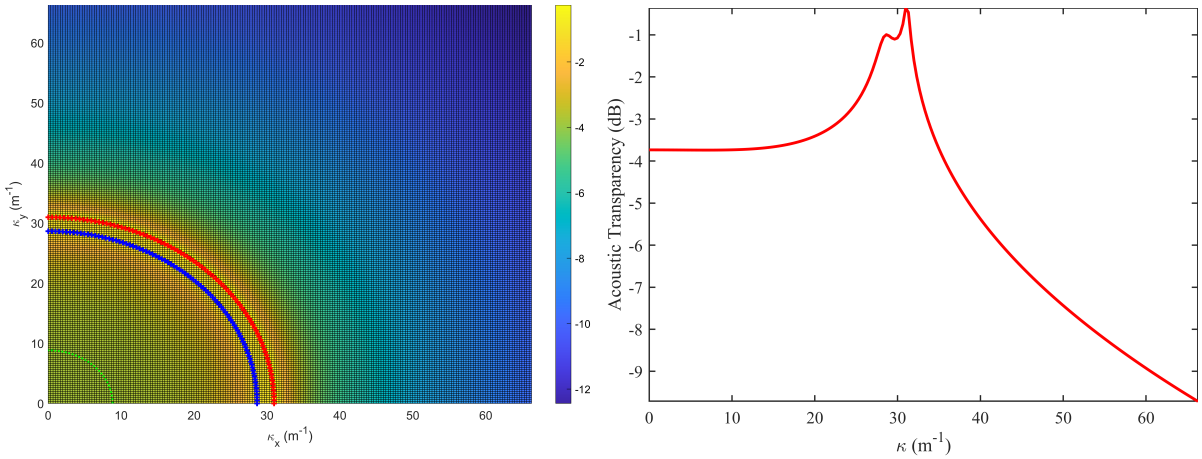

Fig. 5.13. Left: Acoustic Transparency of plane waves from the ambient media at 478 Hz. +: Asymmetric wavenumber. +: Symmetric wavenumber. · · ·: Acoustic wavenumber in air. Right: Acoustic Transparency against the wavenumber at 478 Hz.

(b), the two waves controlling the flexural motion start to have a dominant place in the sound transmission, the symmetric wave also gives a significant contribution to the out-of-plane displacement.

Note that classical analytical methods fail to involve the symmetric motion of sandwich structures with a thick and soft core, as most common plate theories (Kirchhoff-Love, Reissner-Mindlin, etc.) do not include the displacement field corresponding to the symmetric motion [174].

5.5 Wave Coupling Effect of In-plane Waves on the Cross-Laminated Timber Plate

The orthotropic configuration example involves a CLT plate, demonstrating the wave coupling effect of bending and shear wave branches, as well as the high-order waves. The CLT plate consists of six timber layers with a total thickness of 20 cm, and the stacking angle is $[0^o/90^o/0^o/0^o/90^o/0^o]$, the material properties are listed in Tab. 4.1 of Chapter 4.3.3.

The WFE model portrays the CLT plate as a laminate of six orthotropic layers. A UC with sidelengths of $2mm \times 2mm$ is considered, with each layer discretized into four out-of-plane elements and two in-plane elements, enabling accurate modeling and depiction of shear in each layer.

Fig. 5.14 presents the dispersion curves for the waves in x-direction, computed by both WFE and GLM methods. The wavemodes of all wave branches output by the WFE framework are depicted to demonstrate how, at higher frequencies, the behavior becomes much more complicated when the wave veering effect appears and new wave branches cuts-on.

As shown in Fig. 5.14, wave branch 1 is a bending wave with significant transverse shear. Wave branch 2 is an in-plane extensional wave. Wave branch 3, at low frequencies, is an in-plane shear wave with Poisson contraction, transitioning to a through-thickness resonant mode at high frequencies. Wave branches 4 and 5 are the first (Y-direction) and second (X-direction) antisymmetric shear waves, cutting-on at 1160Hz and 1500 Hz, respectively. Wave branch 6, cutting-on at 2350 Hz, is the first (X-direction) symmetric, through-thickness shear wave, akin to the mass-spring-mass resonance of double-skinned panels. Besides, wave branches 3 and 6 are strongly coupled and diverge above 2300 Hz, representing a through-thickness resonant mode and a symmetric shear wave with out-of-plane dynamics, respectively. Wave branch 7 is the second (Y-direction) symmetric shear wave, cutting-on at high frequencies.

Given that GLM construction is based on Mindlin's displacement theory, the original GLM is not built to capture the symmetric motion, layer compression can only be added by extra displacement equations in

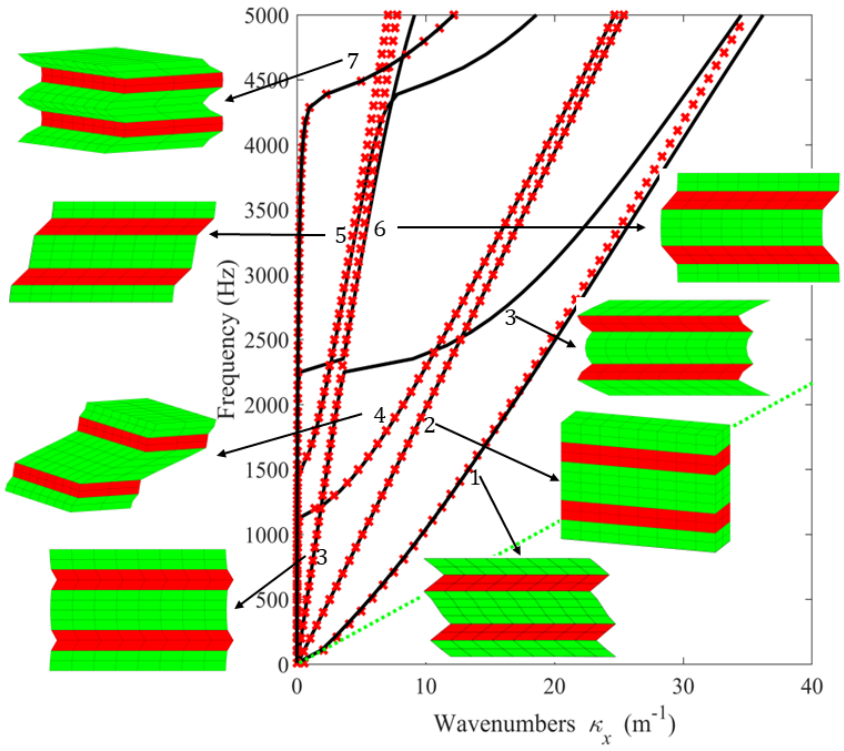

Fig. 5.14. Dispersion curves of CLT plate. -: WFE results. +: GLM results. –: Acoustic wavenumber in air.

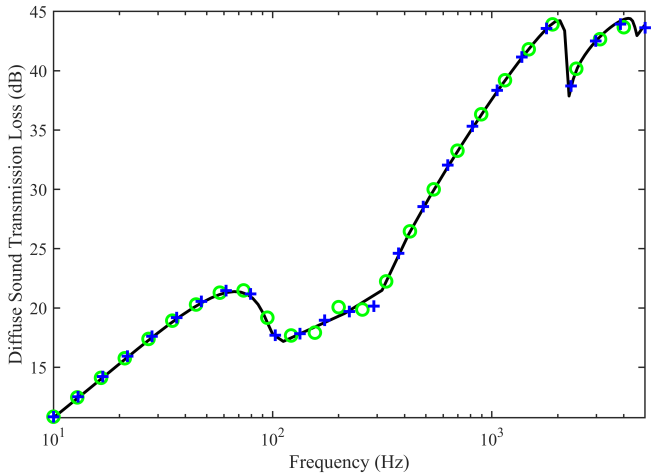

Fig. 5.15. Sound Transmission Loss of CLT plate under Diffuse Acoustic Field. ○: Analytical TMM results. −: WFE results. +: GTMM results.

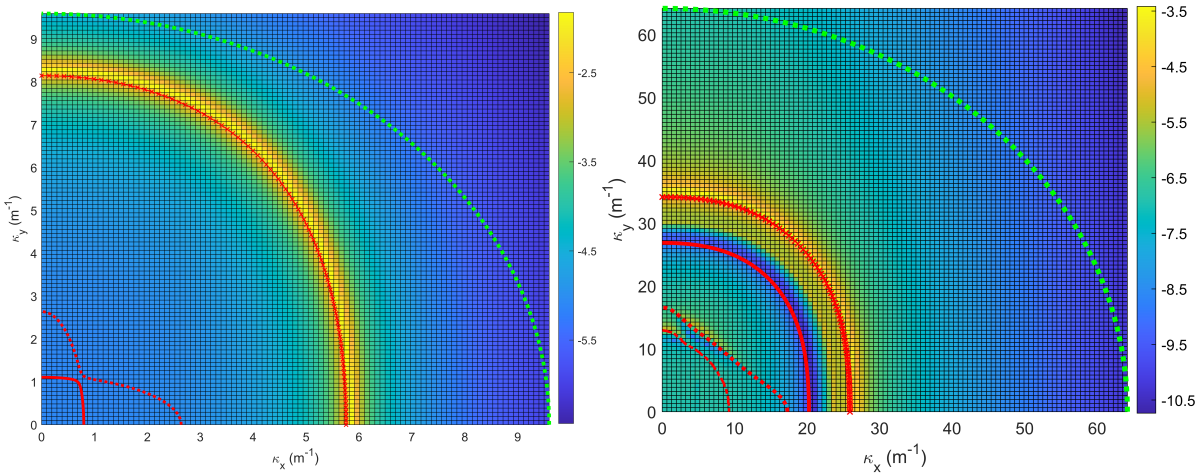

Fig. 5.16. Acoustic Transparency of plane waves from the ambient media and the dispersion curve. +: Bending wave. ···: Extensional wave. -: Shear wave. –: Wave branch 6. –: Acoustic wavenumber in air. Left: 500 Hz. Right: 3500Hz.

the framework presented in Section 2.3.3, leading to inaccuracies at high frequencies where the shear wave (and the veering effect of branches 3 and 6) is not accurately captured. The high-frequency cutting-on effect of the symmetric through-thickness shear waves is also not accurately captured by the GLM [29], resulting in incorrect STL in DAF at this range.

To investigate the wave coupling mechanism of sound transmission in the CLT panel, the STL under DAF excitation is shown in Fig. 5.15. The WFE results align well with analytical TMM results [177], and GTMM results are accurate across all frequencies.

Fig. 5.16 illustrates the acoustic transparency of CLT to plane waves impinging from air, computed by Eq. 2.116. The wavenumber of the main wave branches at different propagation directions is computed by the CI solver presented in Section 3.3.2. At 500 Hz, there is no wave veering effect, and high order wave doesn't yet appear, the bending wave primarily influences the STL due to its strong coupling behavior with the ambient air. At 3500 Hz, the shear wave (wave branch 2) significantly contributes to the overall STL, along with higher-order waves exhibiting through-thickness behavior. Wave modes 1, 3, 5, and 6 contribute to the STL across various frequencies below 5 kHz, primarily because their out-of-plane displacements, if excited, couple well with the air and significantly influence the STL prediction. Other wavemodes do not significantly contribute at any frequency, wave branches like extensional wave (wave branch 2), with primary in-plane displacements, do not couple with acoustic fluids and thus minimally affect the STL behavior of the CLT panel.

5.6 Sound Transmission Loss of Curved Periodic Structures

This section introduces the modeling technique of curved periodic structures in the WFE scheme. The STL of several examples ranging from simple isotropic and orthotopic to sandwich curved structures are calculated and juxtaposed with GTMM results.

5.6.1 Curvature Modeling

Given the homogeneity of the curved structure around the circumference and along the axis, a curved rectangular segment (Fig. 5.17) serves as a UC for periodicity to form the entire structure. Fig. 5.17 depicts the geometric configuration of curved structures, with r_i and r_o as the inner and outer radii of

the curved structure, and h as the total thickness. The mean radius, R, is mathematically defined as the neutral surface's coordinate of the cylinder. The excitation and radiated fields are articulated in the radial coordinate system (Fig. 5.17), with the STL expressed in these two reference coordinate systems using corresponding transformation relations.

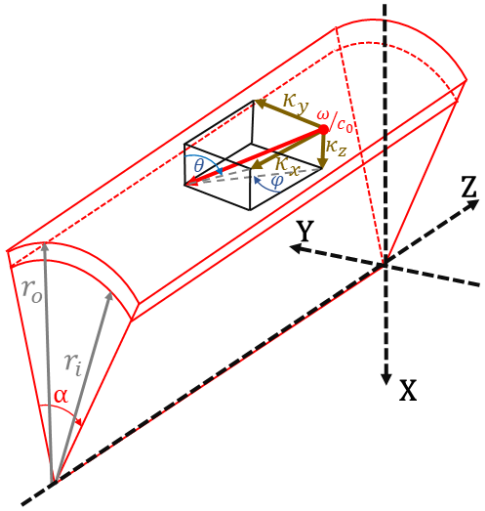

Fig. 5.17. Schematic of the curved structure used for simulation.

For a small curvature angle α, where the approximation $\alpha \simeq sin(\alpha) = L_x/R$ is applicable, the curved UC in Fig. 5.17 can be approximated by a flat rectangular UC with dimensions $\Delta x \times \Delta y$, where $\Delta x = R\alpha$. The rectangular UC's dimension should follow conventional FE analysis guidelines, requiring at least six elements per wavelength to prevent aliasing. A transformation matrix $\mathbf{R}$ is defined to obtain the system matrices of the curved element.

$$\begin{aligned} \mathbf{M} &= \bar{\mathbf{R}}^T \mathbf{M}_{flat} \bar{\mathbf{R}} \\ \mathbf{K} &= \bar{\mathbf{R}}^T \mathbf{K}_{flat} \bar{\mathbf{R}} \end{aligned} \tag{5.2}$$

where $\mathbf{M}_{flat}$ and $\mathbf{K}_{flat}$ represent the UC's mass and stiffness matrices in local coordinates, corresponding to the mass and stiffness matrices of the flat FE model.

The transformation matrix $\mathbf{R}$, comprising repeated submatrices $\mathbf{r}$ for each node, facilitates rotation around the x-axis by an angle α. For solid elements, $\mathbf{r}$ assumes the following form:

$$\mathbf{r} = \begin{bmatrix} cos\,(\alpha) & 0 & \mp sin\,(\alpha) \\ 0 & 1 & 0 \\ \pm sin\,(\alpha) & 0 & cos\,(\alpha) \end{bmatrix} \tag{5.3}$$

for nodal displacements in the X, Y, and Z directions.

For shell elements, $\mathbf{r}$ takes the form:

$$\mathbf{r} = \begin{bmatrix} cos\,(\alpha) & 0 & \mp sin\,(\alpha) & 0 & 0 & 0 \\ 0 & 1 & 0 & 0 & 0 & 0 \\ \pm sin\,(\alpha) & 0 & cos\,(\alpha) & 0 & 0 & 0 \\ 0 & 0 & 0 & cos\,(\alpha) & 0 & \mp sin\,(\alpha) \\ 0 & 0 & 0 & 0 & 1 & 0 \\ 0 & 0 & 0 & \pm sin\,(\alpha) & 0 & cos\,(\alpha) \end{bmatrix} \tag{5.4}$$

This applies to nodal displacements in the X, Y, and Z directions and rotations about the nodal X, Y, and Z axes.

The dispersion relation of infinite curved periodic structures remains consistent with Section 3.3, and vibroacoustic indicators such as the STL to an incident wave and to the DAF excitation can be computed using the same methodology from Section 2.5.5. A curvature of 2 m is considered for all the following study cases.

5.6.2 3mm Steel Curved Structure

The first curved configuration consists of an isotropic curved structure of 3 mm steel with a density of $\rho = 7800\,\mathrm{kg/m^3}$, Young's modulus of $E = 210 \times 10^9$ Pa, Poisson's ratio of $\nu = 0.3$, and a material damping ratio of $\eta = 0.1\%$. The structure has a curvature of 2 m. Fig. 5.18 illustrates the real part of axial wavenumber, κ_z, and circumferential wavenumber, κ_α, and the STL under DAF for this isotropic curved structure.

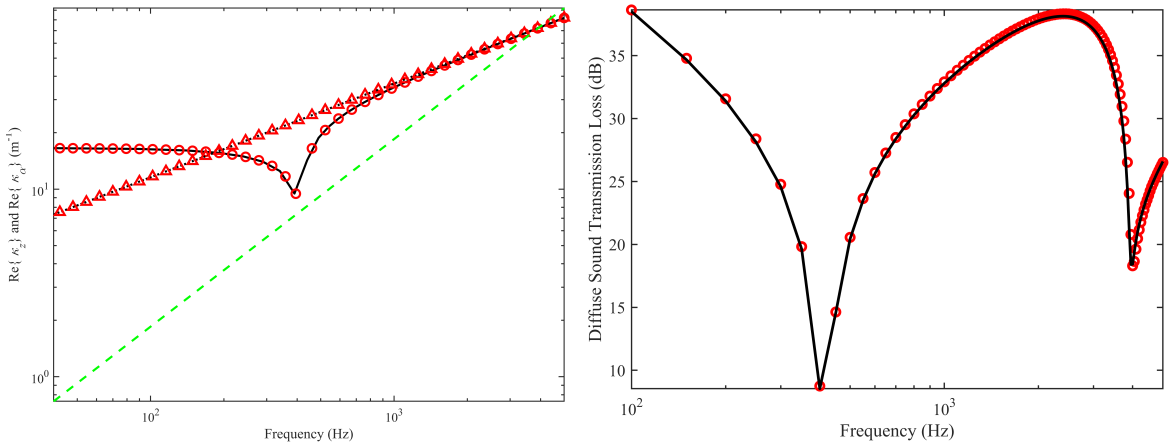

Fig. 5.18. Left: Bending wavenumber of steel curved structure with a radius of 2 m. −: WFE results for axial wave. · · ·: WFE results for circumferential wave. ○: GLM results for axial wave. △: GLM results for circumferential wave. −−: Acoustic wavenumber of air. Right: Sound Transmission Loss of steel curved structure with a radius of 2 m. −: STL from WFE. ○: STL from GTMM.

The UC has 1 mm sidelengths, divided into two elements in the in-plane directions. In the thickness direction, only one element is modeled, generating a total of 4 elements and 18 nodes for the WFE scheme.

In curved shells, the ring frequency is typically defined as the frequency where a single longitudinal wavelength wave matches the curvature perimeter [31]:

$$f_r = \frac{1}{2\pi R}\sqrt{\frac{E}{\rho(1-\nu^2)}} \tag{5.5}$$

For this isotropic curved structure, the ring frequency is 432.52 Hz, and the axial bending wavenumber calculated by the WFE scheme and GLM both shows a dip at the ring frequency where the curvature perimeter equals the wavelength of the axial wave, as depicted in Fig. 5.18 (a). This frequency is crucial in characterizing the dynamics of the curved structure and denotes the frequency range where curvature effects are the most significant. Above the ring frequency, the shell gradually transits to the dynamic behavior of a flat plate, while near and below the ring frequency, the curvature significantly stiffens the structure, leading to more complex dynamic behavior.

Fig. 5.18 (b) illustrates the STL under DAF excitation, the results are more complex compared with the results of a flat plate. The ring frequency and the critical frequency divide three regions showing

different mechanisms for controlling the STL variation in the frequency range: the stiffness-controlled region, the Mass Law region, and the coincidence-controlled region:

- The STL results initially descend to a minimum at the ring frequency f_r, indicating a strong coupling effect of the bending and membrane dynamics, this is the stiffness-controlled region for curved shells.
- After the ring frequency, the STL exhibits another sharp decline at a specific frequency f_{cr}, the STL curve between f_r and the coincidence frequency f_{cr} denotes the mass-controlled region, typically showing an upward trend due to mass effects. For HDS, a damping-controlled region may appear at f_{cr} as shown in Section 5.3.2.
- At the critical frequency, the lowest STL value is known as the coincidence notch, approximately 20 dB for the example in Fig. 5.18(b), indicating minimum resistance to acoustic excitation.
- Beyond f_{cr}, the coincidence-controlled region emerges for most flat or curved structures when structural and acoustic wavelengths align [98].

Other potential regions between the stiffness-controlled and mass-controlled regions have also been identified [112]. Presently, there is an interest in investigating how modifying the frequency ranges of the regions can alter the dynamic behavior of HCS and HDS, thus affecting their vibroacoustic properties; the proposed WFE scheme works as an efficient tool for validating the structural design for such purposes.

5.6.3 10mm Graphite-epoxy Curved Structure

The second curved configuration features an orthotropic 10 mm graphite-epoxy curved structure with a density of $\rho = 1600\,\text{kg/m}^3$, Young's moduli $\{E_x, E_y, E_z\} = \{125, 10, 10\} \times 10^9$ Pa, shear moduli $\{G_{xy}, G_{xz}, G_{yz}\} = \{5.9, 3, 5.9\} \times 10^9$ Pa, Poisson's ratios $\{\nu_{xy}, \nu_{xz}, \nu_{yz}\} = \{0.4, 0.2, 0.2\}$, and a material damping ratio of $\eta = 1\%$.

The UC has 1 mm sidelengths, divided into two elements in the in-plane directions. The UC's thickness is modeled by five elements, generating a total of 20 elements and 54 nodes for the WFE scheme.

Fig. 5.19 (a) presents the bending wavenumber where a ring frequency, 205.6 Hz, is predicted by both the WFE scheme and GLM. Beyond the ring frequency, the acoustic wavenumber of the ambient air intersects with the axial bending wavenumber around 800 Hz, and the circumferential wavenumber around 2650 Hz. Fig. 5.19 (b) depicts the STL under DAF for the orthotropic curved structure.

The STL under DAF excitation initially descends to a minimum at the ring frequency due to the bending and membrane dynamics coupling effect of the curved structure. It's noteworthy that orthotropic curved panels have varying coincidence frequencies in each wave propagation direction. Coincidence frequencies correspond to specific angles and include transition frequency ranges where the structure displays unique dynamic behavior. The transition frequency range can be recognized by the intersection between the acoustic wavenumber and the bending wavenumber in the axial and circumferential heading angles, 800 Hz and 2650 Hz respectively.

5.6.4 Graphite-epoxy Sandwich Structure

The third curved configuration features a 10 mm foam core sandwiched between 3 mm Graphite-epoxy skins having a density of $\rho = 110.4\,\text{kg/m}^3$, Young's modulus $E = 144.8 \times 10^6$ Pa, Poisson's ratio $\nu = 0.2$, material damping ratio $\eta = 1\%$.

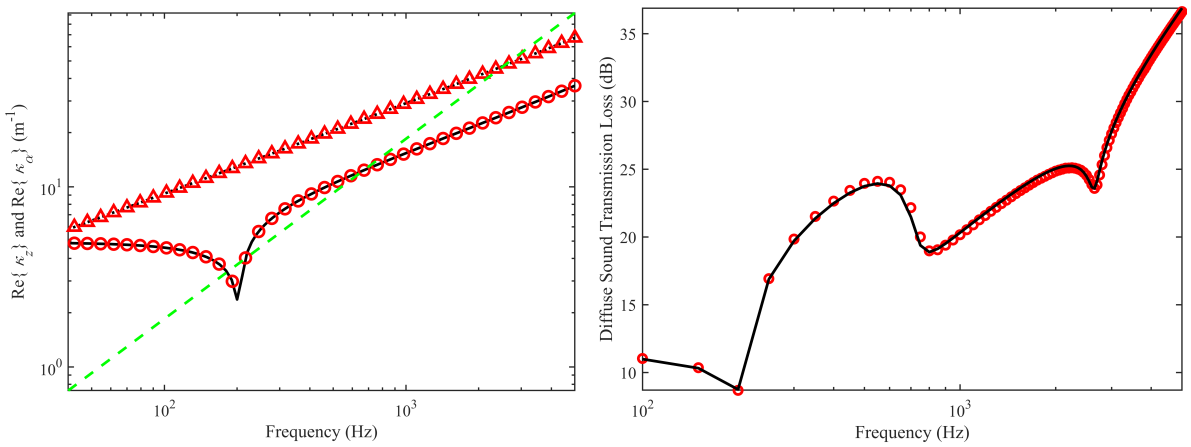

Fig. 5.19. Left: Bending wavenumber of graphite-epoxy curved structure with a radius of 2 m. −: WFE results for axial wave. · · ·: WFE results for circumferential wave. ○: GLM results for axial wave. △: GLM results for circumferential wave. −−: Acoustic wavenumber of air. Right: Sound Transmission Loss of graphite-epoxy curved structure with a radius of 2 m. −: WFE results. ○: GTMM results.

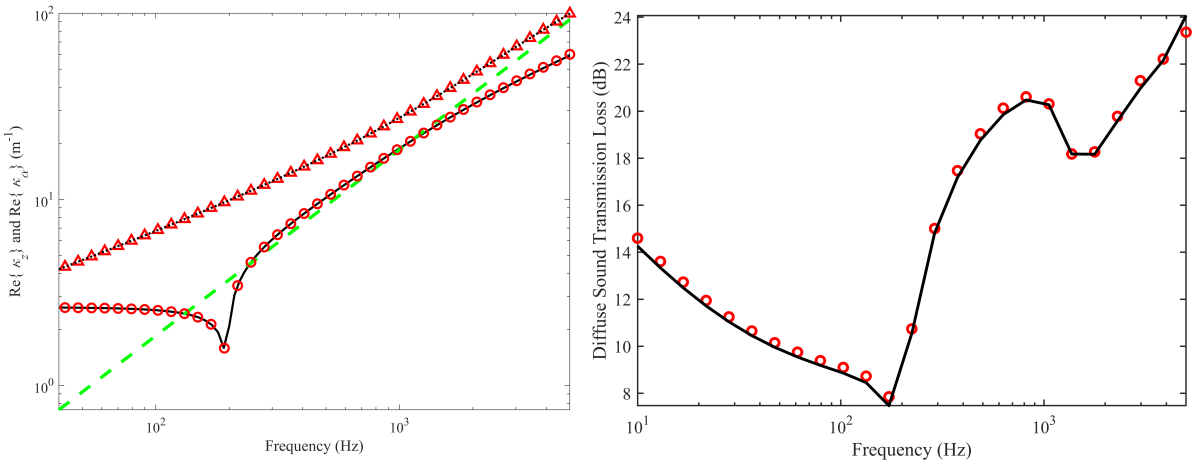

Fig. 5.20. Left: Bending wavenumber of the curved sandwich structure with a radius of 2 m. −: WFE results for axial wave. · · ·: WFE results for circumferential wave. ○: GLM results for axial wave. △: GLM results for circumferential wave. −−: Acoustic wavenumber of air. Right: Sound Transmission Loss of the curved sandwich structure with a radius of 2 m. −: WFE results. ○: GTMM results.

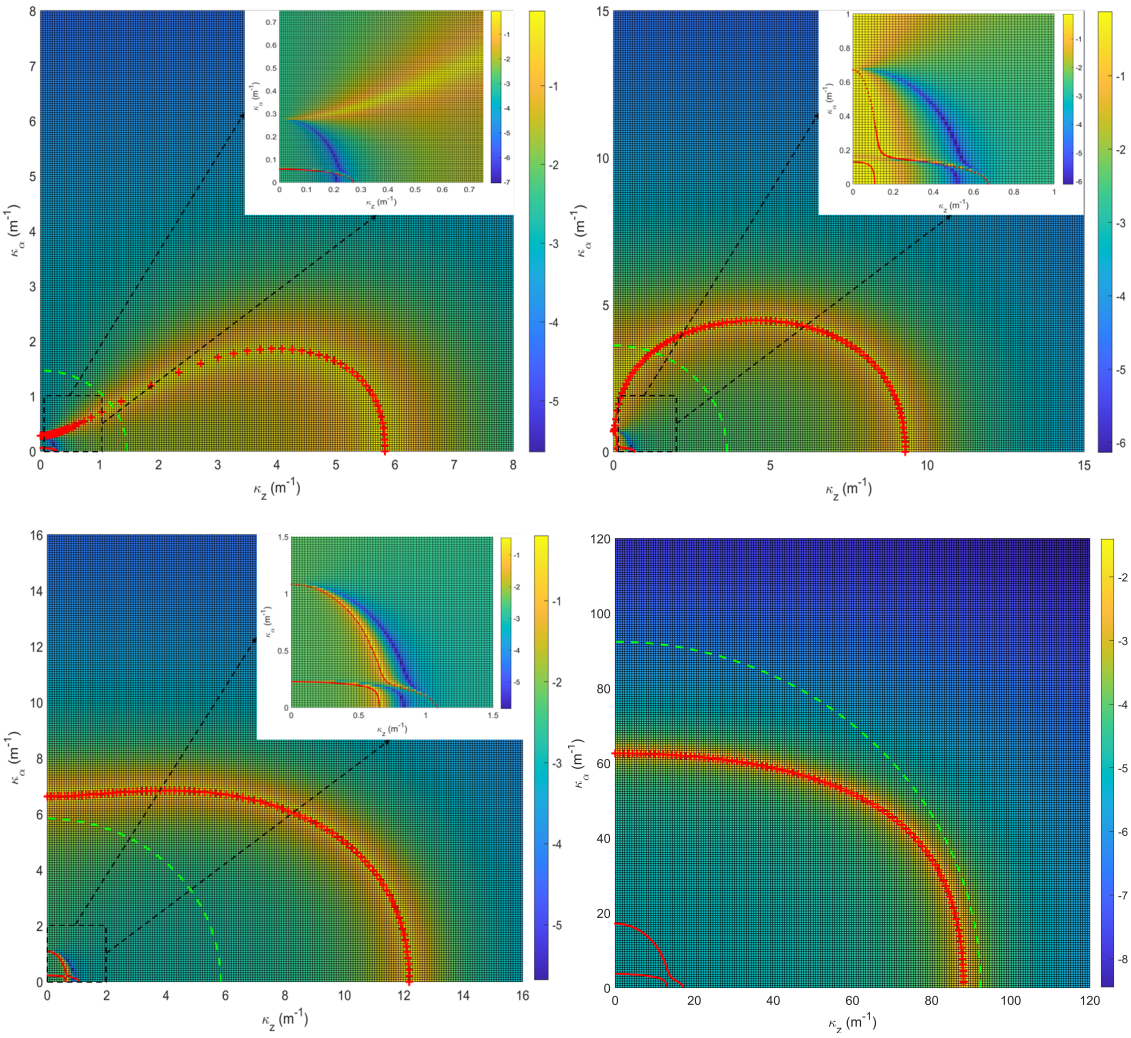

Fig. 5.21. Acoustic transparency of plane waves from the ambient media. Upper left: 79.37 Hz. Upper right: 195.5 Hz. Lower left: 315.81 Hz. Lower right: 5000 Hz. +: Bending wave. · · ·: Extensional wave. −: Shear wave. − −: Wavenumber of ambient air.

The UC has 1 mm sidelengths, divided into two C3D8 elements in the in-plane directions. In the thickness direction, the UC is modeled by five elements for the core and two elements for each skin, generating a total of 36 elements and 90 nodes for the WFE scheme.

The ring frequency is 195.5 Hz and is predicted by the wavenumbers from both the WFE scheme and GLM in Fig. 5.20 (a). Fig. 5.20 (b) presents the STL of a one-third octave band under DAF excitation, computed using both WFE and GTMM approaches, with results closely aligning across all frequency ranges.

Fig. 5.21 shows the acoustic transparency by exciting waves in the wavenumber domain at various frequency steps to study the variation of wave coupling effect in the frequency domain. Although wavenumbers outside the contour of acoustic wave are not accounted for when computing the STL to DAF excitation, a bigger wave domain facilitates the illustration of the role played by each wave branch to the out-of-plane dynamic motion. The wavenumbers of varying propagation direction are computed by the CI solver presented in Section 3.3.2, the number of points is set to 2^7 to traverse all the possible wave solutions inside the contour. The X and Y-axis in the subfigures represent the axial and circumferential

bending wavenumbers, respectively.

- For the acoustic transparency at 79.37 Hz which is below the ring frequency, the bending wave is not the sole dictator of the STL estimation, a membrane wave appears, the membrane wave is coupled with the acoustic excitation from the ambient air to influence the sound transmission, because at this frequency range the membrane wave also contributes to the out-of-plane displacements.

- At the ring frequency of 195.5 Hz, where the circumferential wavelength is equal to the perimeter of the curvature, the coupling between the bending wave and the membrane waves becomes the most significant. The membrane wave evolves into in-plane extensional and shear wave branches, both significantly involved in the out-of-plane dynamics. Near the in-plane waves, a large domain of wavenumbers also contributes to the sound transmission.

- The third frequency, 315.81 Hz, lies near the ring frequency in the mass-controlled region, where a difference remains between the bending wavenumbers in the axial and circumferential directions, but the wave coupling effect in the circumferential direction is reducing as the frequency increases.

- Far beyond the ring frequency at 5000 Hz in the coincidence-controlled region, it is clear that sound transmission is solely affected by the bending wavenumber, similar to a flat plate.

5.7 Conclusions

To complete the previous chapters, the efficiency and accuracy of the computation of acoustic indicators through the proposed WFE method are validated via various structures, including HCS and HDS, sandwich structures with thick cores exhibiting symmetric motion, laminated structures with complex cross-sections demonstrating strong wave coupling effects, and curved heterogeneous metastructures. The main conclusions can be listed as follows:

- The research on the HCS and HDS indicates that, for lightly damped structures, classical theories focusing solely on bending behavior suffice for STL prediction. However, as damping increases (and stiffness decreases) in the HDS, a large region of wavenumber near the bending wavenumber becomes important for the STL.

- To highlight the significance of symmetric motion, strong wave coupling effects, and high-order waves in certain waveguides, the modeshapes of the relevant wave branch are used for κ-wave analysis. The WFE approach provides an intuitive understanding of wave coupling effects. The advantages of the proposed WFE scheme by efficiently accounting all the waves are validated with the analytical TMM and numerical GTMM results.

- The study finally concludes with an examination of the curved periodic structures. The results align well with GLM and GTMM, and the influence of the bending-membrane wave coupling mechanism in the curved periodic structures is investigated by the proposed WFE framework.

In summary, this chapter answered the last research question by demonstrating the accuracy and efficiency of the WFE framework in computing the STL of flat and curved metastructures. The proposed WFE scheme has proved adaptable and accurate for identifying and analyzing the wave coupling phenomena in planar and curved metastructures.

Chapter 6

General Conclusions and Perspectives

6.1 Conclusion

Motivated by advancing the vibroacoustic study of heterogeneous metastructures, this thesis proposes a WFE-based method to predict the vibration and acoustic response of heterogeneous metastructures, particularly on the composite and sandwich structures with high contrasts between layups (HCS) and highly damped components (HDS). The methods also account for heterogeneity and curvature. The thesis makes four main contributions:

1. Implemented a robust and efficient WFE-based scheme that:

    - Addresses the non-linear eigenvalue problem using the Contour Integral method.
    - Employs the energy continuity criterion for accurate wave tracking.
    - Provides stable results for wavenumber space and structural DLF computations in all directions.

2. Assessed the accuracy of existing methods for HCS and HDS:

    - Using WFE as the reference method for comparison, the research examined the robustness and accuracy of two widely used methods for HCS and HDS: the analytical Asymptotic Homogenisation Method (AHM) and the semi-analytical Generalized Laminate Model (GLM). Evaluation metrics included κ-wave space and DLF.
    - Demonstrated that when used within their range of validity, AHM and GLM predictions for various structures align well with the WFE method. However, while the two methods are simple and computationally efficient, they fall short for sandwich structures with thick, highly damped cores and/or flexible cores due to the assumption of uniform core deformation in the thickness direction.
    - In addition, to recall the fact that these methods cannot handle sandwich structures with non-homogeneous components, the example of a metastructure with discrete CLD elements was presented. For the latter, the classical PIM-FEM approach was used to confirm the DLF results from the WFE method.

3. Proposed a computational methodology based on the forced response:

    - Presented a wave synthesis approach using the forced response analysis for HDS and metastructures with in-plane periodicity.

- Demonstrated the accuracy in predicting global DLF confirmed by agreement with the PIM-FEM approach.
- Demonstrated that for lightly damped structures, classical power balance equations suffice for the global DLF calculation. However, for highly dissipative media, the proposed method must be used to account for the excitation type and contributions of all waves.
- Highlighted the importance of including Bloch modes in the forced analysis when large representative UCs are needed to model complex configurations.

4. Demonstrated the robustness of the wave-based approach through the transmission loss computations:

   - By comparison with classical TMM and GLM for various homogeneous HCS and HDS configurations.
   - By studying the importance of symmetric wave to the transmission loss when the cores of the sandwich panel are relatively thick.
   - By investigation on the wave coupling and high-order waves in the laminated structures with complex layups.
   - By comparison with the GTMM for heterogeneous structures depicting complex wave coupling and curvature.

6.2 Perspectives

The central focus of this manuscript revolves around the development of methodologies based on the WFE scheme. As we delve into the industrial application of the approach, future advancements for the computational scheme are:

- The methods proposed in this thesis are generic and are thus applicable in theory to modern lightweight built-up structures, such as stiffened and ribbed panels, extruded panels with attached noise control treatments, and foams with embedded resonators. These complex metastructures often require large representative UCs for accurate modeling in the FE package, which complicates the computation and analysis of their κ-wave space. In particular, it makes wave identification and tracking challenging due to the reflection of waves at the boundary of the Brillouin zone. Future work must address these numerical issues by developing robust methods to handle the complexities inherent in analyzing such metastructures. In particular, the Contour Integral algorithm used in this thesis needs further assessment for these cases.

- Additionally, as computational time becomes a significant concern when dealing with large UCs, future work must also explore reduction schemes to improve efficiency while maintaining accuracy in predicting the vibroacoustic behavior of these lightweight structures.

- Other issues such as accounting for fluid loading and considering various types of generalized excitations must also be handled to render the methods applicable in real-life configurations.

By incorporating these improvements, the proposed methodology will become an efficient tool for analyzing planar periodic structures, thus significantly contributing to the ongoing development of metastructures with excellent vibroacoustic properties.

Chapter 7

Conclusion générale et perspectives

7.1 Conclusion générale

Motivé par l'avancement des études vibroacoustique des métastructures hétérogènes, cette thèse propose une méthode basée sur WFE pour prédire la réponse vibratoire et acoustique des métastructures hétérogènes, en particulier sur les structures composites et sandwich avec des contrastes élevés entre les couches (HCS) et des composants hautement amortis (HDS). Les méthodes prennent également en compte l'hétérogénéité et la courbure. La thèse apporte quatre contributions principales:

1. Implémentation d'un schéma robuste et efficace basé sur le WFE qui:

   - Traite le problème non-linéaire des valeurs propres en utilisant la méthode de l'intégrale de contour.
   - Utilise le critère de continuité énergétique pour un suivi précis des ondes.
   - Fournit des résultats stables pour les calculs de l'espace des nombres d'ondes et du DLF dans toutes les directions.

2. Évaluation de la précision des méthodes existantes pour les HCS et les HDS:

   - En utilisant le WFE comme méthode de référence pour la comparaison, la recherche a évalué la robustesse et la précision de deux méthodes largement utilisées pour les HCS et les HDS: l'AHM et le GLM. Les indicateurs d'évaluation comprenaient l'espace des ondes κ et le DLF.
   - Démontré que, lorsqu'elles sont utilisées dans leur domaine de validité, les prédictions des méthodes AHM et GLM pour diverses structures s'alignent bien avec la méthode WFE. Cependant, bien que ces deux méthodes soient simples et efficaces sur le plan computationnel, elles sont insuffisantes pour les structures sandwich avec des couches centrales épaisses, hautement amorties et/ou flexibles, en raison de l'hypothèse de déformation uniforme du couche centrale dans la direction de l'épaisseur.
   - En outre, pour rappeler le fait que ces méthodes ne peuvent pas traiter les structures sandwich avec des composants non homogènes, l'exemple d'une métastructure avec des éléments d'amortissement en couche contrainte (Constrained Layer Damping, CLD) discrets a été présenté. Pour cette dernière, la méthode classique de PIM basée sur les éléments finis (PIM-FEM) a été utilisée pour confirmer les résultats du DLF obtenus par la méthode WFE.

3. Proposé une méthodologie de calcul basée sur la réponse forcée:

   - Présenté une approche de synthèse d'ondes utilisant l'analyse de la réponse forcée pour les HDS et les métastructures avec périodicité dans le plan.

- Démontré la précision de la prédiction du DLF global, confirmée par concordance avec l'approche PIM-FEM.
- Montré que pour les structures faiblement amorties, les équations classiques de bilan de puissance suffisent pour le calcul du DLF global. Cependant, pour les milieux fortement dissipatifs, la méthode proposée doit être utilisée pour tenir compte du type d'excitation et des contributions de toutes les ondes.
- Mis en avant l'importance d'inclure les modes de Bloch dans l'analyse forcée lorsque de grands UC représentatifs sont nécessaires pour modéliser des configurations complexes.

4. Démontré la robustesse de l'approche basée sur les ondes à travers les calculs de perte de transmission:
   - En comparaison avec les méthodes classiques TMM et GLM pour diverses configurations homogènes de HCS et HDS.
   - En étudiant le couplage des ondes et les ondes d'ordre élevé dans les structures stratifiées avec des sections transversales complexes.
   - En comparaison avec le GTMM pour les structures hétérogènes représentant un couplage d'ondes complexe et une courbure.

7.2 Perspectives

Le foyer central de ce manuscrit tourne autour du développement de méthodologies basées sur le schéma WFE. En explorant l'application industrielle de cette approche, les futurs développements des schémas computationnels incluent:

- Les méthodes proposées dans cette thèse sont générales et donc applicables en théorie aux structures modernes légères telles que les panneaux raidis et nervurés, les panneaux extrudés avec traitements de contrôle du bruit attachés, et les mousses avec résonateurs intégrés. Ces métastructures complexes nécessitent souvent de grandes UCs pour une modélisation précise dans le cadre du FE, ce qui complique le calcul et l'analyse de leur espace d'ondes κ. En particulier, l'identification et le suivi des ondes deviennent difficiles en raison de la réflexion des ondes à la limite de la zone de Brillouin. Les travaux futurs devront résoudre ces problèmes numériques en développant des méthodes robustes pour traiter les complexités inhérentes à l'analyse de telles structures. En particulier, l'algorithme d'intégration de contour utilisé dans cette thèse nécessite une évaluation approfondie pour ces cas.

- De plus, avec le temps de calcul devenant une préoccupation majeure lors du traitement de grandes UCs, les travaux futurs doivent également explorer des schémas de réduction pour améliorer l'efficacité tout en maintenant la précision dans la prédiction du comportement vibroacoustique de ces structures légères.

- En outre, la simulation de courbure peut être intégrée dans le schéma WFE pour modéliser des structures cylindriques et examiner les indicateurs vibroacoustiques pour chaque ordre circonférentiel. Pour le calcul de la perte de transmission, une méthodologie de sommation à travers les ordres circonférentiels pourrait être proposée à l'avenir.

- D'autres problèmes tels que la prise en compte de la charge fluide et la considération de divers types d'excitations généralisées, comme l'excitation "Rain-on-the-Roof", doivent également être abordés pour rendre les méthodes applicables dans des configurations réelles.

En intégrant ces améliorations, la méthodologie proposée deviendra un outil efficace pour l'analyse des structures périodiques planes, contribuant ainsi de manière significative au développement continu des métastructures dotées d'excellentes propriétés vibroacoustiques.

Appendix A

Nomenclature of Asymptotic Homogenization Method

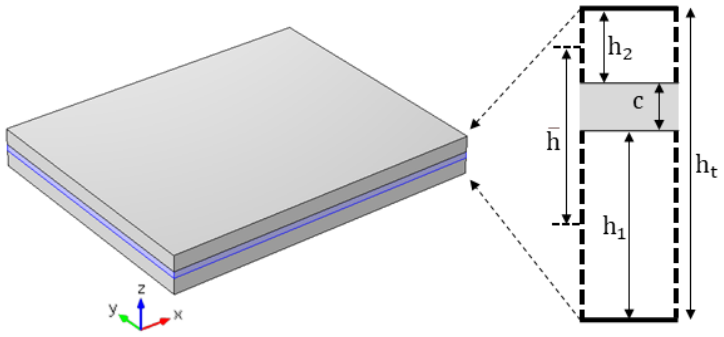

Fig. A.1. Notations for HCS plate along thickness axis.

According to the schematic diagram of a three-layer sandwich panel depicted in Fig. A.1, the nomenclature of the Asymptotic Homogenization Method reads:

- h_1, h_2 and c are respectively the thickness of the bottom and top skins, and of the core; $h_t = h_1+h_2+c$ is the thickness of the overall plate, $\bar{h} = (h_1 + h_2)/2 + c$: distance between the middle plane of the bottom and top skins; $\hat{h} = 1/(h_1^{-1} + h_2^{-1})$.

- $I = I_1 + I_2$ where $I_j = h_j^3/12$, $j = 1, 2$, are the bending inertia of the bottom and top skins; $\mathcal{I} = I + \hat{h}\bar{h}^2$ is the bending inertia of the whole laminate; $a = \mathcal{I}/(\mathcal{I} - I)$.

- E, ν, and $E_0 = E/(1 - \nu^2)$ stand respectively for the Young modulus, the Poisson ratio, and the "plate modulus" of the two stiff skins.

- μ is the shear modulus of the soft central layer; is real constant when the central layer is elastic; is complex and frequency-dependent when the central layer is visco-elastic.

- $K = \mu\bar{h}^2/c$: effective shear rigidity of the core, $A = K/E_0 I$, $\Omega = \Omega^2\rho_t h_t/K$.

- $\rho_t = ((h_1 + h_2)\rho + c\rho_c)/h_t$: mean density of the laminate; ρ and ρ_c are respectively the density of the stiff skins and of the core.

- (x, y) are the in-plane variables, z is the out-of-plane variable. The origin of the frame is on the geometric middle plane of the laminated plate. All the differential operators, such as ∇, div, Δ, are in-plane operators operating on the (x, y) variables.

- $\mathscr{E}$ is the specific differential operator defined by $\mathscr{E}(\boldsymbol{u}) = (1-\nu)\boldsymbol{e}(\boldsymbol{u}) + \nu \mathrm{div}(\boldsymbol{u})\boldsymbol{I}$, where $\boldsymbol{e}(\boldsymbol{u}) = (\boldsymbol{\nabla u} +^t \boldsymbol{\nabla} u)/2$ is the in-plane strain tensor and $\boldsymbol{I}$ is the 2D unit tensor.

Appendix B

Equilibrium equations in General Laminate Model

B.1 Governing Equation

The layered construction of a composite panel is considered, in general, asymmetrical as represented in Fig. B.1.

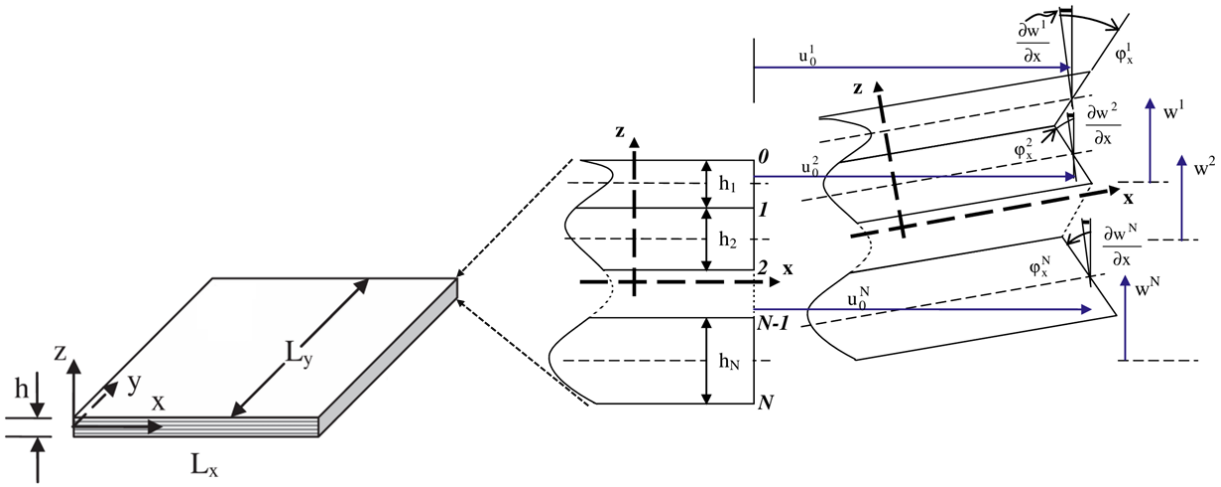

Fig. B.1. Schematic of an N-layer discrete laminate before and after deformation [29].

The membrane and bending displacements as well as rotations are assumed in each layer; as a consequence the displacement field of the i-th discrete layer of the panel is of Mindlin's type:

$$\begin{cases} u^i(x,y,z) = u_0^i(x,y) + z\varphi_x^i(x,y) \\ v^i(x,y,z) = v_0^i(x,y) + z\varphi_y^i(x,y) \\ w^i(x,y,z) = w_0^i(x,y) \end{cases} \tag{B.1}$$

The resultant stress forces and moments of any laminate layer are defined by:

$$\begin{aligned} Q_x^i(x,y,z) &= \int_z \tau_{xz}\,dz = \sum_{k=1}^{n_i} \int_{h_{lk}^i}^{h_{uk}^i} \tau_{xz}^k\,dz \\ Q_y^i(x,y,z) &= \int_z \tau_{yz}\,dz = \sum_{k=1}^{n_i} \int_{h_{lk}^i}^{h_{uk}^i} \tau_{yz}^k\,dz \end{aligned} \tag{B.2}$$

$$\begin{Bmatrix} N_x^i \\ N_y^i \\ N_{xy}^i \end{Bmatrix} = \int_z \begin{Bmatrix} \sigma_x^i \\ \sigma_y^i \\ \tau_{xy}^i \end{Bmatrix} dz = \sum_{k=1}^{n_i} \int_{h_{lk}^i}^{h_{uk}^i} \begin{Bmatrix} \sigma_x^i \\ \sigma_y^i \\ \tau_{xy}^i \end{Bmatrix} dz$$
$$\begin{Bmatrix} M_x^i \\ M_y^i \\ M_{xy}^i \end{Bmatrix} = \int_z \begin{Bmatrix} \sigma_x^i \\ \sigma_y^i \\ \tau_{xy}^i \end{Bmatrix} z dz = \sum_{k=1}^{n_i} \int_{h_{lk}^i}^{h_{uk}^i} \begin{Bmatrix} \sigma_x^i \\ \sigma_y^i \\ \tau_{xy}^i \end{Bmatrix} z dz \tag{B.3}$$

where n_i is the number of plies in a layer.

The integral limits h_{uk}^i and h_{uk}^i in relations B.2 and B.3 are computed using the following relations:

$$h_{uk}^i = z^{i-1} + \sum_{j=1}^{k} h_j^i$$
$$h_{lk}^i = z^{i-1} + \sum_{j=0}^{k-1} h_j^i \tag{B.4}$$

where h_j^i is the thickness of the lamina **j** of the layer **i** ($h_0^i = 0$) and z^{i-1} is the position of the $(i-1)$ surface face delimiting a layer.

The transverse shear stress forces are defined by the following relations:

$$\begin{Bmatrix} Q_x^i \\ Q_y^i \end{Bmatrix} = \begin{bmatrix} F_{45} & F_{55} \\ F_{44} & F_{45} \end{bmatrix}^i \begin{Bmatrix} w_{z,y} + \varphi_y \\ w_{z,x} + \varphi_x \end{Bmatrix}^i \tag{B.5}$$

and the in-plane stress forces:

$$\begin{Bmatrix} N_x^i \\ N_y^i \\ N_{xy}^i \end{Bmatrix} = \begin{bmatrix} A_{11} & A_{12} & A_{16} \\ A_{12} & A_{22} & A_{26} \\ A_{16} & A_{26} & A_{66} \end{bmatrix}^i \begin{Bmatrix} u_x \\ v_y \\ u_{x,y} + v_{y,x} \end{Bmatrix}^i + \begin{bmatrix} B_{11} & B_{12} & B_{16} \\ B_{12} & B_{22} & B_{26} \\ B_{16} & B_{26} & B_{66} \end{bmatrix}^i \begin{Bmatrix} \varphi_{x,x} \\ \varphi_{y,y} \\ \varphi_{x,y} + \varphi_{y,x} \end{Bmatrix}^i \tag{B.6}$$

as well as the stress moments:

$$\begin{Bmatrix} M_x^i \\ M_y^i \\ M_{xy}^i \end{Bmatrix} = \begin{bmatrix} B_{11} & B_{12} & B_{16} \\ B_{12} & B_{22} & B_{26} \\ B_{16} & B_{26} & B_{66} \end{bmatrix}^i \begin{Bmatrix} u_x \\ v_y \\ u_{x,y} + v_{y,x} \end{Bmatrix}^i + \begin{bmatrix} D_{11} & D_{12} & D_{16} \\ D_{12} & D_{22} & D_{26} \\ D_{16} & D_{26} & D_{66} \end{bmatrix}^i \begin{Bmatrix} \varphi_{x,x} \\ \varphi_{y,y} \\ \varphi_{x,y} + \varphi_{y,x} \end{Bmatrix}^i \tag{B.7}$$

The inertial terms derived in the equilibrium Equation 2.22 are expressed by the following relations:

$$m_s^i = \sum_{j=1}^{n} \left[\rho_j \left(h_{uj} - h_{lj}\right)\right]^i$$
$$I_z^i = \sum_{j=1}^{n} \left[\rho_j \frac{\left(h_{uj}^3 - h_{lj}^3\right)}{3}\right]^i$$
$$I_{z2}^i = \sum_{j=1}^{n} \left[\rho_j \frac{\left(h_{uj}^2 - h_{lj}^2\right)}{2}\right]^i \tag{B.8}$$

where m_s^i is the mass per unit area, I_z^i and I_z^{i2} are the rotational inertia and ρ_j is the mass density of the j-th lamina. The rotational inertia I_{z2}^i is zero for symmetrically laminated composite sandwich panels. The detailed elastic constants derived in B.5, B.6 and B.7 are defined by the following relations [29]:

$$\begin{cases} A^i_{\alpha\beta} = \sum_{k=1}^{n_i} \left[Q^k_{\alpha\beta}(h_{uk} - h_{lk}) \right]^i \\ B^i_{\alpha\beta} = \sum_{k=1}^{n_i} \left[Q^k_{\alpha\beta} \frac{h^2_{uk} - h^2_{lk}}{2} \right]^i \quad \alpha, \beta = 1, 2, 6 \\ B^i_{\alpha\beta} = \sum_{k=1}^{n_i} \left[Q^k_{\alpha\beta} \frac{h^3_{uk} - h^3_{lk}}{3} \right]^i \end{cases} \tag{B.9}$$

$$\begin{cases} F^i_{\alpha\beta} = \sum_{k=1}^{n_i} \left[C^k_{\alpha\beta}(h_{uk} - h_{lk}) \right]^i \\ H^i_{\alpha\beta} = \sum_{k=1}^{n_i} \left[C^k_{\alpha\beta} \frac{h^2_{uk} - h^2_{lk}}{2} \right]^i \quad \alpha, \beta = 4, 5 \end{cases} \tag{B.10}$$

In Eq. B.9, $\left[Q^k_{\alpha\beta} \right]^i$ are the elastic constants of the k the lamina of layer i and are defined by the following relations [208]:

$$\begin{aligned} \left[Q^k_{11} \right]^i &= \left[C^k_l c_4 + C^k_T s^4 + 2(C^k_{LT} + 2G^k_{LT}) s^2 c^2 \right]^i \\ \left[Q^k_{12} \right]^i &= \left[(C^k_l - C^k_T - 4G^k_{LT}) s^2 c^2 + C^k_{LT}(c^4 + s^4) \right]^i \\ \left[Q^k_{16} \right]^i &= \left[(C^k_L - C^k_{LT} - 2G^k_{LT}) s c^3 + (C^k_{LT} - C^k_T + 2G^k_{LT}) s^3 c \right]^i \\ \left[Q^k_{22} \right]^i &= \left[C^k_l s_4 + C^k_T c^4 + 2(C^k_{LT} + 2G^k_{LT}) s^2 c^2 \right]^i \\ \left[Q^k_{26} \right]^i &= \left[(C^k_L - C^k_{LT} - 2G^k_{LT}) s^3 c + (C^k_{LT} - C^k_T + 2G^k_{LT}) s c^3 \right]^i \\ \left[Q^k_{66} \right]^i &= \left[(C^k_l + C^k_T - 2(C^k_{LT} + G^k_{LT})) s^2 c^2 + G^k_{LT}(c^4 + s^4) \right]^i \end{aligned} \tag{B.11}$$

with $c = cos\theta_k$, $s = sin\theta_k$, θ_k denotes the stacking angle of the k-th layer as depicted in Fig. B.2.

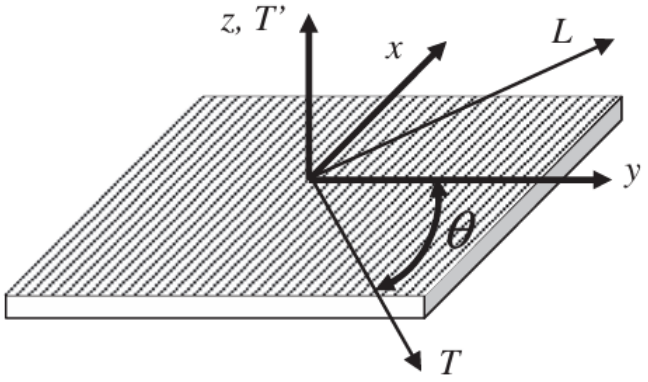

Fig. B.2. Orthotropy directions of a layer $(x, y, z) \rightarrow (L, T, T)$ [29].

For flat panel:

$$\begin{aligned}\left[C_L^k\right]^i &= \left(\frac{E_L^k}{1-\nu_{LT}^k\nu_{TL}^k}\right)^i \\ \left[C_T^k\right]^i &= \left(\frac{E_T^k}{1-\nu_{LT}^k\nu_{TL}^k}\right)^i \\ \left[C_L T^k\right]^i &= \left(\frac{\nu_{LT}^k E_{LT}^k}{1-\nu_{LT}^k\nu_{TL}^k}\right)^i\end{aligned} \tag{B.12}$$

and $\left[C_{\alpha\beta}^k\right]^i$ are the transverse shear elastic constants of the k-th lamina of the layer i and are defined by [208]:

$$\begin{aligned}\left[C_{44}^k\right]^i &= \left[G_{TZ}^k c^2 + G_{LZ}^k s^2\right]^i \\ \left[C_{45}^k\right]^i &= \left[(G_{LZ}^k - G_{TZ}^k)sc\right]^i \\ \left[C_{55}^k\right]^i &= \left[G_{LZ}^k c^2 + G_{TZ}^k s^2\right]^i\end{aligned} \tag{B.13}$$

The dynamic equilibrium equations of the structure are rewritten as:

$$\begin{aligned}A_{11}u_{x,xx} + 2A_{16}u_{y,yy} + A_{66}u_{x,yy} + A_{16}v_{y,xx} + (A_{12}+A_{66})\,v_{y,xy} + A_{26}v_{y,yy} + B_{11} \\ \varphi_{x,xx} + 2B_{16}\varphi_{x,xy} + B_{66}\varphi_{x,yy} + B_{16}\varphi_{y,xx} + (B_{12}+B_{66})\,\varphi_{y,xy} + B_{26}\varphi_{y,yy} = 0\end{aligned} \tag{B.14}$$

$$\begin{aligned}A_{16}u_{x,xx} + (A_{12}+A_{66})\,u_{x,xy} + A_{26}u_{x,yy} + A_{66}v_{y,xx} + 2A_{26}v_{y,xy} + A_{22}v_{y,yy} + B_{16} \\ \varphi_{x,xx} + (B_{12}+B_{66})\,\varphi_{x,xy} + B_{26}\varphi_{x,yy} + B_{66}\varphi_{y,xx} + 2B_{26}\varphi_{y,xy} + B_{22}\varphi_{y,yy} = 0\end{aligned} \tag{B.15}$$

$$\begin{aligned}\left[F_{55}w_{z,xx} + 2F_{45}w_{z,xy} + F_{44}w_{z,yy} + F_{55}\varphi_{x,x} + F_{45}\varphi_{x,y} + F_{45}\varphi_{y,x} + F_{44}\varphi_{y,y}\right]^i + F_z^i \\ -F_z^{i-1} + (m_s w)^i\, w^2 = 0\end{aligned} \tag{B.16}$$

$$\begin{aligned}\left[B_{11}u_{x,xx} + 2B_{16}u_{x,xy} + B_{66}u_{x,yy} + B_{16}v_{y,xx} + (B_{12}+B_{66})\,v_{y,xy} + B_{26}v_{y,yy} + \right. \\ D_{11}\varphi_{x,xx} + 2D_{16}\varphi_{x,xy} + D_{66}\varphi_{x,yy} + D_{16}\varphi_{y,xx} + (D_{12}+D_{66})\,\varphi_{y,xy} + D_{26}\varphi_{y,yy} \\ \left. -F_{55}w_{z,x} - F_{45}w_{z,y} - F_{55}\varphi_x - F_{45}\varphi_y\right]^i + z^i F_x^i - z^{i-1}F_x^{i-1} + (I_z\varphi_x + I_{z2}u)^i\,\omega^2 = 0\end{aligned} \tag{B.17}$$

$$\begin{aligned}\left[B_{16}u_{x,xx} + (B_{12}+B_{66})\,u_{x,xy} + B_{26}u_{x,yy} + B_{66}v_{y,xx} + 2B_{26}v_{y,xy} + B_{22}v_{y,yy}\right. \\ +D_{16}\varphi_{x,xx} + (D_{12}+D_{66})\,\varphi_{x,xy} + D_{26}\varphi_{x,yy} + D_{66}\varphi_{y,xx} + 2D_{26}\varphi_{y,xy} + D_{22}\varphi_{y,yy} \\ \left. -F_{45}w_{z,x} - F_{44}w_{z,y} - F_{45}\varphi_x - F_{44}\varphi_y\right]^i + z^i F_y^i - z^{i-1}F_y^{i-1} + \left(I_z\varphi_y + I_{z2}v\right)^i\,\omega^2 = 0\end{aligned} \tag{B.18}$$

B.2 Dispersion Equation Matrices

The matrices $[\mathbf{A}_0]$, $[\mathbf{A}_1]$, $[\mathbf{A}_2]$ used in Eq. 2.25 in2 are real square matrices of dimension $5N + 3\,(N-1)$ defined as follows:

$$[\mathbf{A}_0] = \begin{bmatrix} [\mathbf{A}] & [\mathbf{F}] \\ [\mathbf{F}] & [\mathbf{0}] \end{bmatrix} \tag{B.19}$$

$$[\mathbf{A}_1] = \begin{bmatrix} [\mathbf{A}_1]^1 & \mathbf{0} & \mathbf{0} & \mathbf{0} & \mathbf{0} \\ \mathbf{0} & [\mathbf{A}_1]^2 & \mathbf{0} & \mathbf{0} & \mathbf{0} \\ \mathbf{0} & \mathbf{0} & \mathbf{0} & \mathbf{0} & \mathbf{0} \\ \mathbf{0} & \mathbf{0} & \mathbf{0} & [\mathbf{A}_1]^N & \mathbf{0} \\ \mathbf{0} & \mathbf{0} & \mathbf{0} & \mathbf{0} & [\mathbf{0}] \end{bmatrix} \tag{B.20}$$

$$[\mathbf{A}_2] = \begin{bmatrix} [\mathbf{A}_2]^1 & \mathbf{0} & \mathbf{0} & \mathbf{0} & \mathbf{0} \\ \mathbf{0} & [\mathbf{A}_2]^2 & \mathbf{0} & \mathbf{0} & \mathbf{0} \\ \mathbf{0} & \mathbf{0} & \mathbf{0} & \mathbf{0} & \mathbf{0} \\ \mathbf{0} & \mathbf{0} & \mathbf{0} & [\mathbf{A}_2]^N & \mathbf{0} \\ \mathbf{0} & \mathbf{0} & \mathbf{0} & \mathbf{0} & [\mathbf{0}] \end{bmatrix} \tag{B.21}$$

where:

$$[\mathbf{A}] = \begin{bmatrix} [\mathbf{A}_0]^1 & \mathbf{0} & \mathbf{0} & \mathbf{0} & \mathbf{0} & \mathbf{0} \\ \mathbf{0} & [\mathbf{A}_0]^2 & \mathbf{0} & \mathbf{0} & \mathbf{0} & \mathbf{0} \\ \mathbf{0} & \mathbf{0} & [\mathbf{A}_0]^3 & \mathbf{0} & \mathbf{0} & \mathbf{0} \\ \mathbf{0} & \mathbf{0} & \mathbf{0} & \mathbf{0} & \mathbf{0} & \mathbf{0} \\ \mathbf{0} & \mathbf{0} & \mathbf{0} & \mathbf{0} & [\mathbf{A}_0]^{N-1} & \mathbf{0} \\ \mathbf{0} & \mathbf{0} & \mathbf{0} & \mathbf{0} & \mathbf{0} & [\mathbf{A}_0]^N \end{bmatrix} \tag{B.22}$$

$$[\mathbf{F}] = \begin{bmatrix} [\mathbf{F}_0]^1 & \mathbf{0} & \mathbf{0} & \mathbf{0} & \mathbf{0} & \mathbf{0} \\ -[\mathbf{F}_0]^1 & [\mathbf{F}_0]^2 & \mathbf{0} & \mathbf{0} & \mathbf{0} & \mathbf{0} \\ \mathbf{0} & -[\mathbf{F}_0]^2 & [\mathbf{A}_0]^3 & \mathbf{0} & \mathbf{0} & \mathbf{0} \\ \mathbf{0} & \mathbf{0} & \mathbf{0} & \mathbf{0} & \mathbf{0} & \mathbf{0} \\ \mathbf{0} & \mathbf{0} & \mathbf{0} & \mathbf{0} & -[\mathbf{F}_0]^{N-2} & [\mathbf{F}_0]^{N-1} \\ \mathbf{0} & \mathbf{0} & \mathbf{0} & \mathbf{0} & \mathbf{0} & -[\mathbf{F}_0]^{N-1} \end{bmatrix} \tag{B.23}$$

and

$$[\mathbf{A}_0]^i = \begin{bmatrix} a_{11} & \mathbf{0} & \mathbf{0} & a_{14} & \mathbf{0} \\ \mathbf{0} & a_{22} & \mathbf{0} & \mathbf{0} & a_{25} \\ \mathbf{0} & \mathbf{0} & a_{33} & \mathbf{0} & \mathbf{0} \\ a_{14} & \mathbf{0} & \mathbf{0} & a_{44} & a_{45} \\ \mathbf{0} & a_{25} & \mathbf{0} & a_{45} & a_{55} \end{bmatrix}^i \tag{B.24}$$

$$[\mathbf{A}_1]^i = \begin{bmatrix} a_{11} & \mathbf{0} & \mathbf{0} & \mathbf{0} & \mathbf{0} \\ \mathbf{0} & \mathbf{0} & \mathbf{0} & \mathbf{0} & \mathbf{0} \\ \mathbf{0} & \mathbf{0} & \mathbf{0} & \alpha_{34} & \alpha_{35} \\ \mathbf{0} & \mathbf{0} & -\alpha_{34} & \mathbf{0} & \mathbf{0} \\ \mathbf{0} & \mathbf{0} & -\alpha_{35} & \mathbf{0} & \mathbf{0} \end{bmatrix}^i \tag{B.25}$$

$$[\mathbf{A}_2]^i = \begin{bmatrix} \beta_{11} & \beta_{12} & \mathbf{0} & \beta_{14} & \beta_{15} \\ \beta_{12} & \beta_{22} & \mathbf{0} & \beta_{24} & \beta_{25} \\ \mathbf{0} & \mathbf{0} & \beta_{33} & \mathbf{0} & \mathbf{0} \\ \beta_{14} & \beta_{24} & \mathbf{0} & \beta_{44} & \beta_{45} \\ \beta_{15} & \beta_{25} & \mathbf{0} & \beta_{45} & \beta_{55} \end{bmatrix}^i \tag{B.26}$$

with coefficients $a^i_{\gamma\delta}$, $\alpha^i_{\gamma\delta}$ and $\beta^i_{\gamma\delta}$ defined as follows:

$$\begin{aligned} a^i_{11} = m_s\omega^2;\ a^i_{14} = I_{z2}\omega^2;\ a^i_{22} = m_s\omega^2;\ a^i_{25} = I_{z2}\omega^2;\ a^i_{33} = m_s\omega^2; \\ a^i_{44} = I_z\omega^2 - F_{55};\ a^i_{45} = -F_{45};\ a^i_{55} = I_z\omega^2 - F_{44}; \end{aligned} \tag{B.27}$$

$$\begin{aligned} \alpha^i_{34} = -F^i_{55}cos\varphi - F^i_{45}sin\varphi \\ \alpha^i_{35} = -F^i_{44}sin\varphi - F^i_{45}cos\varphi \end{aligned} \tag{B.28}$$

and

$$\begin{aligned} \beta^i_{11} &= A^i_{11}cos^2\varphi + 2A^i_{16}cos\varphi sin\varphi + A^i_{66}sin^2\varphi \\ \beta^i_{12} &= A^i_{16}cos^2\varphi + (A_{12} + A_{66})^i cos\varphi sin\varphi + A^i_{26}sin^2\varphi \\ \beta^i_{14} &= B^i_{11}cos^2\varphi + 2B^i_{16}cos\varphi sin\varphi + B^i_{66}sin^2\varphi \\ \beta^i_{15} &= B^i_{16}cos^2\varphi + (B_{12} + B_{66})^i cos\varphi sin\varphi + B^i_{26}sin^2\varphi \\ \beta^i_{22} &= A^i_{66}cos^2\varphi + 2A^i_{26}cos\varphi sin\varphi + A^i_{22}sin^2\varphi \\ \beta^i_{24} &= B^i_{16}cos^2\varphi + (B_{12} + B_{66})^i cos\varphi sin\varphi + B^i_{26}sin^2\varphi \\ \beta^i_{25} &= B^i_{66}cos^2\varphi + 2B^i_{26}cos\varphi sin\varphi + B^i_{22}sin^2\varphi \\ \beta^i_{33} &= F^i_{55}cos^2\varphi + 2F^i_{45}cos\varphi sin\varphi + F^i_{44}sin^2\varphi \\ \beta^i_{44} &= D^i_{11}cos^2\varphi + 2D^i_{16}cos\varphi sin\varphi + D^i_{66}sin^2\varphi \\ \beta^i_{45} &= D^i_{16}cos^2\varphi + (D_{12} + D_{66})^i cos\varphi sin\varphi + D^i_{26}sin^2\varphi \\ \beta^i_{55} &= D^i_{66}cos^2\varphi + 2D^i_{26}cos\varphi sin\varphi + D^i_{22}sin^2\varphi \end{aligned} \tag{B.29}$$

Appendix C

Formulation of the matrices in Eq. 2.37

Fig. 2.5 is first recalled for a clear presentation of the formulation of the matrices in Eq. 2.37.

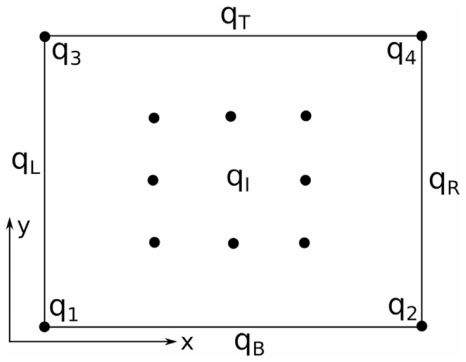

Fig. C.1. Nodes definition of unit cell in two-dimensional periodic structure [84].

Since the internal nodes of the UC are condensed into the reduced dynamic stiffness matrix 2.32 by the dynamic condensation technique, $\widetilde{\mathbf{D}}_c$ can be partitioned as follows:

$$\begin{bmatrix} \widetilde{\mathbf{D}}_{11} & \widetilde{\mathbf{D}}_{12} & \widetilde{\mathbf{D}}_{13} & \widetilde{\mathbf{D}}_{14} & \widetilde{\mathbf{D}}_{1L} & \widetilde{\mathbf{D}}_{1B} & \widetilde{\mathbf{D}}_{1R} & \widetilde{\mathbf{D}}_{1T} \\ \widetilde{\mathbf{D}}_{21} & \widetilde{\mathbf{D}}_{22} & \widetilde{\mathbf{D}}_{23} & \widetilde{\mathbf{D}}_{24} & \widetilde{\mathbf{D}}_{2L} & \widetilde{\mathbf{D}}_{2B} & \widetilde{\mathbf{D}}_{2R} & \widetilde{\mathbf{D}}_{2T} \\ \widetilde{\mathbf{D}}_{31} & \widetilde{\mathbf{D}}_{32} & \widetilde{\mathbf{D}}_{33} & \widetilde{\mathbf{D}}_{34} & \widetilde{\mathbf{D}}_{3L} & \widetilde{\mathbf{D}}_{3B} & \widetilde{\mathbf{D}}_{3R} & \widetilde{\mathbf{D}}_{3T} \\ \widetilde{\mathbf{D}}_{41} & \widetilde{\mathbf{D}}_{42} & \widetilde{\mathbf{D}}_{43} & \widetilde{\mathbf{D}}_{44} & \widetilde{\mathbf{D}}_{4L} & \widetilde{\mathbf{D}}_{4B} & \widetilde{\mathbf{D}}_{4R} & \widetilde{\mathbf{D}}_{4T} \\ \widetilde{\mathbf{D}}_{L1} & \widetilde{\mathbf{D}}_{L2} & \widetilde{\mathbf{D}}_{L3} & \widetilde{\mathbf{D}}_{L4} & \widetilde{\mathbf{D}}_{LL} & \widetilde{\mathbf{D}}_{LB} & \widetilde{\mathbf{D}}_{LR} & \widetilde{\mathbf{D}}_{LT} \\ \widetilde{\mathbf{D}}_{B1} & \widetilde{\mathbf{D}}_{B2} & \widetilde{\mathbf{D}}_{B3} & \widetilde{\mathbf{D}}_{B4} & \widetilde{\mathbf{D}}_{BL} & \widetilde{\mathbf{D}}_{BB} & \widetilde{\mathbf{D}}_{BR} & \widetilde{\mathbf{D}}_{BT} \\ \widetilde{\mathbf{D}}_{R1} & \widetilde{\mathbf{D}}_{R2} & \widetilde{\mathbf{D}}_{R3} & \widetilde{\mathbf{D}}_{R4} & \widetilde{\mathbf{D}}_{RL} & \widetilde{\mathbf{D}}_{RB} & \widetilde{\mathbf{D}}_{RR} & \widetilde{\mathbf{D}}_{RT} \\ \widetilde{\mathbf{D}}_{T1} & \widetilde{\mathbf{D}}_{T2} & \widetilde{\mathbf{D}}_{T3} & \widetilde{\mathbf{D}}_{T4} & \widetilde{\mathbf{D}}_{TL} & \widetilde{\mathbf{D}}_{TB} & \widetilde{\mathbf{D}}_{TR} & \widetilde{\mathbf{D}}_{TT} \end{bmatrix} \begin{pmatrix} \mathbf{q}_1 \\ \mathbf{q}_2 \\ \mathbf{q}_3 \\ \mathbf{q}_4 \\ \mathbf{q}_L \\ \mathbf{q}_B \\ \mathbf{q}_R \\ \mathbf{q}_T \end{pmatrix} = \begin{pmatrix} \mathbf{f}_1 \\ \mathbf{f}_2 \\ \mathbf{f}_3 \\ \mathbf{f}_4 \\ \mathbf{f}_L \\ \mathbf{f}_B \\ \mathbf{f}_R \\ \mathbf{f}_T \end{pmatrix} \tag{C.1}$$

Using the transformation matrices Λ_L and Λ_R defined in Eq. 2.35 and Eq. 2.34, the product $\mathbf{\Lambda}_L\left(\lambda_x, \lambda_y\right)\mathbf{D}\left(\omega\right)\mathbf{\Lambda}_R\left(\lambda_x, \lambda_y\right)$ can be developed using the decomposition proposed for $\mathbf{D}$. Therefore, the coefficients A, B and C are constant in a given $\left(\omega, \lambda_y\right)$ formulation. Eq. 2.36 becomes a quadratic EVP in λ_x, written:

$$\left(\lambda_x \begin{bmatrix} \mathbf{A}_{11} & \mathbf{A}_{1L} & \mathbf{A}_{1B} \\ \mathbf{A}_{L1} & \mathbf{A}_{LL} & \mathbf{A}_{LB} \\ \mathbf{A}_{B1} & \mathbf{A}_{BL} & \mathbf{A}_{BB} \end{bmatrix} + \begin{bmatrix} \mathbf{B}_{11} & \mathbf{B}_{1L} & \mathbf{B}_{1B} \\ \mathbf{B}_{L1} & \mathbf{B}_{LL} & \mathbf{B}_{LB} \\ \mathbf{B}_{B1} & \mathbf{B}_{BL} & \mathbf{B}_{BB} \end{bmatrix} + \frac{1}{\lambda_x} \begin{bmatrix} \mathbf{C}_{11} & \mathbf{C}_{1L} & \mathbf{C}_{1B} \\ \mathbf{C}_{L1} & \mathbf{C}_{LL} & \mathbf{C}_{LB} \\ \mathbf{C}_{B1} & \mathbf{C}_{BL} & \mathbf{C}_{BB} \end{bmatrix}\right)\begin{pmatrix} \mathbf{q}_1 \\ \mathbf{q}_L \\ \mathbf{q}_B \end{pmatrix} = \mathbf{0} \tag{C.2}$$

where λ_x coefficients are:

$$\begin{aligned}
\mathbf{A}_{11} &= \mathbf{D}_{12} + \mathbf{D}_{34} + \mathbf{D}_{32}\lambda_y^{-1} + \mathbf{D}_{14}\lambda_y \\
\mathbf{A}_{1L} &= \mathbf{D}_{1R} + \mathbf{D}_{3R}\lambda_y^{-1} \\
\mathbf{A}_{L1} &= \mathbf{D}_{L2} + \mathbf{D}_{L4}\lambda_y \\
\mathbf{A}_{LL} &= \mathbf{D}_{LR} \\
\mathbf{A}_{B1} &= \mathbf{D}_{B2} + \mathbf{D}_{T4} + \mathbf{D}_{T2}\lambda_y^{-1} + \mathbf{D}_{B4}\lambda_y \\
\mathbf{A}_{BL} &= \mathbf{D}_{BR} + \mathbf{D}_{TR}\lambda_y^{-1} \\
\mathbf{A}_{1B} &= \mathbf{A}_{LB} = \mathbf{A}_{BB} = \mathbf{0}
\end{aligned} \tag{C.3}$$

the constant coefficients are:

$$\begin{aligned}
\mathbf{B}_{11} &= \mathbf{D}_{11} + \mathbf{D}_{22} + \mathbf{D}_{33} + \mathbf{D}_{44} + (\mathbf{D}_{31} + \mathbf{D}_{42})\,\lambda_y^{-1} + (\mathbf{D}_{13} + \mathbf{D}_{24})\,\lambda_y \\
\mathbf{B}_{1L} &= \mathbf{D}_{1L} + \mathbf{D}_{2R} + (\mathbf{D}_{3L} + \mathbf{D}_{4R})\,\lambda_y^{-1} \\
\mathbf{B}_{1B} &= \mathbf{D}_{1B} + \mathbf{D}_{3T} + \mathbf{D}_{3B}\lambda_y^{-1} + \mathbf{D}_{1T}\lambda_y \\
\mathbf{B}_{L1} &= \mathbf{D}_{L1} + \mathbf{D}_{R2} + \mathbf{D}_{L3}\lambda_y + \mathbf{D}_{R4}\lambda_y \\
\mathbf{B}_{LL} &= \mathbf{D}_{LL} + \mathbf{D}_{RR} \\
\mathbf{B}_{LB} &= \mathbf{D}_{LB} + \mathbf{D}_{LT}\lambda_y \\
\mathbf{B}_{B1} &= \mathbf{B}_{B1} + \mathbf{B}_{T3} + \mathbf{B}_{T1} + \mathbf{B}_{B3}\lambda_y \\
\mathbf{B}_{BL} &= \mathbf{B}_{BL} + \mathbf{B}_{TL}\lambda_y^{-1} \\
\mathbf{B}_{BB} &= \mathbf{B}_{BB} + \mathbf{B}_{TT} + \mathbf{B}_{TB}\lambda_y^{-1} + \mathbf{B}_{BT}\lambda_y
\end{aligned} \tag{C.4}$$

and the coefficients in $\frac{1}{\lambda_x}$ are:

$$\begin{aligned}
\mathbf{C}_{11} &= \mathbf{D}_{21} + \mathbf{D}_{43} + \mathbf{D}_{41}\lambda_y^{-1} + \mathbf{D}_{23}\lambda_y \\
\mathbf{C}_{1L} &= \mathbf{D}_{2L} + \mathbf{D}_{4L}\lambda_y^{-1} \\
\mathbf{C}_{1B} &= \mathbf{D}_{2B} + \mathbf{D}_{4T}\lambda_y \\
\mathbf{C}_{L1} &= \mathbf{D}_{R1} + \mathbf{D}_{R3\,y} \\
\mathbf{C}_{LL} &= \mathbf{D}_{RR} \\
\mathbf{C}_{LB} &= \mathbf{D}_{RB} + \mathbf{D}_{RT}\lambda_y \\
\mathbf{C}_{B1} &= \mathbf{C}_{BL} = \mathbf{C}_{BB} = \mathbf{0}
\end{aligned} \tag{C.5}$$

List of Figures

List of Tables

Bibliography

[1] M. Behl, A. Lendlein, Shape-memory polymers, Materials Today 10 (2007) 20–28. doi:10.1016/S1369-7021(07)70047-0.

[2] B. Dietsch, T. Tong, A review - features and benefits of shape memory polymers (smps), Journal of Advanced Materials 39 (2007) 3–12. doi:https://www.scopus.com/record/display.uri?eid=2-s2.0-34147169488&origin=inward.

[3] L. Sun, W. Huang, Z. Ding, Y. Zhao, C. Wang, H. Purnawali, C. Tang, Stimulus-responsive shape memory materials: A review, Materials Design 33 (2012) 577–640. doi:10.1016/j.matdes.2011.04.065.

[4] Y. Liu, H. Du, L. Liu, J. Leng, Shape memory polymers and their composites in aerospace applications: A review, Smart Materials and Structures 23 (2014) 023001. doi:10.1088/0964-1726/23/2/023001.

[5] P. Butaud, E. Foltête, M. Ouisse, Sandwich structures with tunable damping properties: On the use of shape memory polymer as viscoelastic core, Composite Structures 153 (2016) 401–408. doi:10.1016/j.compstruct.2016.06.040.

[6] Glass-Genius-Company, Laminated glass vs tempered glass: The difference, https://blog.51cto.com/shijianfeng/4968624, Website last accessed on 22-06-15 (2022).

[7] J. Ryu, S.-H. Lho, C.-H. Lee, Y. K. Ju, Flexural behavior of prestressed sandwich plate system composite beams, Engineering Structures 215 (2020) 110705. doi:10.1016/j.engstruct.2020.110705.

[8] I. Elishakoff, T. Fang, C. Jiang, Free, forced, and random vibrations of a beam composed of highly contrasting materials, Applied Mathematical Modelling 89 (2) (2021) 1696–1720. doi:10.1016/j.apm.2020.07.050.

[9] J. Hooper, On the bending of architectural laminated glass, International Journal of Mechanical Sciences 15 (1973) 309–323. doi:10.1016/0020-7403(73)90012-X.

[10] D. Cui, M. Ichchou, A.-M. Zine, N. Atalla, Multi-scale dynamics and nonlinear eigenvalue problem of heterogeneous metastructures using a wave finite element scheme and modal strain energy method, Marrakech, Morocco, 2024. doi:10.1007/978-981-99-7958-5_11.

[11] H. S. Norville, K. W. King, J. L. Swofford, Behavior and strength of laminated glass, Journal of Engineering Mechanics 124 (1998) 46–53. doi:10.1061/(ASCE)0733-9399(1998)124:1(46).

[12] C. Boutin, K. Viverge, Generalized plate model for highly contrasted laminates, European Journal of Mechanics - A/Solids 55 (2016) 149–166. doi:10.1016/j.euromechsol.2015.08.008.

[13] C. Boutin, K. Viverge, S. Hans, Dynamics of contrasted stratified elastic and viscoelastic plates - application to laminated glass, Composites Part B: Engineering 212 (11) (2021) 108551. doi:10.1016/j.compositesb.2020.108551.

[14] D. Ross, E. E. Ungar, E. Kerwin, Damping of plate flexural vibrations by means of viscoelastic laminae, Structural Damping, ASME 3 (1959) 44–87. doi:10.1121/1.1907821.

[15] E. M. Kerwin, Damping of flexural waves by a constrained viscoelastic layer, Journal of the Acoustical Society of America 31 (1959) 952–962. doi:10.1121/1.1907821.

[16] E. E. Ungar, E. M. Kerwin, Loss factors of viscoelastic systems in terms of energy concepts, The Journal of The Acoustical Society of America 34 (1962) 954–957. doi:10.1121/1.1918227.

[17] S. Hwang, R. Gibson, The use of strain energy-based finite element techniques in the analysis of various aspects of damping of composite materials and structures, Journal of Composite Materials 26 (17) (1992) 2585–2605. doi:10.1177/002199839202601707.

[18] O. Foin, N. Atalla, J. Nicolas, A formulation for the vibro-acoustic behavior of a rectangular plate with constrained-layer damping, Vol. 21, 1993, pp. 59–60. doi:https://jcaa.caa-aca.ca/index.php/jcaa/article/view/774.

[19] O. Foin, J. Nicolas, N. Atalla, An efficient tool for predicting the structural acoustic and vibration response of sandwich plates in light or heavy fluid, Applied Acoustics 57 (1999) 213–242. doi:10.1016/S0003-682X(98)00059-0.

[20] E. Manconi, S. Sorokin, On the effect of damping on dispersion curves in plates, International Journal of Solids and Structures 50 (11–12) (2013) 1966–1973. doi:10.1016/j.ijsolstr.2013.02.016.

[21] E. Manconi, B. R. Mace, Estimation of the loss factor of viscoelastic laminated panels from finite element analysis, Journal of Sound and Vibration 329 (19) (2010) 3928–3939. doi:10.1016/j.jsv.2010.04.014.

[22] C. W. Chan, P. Cawley, Lamb waves in highly attenuative plastic plates, Journal of the Acoustical Society of America 104 (1998) 874–881. doi:10.1121/1.423332.

[23] A. Bernard, M. J. S. Lowe, M. Deschamps, Guided waves energy velocity in absorbing and non-absorbing plates, Journal of the Acoustical Society of America 110 (2001) 186–196. doi:10.1121/1.1375845.

[24] F. Simonetti, P. Cawley, On the nature of shear horizontal wave propagation in elastic plates coated with viscoelastic materials, Procedings of the Royal Society A Mathematical Physical and Engineering Sciences 460 (2004) 2197–2221. doi:10.1098/rspa.2004.1284.

[25] F. Simonetti, M. J. S. Lowe, On the meaning of lamb mode nonpropagating branches, Journal of the Acoustical Society of America 118 (2005) 186–192. doi:10.1121/1.1938528.

[26] I. Bartoli, A. Marzani, F. L. di Scalea, E. Viola, Modeling wave propagation in damped waveguides of arbitrary cross-section, Journal of Sound and Vibration 295 (2006) 685–707. doi:10.1016/j.jsv.2006.01.021.

[27] L. Taupin, A. Lhémery, G. Inquiété, A detailed study of guided wave propagation in a viscoelastic multilayered anisotropic plate, Journal of Physics: Conference Series 269 (2011) 012002. doi:10.1088/1742-6596/269/1/012002.

[28] M. Collet, M. Ouisse, M. Ichchou, M. Ruzzene, Semi-active optimization of 2d wave's dispersion into mechanical systems by the mean of periodically distributed shunted piezoelectric patches: A new class of adaptive metamaterials, 2011. doi:10.1117/12.883118.

[29] S. Ghinet, N. Atalla, Modeling thick composite laminate and sandwich structures with linear viscoelastic damping, Computers Structures 89 (15-16) (2011) 1547–1561. doi:10.1016/j.compstruc.2010.09.008.

[30] D. Cui, N. Atalla, M. Ichchou, A.-M. Zine, Damping prediction of highly dissipative meta-structures through a wave finite element methodology, Mechanical Systems and Signal Processing 215 (2024) 111408. doi:10.1016/j.ymssp.2024.111408.

[31] L. Cremer, M. A. Heckl, E. E. Ungar, T. Northwood, Structure-borne Sound, 2nd Edition, Springer-Verlag, Berlin, Heidelberg, Germany, 1974. doi:10.1007/978-3-662-10121-6.

[32] P. G. Ciarlet, P. Destuynder, Justification of the two-dimensional linear plate model, Computer Methods in Applied Mechanics and Engineering 18 (2) (1979) 315–344. doi:10.1016/0045-7825(79)90089-6.

[33] G. Allaire, M. Briane, M. Vanninathan, A comparison between two-scale asymptotic expansions and bloch wave expansions for the homogenization of periodic structures, Computer Methods in Applied Mechanics and Engineering 73 (3) (2016) 237–259. doi:10.1007/s40324-016-0067-z.

[34] L. Jakabčin, P. Seppecher, On periodic homogenization of highly contrasted elastic structures, Journal of the Mechanics and Physics of Solids 144 (3) (2020) 104104. doi:10.1016/j.jmps.2020.104104.

[35] V. L. Berdichevsky, An Asymptotic Theory of Sandwich Plates, International Journal of Engineering Science 48 (3) (2010) 383–404. doi:10.1016/j.ijengsci.2009.09.001.

[36] E. Reissner, Reflexion on the theory of elastic plates, Applied Mechanics Review 38 (11) (1985) 1453–1464. doi:10.1115/1.3143699.

[37] J. N. Reddy, A simple higher-order theory for laminated composite plates, ASME. Journal of Applied. Mechanics 51 (4) (1984) 745–752. doi:10.1115/1.3167719.

[38] R. Khandan, S. Noroozi, P. Sewell, J. Vinney, The development of laminated composite plate theories: a review, Journal of Materials Science 47 (2012) 5901–5910. doi:10.1007/s10853-012-6329-y.

[39] J. M. Whitney, N. J. Pagano, Shear deformation in heterogeneous anisotropic plates, Journal of Applied Mechanics 37 (1970) 1031–1036. doi:10.1115/1.3408654.

[40] A. Khdeir, J. Reddy, Free vibrations of laminated composite plates using second-order shear deformation theory, Computers Structures 71 (6) (1999) 617–626. doi:10.1016/S0045-7949(98)00301-0.

[41] L. Librescu, A. A. Khdeir, J. N. Reddy, A comprehensive analysis of the state of elastic anisotropic flat plates using refined theories, International Journal of Solids and Structures 70 (1987) 57–81. doi:10.1007/BF01174647.

[42] K. Renji, P. S. Nair, Modal density of composite honeycomb sandwich panels, Journal of Sound and Vibration 195 (5) (1996) 687–699. doi:10.1006/jsvi.1996.0456.

[43] D. Bhaskar, A.G.Thakur, I. Sayyad, S. Bhaskar, Numerical analysis of thick isotropic and transversely isotropic plates in bending using fe based new inverse shear deformation theory, International Journal of Automotive and Mechanical Engineering 18 (3) (2021) 8882 – 8894. doi:10.15282/ijame.18.3.2021.04.0681.

[44] C. T. Hoang, A. Ferreira, H. Nguyen-Xuan, L. Nguyen, P. van Phuc, A nonlocal strain gradient analysis of laminated composites and sandwich nanoplates using meshfree approach, Engineering with Computers 39 (2023) 1835–1841. doi:10.1007/s00366-021-01501-9.

[45] E. Carrera, Historical review of zig-zag theories for multilayered plates and shells, Applied Mechanics Review 56 (2003) 287–308. doi:10.1115/1.1557614.

[46] D. Li, Layerwise theories of laminated composite structures and their applications: A review, Archives of Computational Methods in Engineering 28 (2021) 577–600. doi:10.1007/s11831-019-09392-2.

[47] E. Reissner, The effect of transverse shear deformation on the bending of elastic plates, Journal of Applied Mechanics 12 (1945) A69–A77. doi:10.1115/1.4009435.

[48] J. N. Reddy, J. A. Mitchell, On refined nonlinear theories of laminated composite structures with piezoelectric laminae, Sadhana 20 (1995) 721–747. doi:10.1007/BF02823215.

[49] K. Naumenko, V. A. Eremeyev, A layer-wise theory for laminated glass and photovoltaic panels, Composite Structures 112 (2021) 283–291. doi:10.15282/ijame.18.3.2021.04.0681.

[50] H. Altenbach, V. A. Eremeyev, K. Naumenko, On the use of the first order shear deformation plate theory for the analysis of three-layer plates with thin soft core layer, Journal of Applied Mathematics and Mechanics 95 (10) (2015) 1004–1011. doi:10.1002/zamm.201500069.

[51] H. Altenbach, V. Eremeyev, Analysis of the viscoelastic behavior of plates made of functionally graded materials, Journal of Applied Mathematics and Mechanics 88 (5) (2008) 332–341. doi:10.1002/zamm.201500069.

[52] H. Altenbach, V. Eremeyev, On the bending of viscoelastic plates made of polymer foams, Acta Mechanica 204 (2009) 137–154. doi:10.1007/s00707-008-0053-3.

[53] E. Carrera, A. Ciuffreda, A unified formulation to assess theories of multilayered plates for various bending problems, Composite Structures 69 (3) (2005) 271–293. doi:10.1016/j.compstruct.2004.07.003.

[54] P. Foraboschi, Three-layered plate: Elasticity solution, Composites Part B: Engineering 60 (2014) 764–776. doi:10.1016/j.compositesb.2013.06.037.

[55] A. Figotin, P. Kuchment, Spectral properties of classical waves in high-contrast periodic media, SIAM Journal on Applied Mathematics 58 (1998) 683–702. doi:10.1137/S0036139996297249.

[56] V. P. Smyshlyaev, Propagation and localization of elastic waves in highly anisotropic periodic composites via two-scale homogenization, Mechanics of Materials 41 (2009) 434–447. doi:10.1016/j.mechmat.2009.01.009.

[57] M. Cherdantsev, K. Cherednichenko, Two-scale -convergence of integral functionals and its application to homogenisation of nonlinear high-contrast periodic composites, Arch Rational Mech Anal 204 (2012) 445–478. doi:10.1007/s00205-011-0481-4.

[58] C. J. Chapman, An asymptotic decoupling method for waves in layered media, Proceedings of the Royal Society A 469 (2013) 20120659. doi:10.1098/rspa.2012.0659.

[59] J. Kaplunov, A.Nobili, Multi-parametric analysis of strongly inhomogeneous periodic waveguides with internal cutoff frequencies, Mathematical Methods in the Applied Sciences 40 (2016) 3381–3392. doi:10.1002/mma.3900.

[60] P. E. Tovstik, T. P. Tovstik, Generalized timoshenko-reissner models for beams and plates, strongly heterogeneous in the thickness direction, ZAMM - Journal of Applied Mathematics and Mechanics 97 (2016) 296–308. doi:10.1002/zamm.201600052.

[61] A. Kudaibergenov, A. Nobili, L. Prikazchikova, On low-frequency vibrations of a composite string with contrast properties for energy scavenging fabric devices, Journal of Mechanics of Materials and Structures 11 (2016) 3231–3243. doi:10.2140/jomms.2016.11.n3p3.

[62] J. R. Willis, The overall elastic response of composite materials, Journal of Applied Mechanics 50 (4b) (1983) 1202–1209. doi:10.1115/1.3167202.

[63] V. L. Berdichevsky, Homogenization and two-scale convergence, SIAM Journal on Mathematical Analysis 23 (6) (1992) 1482–1518. doi:10.1137/0523084.

[64] A. Braides, V. C. Piat, A. Piatnitski, A variational approach to double porosity problems, Asymptotic Analysis 39 (3) (2004) 281–308.

[65] A. Benssousan, J. Lions, G. Papanicoulau, Asymptotic Analysis for Periodic Structures, 5th Edition, North Holland Publishing Company, Amesterdam, Holland, 1978.

[66] A. L. Kalamkarov, I. V. Andrianov, V. V. Danishevskyy, Asymptotic homogenization of composite materials and structures, Applied Mechanics Reviews 62 (3) (2009) 030802. doi:10.1115/1.3090830.

[67] D. Caillerie, Thin elastic and periodic plates, Mathematical Methods in the Applied Sciences 6 (1) (1984) 159–191. doi:10.1002/mma.1670060112.

[68] T. Lewinsky, J. J. Telega, Plates, Laminates and Shells - Asymptotic Analysis and Homogenization, 5th Edition, World Scientific, Singapour, 2020.

[69] D. Cioranescu, J. S. J. Paulin, Homogenization in open sets with holes, Journal of Mathematical Analysis and Applications 71 (2) (1979) 590–607. doi:10.1016/0022-247X(79)90211-7.

[70] C. Boutin, J. Soubestre, Generalized inner bending continua for linear fiber reinforced materials, International Journal of Solids and Structures 48 (3-4) (2011) 517–534. doi:10.1016/j.ijsolstr.2010.10.017.

[71] E. Sanchez-Palencia, Non-Homogeneous Media and Vibration Theory, 1st Edition, Springer Verlag, Berlin, Deutschlan, 1980.

[72] J.-L. Auriault, C. Boutin, C. Geindreau, Homogenization of Coupled Phenomena in Heterogenous Media, 1st Edition, ISTE and Wiley, London, Great Britain, 2009.

[73] M. Z. Aşık, S. Tezcan, Laminated glass beams: Strength factor and temperature effect, Computers Structures 84 (2006) 364–373. doi:10.1016/j.compstruc.2005.09.025.

[74] L. Galuppi, G. Royer-Carfagni, Laminated beams with viscoelastic interlayer, International Journal of Solids and Structures 49 (2012) 2637–2645. doi:10.1016/j.ijsolstr.2012.05.028.

[75] J. Kaplunov, D. Prikazchikov, L. Prikazchikova, Dispersion of elastic waves in a strongly inhomogeneous three-layered plate, International Journal of Solids and Structures 49 (2017) 113–114. doi:10.1016/j.ijsolstr.2017.01.042.

[76] B. Zhu, L. Nechak, O. Bareille, Kriging metamodeling approach for predicting the dispersion curves for wave propagating in complex waveguide, Journal of Sound and Vibration 551 (2023) 117595. doi:10.1016/j.jsv.2023.117595.

[77] D. Chronopoulos, B. Troclet, M. Ichchou, J. Lainé, A unified approach for the broadband vibroacoustic response of composite shells, Composites Part B: Engineering 43 (2012) 1837–1846. doi:10.1016/j.compositesb.2012.01.059.

[78] G. Tufano, K-space analysis of complex large-scale periodic structures, Ph.D. thesis, École Centrale de Lyon KU Leuven (2020).

[79] L. Brillouin, Wave Propagation in Periodic Structures, 2nd Edition, McGraw-Hill Book Company, Canada, 1946. doi:10.1002/9780470747339.

[80] D. J. Mead, Free wave propagation in two-dimensional periodic plates, Journal of Sound and Vibration 64 (3) (1979) 325–348. doi:10.1016/0022-460X(79)90581-9.

[81] A. L. Abrahamson, Flexural wave mechanics - an analytical approach to the vibration of periodic structures forced by convected pressure fields, Journal of Sound and Vibration 28 (3) (1973) 247–258. doi:10.1016/S0022-460X(73)80105-1.

[82] R. Orris, M. Petyt, A finite element study of harmonic wave propagation in periodic structures, Journal of Sound and Vibration 33 (2) (1974) 223–236. doi:10.1016/S0022-460X(74)80108-2.

[83] R. M. Orris, Random response of periodic structures by a finite element technique, Journal of Sound and Vibration 43 (1) (1975) 1–8. doi:10.1016/0022-460X(75)90199-6.

[84] C. Zhou, Wave and modal coupled approach for multi-scale analysis of periodic structures, Ph.D. thesis, École Centrale de Lyon (2014).

[85] V. Cool, L. V. Belle, C. Claeys, E. Deckers, W. Desmet, Impact of the unit cell choice on the efficiency of dispersion curve calculations using gbms, Journal of Vibration and Acoustics 144 (2) (2022) 024501. doi:10.1115/1.4051817.

[86] J.-M. Mencik, M. Ichchou, Multi-mode propagation and diffusion in structures through finite elements, European Journal of Mechanics – A/Solids 24 (5) (2005) 877–898. doi:10.1016/j.euromechsol.2005.05.004.

[87] J.-M. Mencik, M. Ichchou, A substructuring technique for finite element wave propagation in multi-layered systems, Computer Methods in Applied Mechanics and Engineering 197 (6-8) (2008) 505–523. doi:10.1016/j.cma.2007.08.002.

[88] C. Droz, R. Boukadia, M. Ichchou, W. Desmet, Diffusion-based design of locally resonant subsystems using a reduced wave finite element framework, 2018, pp. 3071–3084.

[89] Z. Changwei, J.-P. LAINÉ, M. ICHCHOU, A.-M. ZINE, Multi-scale modelling for two-dimensional periodic structures using a combined mode/wave based approach, Computers Structures 154 (6) (2015) 556–575. doi:10.1016/j.compstruc.2015.03.006.

[90] C. Zhou, J.-P. Lainé, M. Ichchou, A.-M. Zine, Numerical and experimental investigation on broad-band wave propagation features in perforated plates, Mechanical Systems and Signal Processing 12 (6) (2016) 556–575. doi:10.1016/j.ymssp.2015.12.006.

[91] C. Zhou, X. Zhou, M. Ichchou, A.-M. Zine, J.-P. Lainé, S. Hans, C. Boutin, Investigation of dynamics of discrete framed structures by a numerical wave-based method and an analytical homogenization approach, Chinese Journal of Aeronautics 30 (1) (2017) 66–74. doi:10.1016/j.cja.2016.12.002.

[92] X. Sun, C. Zhou, M. Ichchou, J.-P. Lainé, A.-M. Zine, Multi-scale homogenization of transversal waves in periodic composite beams, International Journal of Applied Mechanics 09 (3) (2017) 1750039. doi:10.1142/S1758825117500399.

[93] V. Thierry, L. Brown, D. Chronopoulos, Multi-scale wave propagation modelling for two-dimensional periodic textile composites, Composites Part B: Engineering 150 (2018) 144–156. doi:10.1016/j.compositesb.2018.05.052.

[94] J.-L. Christen, M. Ichchou, A. Zine, B. Troclet, Wave finite element formulation of the acoustic transmission through complex infinite plates, Acta Acustica United Acustica 102 (6) (2016) 984–991. doi:10.3813/AAA.919013.

[95] Z. Zergoune, Approches méso-macro pour la modélisation de la transmission acoustique des sandwiches, Ph.D. thesis, École Centrale de Lyon, Université de Lyon (2016).

[96] J.-M. Mencik, A wave finite element approach for the analysis of periodic structures with cyclic symmetry in dynamic substructuring, Journal of Sound and Vibration 431 (2018) 441–457. doi:10.1016/j.jsv.2018.05.027.

[97] R. Boukadia, E. Deckers, C. Claeys, M. Ichchou, W. Desmet, A wave-based optimization framework for 1d and 2d periodic structures, Mechanical Systems and Signal Processing 139 (2020) 106603. doi:10.1016/j.ymssp.2019.106603.

[98] N. Guenfoud, C. Droz, M. Ichchou, O. Bareille, E. Deckers, W. Desmet, On the multi-scale vibroacoustic behavior of multi-layer rectangular core topology systems, Mechanical Systems and Signal Processing 143 (2020) 106629. doi:10.1016/j.ymssp.2020.106629.

[99] B. Yang, C. Droz, A. Zine, M. Ichchou, Dynamic analysis of second strain gradient elasticity through a wave finite element approach, Composite Structures 263 (2021) 113425. doi:10.1016/j.compstruct.2020.113425.

[100] B. Yang, M. Ichchou, A. Zine, C. Droz, Multi-mode propagation and diffusion analysis using the three-dimensional second strain gradient elasticity, Mechanical Systems and Signal Processing 187 (2023) 109970. doi:10.1016/j.ymssp.2022.109970.

[101] B. Yang, A. Zine, C. Droz, M. Ichchou, Two-dimensional periodic structures modeling based on second strain gradient elasticity for a beam grid, International Journal of Mechanical Sciences 222 (2022) 107199. doi:10.1016/j.ijmecsci.2022.107199.

[102] F. Errico, M. Ichchou, S. D. Rosa, O. Bareille, F. Franco, The modelling of the flow-induced vibrations of periodic flat and axial-symmetric structures with a wave-based method, Journal of Sound and Vibration 424 (2018) 32–47. doi:10.1016/j.jsv.2018.03.012.

[103] F. Errico, F. Franco, S. D. Rosa, G. Petrone, M. Ichchou, Aeroelastic effects on wave propagation and sound transmission of plates and shells, AIAA JOURNAL 58 (2019) 1–7. doi:10.2514/1.J058722.

[104] F. Errico, S. D. Rosa, M. Ichchou, F. Franco, O. Bareille, Dispersion curves of infinite laminate panels through a modal analysis of finite cylinders, Wave Motion 83 (2018) 80–93. doi:10.1016/j.wavemoti.2018.08.007.

[105] F. Errico, G. Tufano, O. Robin, N. Guenfoud, M. Ichchou, N. Atalla, Simulating the sound transmission loss of complex curved panels with attached noise control materials using periodic cell wavemodes, Applied Acoustics 156 (2019) 21–28. doi:10.1016/j.apacoust.2019.06.027.

[106] F. Errico, M. Ichchou, F. Franco, S. D. Rosa, O. Bareille, C. Droz, Schemes for the sound transmission of flat, curved and axisymmetric structures excited by aerodynamic and acoustic sources, Journal of Sound and Vibration 456 (2019) 221–238. doi:10.1016/j.jsv.2019.05.041.

[107] F. Errico, M. Ichchou, S. D. Rosa, F. Franco, O. Bareille, Investigations about periodic design for broadband increased sound transmission loss of sandwich panels using 3d-printed models, Mechanical Systems and Signal Processing 136 (2020) 106432. doi:10.1016/j.ymssp.2019.106432.

[108] E. Manconi, Modelling wave propagation in two-dimensional structures using a wave/finite element technique, Ph.D. thesis, University of Parma (2008).

[109] E. Manconi, B. R. Mace, R. Garziera, Wave propagation in laminated cylinders with internal fluid and residual stress, Applied Sciences 13 (2023) 5227. doi:10.3390/app13095227.

[110] Y. Yang, B. R. Mace, M. J. Kingan, Prediction of sound transmission through, and radiation from, panels using a wave and finite element method, The Journal of the Acoustical Society of America 141 (2017) 2452. doi:10.1121/1.4977925.

[111] Y. Yang, B. R. Mace, M. J. Kingan, Wave and finite element method for predicting sound transmission through finite multi-layered structures with fluid layers, Computers Structures 204 (2018) 20–30. doi:10.1016/j.compstruc.2018.04.003.

[112] Y. Yang, C. Fenemore, M. J. Kingan, B. R. Mace, Analysis of the vibroacoustic characteristics of cross laminated timber panels using a wave and finite element method, Journal of Sound and Vibration 494 (2021) 115842. doi:10.1016/j.jsv.2020.115842.

[113] B. Yang, A. Zine, C. Droz, M. Ichchou, Two-dimensional periodic structures modeling based on second strain gradient elasticity for a beam grid, International Journal of Mechanical Sciences 222 (2023) 107199. doi:10.1016/j.ijmecsci.2022.107199.

[114] Y. Yang, B. R. Mace, M. J. Kingan, Vibroacoustic analysis of periodic structures using a wave and finite element method, Journal of Sound and Vibration 457 (2019) 333–353. doi:10.1016/j.jsv.2019.06.009.

[115] B. Yang, C. Droz, A. Zine, M. Ichchou, Dynamic analysis of second strain gradient elasticity through a wave finite element approach, Composite Structures 263 (2021) 113425. doi:10.1016/j.compstruct.2020.113425.

[116] W. Desmet, A wave-based prediction technique for coupled vibro-acoustic analysis, Ph.D. thesis, Katholieke Universiteit Leuven (Catholic University of Leuven) (1998).

[117] C. Zhou, J.-P. Lainé, M. Ichchou, Wave finite element method based on reduced model for one-dimensional periodic structures, International Journal of Applied Mechanics 07 (02) (2015) 1550018. doi:10.1142/S1758825115500180.

[118] L. Alimonti, N. Atalla, B. Gardner, Assessment of a contour integral method for the nonlinear eigenvalue problem arising from the wave finite element description of two-dimensional periodic waveguides involving dissipative and frequency dependent properties media, 2018.

[119] A. Bocquillet, M. Ichchou, L. Jezequel, Energetics of axisymmetric fluid-filled pipes up to high frequencies, Journal of Fluids and Structures 17 (4) (2003) 491–510. doi:10.1016/S0889-9746(02)00161-5.

[120] Q. Serra, M. Ichchou, J.-F. Deü, Wave properties in poroelastic media using a wave finite element method, Journal of Sound and Vibration 335 (2015) 125–146. doi:10.1016/j.jsv.2014.09.022.

[121] Q. Serra, M. N. Ichchou, J.-F. Deü, On the use of transfer approaches to predict the vibroacoustic response of poroelastic media, Journal of Computational Acoustics 24 (02) (2016) 1550020. doi:10.1142/S0218396X15500204.

[122] M. Ichchou, J.-M. Mencik, W. Zhou, Wave finite elements for low and mid-frequency description of coupled structures with damage, Computer Methods in Applied Mechanics and Engineering 198 (15-16) (2009) 1311–1326. doi:10.1016/j.cma.2008.11.024.

[123] B. Mace, E. Manconi, Wave motion and dispersion phenomena: Veering, locking and strong coupling effects, Journal of the Acoustical Society of America 131 (15-16) (2012) 1015–1028. doi:10.1121/1.3672647.

[124] S. Güttel, The nonlinear eigenvalue problem, Acta Numerica 26 (2017) 1–94. doi:10.1017/S0962492917000034.

[125] B. Bloss, M. D. Rao, Measurement of damping in structures by the power input method, Experimental Techniques 26 (2002) 30–32. doi:10.1111/j.1747-1567.2002.tb00066.x.

[126] M. Bolduc, N. Atalla, A. Wareing, Measurement of sea damping loss factor for complex structures, Université de Sherbrooke, Canada, 2005.

[127] G. A. Papagiannopoulos, G. D. Hatzigeorgiou, On the use of the half-power bandwidth method to estimate damping in building structures, Soil Dynamics and Earthquake Engineering 31(7) (2011) 1075–1079. doi:10.1016/j.soildyn.2011.02.007.

[128] C. Liu, G. Goetchius, Estimation of damping loss factors by using the hilbert transform and exponential average method, SAE Technical Paper 01 (2001) 1075–1079. doi:10.4271/2001-01-1408.

[129] N. Atalla, F. Sgard, Finite Element and Boundary Methods in Structural Acoustics and Vibration, Taylor Francis Group, London, England, 2015.

[130] R. H. Lyon, R. G. DeJong, Fundamentals of Vibrations, 2nd Edition, Butterworth-Heinemann, Oxford, Great Britain, 2001. doi:10.1016/C2009-0-26747-X.

[131] M. BOLDUC, N. Atalla, Measurement of sea damping loss factor for complex structures, Journal of the Acoustical Society of America 3060 (123) (2008) 226–240. doi:10.1121/1.2932796.

[132] M. Bolduc, Acquiring statistical energy analysis dainping loss factor for complex structures with low to high dainping characteristics, Ph.D. thesis, Université de Sherbrooke (2007).

[133] F. Jacobsen, A note on acoustic decay measurements, Journal of Sound and Vibration 115 (1) (1987) 163–170. doi:10.1016/0022-460X(87)90497-4.

[134] R. H. Lyon, Statistical Energy Analysis of Dynamical Systems: Theory and Applications, 1st Edition, The MIT Press, Cambridge, UK, 1975.

[135] Standard test method for sound absorption and sound absorption coefficients by the reverberation room method, Standard, American Society for Testing and Materials Committee, New York, USA (october 2008). doi:10.1520/C0423-22.

[136] M. Ichchou, B. Hiverniau, B. Troclet, Equivalent 'rain-on-the-roof' loads for random spatially correlated excitations in the mid–high frequency range, Journal of Sound and Vibration 322 (2008) 926–940. doi:10.1016/j.jsv.2008.11.050.

[137] F. Fahy, Energy flow between oscillators: Special case of point excitation, Journal of Sound and Vibration 11 (4) (1970) 481–483. doi:10.1016/S0022-460X(70)80012-8.

[138] M. N. B. Fazail, J.-D. Chazot, G. Lefebvre, N. Atalla, Damping loss factor characterization of complex structures using a green's function-based model, Journal of Sound and Vibration 552 (2023) 117642. doi:10.1016/j.jsv.2023.117642.

[139] B. Bloss, M. D. Rao, A comparison between power injection and impulse response decay methods for estimating frequency averaged loss factors for sea, Journal of Passenger Car: Mechanical Systems Journal 112 (2003) 1878–1890. doi:10.4271/2003-01-1566.

[140] F. Marchetti, K. Ege, Q. Leclère, N. Roozen, On the structural dynamics of laminated composite plates and sandwich structures; a new perspective on damping identification, Journal of Sound and Vibration 474 (2020) 115256. doi:10.1016/j.jsv.2020.115256.

[141] L. Cremer, M. Heckl, E. E. Ungar, T. D. Northwood, Structure-Borne Sound, 1988.

[142] I. L. Ver, L. L. Beranek, Noise and Vibration Control Engineering, 2nd Edition, Wiley, New York, United States, 1992.

[143] F. Errico, Flow-induced vibrations and noise in periodic structural systems, Ph.D. thesis, École Centrale de Lyon (2020).

[144] F. G. Leppington, Resonant and non-resonant acoustic properties of elastic panels ii: the transmission problem, Vol. 412, London, UK, 1987. doi:10.1007/978-981-99-7958-5_11.

[145] M. Villot, C. Guigou, L. Gagliardini, Predicting the acoustical radiation of finite size multi-layered structures by applying spatial windowing on infinite structures, Journal of Sound and Vibration 245 (2001) 433–455. doi:10.1006/jsvi.2001.3592.

[146] S. Ljunggren, A new type of solution for plate vibrations at low frequencies, Journal of Sound and Vibration 116 (1987) 125–136. doi:10.1016/S0022-460X(87)81324-X.

[147] A. E. H. Love, The small free vibrations and deformation of a thin elastic shell, Philosophical Transactions of the Royal Society A 179 (1988) 491–546. doi:10.1098/rsta.1888.0016.

[148] J. L. Davy, Predicting the sound insulation of single leaf walls: Extension of cremer's model, The Journal of the Acoustical Society of America 126 (2009) 1871–1877. doi:10.1121/1.3206582.

[149] H. Manfred, D. Ulrich, Acoustic absorption of thick walls, Rundfunktechnische Mitteilungen 29 (1985) 287 – 291. doi:https://www.scopus.com/record/display.uri?eid=2-s2.0-0022150620&origin=inward.

[150] R. D. Mindlin, Influence of rotatory inertia and shear on flexural motions of isotropic, elastic plates, Journal of Applied Mechanics 18 (1951) 31–38. doi:10.1115/1.4010217.

[151] E. Reissner, The effect of transverse shear deformation on the bending of elastic plates, Journal of Applied Mechanics 12 (1945) A69–A7. doi:10.1115/1.4009435.

[152] H. Hencky, Über die berücksichtigung der schubverzerrung in ebenen platten [on the introduction of shear motion in flat plates], Ingenieur-Archiv 16 (1947) 72–76. doi:10.1007/BF00534518.

[153] S. Ljunggren, Forced vibrations of infinite plates, Journal of Sound and Vibration 121 (1988) 221–236. doi:10.1016/S0022-460X(88)80026-9.

[154] S. Ljunggren, Airborne sound insulation of thick walls, The Journal of the Acoustical Society of America 89 (1991) 2338–2345. doi:10.1121/1.400972.

[155] E. Carrera, An assessment of mixed and classical theories on global and local response of multilayered orthotropic plates, Composite Structures 50 (2000) 183–198. doi:10.1016/S0263-8223(00)00099-4.

[156] E. Carrera, Theories and finite elements for multilayered, anisotropic, composite plates and shells, Archives of Computational Methods in Engineering 9 (2002) 87 – 140. doi:10.1007/BF02736649.

[157] M. Levinson, An accurate, simple theory of the statics and dynamics of elastic plates, Mechanics Research Communications 7 (1980) 343–350. doi:10.1016/0093-6413(80)90049-X.

[158] M. Touratier, An efficient standard plate theory, International Journal of Engineering Science 29 (1991) 901–916. doi:10.1016/0020-7225(91)90165-Y.

[159] M. Karama, K. Afaq, S. Mistou, Mechanical behaviour of laminated composite beam by the new multi-layered laminated composite structures model with transverse shear stress continuity, International Journal of Solids and Structures 40 (2003) 1525–1546. doi:10.1016/S0020-7683(02)00647-9.

[160] X. Lu, D. Liu, Interlayer shear slip theory for cross-ply laminates with nonrigid interfaces, AIAA Journal 30 (1992) 1063–1073. doi:10.2514/3.11028.

[161] C.-T. Sun, J. M. Whitney, Interlayer shear slip theory for cross-ply laminates with nonrigid interfaces, AIAA Journal 11 (1973) 178–183. doi:10.2514/3.50448.

[162] R. Ford, P. Lord, A. Walker, Sound transmission through sandwich constructions, Journal of Sound and Vibration 5 (1967) 9–21. doi:10.1016/0022-460X(67)90173-3.

[163] C. P. Smolenski, E. M. Krokosky, Dilational-mode sound transmission in sandwich panels, The Journal of Acoustical Society of America 54 (1967) 1449–1457. doi:10.1121/1.1914444.

[164] J. A. Moore, R. H. Lyon, Sound transmission loss characteristics of sandwich panel constructions, The Journal of Acoustical Society of America 89 (1991) 777–791. doi:10.1121/1.1894638.

[165] S. Narayanan, R. Shanbhag, Sound transmission through a damped sandwich panel, Journal of Sound and Vibration 80 (1982) 315–327. doi:10.1016/0022-460X(82)90273-5.

[166] S. Srinivas, A refined analysis of composite laminates, Journal of Sound and Vibration 30 (1973) 495–507. doi:10.1016/S0022-460X(73)80170-1.

[167] J. Guyader, C. Lesueur, Acoustic transmission through orthotropic multilayered plates, part i: Plate vibration modes, Journal of Sound and Vibration 58 (1978) 51–68. doi:10.1016/S0022-460X(78)80060-1.

[168] J. Guyader, C. Lesueur, Acoustic transmission through orthotropic multilayered plates, part ii: Transmission loss, Journal of Sound and Vibration 58 (1978) 69 – 86. doi:10.1016/S0022-460X(78)80061-3.

[169] C. Lee, D. Liu, Layer reduction technique for composite laminate analysis, Computers Structures 44 (1992) 1305–1315. doi:10.1016/0045-7949(92)90374-9.

[170] R. L. Woodcock, Free vibration of advanced anisotropic multilayered composites with arbitrary boundary conditions, Journal of Sound and Vibration 312 (2008) 769–788. doi:10.1016/j.jsv.2007.11.015.

[171] A. Loredo, A. Castel, A multilayer anisotropic plate model with warping functions for the study of vibrations reformulated from woodcock's work, Journal of Sound and Vibration 332 (2013) 102–125. doi:10.1016/j.jsv.2012.07.033.

[172] A. Loredo, A multilayered plate theory with transverse shear and normal warping functions, Composite Structures 156 (2016) 361–374. doi:10.1016/j.compstruct.2015.08.084.

[173] J.-L. Guyader, C. Cacciolati, Viscoelastic properties of single layer plate material equivalent to multi-layer composites plate, ISTANBUL, Turkey, 2007.

[174] U. Arasan, F. Marchetti, F. Chevillotte, G. Tanner, D. Chronopoulos, E. Gourdon, On the accuracy limits of plate theories for vibro-acoustic predictions, Journal of Sound and Vibration 493 (2021) 115848. doi:10.1016/j.jsv.2020.115848.

[175] S. Ghinet, N. Atalla, H. Osman, Diffuse field transmission into infinite sandwich composite and laminate composite cylinders, Journal of Sound and Vibration 289 (2006) 745–778. doi:10.1016/j.jsv.2005.02.028.

[176] S. Ghinet, N. Atalla, The transmission loss of curved laminates and sandwich composite panels, The Journal of the Acoustical Society America 118 (2005) 774–790. doi:10.1121/1.1932212.

[177] J. F. Allard, N. Atalla, Propagation of Sound in Porous Media: Modelling Sound Absorbing Materials, 2nd Edition, John Wiley Sons Ltd, Chichester, United Kingdom, 2009. doi:10.1002/9780470747339.

[178] A. Mejdi, F. Sgrad, N. Atalla, Validity of transfer matrix method for prediction of the transmission loss of curved panels, Journal of the Acoustical Society of America 133 (5) (2013) 3600. doi:10.1121/1.4806666.

[179] A. Parrinello, G. Ghiringhelli, N. Atalla, Generalized transfer matrix method for periodic planar media, Journal of Sound and Vibration 464 (2020) 114993. doi:10.1016/j.jsv.2019.114993.

[180] A. Parrinello, K. Kesour, G. Ghiringhelli, N. Atalla, Diffuse field transmission through multilayered cylinders using a transfer matrix method, Mechanical Systems and Signal Processing 136 (2020) 106514. doi:10.1016/j.ymssp.2019.106514.

[181] A. Parrinello, W. Belgacem, S. Ghinet, N. Atalla, Sound transmission through baffled multilayered curved shells using a transfer matrix method, Frontiers in Mechanical Engineering 8 (2022) 1034555. doi:10.3389/fmech.2022.1034555.

[182] A. Parrinello, G. L. Ghiringhelli, Transfer matrix representation for periodic planar media, Journal of Sound and Vibration 371 (2016) 196–209. doi:10.1016/j.jsv.2016.02.005.

[183] N. Atalla, R. Panneton, P. Debergue, A mixed displacement-pressure formulation for poroelastic materials, The Journal of Acoustical Society of America 104 (1998) 1444–1452. doi:10.1121/1.424355.

[184] D. Cui, M. Ichchou, N. Atalla, A.-M. Zine, On the wave-based approaches for wavespace of highly contrasted structures with viscoelastic damping, Chinese Journal of Aeronautics Accpetd for publication (2024).

[185] P. Ciarlet, Theory of Plates - Mathematical Elasticity, 1st Edition, SIAM, North Holland, 1997.

[186] M. Abramowitz, I. Stegun, Handbook of mathematical functions with formulas, graphs, and mathematical tables, illustrated edition Edition, Martino Fine Books, New York, United States of America, 1965.

[187] W.-J. Beyn, An integral method for solving nonlinear eigenvalue problems, linear algebra and its applications, Linear Algebra Application 436 (2012) 3839–3863. doi:10.1016/j.laa.2011.03.030.

[188] J. Asakura, T. Sakurai, H. Tadano, T. Ikegami, K. Kimura, A numerical method for nonlinear eigenvalue problems using contour integrals, Japan Society for Industrial and Applied Mathematics Letters 1 (2009) 52–55. doi:10.14495/jsiaml.1.52.

[189] S. Iwase, Y. Futamura, A. Imakura, T. Sakurai, T. Ono, Efficient and scalable calculation of complex band structure using sakurai-sugiura method, 2017. doi:10.1145/3126908.3126942.

[190] S. E. Laux, Solving complex band structure problems with the feast eigenvalue algorithm, Physical Review B 86 (2012) 075103. doi:10.1103/PhysRevB.86.075103.

[191] M. Mazzotti, I. Bartoli, A. Marzani, E. Viola, A coupled safe-2.5d bem approach for the dispersion analysis of damped leaky guided waves in embedded waveguides of arbitrary cross-section, Ultrasonics 53 (2013) 1227–1241. doi:10.1016/j.ultras.2013.03.003.

[192] J. Brenneck, E. Polizzi, An iterative method for contour-based nonlinear eigensolvers, arXiv preprint (2020). doi:10.48550/arXiv.2007.03000.

[193] T. Sakurai, J. Asakura, H. Tadano, T. Ikegami, Error analysis for a matrix pencil of hankel matrices with perturbed complex moments, Japan Society for Industrial and Applied Mathematics Letters 1 2 (2009) 76–79. doi:10.14495/jsiaml.1.76.

[194] M. V. Barel, P. Kravanja, Nonlinear eigenvalue problems and contour integrals, Journal of Computational and Applied Mathematics 292 (2016) 526–540. doi:10.1016/j.cam.2015.07.012.

[195] C. Kittel, Introduction to Solid State Physics, 8th Edition, Wiley, Canada, 2005.

[196] L. Quinteros, V. Meruane, E. L. Cardoso, R. O. Ruiz, Phononic bandgap optimization in sandwich panels using cellular truss cores, Materials 14 (18) (2021) 5236. doi:10.3390/ma14185236.

[197] Y. Futamura, H. Tadano, T. Sakurai, Parallel stochastic estimation method of eigenvalue distribution, Japan Society for Industrial and Applied Mathematics Letters 1 2 (2010) 127–130. doi:10.14495/jsiaml.2.127.

[198] I. Rzig, Modélisation des structures sandwich avec un amortissement viscoélastique intégré par une méthode hybride fem-tmm, Ph.D. thesis, Université de Sherbrooke (2016).

[199] R. J. Allemang, D. L. Brown, A correlation coefficient for modal vector analysis, 1982, pp. 110–116.

[200] M. Brehm, V. Zabel, C. Bucher, An automatic mode pairing strategy using an enhanced modal assurance criterion based on modal strain energies, Journal of Sound and Vibration 329 (2010) 5375–5392. doi:10.1016/j.jsv.2010.07.006.

[201] D. Ross, E. Ungar, E. J. Kerwin, Damping of plate flexural vibrations by means of viscoelastic laminae, Structural Damping 6 (6) (1959) 49–97. doi:10.1121/1.1907821.

[202] P. D'Haene, G. Savineau, Mechanical properties of laminated safety glass - fem study, in: Proceedings of GPD2007 - glass performance day, Tampere, Finland, 15th-18th June,2007, https://www.yumpu.com/en/document/view/560248/mechanical-properties-of-laminated-glass-fem-study-sun-tecch.

[203] E. Manconi, B. R. Mace, Wave characterization of cylindrical and curved panels using a finite element method, The Journal Acoustical Society of America 125 (2009) 154–163. doi:110.1121/1.3021418.

[204] R. Cherif, J.-D. Chazot, N. Atalla, Damping loss factor estimation of two-dimensional orthotropic structures from a displacement field measurement, Journal of Sound and Vibration 356 (2015) 61–71. doi:10.1016/j.jsv.2015.06.042.

[205] E. A. Magliula, J. G. McDaniel, A. D. Pierce, Far-field approximation for a point-excited anisotropic plate, The Journal of the Acoustical Society of America 131 (2012) 4535. doi:10.1121/1.4707482.

[206] Y. Waki, B. R. Mace, M. J. Brennan, Numerical issues concerning the wave and finite element method for free and forced vibrations of waveguides, Journal of Sound and Vibration 327 (2009) 92–108. doi:10.1016/j.jsv.2009.06.005.

[207] T. Wang, V. Sokolinsky, S. Rajaram, S. R. Nutt, Consistent higher-order free vibration analysis of composite sandwich plates, Composite Structures 82 (2008) 609–621. doi:10.1016/j.compstruct.2007.02.009.

[208] J.-M. Berthelot, Composite Materials, Mechanical Behaviour and Structural Analysis, 1st Edition, Spring-Verlag, New York, 1999. doi:10.1007/978-1-4612-0527-2.

dernière page de la thèse

AUTORISATION DE SOUTENANCE

Vu les dispositions de l'arrêté du 25 mai 2016 modifié par l'arrêté du 26 août 2022,

Vu la demande des directeurs de thèse

Messieurs M. ICHCHOU, N. ATALLA et A. ZINE

et les rapports de

Mme E. MANCONI
Professeure - Università di Parma - Dipartimento di Ingegneria e Architettura
Pal. 8Parco Area delle Scienze 181/A - I-43124 Parma - Italie

et de

M. S. MOREAU
Professeur - Université de Sherbrooke - Faculté de Génie Mécanique
2500, boul. de l'Université - Sherbrooke (Québec) J1K 2R1 - Canada

Monsieur CUI Dongze

est autorisé à soutenir une thèse pour l'obtention du grade de **DOCTEUR**

Ecole doctorale Mécanique, Energétique, Génie Civil, Acoustique

Fait à Ecully, le 18 septembre 2024

Pour le directeur de l'École Centrale de Lyon
Le directeur de la recherche

Christophe CORRE